



Facultat de Ciències - Departament de Física  
Estudis de doctorat en Física

Institut Català de Nanociència i Nanotecnologia (ICN2)  
Consejo Superior de Investigaciones Científicas (CSIC)

# ALL-OPTICAL PHASE MODULATION FOR ADVANCED INTERFEROMETRIC POINT-OF-CARE BIOSENSORS

DOCTORAL THESIS - SEPTEMBER 2014

Prof. L. M. Lechuga  
Director

Prof. J. Pascual  
Tutor

Stefania Dante  
Author



*A mamma e papà*



# Abstract

During the last decades impressive efforts have been devoted to the implementation of compact and highly sensitive lab-on-chip platforms for a wide range of decentralized applications. Among optical devices, those based on integrated optics have been underlined as promising candidates since they combine a high sensitivity in a label-free approach with a cost-effective fabrication through standard Si microfabrication technology, rendering in potential mass production. In particular interferometric arrangements have shown superior performances in terms of resolution and limits of detection compared to other integrated optics solutions as resonators or grating structures. However the complexity of their read-out, consequence of the periodicity of the output signal with the phase variation, still hinders their successful commercialization and adoption in the clinical practice.

In order to solve the limitations of standard integrated interferometric biosensors and to allow a complete integration onto a lab-on-chip platform, an innovative method for linearization of the interferometric output is theoretically and experimentally analyzed. The proposed phase modulation system is based on tuning of the emission wavelength of the laser source. In order to keep a compact and cost-effective platform, the wavelength modulation is introduced by taking advantage of the power-wavelength dependence of commercial laser diodes. Thanks to our research Group experience in the design and fabrication of integrated optical biosensors, two different platforms have been analyzed along this Thesis, namely the well-known Mach-Zehnder interferometer and the recently proposed Bimodal Waveguide interferometric biosensors. The wavelength modulated interferometric biosensors allow a direct, unambiguous, highly sensitive real-time read-out, as required by real biosensing applications.



# Resumen

Durante las últimas décadas un gran número de trabajos se han centrado en la implementación de plataformas *lab-on-chip* compactas y de alta sensibilidad, para una amplia gama de aplicaciones descentralizadas. Los dispositivos basados en óptica integrada se han revelado como candidatos prometedores, ya que combinan una alta sensibilidad en ensayos directos sin marcadores, con una fabricación de bajo coste a través de la tecnología estandar microelectrónica, permitiendo su producción en masa. En particular las configuraciones interferométricas han demostrado las prestaciones superiores, en términos de resolución y límite de detección, en comparación con otros dispositivos de óptica integrada como los resonadores o las redes de difracción. Sin embargo, la complejidad en la interpretación de su señal de respuesta, consecuencia de su periodicidad con las variaciones de fase, dificulta su comercialización y su adopción en la práctica clínica.

Para resolver las limitaciones de los biosensores interferométricos tradicionales y permitir una integración completa en una plataforma *lab-on-chip*, se ha estudiado teórica y experimentalmente un nuevo método para la linearización de la señal de salida. Este método se basa en la variación de la longitud de onda de emisión de la fuente láser, que se traduce en una modulación de fase. A fin de mantener una plataforma compacta y rentable, la modulación se introduce aprovechando la dependencia entre la longitud de onda y la potencia de los diodos láser comerciales. El método se ha aplicado a dos plataformas, los interferómetros Mach-Zehnder y de guía de onda bimodal, desarrollados en el grupo de investigación donde se ha realizado este trabajo. Los sensores interferométricos modulados en longitud de onda permiten una lectura directa en tiempo real y sin ambigüedades, con una alta sensibilidad tal y como requieren las aplicaciones biosensoras en ámbitos reales.





# Acknowledgments

Para concluir este trabajo es oportuno agradecer la ayuda y soporte de todos los que han permitido su realización, acompañandome a lo largo de este camino, tanto en el lado profesional como personal.

In primis, il grazie piú grande va sicuramente a mamma e papà che non hanno mai smesso di credere in me e di tenermi in piedi in ogni momento.. la distanza non ha influito sul vostro sostegno. Grazie dal piú profondo del cuore. E grazie a Giorgino, che si é sempre fatto trovare nel momento del bisogno.

Desde aquí quiero agradecer a Laura Lechuga su confianza en mi y la posibilidad que me ofreció, hace ya unos cuantos años, de empezar un doctorado en su grupo. Gracias por creer en mi y hacerme empezar esta aventura, de la cual aprendí muchísimo.

Todos los miembros del grupo nanoB2A han sido maravillosos conmigo, y no sé por donde empezar.. Gracias a Ana, que desde que era la pequeña Estefanía recién llegada, en mi estancia de solo unos meses (...), siempre me has acompañado (y vigilado) tanto en el lab como fuera. Gracias a Daphné, que has aparecido en mi camino llevandome hasta la luz y demostrado ser una óptima referencia tanto científica como personal. Merci pour tout!! Gracias a mis compañeros de despacho, que me han aguantado todo este tiempo con mis manías y cafés! Bert (BOtte!!!!), David F. (ay Fari!!! cuántas cosas en los últimos meses, un gracias particular!!), Sam (o Zam?), Jesús (a pesar de no estar nunca en el despacho!!) y Daniel recién reincorporado. Gracias por los momentos y sobre todo los cafés compartidos! No olvidaré las largas tardes y las charlas con vosotros! Gracias a los seniors del grupo Borja, Mar y M-Carmen, que siempre han sabido guiarme en función de su experiencia. Habéis sido pilares importantes en mi camino por aquí. Gracias a "mis niños", alias César y María, que han intentado con todas sus

---

fuerzas no hacerme enloquecer completamente y recordarme lo que hay fuera del lab. Cambiando de despacho gracias a Irais (OK!), Silvia, Joel, y los visitantes que nos han acompañado. Carlos y Sonia, recién incorporados, habeis traído aire nuevo en el grupo! y Rebe!! Que decirte.. eres increíble! Gracias por tu ayuda en estos meses.

Gracias a los que estuvieron en el grupo.. Orlando que me hizo mover los primeros pasos, David R. (Daviddddd!!!) que a través de su codo me ha transmitido mucho conocimiento, Elena, con la cual compartimos una buena temporada. Gracias a los que han pasado por temporadas mas o menos largas y los que volveran (Adriaaannnnnnn).

Gracias a Xavi Ros-Dos o lo que prefieras, has sido una referencia en todos estos años.

Fuera del grupo, quiero agradecer la ayuda de Pablo y Mireia por las medidas de AFM.

I would like to thank the members of the Photonics Research group of Gent university, where I spent an important period of my PhD. In particular I would like to thank Prof. Peter Bienstman for accepting me there, and the biosensor team who welcomed me: Cristina, Daan, Jan-Willem and Sam. Thank you guys for sharing your experience with me!

Volviendo al ICN2... Gracias a Sofia, por tus sonrisas y animos en el pasillo! Es siempre un placer cruzarse contigo!! Grazie a Flavio (uccil!!!) per tutto quello che abbiamo condiviso in questi anni.. senza te non sarebbe stata la stessa cosa! Grazie veramente.. Grazie ad Alberto per la stagione condivisa: le nostre birrette ci mancano proprio!

Uscendo dal lab posso finalmente ringraziare i membri, ufficiali e non, di casa Vallirana, istituzione fondamentale in questi anni di dottorato! Grazie specialmente a Sara ed Umbi, pilastri insostituibili che non mi hanno mai lasciato cadere... Grazie alle fanciulle Vero ed Eugi, che sono passate a portare un po' di giovinezza e spensieratezza nella nostra quotidianità. Grazie a Darío, ometto di casa, per aiutare nel momento del bisogno; grazie a Weppino (Chi, io??) per la sua allegria ed entusiasmo costanti!! E non si possono nominare tutti gli altri lampi fugaci che sono passati in questi anni... la lista sarebbe troppo lunga!

E finalmente, un grazie ad Enrico, per esserci sempre stato nonostante tutto... si gira una pagina e se ne apre un'altra, in cui ho molta fiducia..

# Contents

<b>Abstract</b>	<b>v</b>
<b>Resumen</b>	<b>vii</b>
<b>Acknowledgments</b>	<b>ix</b>
<b>Table of contents</b>	<b>xi</b>
<b>Motivation, aim and thesis outline</b>	<b>xv</b>
<b>1 Introduction</b>	<b>1</b>
1.1 Optical biosensors . . . . .	3
1.2 Integrated optics biosensors . . . . .	6
1.3 Lab-on-chip integration . . . . .	15
1.4 Interferometric limitations . . . . .	17
<b>2 Theory and modelization of IO interferometric biosensors</b>	<b>23</b>
2.1 Light propagation in optical waveguides . . . . .	23
2.2 Waveguide design . . . . .	36
2.3 Interferometric biosensor design . . . . .	40
2.4 Conclusions . . . . .	54
<b>3 Fabrication and characterization of IO interferometric biosensors</b>	<b>57</b>
3.1 Fabrication . . . . .	57
3.2 Morphological characterization . . . . .	60
3.3 Materials and methods . . . . .	64

3.4	Experimental set-up . . . . .	67
3.5	Optical characterization . . . . .	71
3.6	Homogeneous sensing evaluation . . . . .	71
3.7	Conclusions . . . . .	75
<b>4</b>	<b>Phase linearization for IO interferometric biosensors</b>	<b>77</b>
4.1	Phase linearization: overview . . . . .	77
4.2	Mathematical model of the phase modulation . . . . .	81
4.3	All-optical phase modulation . . . . .	85
4.4	Implementation of the all-optical phase modulation . . . . .	89
4.5	Conclusions . . . . .	100
<b>5</b>	<b><math>\lambda</math>M-BiMW biosensor</b>	<b>101</b>
5.1	General formulation of the wavelength modulation technique . . .	101
5.2	Experimental demonstration . . . . .	104
5.3	Bulk characterization . . . . .	109
5.4	Overcoming the critical effects . . . . .	112
5.5	Conclusions . . . . .	118
<b>6</b>	<b>Biosensor validation</b>	<b>119</b>
6.1	Biosensing: overview . . . . .	119
6.2	Surface biofunctionalization . . . . .	120
6.3	Biosensing validation . . . . .	121
6.4	Clinical applications of the $\lambda$ M-BiMW . . . . .	126
6.5	Conclusions . . . . .	131
<b>7</b>	<b>Towards a lab-on-chip platform</b>	<b>133</b>
7.1	Specifications and requirements . . . . .	133
7.2	Light in-coupling by diffraction gratings . . . . .	135
7.3	Multiplexed sensor schemes . . . . .	142
7.4	Surface biofunctionalization . . . . .	145
7.5	Microfluidics . . . . .	147
7.6	Optical read-out and electronics . . . . .	149
7.7	Multiplexed biosensing . . . . .	153
7.8	Conclusions . . . . .	156
	<b>General conclusions and future perspectives</b>	<b>159</b>
<b>A</b>	<b>Fourier expansion</b>	<b>163</b>

<b>B</b>	<b><math>\lambda</math>M-MZI complete modelization</b>	<b>165</b>
	Publications related to this doctoral thesis	169
	List of figures	173
	List of tables	179
	List of acronyms	181
	Bibliography	185



# Motivation, aim and Thesis outline

Nowadays, most clinical tests are time-consuming, expensive and have to be performed by specialized technicians in laboratory environments. These techniques typically require labeling of the samples or reagents with fluorescent or radioactive tags. Therefore, there is an unmet need of having reliable diagnostic tools that ensure a sensitive, rapid, affordable and simple analysis, particularly in the clinical practice. This could enable the decentralization of clinical diagnostics to Point-of-Care (POC) settings, allowing tests in primary care facilities and outpatient clinics, in hospital units, workplaces and homes, among others.

During the last decades an increasing number of scientific researches have been devoted to the realization of such integrated system trying to fulfill the above requirements. The basic idea of an integrated system is to gather in the same platform all the different operations necessary to perform an assay: from sample preparation (filtration, homogenization) to sensing and data processing. One of the most promising approaches employ micro/nano devices due to the advantages offered by the nanoscale approach, leading to smaller, faster and advanced devices. Reactions can take place in reduced fluid chambers, meaning a lower consumption of reagents and shorter analysis time. Furthermore the highly matured silicon technology can be adopted and adapted to the field of biosensor devices and life science applications. However, even if the technology for each component fabrication is mature, their integration is still a compelling challenge.

In this context, the research activity of our Group is focused on the development of highly-sensitive biosensors based on integrated photonics. Integrated Optics (IO) sensors have indeed demonstrated improved performances with respect to their counterparts as electro-chemical or nanomechanical sensors. One of the main advantages is the possibility of having on-chip detection in a label-free

---

assay format, which results into compact platforms, reduced sample volumes and higher reliability. Furthermore the compatibility with microelectronics fabrication processes allows the implementation of a truly integrated Lab-On-Chip (LOC).

In particular interferometric arrangements have shown the lowest limits of detection among IO configurations due to the extreme sensitivity offered by the phase detection and the possibility for internal referencing. However, for real application in the clinical practice, some issues still have to be addressed in order to provide a reliable, user-friendly platform to be employed even by non-trained personal. One of the main drawbacks of the interferometric read-out is given by the ambiguities of the sensor response induced by the periodicity of the light phase.

This Thesis presents the study and development of a novel phase linearization method for integrated interferometers which is compatible with a further integration onto LOC platform, since it does not require any additional fabrication process nor external equipment. In particular the Bimodal Waveguide (BiMW) sensor device is one of the most promising solutions for the achievement of an integrated platform due to its improved performances with respect to the well-known Mach-Zehnder Interferometer (MZI). While the final detection limits are comparable for the two sensors, the simpler fabrication of the BiMW renders into a higher reproducibility and tolerance to fabrication variations.

The main objectives of this Thesis can be summarized as:

- Study and modelization of a phase modulation system able to solve the limitations affecting traditional interferometric biosensors, while keeping the compatibility with truly integration onto a lab-on-chip platform.
- Implementation of the phase modulation system and validation of the phase linearized sensors for biosensor applications.
- Development of the first steps towards the integration onto a LOC platform using the BiMW technology and the linearized read-out

The Thesis is structured as follows:

**Chapter 1** contains an introduction to this doctoral Thesis and a description of the state-of-the-art in IO biosensors for LOC implementation. The limitations of the interferometric detection are discussed, along with the solutions for the signal linearization.



---

**Chapter 2** introduces the theory of integrated waveguide sensors and the modelization of the BiMW device. Numerical simulations are provided to assess the device sensitivity and the spectral response.

**Chapter 3** describes the fabrication processes of the BiMW sensors at the Clean Room facilities and their characterization (optical and morphological). The devices are characterized for bulk sensing by using the standard monochromatic approach and the limitations of this technique are detailed.

**Chapter 4** introduces the different solutions to achieve a linear read-out of the response of interferometric sensors and presents a novel approach based on an all-optical phase modulation technique. The working principle of the all-optical phase modulation is demonstrated for the case of a MZI device.

**Chapter 5** deals with the experimental implementation of the all-optical phase modulation for the BiMW biosensor. The numerical modelization of the required modulation depth is presented, along with the experimental sensor calibration to bulk detections.

**Chapter 6** describes the requirements for a reliable biofunctionalization of the sensor surface and the protocols employed. Evaluation of biomolecular interactions is demonstrated for the wavelength-modulated interferometric sensors.

**Chapter 7** describes the work performed and the on-going activity for the achievement of a complete LOC platform, including the design and fabrication of diffraction gratings for light in-coupling, of a microfluidic network to address multiple sensors and the near future possibilities for a multiplexed detection.

Finally, the general conclusions and future perspectives of this work will be highlighted.



# Chapter 1

## Introduction

The achievements of the last decades in nanotechnology, microelectronics and microfluidics fields have created great excitement about the possibility of implementing smart, compact and functional Lab-On-Chip (LOC) devices for fast and accurate multi-parametric analysis. Areas as photonics and fluidics are indeed facing a revolution similar to the one encountered by electronics in the last 50 years, passing from discrete components to integrated circuits and opening the way for a new generation of such smart integrated microchips.

The term LOC refers to a miniaturized platform able to perform all the steps required for an assay, from sample preparation to target detection. Fig. 1.1 pictures the ideal LOC platform [Gervais et al., 2011], where all the functionalities are integrated on the same chip and the result is displayed on a digital screen. It is clear that the application of such a portable, easy-to-use and highly sensitive LOC for real-time analysis could offer significant advantages over current analysis methods, usually based on time-consuming and expensive protocols, performed by trained personal in controlled laboratory facilities. Apart from clinical diagnostics other areas would take great advantage of the introduction of these smart platforms as environmental monitoring, food industry, industrial process control, forensics science and homeland security among others.

However, despite the intense research in this field and the progresses made in the last years towards an integrated system, very few complete working prototypes have emerged and have been commercialized [Ligler, 2009, Chin et al., 2012]. In fact, even if the technology for each component is mature, their integration is still a compelling challenge which must be carefully engineered. In addition, due to the high interdisciplinarity of the field, it is difficult to achieve a working prototype

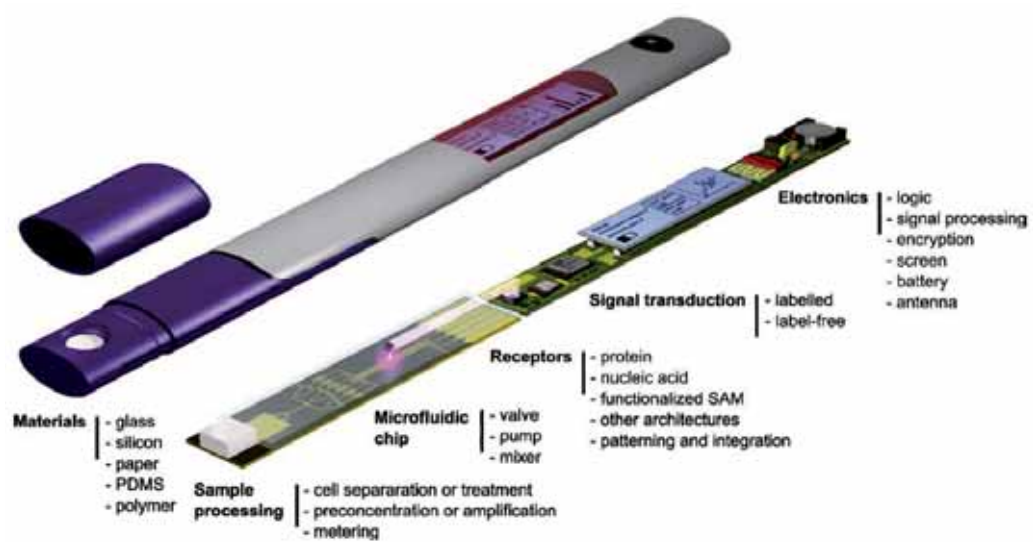


**Figure 1.1:** Ideal LOC platform integrating sample treatment, specific receptors, signal transducer and electronics. Ideally multi-analyte detection would be possible from very reduced body fluid sample ( $1 \mu\text{l}$ ) and a real-time result is displayed on a incorporated screen. From [Gervais et al., 2011].

of integrated systems while demonstrating at the same time its viability for real clinical applications.

The hearth of these integrated platforms for bio-chemical analysis is a biosensor, i.e. a self-contained device constituted by a **bioreceptor** and a **transducer**. The bioreceptor is in charge of selectively binding the target of interest through a biomolecular recognition process and the transducer converts this biomolecular interaction into a detectable, generally electrical, signal. According to the transduction mechanisms, biosensors can be classified as electro-chemical, optical or nanomechanical.

Compared to other detection schemes, optical sensors have remarkable advantages as they are non-invasive, rapid, highly sensitive and immune to electro-magnetic interferences and are promising candidates for being integrated onto a complete system.

## 1.1 Optical biosensors

Optical biosensors can be defined as sensors which make use of optical principles for the transduction of a biochemical interaction into a suitable output signal [Lechuga, 2005]. This variation of the light properties can be detected through any of the light parameters as intensity, phase, polarization or wavelength according to the employed transducer, resulting in a spread family of sensors including absorption, fluorescence, luminescence, Raman spectroscopy or refractive index-based techniques.

Optical biosensors can be divided in two categories according to the detection protocol: *fluorescence based* and *label-free* detection. In the case of fluorescence-based detection, fluorescent markers are employed to reveal the presence of the target species. Despite the extremely high sensitivity of this approach, the labeling procedure is laborious, subject to possible contamination and operator errors and can even affect the functionality of the biomolecule. Furthermore a quantitative analysis is compromised by the ability to precisely control the number of fluorescent tags for each target [Fan et al., 2008].

In the label-free approach molecules are detected in their natural form, without the need for fluorescent or other labeling markers, resulting in simpler and cost-effective detections enabling quantitative evaluation of biomolecular interactions even in complex samples (i.e. blood, urine, tears, etc.). Among label-free sensors the main configurations involve refractive index sensing (evanescent wave sensors), optical absorption or Raman spectroscopy techniques. In the following we will focus on refractive index sensors, whose working principle is based on the

evanescent field detection.

### 1.1.1 Evanescent field working principle

Evanescent field-based sensors exploit the possibility of electro-magnetic field confinement in certain dielectric and/or metal structures. Part of the confined light extends into the external medium, originating the so-called evanescent field. Variations in the refractive index of the external medium will cause a change of the optical properties of the excited optical mode through this evanescent tail, resulting in a variation of its effective refractive index. This relative change allows a quantitative measurement of the analyte involved in a given biomolecular interaction. Due to the exponential decay of the evanescent field in the external medium (usually few tens to a few hundreds of nanometers), only changes occurring in close proximity to the interface will be sensed, with a natural filtering of background from the surrounding medium. As a consequence, biosensors relying on the evanescent field principle are seen as ideal candidates for affinity-related analyte detections without the need for any molecular marker, allowing therefore on-chip label-free detection [Fan et al., 2008].

Figure 1.2 shows the two main configurations employed in evanescent wave sensors: those based on conventional dielectric waveguides (left panel) and those based on surface plasmon polaritons (right panel).

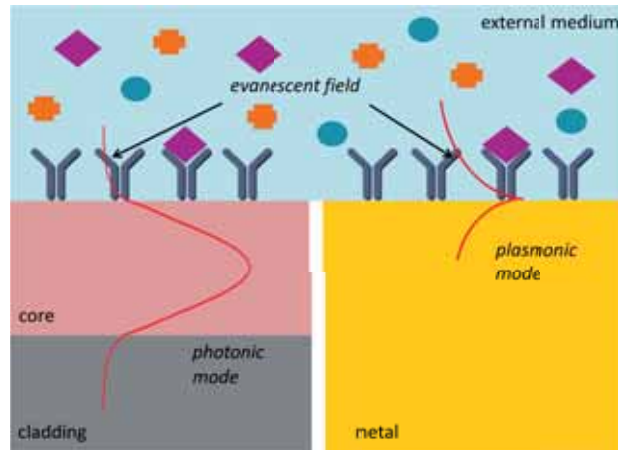


**Figure 1.2:** Scheme illustrating the sensing principle of evanescent wave sensors based on propagating electro-magnetic modes, distinguishing the cases of optical waveguides (left) and plasmon resonance (right).

### 1.1.2 Surface Plasmon Resonance sensor

The most common evanescent field based platform is the well-known Surface Plasmon Resonance (SPR) sensor [Homola, 2003]. The working principle is based on the variation of the excitation condition for a plasmon resonance, i.e. oscillation of the metal's electrons, occurring at the interface between a thin gold layer and a dielectric medium, which can be detected as an intensity, angular, spectral or phase variation of the reflected light beam. A properly functionalized surface allows selective and sensitive detections of biomolecules, with detection limits in the pico-nanomolar range.

Taking advantage of the simplicity and versatility of this label-free platform several companies commercialize SPR biosensors as Biacore<sup>1</sup>, Bio-rad<sup>2</sup>, Biosensing Instrument<sup>3</sup>, XanTec bioanalytics<sup>4</sup>, Reichert<sup>5</sup>, Texas Instruments<sup>6</sup>, Analytical  $\mu$ -Systems<sup>7</sup>, Metrohm<sup>8</sup>, Biosuplar (Mivitec GmbH)<sup>9</sup> or Sensia<sup>10</sup>, this last one being a spin-off of our research Group.

The need for bulky prisms to achieve the plasmonic excitation, together with movable components to observe the changes of the reflectance angle and the reduced multiplexing capabilities are some of the limitations encountered for the integration of SPR sensors onto LOC platforms.

Taking advantage of the benefits offered by imaging techniques, to address a higher level of multiplexing compared to the standard SPR platform, Surface Plasmon Resonance imaging (SPRi) sensors have been published since the late 80's [Rothenhäusler and Knoll, 1988, Brockman et al., 2000, Wong and Olivo, 2014] and commercialized. Some examples of SPRi platforms are provided by the companies GWC Technologies<sup>11</sup>, Horiba Scientific<sup>12</sup>, IBIS<sup>13</sup> or K-MAC<sup>14</sup>. However the limits of detection demonstrated by the SPRi platform are still unsatisfactory for many real diagnostic applications.

To overcome the limitations of the plasmonics-based sensors, photonics sensors based on integrated waveguides appear as a promising solution due to the higher sensitivity they offer, the possibility for dimension scaling and multiplexing and a cost-effective fabrication through complementary metal oxide semiconductor (CMOS) compatible processes, widely developed in the microelectronics field and available for mass-production [Washburn and Bailey, 2011, Estevez et al., 2012]. Integrated Optics (IO)-based sensors are analyzed in section 1.2, however to allow the comparison between different configurations some definitions must be

<sup>1</sup> [www.biacore.com](http://www.biacore.com)      <sup>2</sup> [www.bio-rad.com](http://www.bio-rad.com)      <sup>3</sup> [www.biosensingusa.com](http://www.biosensingusa.com)  
<sup>4</sup> <http://www.xantec.com/>      <sup>5</sup> [www.reichertspr.com](http://www.reichertspr.com)      <sup>6</sup> [www.ti.com](http://www.ti.com)      <sup>7</sup> [www.biosuplar.de](http://www.biosuplar.de)  
<sup>8</sup> <http://www.metrohm.co.th>      <sup>9</sup> <http://www.biosuplar.de/>      <sup>10</sup> [www.sensia.es](http://www.sensia.es)  
<sup>11</sup> <http://www.gwcinstruments.com>      <sup>12</sup> [www.horiba.com](http://www.horiba.com)      <sup>13</sup> [www.ibis-spr.nl](http://www.ibis-spr.nl)  
<sup>14</sup> <http://www.kmac.com>

introduced.

### 1.1.3 Parameters of sensor evaluation

*Sensitivity* ( $S$ ) is one of the fundamental parameters to evaluate the sensor performance, since it represents the magnitude of transducer response ( $S_r$ ) to the change in the analyte concentration. Since it depends on the type of transducer and on the nature of the analyte, a direct comparison between different configurations is not always viable through this parameter alone.

The concept of *resolution* indicates the ability to precisely measure the sensor signal variation induced by a sample, and corresponds to the smallest variation that can be accurately measured  $\Delta S_{r,min}$ . The resolution depends on the noise sources of the employed set-up (i.e. light source variations, thermal and detector noise, etc.) and is usually estimated as three times the standard deviation ( $\sigma$ ) of the total system noise [White and Fan, 2008]. Depending on the sensing scheme, parameters such as the spectral width of a resonant sensor or the visibility factor in the case of interferometers should be taken into account.

Sensitivity and resolution are combined to define the *Limit of Detection* ( $LOD$ ), which enables to compare different sensor configurations:

$$LOD = \frac{\Delta S_{r,min}}{S} \quad (1.1)$$

where  $S$  is the sensor sensitivity.

For refractometric sensing, where all the evanescent field region is subjected to an homogeneous index variation, expressing the LOD in terms of Refractive Index Units (RIUs) is therefore a natural choice [Fan et al., 2008].

In the case of surface sensing, where the variation of refractive index induced by a biomolecular interaction takes place only in a thin layer in proximity of the sensor surface, the LOD represents the minimum amount of analyte which can be accurately quantified. Expressing the surface sensing detection limit in terms of analyte concentration is therefore the immediate choice, however, since it depends on the specific target molecule and its affinity constants, it is more accurate to express the LOD in terms of surface density [Duval and Lechuga, 2014].

## 1.2 Integrated optics biosensors

IO biosensors are based on dielectric waveguides, where light is confined by Total Internal Reflection (TIR) into a medium with high refractive index (the core)



surrounded by mediums of lower index (the claddings). According to Maxwell's theory, light can propagate in such structure in the form of guided modes, characterized by their effective refractive index. A variation of the refractive index medium will be translated into a variation of the effective refractive index of the propagating mode, which can be detected at the sensor output through different working principles.

Biosensors based on integrated optics appear to be exceptionally amenable to chip integration and miniaturisation and by using evanescent wave as a detection mechanism, sensitivities can be extremely high (pM in a label-free scheme). In the last years, several IO devices have been implemented for biosensing. Grating-couplers, optical resonators and interferometric arrangements constitute the most developed configurations.

### 1.2.1 Grating couplers

Grating-coupled waveguide sensors are one of the first transducers developed, since the late 80's. Starting from the work of Lukosz and coworkers [Nellen et al., 1988] after observing the variation in the transmission of  $\text{SiO}_2$  - $\text{TiO}_2$  thin films due to humidity variations, a considerable work has been done employing grating as input, output or waveguiding configurations.

The basic working principle relies on the variation of light coupling condition in response to the binding of target molecules onto the sensor surface, according to the condition:

$$N_{eff} = \sin \theta + m \frac{\lambda}{\Lambda} \quad (1.2)$$

where  $N_{eff}$  is the effective refractive index of the waveguide mode,  $\theta$  is the angle of incidence of light,  $\Lambda$  the grating period and  $m$  the diffraction order. It is clear from Eq.(1.2) that a variation in the effective refractive index of the guided mode, as in response to a biomolecular interaction taking place on the sensor surface, will affect the coupling condition through the resonance angle or the resonance wavelength. According to the selected parameter, grating-based biosensors can be classified in two categories: angular and wavelength interrogation, as schematically shown in Fig. 1.3.

In the **angular interrogation** scheme the intensity corresponding to different incidence angles is recorded for a fixed wavelength: light is coupled through an input grating and the output of the waveguide is monitored with a standard photodiode (Fig. 1.3a). Limits of detection in the range of  $10^{-6}$  RIU were reported,

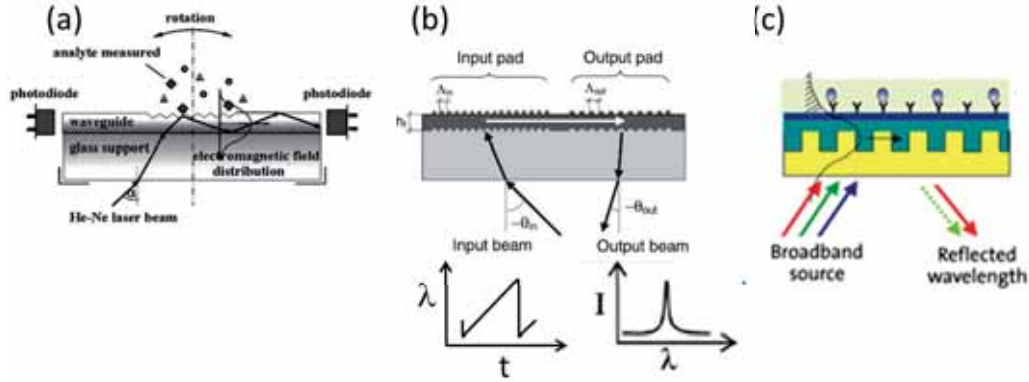


**Figure 1.3:** Comparison of the grating-based biosensor interrogation schemes. (a) angular interrogation (image from [Washburn and Bailey, 2011]), (b) Wavelength interrogation [Cottier et al., 2003] and (c) resonant grating<sup>18</sup>.

along with preliminary biosensing results with the detection of the immunoreaction of the pair IgG/anti-IgG.

In the case of **spectral interrogation** the incidence angle is kept unchanged and the incident wavelength is scanned, usually requiring a tunable laser (Fig. 1.3b). Since in the wavelength interrogation approach the chip position is kept fixed, some of the limitations of the angular approach, consisting in the use of a mechanically actuated goniometer, are solved. In the case of Wavelength Interrogated Optical Sensor (WIOS), LODs lower than  $10^{-6}$  for bulk sensing and  $0.3 \text{ pg/mm}^2$  for surface sensing have been achieved [Wiki and Kunz, 2000, Cottier et al., 2003].

The success of the grating based sensors lead to commercialization of some platforms as the BIOS-1 instrument [Bernard and Bosshard, 1995] (Artificial Sensing Instruments ASI AG)<sup>15</sup> and the Optical Waveguide Light Spectroscopy (OWLS) platform, commercialized by MicroVacuum Ltd.<sup>16</sup>.

Another detection approach consists in using the diffraction grating as a reflector: a broad-band light spectrum is sent towards the chip and only a single wavelength is reflected, whose value depends on the medium surrounding the grating element (Fig. 1.3c). The Epic system (Corning)<sup>17</sup> exploits the principle of resonant grating and the transducers have been integrated into standard 384-well plates for a highly multiplexed analysis.

<sup>15</sup> <http://www.asiag.ch>

<sup>16</sup> [www.owls-sensors.com/label-free-biosensor](http://www.owls-sensors.com/label-free-biosensor)

<sup>17</sup> [www.corning.com/lifesciences](http://www.corning.com/lifesciences)

### 1.2.2 Optical resonators

Optical resonators are considered to be very promising to obtain high sensitivities and, due to their reduced footprint, they are also especially attractive for the implementation of an array format for parallel multi-analyte detection. The working principle relies on the propagation of Whispering Gallery Modes (WGMs) in the resonant structure, whose optical properties strongly depend on the surrounding medium. The binding of a target molecule will induce a spectral shift of this resonance, as schematized in Fig. 1.4a, according to the equation:

$$\lambda = \frac{2\pi r}{m} N_{eff} \quad (1.3)$$

where  $\lambda$  is the resonant wavelength,  $r$  is the ring radius,  $N_{eff}$  is the effective refractive index of the WGM and  $m$  is an integer.

Ring and disk resonator geometries were the first ones to be proposed for biosensing applications and seem to be the most prominent resonators in biosensing [Krioukov et al., 2002, Ksendzov and Lin, 2005, De Vos et al., 2007, Iqbal et al., 2010]. They are fabricated with photolithographic techniques in different materials as silicon, silicon nitride, silica, oxynitrides and organic polymers [Vollmer and Yang, 2012] and large sensor arrays can be obtained.

Several applications have been demonstrated with Silicon on Insulator (SOI) sensors, showing detection limits in the range of ng/ml for direct label-free assays [De Vos et al., 2007, Washburn et al., 2009b, McClellan et al., 2012, Park et al., 2013]. A detection limit of 0.3 pg/mm<sup>2</sup> was demonstrated by Xu *et al.* employing a Si-nanowire based platform [Xu et al., 2010].

The advantages coming from a simple fabrication and integration flexibility led to the commercialization of the multiplexed platform Maverick by the US company Genalyte<sup>19</sup>, based on SOI ring sensor geometry, shown in Fig. 1.4.

### 1.2.3 Interferometric sensors

Interferometers based on optical waveguides typically have one or even two orders of magnitude better detection limit for surface mass density and refractive index changes than microring resonators and grating coupler sensors [Kozma et al., 2014].

The most common configurations are the **Mach-Zehnder Interferometer (MZI)** [Heideman et al., 1993, Prieto et al., 2003, Densmore et al., 2009] and **Young Interferometers (YIs)** [Brandenburg and Henninger, 1994, Ymeti et al.,

<sup>19</sup> genalyte.com

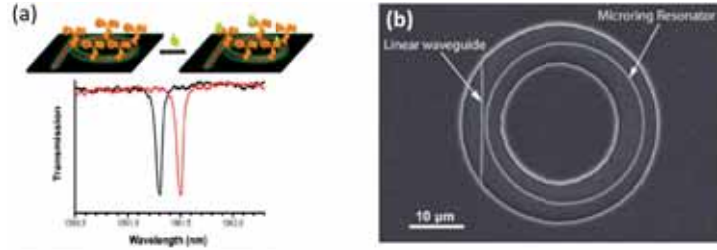


**Figure 1.4:** (a) Working principle of the optical resonator structure: a spectral shift of the resonant wavelength is induced by the target binding on the sensor surface and (b) SOI planar ring resonator with input waveguide, as employed in the Maverick platform (images from [Washburn et al., 2009a]).

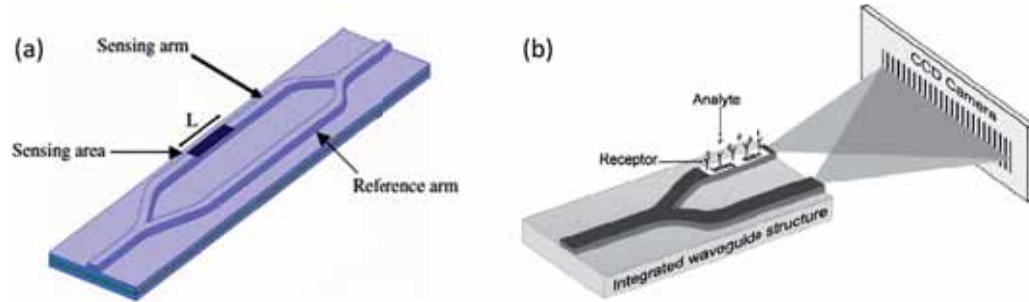


**Figure 1.5:** Comparison of (a) Mach-Zehnder (image from [Sepúlveda et al., 2006]) and (b) Young (image from [Mulder et al., 2012]) interferometric biosensors.

2002], which have been implemented as totally integrated, i.e. beam splitting and recombination take place on the chip, or hybrid configurations, i.e. external optical components are required.

In their basic configurations, both MZI and YI have an input single-mode waveguide which originates two arms after a Y-junction: one of the two arms is exposed to the external medium, while the other is employed as a reference. In the case of MZI (see Fig. 1.5(a)) the two arms are recombined through a second Y-junction into a single output waveguide, while in the case of YI (Fig. 1.5(b)) the intensity distributions originating from the two waveguides are superposed over a screen, resulting in both cases in an interference pattern. Due to their geometry involving two spatially separated arms, they are often referred to as double-path interferometers.

In the case of the MZI, the phase difference between the two propagating modes is given by:

$$\Delta\varphi_S = 2\pi \frac{L}{\lambda} (N_S - N_R) \quad (1.4)$$

where  $N_S$  and  $N_R$  are the effective refractive indices of the guided modes in the sensor and reference arms, respectively,  $\lambda$  is the wavelength of the traveling light and  $L$  is the length of the sensing area. The phase change induced by a bio-reaction taking place in the sensing area is evaluated by monitoring the output intensity,  $I_T$ , expressed as:

$$I_T = I_S + I_R + 2\sqrt{I_S I_R} \cos(\Delta\varphi_S) \quad (1.5)$$

where  $I_S$  and  $I_R$  are the intensities of the light in the sensor and reference arms, respectively.

For the Young configuration the interference pattern is generated off-chip by projecting the two light beams onto a screen or Charge-Coupled Device (CCD) camera. The phase difference between the two interfering beams is given by:

$$\Delta\varphi(t) = \frac{2\pi}{\lambda} \left[ \frac{d \cdot x}{f} - (N_S(t) - N_R)L \right] \quad (1.6)$$

where  $d$  is the distance between the two arms,  $f$  is the distance between the sensor output and the camera and  $x$  is the position of the interference pattern on the screen. A biomolecular interaction taking place in the sensing area will induce a shift of the interference pattern along the camera surface  $\Delta x$ , which can be evaluated and related to the variation of the refractive index.

The two detection approaches can be generalized to other interferometric arrangements, which are distinguished as MZI-type detection if a single beam intensity is monitored or as Young-type if an interference pattern is created and analyzed.

For biosensing applications, Si-based interferometers demonstrated to be the most sensitive with detection limits of  $10^{-7} - 10^{-8}$  RIU for bulk sensing and fractions of  $\text{pg}/\text{mm}^2$  for mass coverage [Schipper et al., 1997, Rio et al., 2007, Ymeti et al., 2002, Schmitt et al., 2007]. Solutions based on polymeric waveguides have been proposed and despite the lower sensitivity achieved, they can offer an interesting alternative in order to produce a low-cost disposable platform [Bruck et al., 2011, Wang et al., 2012, Yang et al., 2014].

However, despite the extremely low detection limits demonstrated in laboratory conditions, very few solutions are commercially available to date. One example is given by a MZI sensor commercialized by the company Optisense<sup>20</sup>, with

---

<sup>20</sup> [www.optisense.nl/](http://www.optisense.nl/)

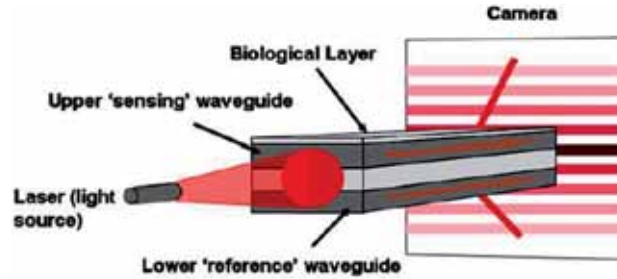


**Figure 1.6:** Scheme of the dual polarization interferometer (from [Swann et al., 2004]).

a main application in water quality analysis<sup>21</sup>. On the other side, the YI sensor is employed as transduction principle in the Interferometric biosensor IBS101 developed at Fraunhofer Institute<sup>22</sup> and in a four-channel sensor platform provided by the company Ostendum<sup>23</sup>.

A notable version of the Young interferometer is the **Dual Polarization Interferometry (DPI)** sensor, which is constituted by a multi-stack of five dielectric media, forming two planar waveguides, as shown in Fig. 1.6. Light is injected at the chip input and propagates in the two waveguides: the upper one is responsible for sensing of changes occurring on its surface, while the lower waveguide is used as a reference. One of the main advantages of this approach relies on the extremely improved tolerance for light in-coupling affecting traditional interferometric approaches due to the use of slab waveguides instead of channel ones. Furthermore the use of a double polarization allows to resolve for both the refractive index and the thickness of an immobilized bio-layer [Cross et al., 2003]. A resolution of  $10^{-7}$  RIU and a mass surface sensitivity of  $0.1 \text{ pg/mm}^2$  have been reported [Estevez et al., 2012].

In order to solve some of the limitations affecting dual-path interferometers, as a strong dependence on fabrication and critical light in-coupling conditions, alternative structures based on a single-path configuration were introduced. The main advantages come from a simplified design, improved tolerances to fabrication deviations and generally reduced dimensions since no physical beam separation is required. In the general case, two modes of different order or polarization propagate in the same channel. They both probe the sample solution but with different sensitivities, consequence of their distinct confinement factors. The resulting rela-

---

<sup>21</sup> <http://www.optiqua.com>

<sup>22</sup> <http://www.ipm.fraunhofer.de/en/ideas-expertise/sensor-technology/sensor-technology-in-microsystems.html>

<sup>23</sup> <http://www.ostendum.com>

tive phase difference can be evaluated from the spatial light distribution (Young) or intensity (MZI) approaches. While in the case of standard dual-path interferometers only the fundamental mode propagates, in the case of single-path sensors different order modes are involved. As a consequence, dual-path interferometers can also be referred to as homo-modal, while single-path are also called hetero-modal.

One of the first examples of single-path interferometers is given by the **difference interferometer**. The working principle is based on the different responses shown by the fundamental  $TE_0$  and  $TM_0$  modes which propagate along the same waveguide, resulting into a phase shift which can be detected at the device output [Lukosz et al., 1997]. Some of the disadvantages of this configuration rely on the complex external equipments required for the off-chip detection of the interference pattern and on the loss of information by combining TE and TM polarizations for the standard detection.

In alternative to the use of external components for beams manipulation, a fully integrated version of the difference interferometer was proposed, showing a phase sensitivity of  $1096 \cdot 2\pi$  rad/RIU and a refractive index resolution of  $1 \cdot 10^{-6}$  RIU [Koster and Lambeck, 2002].

More recently, our Group proposed a two-mode integrated interferometer, the **Bimodal Waveguide (BiMW) device** [Zinoviev et al., 2011, González-Guerrero, 2012], where two modes of same polarization and different orders propagate along the same straight waveguide. A scheme of the device is shown in Fig. 1.7: polarized light is injected in the input single-mode section of the device. After a modal splitter, two modes, the fundamental and the first order one, propagate till the end of the device, resulting in an intensity distribution which depends on the phase difference between the two modes accumulated along the propagation length.

The phase shift induced by a biomolecular interaction taking place on the sensor surface is quantified from the variation of the output intensity distribution, by monitoring the signal  $S_R$ :

$$S_R = \frac{I_{up} - I_{down}}{I_{up} + I_{down}} \quad (1.7)$$

where  $I_{up}$  and  $I_{down}$  are the intensity measured by the upper and lower sections of a two-section photodetector, respectively.

The indirect excitation of the two modes, which occurs at sensor level through a modal splitter (i.e. step junction), the normalization to the total output power

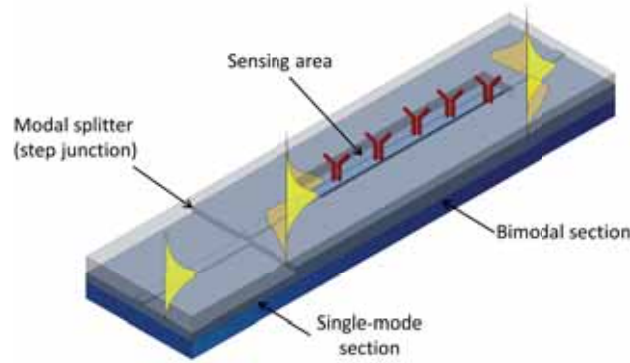


**Figure 1.7:** Scheme of the Bimodal Waveguide interferometric biosensor. Light is injected in the single-mode input waveguide and after a modal splitter two modes are excited and propagate till the device output.

and the use of a two-section photodiode placed in close proximity of the waveguide output results in an improved tolerance to mechanical vibrations and laser fluctuations. A detection limit in the range of  $10^{-7}$  RIU, competitive with the most sensitive optical detection methods, was demonstrated [Zinoviev et al., 2011].

To summarize the overview of optical biosensors detailed in this chapter, Table 1.1 includes a comparison of the published limit of detection.

**Table 1.1:** Integrated optical biosensors compared in terms of architecture and detection limits.

Device configuration	RI detection limit (RIU)	Mass detection limit ( $\text{pg}/\text{mm}^2$ )
SPR	$10^{-5} - 10^{-7}$	1 – 5
Gratings	$10^{-6}$	0.3 – 5
Interferometers	$10^{-7} - 10^{-8}$	0.02 – 1
Ring resonators	$10^{-5} - 10^{-7}$	0.3 – 3

The standard configurations described in this chapter have also been implemented with Si-nanowires, photonic crystals, slot waveguides or porous silicon to enhance sensitivity via a stronger light confinement or a larger surface area [Xu et al., 2008, Chow et al., 2004, Barrios, 2009, Jane et al., 2009]. A deeper description and comparison of photonic biosensors can be found in specialized reviews [Fan et al., 2008, Estevez et al., 2012], while specific resonator structures are treated in greater detail in references [Bogaerts et al., 2012, Luchansky and



Bailey, 2012, Vollmer and Yang, 2012]. Reference [Kozma et al., 2014] critically analyzes the different interferometric arrangements.

### 1.3 Lab-on-chip integration

A complete LOC platform must include different components: i) the (photonic) sensors, (ii) the flow delivery system, iii) the emitters and detectors, iv) processing electronics and (v) final packaging with required firmware and software. The integration of all these components can be hybrid, i.e. functionalities separated on different chips, or monolithic, i.e. all functionalities are integrated on the same chip. The result of a monolithic integration will generally be an expensive platform, not disposable due to the processing cost of lasers and detectors. On the other side, with the hybrid approach, optoelectronics and read-out components can be reused while the sensors and the microfluidics can be implemented on a cost-effective disposable cartridge.

Among the few examples of published lab-on-chip devices based on IO sensors, the majority is based on interferometers and resonators arrangements.

For example, Jokerst's group demonstrated the integration at chip level of an array of MZI sensors with thin-film detectors, fully compatible with Si-CMOS processes, resulting in a detection limit of  $2.5 \cdot 10^{-6}$  RIU [Lillie et al., 2006, Jokerst et al., 2009]. Following work led to the integration of polymeric microresonators with detectors and a digital electrowetting-on-dielectric system for fluid delivery [Luan et al., 2012]. The building block for the chip-scale optical sensing system is shown in Fig. 1.8(a). However the validation of the integrated sensing platforms for biosensing applications has not been reported yet.

An array of optical slot-waveguide ring resonators was successfully integrated with microfluidics on a compact cartridge [Carlborg et al., 2010] (see Fig. 1.8(b)). Due to their alignment tolerance, grating couplers were adopted to enable a quick replacement of the cartridge in the read-out system. The use of reference signals allowed to compensate for different noise contributions, resulting in limits of detection of  $5 \cdot 10^{-6}$  RIU and  $0.9 \text{ pg/mm}^2$  for bulk and surface sensing, respectively.

A monolithic platform based on integrated MZI sensors was developed and demonstrated by Makarona *et al.*, including light emitting diodes and photodetector fabricated by standard silicon technology, as shown in Fig. 1.8(c) [Makarona et al., 2011]. The detection principle is based on the frequency-resolved MZI (see section 1.4). For bulk sensing a detection limit of  $5 \cdot 10^{-6}$  RIU was calculated and the biosensor capabilities were demonstrated through the evaluation of biotin/streptavidin interaction at the pM range, together with preliminary results

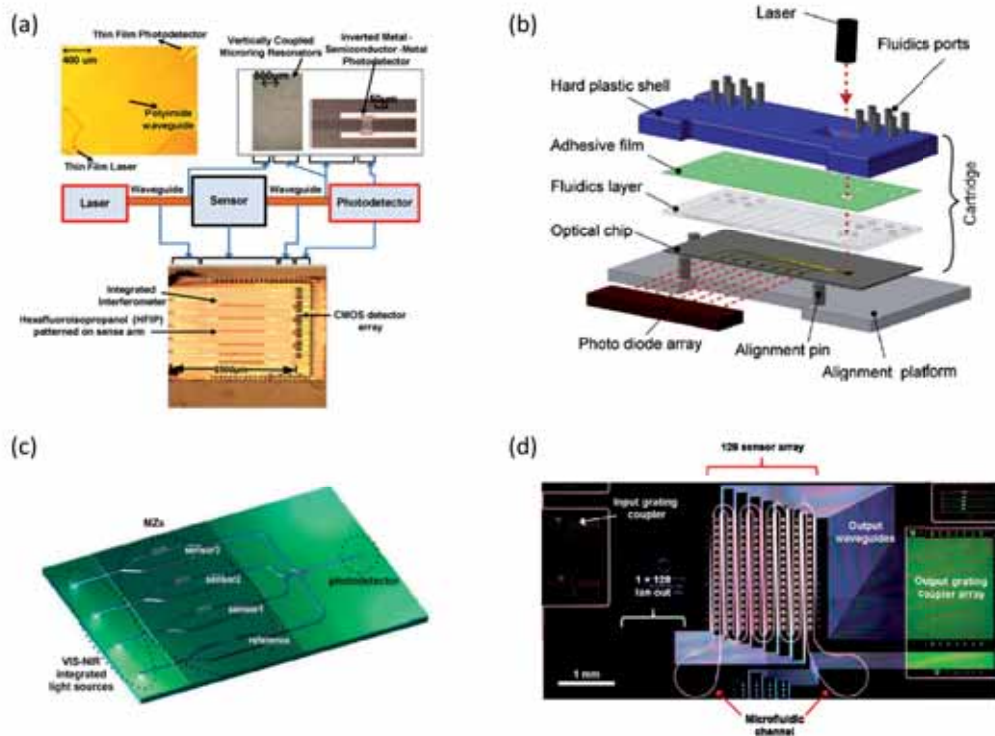


**Figure 1.8:** Comparison of different LOC architectures. (a) Building blocks of planar chip-scale optical sensing systems including lasers, waveguide interconnections, optical sensors and photodetectors (image from [Jokerst et al., 2009]), (b) schematic view of the cartridge above the alignment platform, containing the optical chip and the microfluidic layer (image from [Carlborg et al., 2010]), (c) scheme of an array of monolithically integrated MZIs sensors (image from [Makarona et al., 2011]) and (d) microscope image of the photonic wire microarray chip containing 128 sensors, microfluidic channels and grating couplers (image from [Janz et al., 2013]).

on the detection of prostate specific antigen. Ten sensors have been accommodated on a chip area of  $9.3 \times 4.0 \text{ mm}^2$ .

By employing Si nanowires waveguides, Janz *et al.* demonstrated a complete biosensor microarray chip including up to 128 sensors which can be independently interrogated [Janz et al., 2013]. Due to the reduced waveguide cross-section, folded spiral resonators sensors were designed with very reduced footprint ( $50 \mu\text{m}$  diameter) while keeping a millimeter length to ensure a satisfactory sensitivity. Microfluidic channels are monolithically integrated on the sensor chip and light in-coupling is accomplished through arrays of sub-wavelength surface grating couplers, which are defined with the same etch step required for the waveguide patterning. Figure 1.8(d) shows a microscope image of the complete microarray chip. The validation as a biosensor was demonstrated through a serotyping assay for *Escherichia coli* but a complete evaluation has not been reported yet.

As an alternative to the traditional approach, in the last years an increasing numbers of publications described the use of cellphones as source or detector for biosensing applications. The widespread diffusion of mobile devices all over the world, in combination with the current status of wireless technologies, exhibits a promising potential for point-of-care health-care applications, even in developing areas where traditional medical facilities are scarce [Azzazy and Elbeheri, 2014, Ozcan, 2014]. These works involve both fluorescence-based and label-free detection schemes, as demonstrated in the case of SPR or photonic crystals sensors [Zhu et al., 2011, Preechaburana et al., 2012, Gallegos et al., 2013].

Despite the higher sensitivity shown by the interferometric arrangement, most of the efforts for a complete integration are directed to resonators configurations. One of the main reasons is due to the complex read-out of the interferometric arrangements, as it will be detailed in the next section.

## 1.4 Interferometric limitations

Although the extreme sensitivity of the interferometric configuration (MZI, Young, modal, etc) is well established, the lack of a clear and unambiguous output still prevents a successful commercialization and the use in analysis laboratories.

In addition to the sensor itself, the realization of a good and reliable signal processing scheme has to be taken into account to achieve a competitive platform employing interferometric architectures. Due to the interferometric nature of the detection, the output is periodic as a consequence of the cosine dependence with

the phase difference between the two propagating modes (see Eq.(1.5)). This periodicity induces some drawbacks, which can be summarized as:

- **Sensitivity fading**

The sensitivity is defined as the derivative of the output with respect to a stimulus variation and it will also show a sinusoidal dependence with the phase difference. Therefore it will vary along the measurement, being maximum in correspondence of the quadrature points and minimum at curve extremes. This implies that different sensor responses will be obtained according to the initial conditions.

- **Fringe order ambiguity**

If only one intensity value is measured, corresponding to  $I_{out1}$  in Fig. 1.9, any  $\Delta\varphi'_m = \Delta\varphi_m + 2\pi \cdot k$ , with  $k$  an integer number, is an equally probable solution.

- **Directional ambiguity**

If the detection starts from an extremum of the transfer function, the direction of the phase change cannot be retrieved from the final intensity value  $I_{out1}$  alone.

- **Relative measurement**

When a complete fringe is not induced by the reaction, a reference signal is required for the phase evaluation.

Figure 1.9 shows a graphical representation of the illustrated interferometric ambiguities.

All these drawbacks, arising from the non linearity of the transmission curve obtained by monitoring a single intensity signal, can be overcome by alternative signal processing methods, involving active modulation approaches or alternative detection schemes [Brandenburg, 1996].

### Overcoming the ambiguities

Since the demonstration of integrated interferometers as highly-sensitive biosensor platforms at the beginning of 90's, consistent efforts have been devoted to achieve smart detection schemes to overcome the limitations imposed by the periodic interferometric response.

The proposed solutions involve different approaches which can be grouped as modification of the interferometer configuration, modification of the interrogation scheme or application of phase modulation techniques.

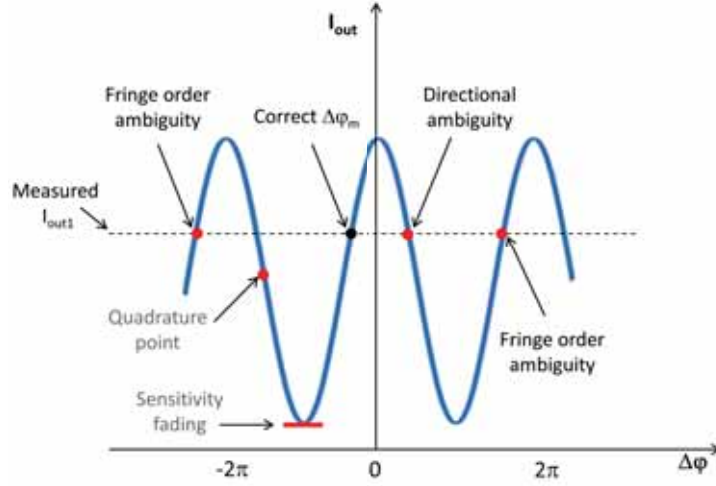


**Figure 1.9:** Interferometric output ambiguities: sensitivity fading, fringe order ambiguity and directional ambiguity. Quadrature point where sensitivity is maximum is highlighted.

In the case of integrated MZI biosensors, a partial solution to compensate for the problems of sensitivity fading and intensity dependence involves the generation of multiple outputs, at least three, with a phase difference of  $120^\circ$  between each other. In this configuration at least one of the three outputs will show a satisfactory sensitivity to refractive index changes, as shown in Fig. 1.10(a) [Drapp et al., 1997, Luff et al., 1998]. Furthermore the normalization to the total in-coupled power, given by the sum of the three outputs, eliminates the dependence with laser source drift and fluctuations, resulting in improved Signal-to-noise-ratio (SNR).

The need for fringe counting can be solved by introducing a second interferometer with a lower sensitivity than the main sensing one (dual interferometer configuration) and collecting the information from the two sensors simultaneously. Each of the two interferometers terminates with a three-waveguide coupler, whose output variations can be monitored with a CCD camera [Hua et al., 2002] (see Fig.1.10(b)). In this dual approach, the ambiguity can be solved over a wide range of refractive indices, however the complex fabrication can result in important non-idealities in the global sensor response.

With a geometry similar to the three-waveguide output coupler, employing in this case a  $2 \times 3$  multimode interference coupler, Halir *et al.* recently demonstrated

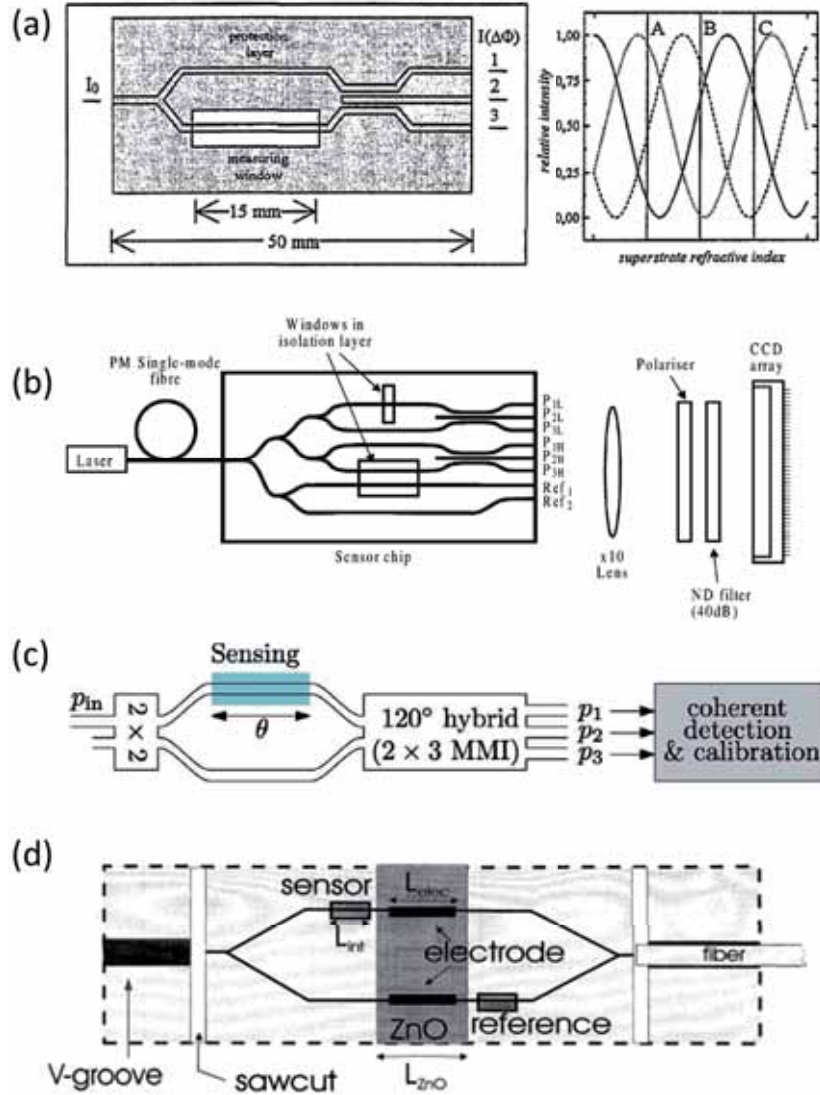


**Figure 1.10:** Comparison of MZI architectures proposed for overcoming traditional output ambiguities. (a) Three-output coupler MZI and resulting transmission curves: at all operating points A, B and C one output provides satisfactory sensitivity (image from [Drapp et al., 1997]). (b) Experimental sensor system for the dual MZI sensor (image from [Hua et al., 2002]). (c) Scheme of coherently detected MZI sensor with calibration system (image from [Halir et al., 2013]). (d) Scheme of the MZI sensor with electro-optic phase modulator (image from [Heideman and Lambeck, 1999]).

a complete amplitude and phase recover from a MZI sensor output by jointly processing the three output powers and applying coherent receiver techniques [Halir et al., 2013]. A schematic view of the coherently detected sensor is shown in Fig. 1.10(c). The effects of imperfections in the sensor hardware are canceled by a blind calibration scheme. The result is a constant sensitivity linear response for the optical phase shift produced along the sensing area and a reduction in the detection limit compared to traditional sensors.

Unambiguity of the phase order was demonstrated for an integrated YI by employing low coherence light, as a consequence of the relation between the fringe visibility and the degree of coherence [Brandenburg and Henninger, 1994]. The input light source is constituted by a laser diode operated below threshold and the detection is performed with a CCD camera. Fourier deconvolution of the output signature allows to retrieve the required position information from the phase spectrum, resulting in a linear response.

Another solution for solving the phase ambiguity is provided by a spectral interrogation in substitution to the traditional monochromatic interrogation scheme. Similarly to the working principle of optical resonators, the transmission spectrum of an integrated interferometer is spectrally shifted in response to a variation in the sensing area medium.

In an asymmetric interferometer, fringes in the wavelength dependent transmission curve can be detected by scanning a sufficiently large spectral region with a tunable laser [Crespi et al., 2010]. The fringe shift, directly proportional to the refractive index change produced in the sensing area, can be accurately retrieved from a Fourier Transform of the MZI transmission spectrum. However, due to the finite time required for the spectral scanning, only static detections were demonstrated with this approach and dynamic measurements were done at constant wavelength.

In order to solve the limitations of single-wavelength sensors, Kitsara *et al.* introduced the frequency-resolved MZI biosensor, based on white-light excitation instead of the traditional monochromatic lasers [Kitsara et al., 2010]. For the detection a spectrophotometer is required. The use of multiple wavelengths allows to circumvent the problems of ambiguity and signal fading since each wavelength will be affected in a different way by a refractive index variation. In an advanced configuration, Discrete Fourier Transform deconvolution was applied to directly and unambiguously retrieve the phase information from the sinusoidal transmission curves for each polarization [Misiakos et al., 2014].

Similar to the working principle of the dual MZI sensor, where the responses from two sensors characterized by different sensitivities are combined to solve



the order ambiguity, a numerical study demonstrated that for spectrally interrogated modal interferometers, the sensor response takes place onto two scales with different sensitivities, of which the lowest one can be employed for period counting [Hutter et al., 2013].

The third group includes phase modulation techniques, which solve sensitivity fading and directional ambiguity by dynamically varying the phase difference between the two interfering modes.

Different optical effects can be used to introduce the required modulation, as described in greater detail in Chapter 4, the most common are based on electro-optical [Heideman and Lambeck, 1999, Preston et al., 2009], acousto-optical [Duhring and Sigmund, 2009], thermo-optical [Passaro et al., 2005] or magneto-optical [Sepúlveda et al., 2007] working principles. Figure 1.10(d) shows a scheme of a phase modulated MZI sensor, in the case of electro-optical principle.

An all-optical phase modulation principle has been described by Dér *et al.* [Dér et al., 2010], where they tuned the refractive index of a light-sensitive adlayer deposited on the reference arm by means of light intensity variations.

The disadvantages of all the above techniques rely on the need of complex fabrication processes, often requiring non standard CMOS compatible materials, on the need of electrodes and electrical connections, conflicting with microfluidics and increasing the technological complexity, and on the complex electronic equipment for the read-out, seriously hindering the miniaturization of the interferometric devices for LOC implementation.

Therefore, in order to take full advantage of the high sensitivity of the interferometric arrangement and to help in a successful commercialization of the interferometric LOC platform, a simple, integrable and reliable phase linearization approach must be developed.

For this reason a phase modulation system based on an all-optical principle has been studied and modeled along this Thesis. A variation of the phase difference between the propagating modes can be introduced by a variation of the incident wavelength, avoiding the use of external modulators. If this variation is periodical, a Fourier deconvolution scheme can be applied to directly retrieve the phase information, immune to ambiguities. In order to achieve a compact and cost-effective platform laser diodes are employed as light source.



# Chapter 2

## Theory and modelization of IO interferometric biosensors

In order to understand the physics of the MZI and BiMW interferometric biosensors a brief introduction to the light propagation in a waveguide according to the electromagnetic theory is required. For this description, an analytical derivation is only possible in the case of planar waveguides, as presented in subsection 2.1.2, however 3D structures can only be treated with approximate methods or numerical approach, as described in subsection 2.1.3.

The second part of the chapter is dedicated to the study of the BiMW sensor, analyzing the requirements for the expected modal behavior, the sensitivity (bulk and surface), the mode splitter and the complete device modelization through its transfer function. Finally the spectral response of the sensor is analyzed, highlighting the so-called critical effects, which are typical of hetero-modal interferometers.

### 2.1 Light propagation in optical waveguides

To determine the characteristics of the propagating electro-magnetic fields across a waveguide structure, Maxwell's equations must be solved imposing the boundary conditions corresponding to the different layers constituting the optical waveguide.

#### 2.1.1 Maxwell's equations in a dielectric medium

Considering a dielectric (conductivity  $\sigma = 0$ ), non-magnetic (magnetic permeability  $\mu = \mu_0$ ), isotropic and linear ( $\mathbf{D} = \epsilon\mathbf{E}$ ) medium, Maxwell's equations are

simplified to:

$$\nabla \times \mathbf{E} = -\mu_0 \frac{\partial \mathbf{H}}{\partial t} \quad (2.1)$$

$$\nabla \times \mathbf{H} = \epsilon_0 n_i^2 \frac{\partial \mathbf{E}}{\partial t} \quad (2.2)$$

$$\nabla \cdot \mathbf{E} = 0 \quad (2.3)$$

$$\nabla \cdot \mathbf{H} = 0 \quad (2.4)$$

$$(2.5)$$

where  $t$  is the time,  $\mathbf{r}$  is the position vector,  $\mathbf{E}(\mathbf{r}, t)$  is the electric field strength,  $\mathbf{H}(\mathbf{r}, t)$  the magnetic field strength,  $\epsilon_0$  the vacuum electric permittivity (dielectric constant),  $\mu_0$  the vacuum magnetic permittivity and  $n_i$  the medium refractive index.

By combining Maxwell's equations and using vector identities, the following equation is obtained:

$$\nabla^2 \mathbf{E} = \mu_0 \epsilon_0 n_i^2 \frac{\partial^2 \mathbf{E}}{\partial t^2}. \quad (2.6)$$

By assuming a harmonic time-dependence of the type  $e^{i\omega t}$ , Eq.(2.6) can be simplified to the standard notation:

$$\nabla^2 \mathbf{E} + k_0^2 n_i^2 \mathbf{E} = 0 \quad (2.7)$$

which constitutes the wave equation for a uniform dielectric medium with refractive index  $n_i$ . The wave-vector is given by  $k_0 \equiv \frac{2\pi}{\lambda_0} = \frac{\omega}{c}$ , where  $\lambda_0$  is the wavelength of the light in the free space, related to the angular frequency by  $\omega = \frac{2\pi c}{\lambda_0}$ .

### 2.1.2 Dielectric slab waveguide

The slab, or planar, waveguide reported in Fig. 2.1 is the simplest example of an optical waveguide structure. It is constituted by a high refractive index material ( $n_1$ ) surrounded by two media of lower refractive index ( $n_2$  and  $n_3$ ), satisfying the condition  $n_1 > n_2 \geq n_3$ . If  $n_2 = n_3$  the waveguide is symmetric. Light can propagate in such structure in the form of **guided modes**, which are characterized by a unique field distribution and propagation velocity, which

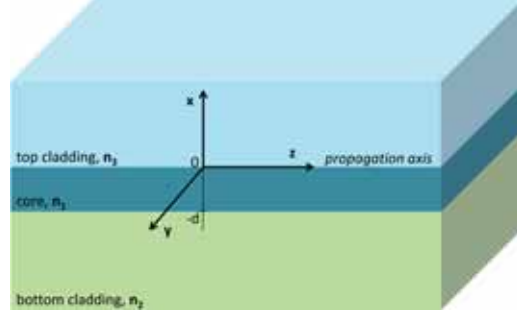


**Figure 2.1:** Asymmetric slab waveguide configuration.

depend on the waveguide structure (dimensions and material composition) and on the wavelength.

In the case of a slab waveguide the material inhomogeneity is reduced to the  $x$ -direction,  $n_i = n_i(x)$ , and the structure is assumed to be invariant and spatially infinite along the  $y$ -direction ( $d/dy = 0$ ). Assuming that the propagation occurs along the  $z$  direction, the following solutions can be postulated for the propagating modes:

$$\mathbf{E}(\mathbf{r}, t) = \mathbf{E}(x)e^{i(\omega t - \beta z)} \quad (2.8)$$

$$\mathbf{H}(\mathbf{r}, t) = \mathbf{H}(x)e^{i(\omega t - \beta z)} \quad (2.9)$$

where  $\omega$  is the wave angular frequency and  $\beta$  the longitudinal propagation constant of the specific mode. Under these assumptions, the wave equation (2.7) can be simplified to:

$$\frac{d^2 \mathbf{E}}{dx^2} + (k_0^2 n_i^2 - \beta^2) \mathbf{E} = 0 \quad (2.10)$$

which is the well-known Helmholtz equation.

In order to study the properties of the modes which can propagate in such structure, it is convenient to separate the two situations of transverse electric (TE) and transverse magnetic (TM) modes, as illustrated in Fig. 2.2.

For TE modes, the electric field exhibits only a component perpendicular to the incidence plane, corresponding to  $E_y$  ( $E_x = E_z = 0$ ). As a consequence, Eq.(2.10) is simplified to:

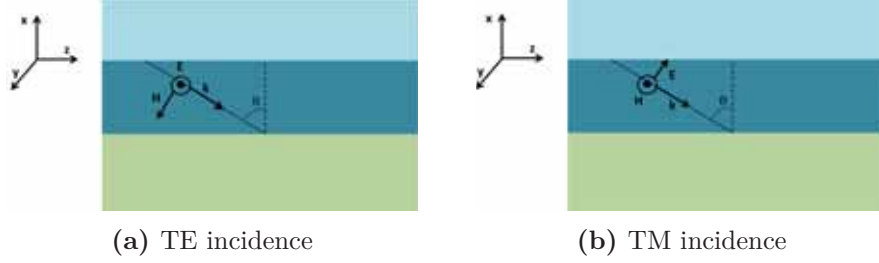


**Figure 2.2:** (a) TE and (b) TM modes propagation in an asymmetric planar waveguide.

$$\frac{d^2 E_y(x)}{dx^2} + [k_0^2 n_i^2 - \beta^2] E_y(x) = 0 \quad (2.11)$$

As a consequence of Eq.(2.1), for the associated magnetic field  $H_y = 0$  and the remaining components  $H_x$  and  $H_z$  are related to the  $E_y$  component by the following relations:

$$H_x = -\frac{\beta}{\omega \mu_0} E_y \quad (2.12)$$

$$H_z = \frac{i}{\omega \mu_0} \frac{\partial E_y}{\partial x} \quad (2.13)$$

In the case of TM polarization, the modes are characterized by an electric field vector parallel to the incident plane ( $E_x, E_z \neq 0$  and  $E_y=0$ ), imposing  $H_x = H_z = 0$  and  $H_y \neq 0$ . In this case, the wave equation governing  $H_y$  is given by:

$$\frac{d^2 H_y(x)}{dx^2} + [k_0^2 n_i^2 - \beta^2] H_y(x) = 0 \quad (2.14)$$

The non-null components of the associated electric field are related to  $H_y$  by the expressions:

$$E_x = \frac{\beta}{\omega \epsilon_0 n_i^2} H_y \quad (2.15)$$

$$E_z = \frac{1}{i \omega \epsilon_0 n_i^2} \frac{\partial H_y}{\partial x} \quad (2.16)$$

The propagating modes are often described in terms of effective refractive index  $N_{eff}$ , which is related to the propagation constant  $\beta$  through:

$$\beta \equiv k_0 N_{eff} \quad (2.17)$$

The effective refractive index represents the refractive index encountered by the mode propagating along the  $z$ -direction, corresponding to the quantity  $n_1 \sin \theta$  in the ray-optics modelization, being  $\theta$  the incidence angle [Kogelnik, 1975]. The condition for the propagation constant for a guided mode is given by:

$$k_0 n_2 < \beta < k_0 n_1 \quad (2.18)$$

which can be rewritten as a function of the effective refractive index as:

$$n_2 < N_{eff} < n_1 \quad (2.19)$$

The Helmholtz equations encountered for TE and TM modes, (2.11) and (2.14), can be made explicit for the three spatial regions constituting the slab waveguide, resulting in a system of three scalar equations which must be solved. In the case of TE polarization, the system is given by:

$$\frac{d^2 E_y}{dx^2} - \gamma_3^2 E_y = 0 \quad x \geq 0 \quad (\text{top cladding}) \quad (2.20)$$

$$\frac{d^2 E_y}{dx^2} + k_1^2 E_y = 0 \quad -d < x < 0 \quad (\text{core}) \quad (2.21)$$

$$\frac{d^2 E_y}{dx^2} - \gamma_2^2 E_y = 0 \quad x \leq -d \quad (\text{bottom cladding}) \quad (2.22)$$

where  $d$  is the thickness of the guiding layer (core) and the three parameters  $k_1$ ,  $\gamma_2$  and  $\gamma_3$ , representing the transversal propagation constant for the core region ( $k_1$ ) and the attenuation coefficients for the cladding regions ( $\gamma_2$  and  $\gamma_3$ ), are given by:

$$\gamma_3 = \sqrt{\beta^2 - k_0^2 n_3^2} \quad (2.23)$$

$$k_1 = \sqrt{k_0^2 n_1^2 - \beta^2} \quad (2.24)$$

$$\gamma_2 = \sqrt{\beta^2 - k_0^2 n_2^2} \quad (2.25)$$

After solving equations (2.20) - (2.22), the electric field component  $E_y$  can be expressed as:

$$E_y = \begin{cases} Ae^{-\gamma_3 x} & x \geq 0 \\ Be^{ik_1 x} + Ce^{-ik_1 x} & -d < x < 0 \\ De^{\gamma_2 x} & x \leq -d \end{cases} \quad (2.26)$$

where we have neglected the two exponential terms that would have led to divergences for the confined modes, since they do not have physical meaning.

The constants  $A, B, C$  and  $D$  and  $\beta$  are obtained by imposing the continuity of  $E_y$  and  $dE_y/dx$  at the interfaces  $x = 0$  and  $x = -d$ , which result in four equations. After solving this set of equations the expression:

$$k_1 d = m\pi + \arctan \frac{\gamma_2}{k_1} + \arctan \frac{\gamma_3}{k_1} \quad (2.27)$$

is obtained, which represents the eigenvalue equation for the TE modes in the case of asymmetric planar waveguide.

Following a similar reasoning as described for TE modes, the eigenvalue equation can be made explicit also for TM modes. A general equation including both cases of polarization can be written by introducing the additional coefficients  $\eta_a = (\frac{n_1}{n_2})^2$  and  $\eta_b = (\frac{n_1}{n_3})^2$  which take into account the discontinuity of the magnetic field at the core-cladding interfaces, resulting in the general expression:

$$k_1 d = m\pi + \arctan \left( \eta_a \frac{\gamma_2}{k_1} \right) + \arctan \left( \eta_b \frac{\gamma_3}{k_1} \right) \quad (2.28)$$

where  $\eta_a = (\frac{n_1}{n_2})^2$  and  $\eta_b = (\frac{n_1}{n_3})^2$  for TM polarization and  $\eta_a = \eta_b = 1$  for TE polarization.

The periodic nature of the tangent function allows multiple solutions ( $TE_m$ ,  $TM_m$ ) indexed by the integer  $m$ , defined as the mode order, and univocally defined by their propagation constants,  $\beta_m$ . The solutions, i.e. their form and number, depend on the waveguide geometry (core thickness,  $d$ , and refractive indices,  $n_1, n_2$  and  $n_3$ ) and on the working wavelength,  $\lambda$ . Waveguides admitting only one solution for the propagation constants  $\beta_m$  are called single-mode, while structures supporting more than one mode are referred to as multi-mode waveguides. It can also happen that no modes can propagate: in this situation the waveguide is said to be in cut-off for a given wavelength.

Once determined the propagation constant  $\beta$  from (2.28), it is possible to make explicit the electric field distribution of a given TE mode, given by equation (2.26):

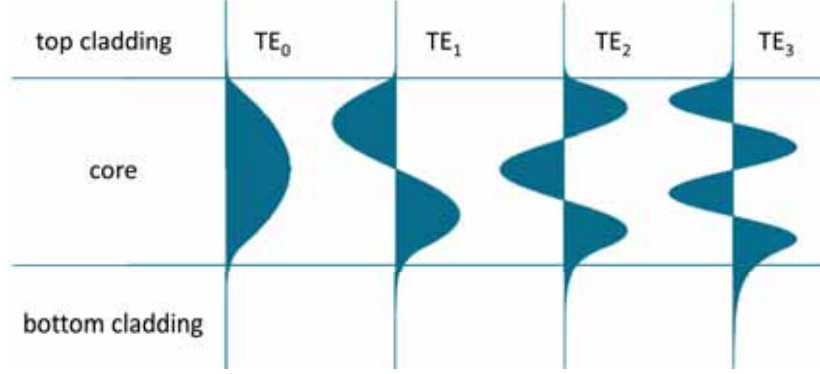


**Figure 2.3:** TE modes profile for an asymmetric slab waveguide,  $n_3 < n_2 < n_1$ .

$$E_y = \begin{cases} Ae^{-\gamma_3 x} & x \geq 0 \\ A \left( \cos(k_1 x) - \frac{\gamma_3}{k_1} \sin(k_1 x) \right) & -d < x < 0 \\ A \left( \cos(k_1 d) + \frac{\gamma_3}{k_1} \sin(k_1 d) \right) e^{\gamma_2(x+d)} & x \leq -d \end{cases} \quad (2.29)$$

From the previous expression we can notice how the electric field shows a sinusoidal dependence in the core and exponentially decreases in the claddings. The unknown  $A$ , representing the field amplitude, is related to the energy carried by the mode. Once described the electric field component,  $E_y$ , the magnetic field components  $H_x$  and  $H_z$  can be evaluated from (2.12) and (2.13), giving a complete description of the propagating mode.

Figure 2.3 shows the mode profiles for the case of TE polarization, for an asymmetric waveguide satisfying the condition  $n_3 < n_2 < n_1$  [Lifante, 2003].

The derivation of TM modes is similar to the one described above for TE modes, solving in this case the wave equation for the  $H_y$  component and applying the corresponding boundary conditions. The magnetic field component,  $H_y$ , can be made explicit in the three regions of the planar waveguide as:

$$H_y = \begin{cases} Ae^{-\gamma_3 x} & x \geq 0 \\ A \left( \cos(k_1 x) - \frac{\gamma_3}{k_1} \frac{n_1^2}{n_2^2} \sin(k_1 x) \right) & -d < x < 0 \\ A \left( \cos(k_1 d) + \frac{\gamma_3}{k_1} \frac{n_1^2}{n_2^2} \sin(k_1 d) \right) e^{\gamma_2(x+d)} & x \leq -d \end{cases} \quad (2.30)$$

The main difference for TM modes with respect to TE ones is a discontinuity observed at the guiding film interfaces due to the imposition of the continuity condition for  $(1/n^2)dH_y/dx$  (in  $x = 0$  and  $x = -d$ ).

To fully characterize the TM mode profile, the electric field components  $E_x$  and  $E_z$  must be evaluated from (2.15) and (2.16).

To describe the evanescent decay in the cladding regions it is useful to introduce the concept of *penetration depth*  $d_p$ , defined as the distance at which the intensity of the electromagnetic field drops to  $1/e$  of its value at the interface, corresponding to  $1/\gamma_2$  and  $1/\gamma_3$  for the bottom and top cladding regions, respectively. From the definitions of the attenuation coefficients,  $\gamma_i$ , we can make explicit the decay length (penetration depth) in the  $i$ -region (top or bottom claddings) as:

$$d_p = \frac{1}{\gamma_i} = \frac{\lambda_0}{2\pi} \frac{1}{\sqrt{N_{eff}^2 - n_i^2}} \quad (2.31)$$

where  $N_{eff}$  is the effective refractive index of the propagating mode.

This evanescent field is the basis for most of the IO-based sensors: a refractive index variation occurring on the transducer surface is perceived and induces a variation in the effective refractive index of the guided mode which can be detected at the waveguide output. It is important to notice that the evanescent field penetration depth increases by increasing the mode order.

### Guided modes cut-off

For many practical applications it is important to determine the minimum thickness which allows a given mode to propagate, for example, when designing a single mode waveguide, the second order mode must not be guided. As previously described, a guide is said to be in cut-off for a certain wavelength if there is no solution for a guided mode to be propagated. As a consequence, the cut-off thickness is defined as the minimum thickness which permits to propagate a certain wavelength mode. This condition is found by considering that at the cut-off frequency the effective refractive index  $N_{eff}$  assumes the value of the lower bound  $n_2$  of condition (2.19).

The cut-off thicknesses for a  $m$ -order mode can be derived from Eq.(2.28), for both TE and TM polarizations, by setting the cut-off condition,  $\beta = n_2 k_0$ .



$$d_{CO,m} = \frac{\lambda}{2\pi} \frac{1}{\sqrt{n_1^2 - n_2^2}} \cdot \left[ \arctan \left( \eta_b \sqrt{\frac{n_2^2 - n_3^2}{n_1^2 - n_2^2}} \right) + m\pi \right] \quad (2.32)$$

where

$$\eta_b = \begin{cases} 1 & \text{TE} \\ \left(\frac{n_1}{n_3}\right)^2 & \text{TM} \end{cases} \quad (2.33a)$$

$$(2.33b)$$

From these equations we can deduce that if a waveguide is in cut-off for the  $\text{TE}_m$  mode, it will be also in cut-off for the corresponding  $\text{TM}_m$ , but is not valid vice-versa. For the particular case of symmetric waveguides, we can also notice that there is no cut-off for the fundamental mode, since  $d_{CO,m} = 0$ .

For example, for a slab waveguide constituted by silicon nitride ( $n=2.00$ ) over a silicon dioxide cladding ( $n=1.46$ ) exposed to air ( $n=1.00$ ), the minimum film thickness needed to propagate the fundamental mode at  $\lambda = 633$  nm is 49 nm for TE and 93 nm for TM, respectively.

For an exhaustive analysis of light propagation in optical waveguides, the reader can look for references [Snyder and Love, 1983, Tamir, 1988, Nishihara et al., 1989] or more recent dissertations as [Lifante, 2003].

### 2.1.3 Dielectric 3D waveguides

The above modelization is valid for planar waveguides, where light confinement occurs along one axis only ( $x$  axis in our notation). 3D, or channel, waveguides are obtained by introducing light confinement along a second direction ( $y$  axis). In these structures, since the homogeneity along the  $y$  axis is lost, the intensity profile for a mode propagating along  $z$  will not depend only on  $x$  direction, as shown in the case of planar waveguides, but also on  $y$ . Under this hypothesis, no analytical solution can be found employing the electromagnetic approach.

For many applications the confinement offered by the slab waveguide is not sufficient and the light must be confined in a more localized region of space, directing the optical power and the related information to the region of interest, whether it is a sensing area as in the case of biosensors, or a sector of an integrated circuit or a photodetector. For these reasons, different kinds of 3D waveguides with light confinement along two directions have been designed and implemented. The most common configurations are the raised strip, the embedded strip or the rib waveguide, as shown in Fig. 2.4 [Tamir, 1988].

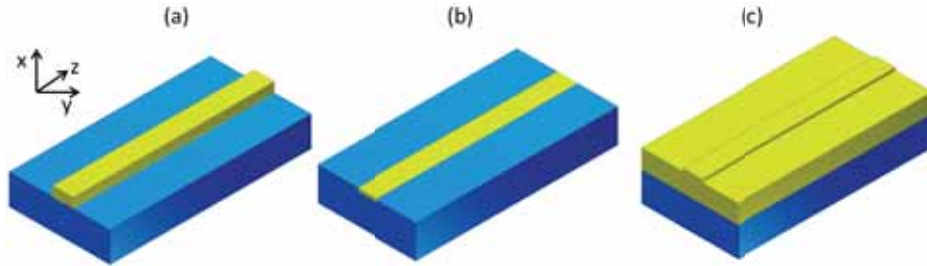


**Figure 2.4:** Main types of 3D-waveguides: (a) raised strip waveguide, (b) embedded strip and (c) rib waveguide.

In 3D optical waveguides there are no pure TE and TM modes, but there are two families of hybrid transverse electromagnetic modes (TEM). The TEM modes that propagate in the waveguide are strongly polarized along the  $x$  or  $y$  direction, allowing a classification according to the dominant component of the electric field [Lifante, 2003]. *Quasi-TE* modes are characterized by a dominant  $E_y$  component, while *quasi-TM* modes show a main electric field component along the  $x$  axis. For this reason they are commonly referred to as TE or TM modes.

The classification of the guided modes,  $TE_{m,n}$  and  $TM_{m,n}$ , is achieved by employing two indices  $m$  and  $n$ , which count the number of nodes of the field distribution along one direction of confinement. The first subscript  $m$  corresponds to the first confinement direction, while  $n$  corresponds to the second one. Figure 2.5 shows an example of the fundamental  $TE_{00}$ , the first order vertical mode  $TE_{10}$  and  $TE_{01}$  the first order lateral mode evaluated for a  $\text{SiO}_2/\text{Si}_3\text{N}_4/\text{SiO}_2$  rib waveguide.

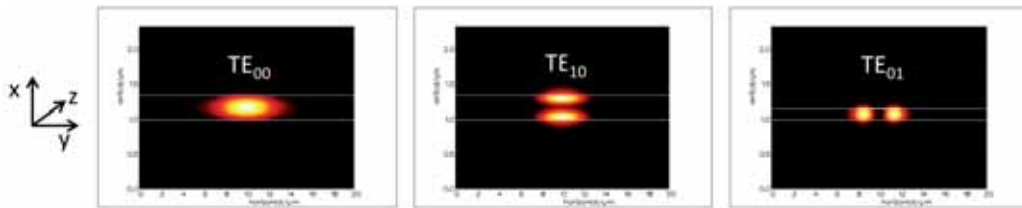


**Figure 2.5:** Guided modes labeling according to the cartesian reference system employed in the theoretical waveguide modeling. From left to right: fundamental mode  $TE_{00}$ , first order vertical mode  $TE_{10}$  and first order horizontal mode  $TE_{01}$ .

To study these configurations, approximate methods must be introduced. The most common are the Marcatili's method [Marcatili, 1969], the Effective Index

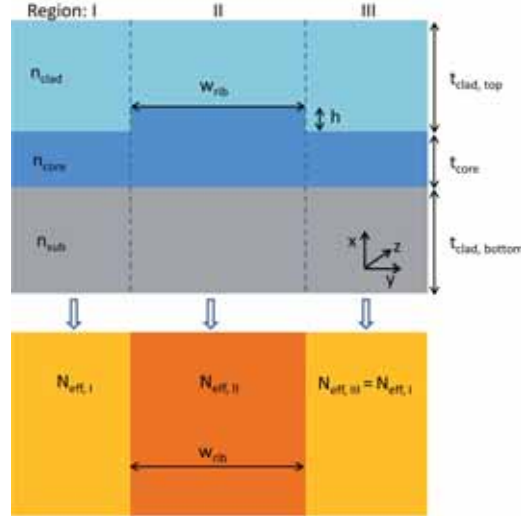


**Figure 2.6:** Graphical scheme of the effective index method. A 3D channel waveguide can be analytically solved by its decomposition into two planar waveguides, sequentially analyzed.

(EI) method [Chiang, 1986], perturbation approaches [Kumar et al., 1983] or finite elements methods. Due to the wider applicability, the simplicity and the satisfactory results provided by the Effective Index approach, it is the one selected in this Thesis and will be detailed in the following.

From now on we will focus on a rib waveguide, the geometry chosen for the construction of the integrated interferometers employed in this work.

### Effective index method

In order to find the solution for the two-dimensional problem of light confinement in channel waveguides, it is possible to employ an approximate method which sequentially solves two one-dimensional problems, using the tools developed for planar waveguides [Ramaswamy, 1974].

The method is based on two steps, which are graphically schematized in Fig.2.6 for the case of a rib waveguide.

1. The channel waveguide is divided into three regions to be independently analyzed, each of which is a planar waveguide for which a rigorous solution can be found. Since the core thickness is higher in the central region, the

effective refractive index in this region will be higher than in the neighboring ones, resulting in a transversal light confinement below the rib.

2. After calculating the effective refractive indexes of the two first regions (the third one is equal to the first) an equivalent three layer-waveguide is constructed. The refractive indices of these layers are given by the effective refractive indices computed in the first step and the thickness of the core is given by the width of the channel waveguide. The effective index of the equivalent planar waveguide will correspond to the effective index of the initial channel waveguide.

Care must be taken in considering the correct polarizations: considering the original 3D waveguide and the equivalent effective waveguide, the cartesian coordinates are rotated. If we are interested in quasi-TE modes in the 3D structure, we will have to solve for TM modes in the slab waveguides and vice-versa for quasi-TM.

An immediate application of the EI method is given by the assessment of the cut-off width:

$$W_C^{TE_{0m}} = W_C^{TM_{0m}} = \frac{m\lambda}{2\sqrt{N_{eff,II}^2 - N_{eff,I}^2}} \quad (2.34)$$

where  $N_{eff,II}$  and  $N_{eff,I}$  are the effective refractive indices of the slab waveguides of regions II (below the rib) and I (lateral), respectively (see Fig. 2.6). Equation (2.34) provides the minimum rib width allowing the propagation of the  $m$ -order mode for a given rib height.

The simplicity of this method together with the accurate results provided make it a proper choice for many engineering applications [Batrak and Plisyuk, 2006]. For this reason it is the method chosen in this Thesis to study the modal behavior in the waveguide cross-section. However, for a complete study of the light propagation along the interferometer, other tools are required. For this reason we have used a commercial software, Photon Design<sup>1</sup>, to assess both modal behavior and propagation characteristics. In particular the modules Fimmwave and Fimmprop have been employed to study the transverse cross-section or the propagation, respectively.

### **Eigenmode expansion: Photon Design**

A variety of simulations tools have been developed in the last decades based on different principles, the most common are Finite Difference Time Domain (FDTD)

---

<sup>1</sup> [www.photond.com](http://www.photond.com)

method, Finite Element Method (FEM), Beam Propagation Method (BPM) or Eigenmode Expansion (EME) solvers.

Modal solvers offer a powerful approach to waveguide design. Just as plane waves are the natural modes of free space, modal analysis allows the user to determine the natural modes of a waveguide. Unlike gridded methods, as FEM or FDTD, which approximate the solution at a discrete set of points, mode-based solutions discretize in a different way by considering a finite number of local modes. Similarly to quantum mechanics where a system's state is described as a linear combination of its eigenvalues, the light propagation in a waveguide is given by a linear combination of its eigenmodes.

One of the main advantages of EME, as implemented by Photon Design, is that it provides a rigorous solution of Maxwell's equations but is also able to deal with very long structures [Gallagher and Felici, 2003], as in the case of interferometric devices analyzed in this Thesis ( $\approx 3$  cm).

The algorithm is inherently bi-directional and utilizes the scattering matrix (S-matrix) technique to join different sections of the waveguide or to model nonuniform structures. With this approach, the incoming waves (modes) coming from a waveguide section  $A$  are related to the modes in a section  $B$  through the coupling coefficients, which describe the overlap between two mode profiles and the consequent transfer of energy.

Assuming propagation along the  $z$  axis, in any section of the device the electromagnetic field can be expanded in terms of the local modes  $\xi(x, y)$ :

$$\Psi(x, y, z) = \sum_{m=1}^N \xi_m(x, y) \cdot (c_m^f e^{j\beta_m z} + c_m^b e^{-j\beta_m z}) \quad (2.35)$$

where  $\beta_m$  is the propagation constant of the mode  $m$  and  $c_m^f$  and  $c_m^b$  are the amplitudes of the modes in the forward and backward  $z$  directions, respectively, which are computed through the scattering matrix. Since the number of eigenmodes is limited to a finite value  $N$ , the higher the value of  $N$ , the more accurate the representation.

The S-matrices for each couple of sections can be combined to obtain a global S-matrix describing the whole device, relating the modes injected at the device input, for example through an incident laser beam, to the device output.

In the environment of Photon Design, it is also possible to evaluate the far-field pattern of a given mode (or modes combination). The far-field algorithm is based in a plane wave expansion of the field in the structure, resulting in the form:

$$E = \sum_n A_n \cdot e^{j2\pi \cdot k_x \cdot x} \cdot e^{j2\pi \cdot k_y \cdot y} = \sum_n A_n \cdot e^{j2\pi \cdot \frac{\cos \theta_x}{\lambda} \cdot x} \cdot e^{j2\pi \cdot \frac{\cos \theta_y}{\lambda} \cdot y} \quad (2.36)$$

being  $A$  the amplitude of the plane wave traveling at angles  $(\theta_x, \theta_y, \theta_z)$ , where  $\theta_i$  is the angle of the propagation direction with respect to the  $i$  axis.

The planar projection will provide the power flowing through a unit area on a plane of constant  $z$  as a function of  $x$  and  $y$ . Since it is possible to define a finite window of arbitrary dimensions over the  $x - y$  plane, the behavior of a detector placed at the device output can be easily modeled.

## 2.2 Waveguide design

### 2.2.1 Choice of waveguide materials

In order to design a highly sensitive device, while ensuring a cost-effective fabrication and a further integration onto a complete LOC platform, different considerations have to be taken into account:

1. A high index contrast between the core layer and the cladding will be translated into a high sensitivity, due to the increased penetration depth given by Eq.(2.31).
2. Materials compatible with standard microelectronics technology will be preferred, since the fabrication processes are well optimized and the costs can be reduced through mass fabrication.
3. The designed dimensions must be achieved using standard optical lithographic techniques, to keep fabrication times and costs reduced.
4. The waveguide must have low propagation losses, to allow the use of low power laser sources and to obtain high SNR.

These requirements clearly fix some guidelines for the choice of materials and structure: as the transducers are designed for biosensor applications, silicon dioxide/silicon nitride/silicon dioxide ( $\text{SiO}_2/\text{Si}_3\text{N}_4/\text{SiO}_2$ ) waveguides were selected [Prieto et al., 2003], ensuring low propagation losses and high sensitivity to surface changes, for working wavelengths in the range of 600-700 nm to avoid light absorption by the biomolecules and to simplify the experimental set-ups.

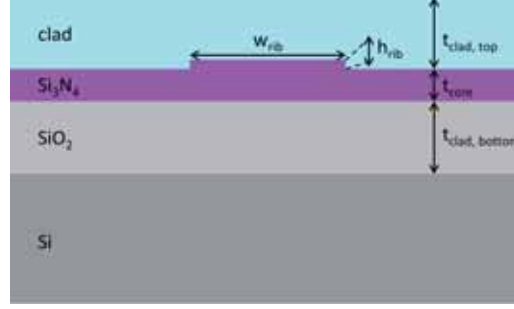


**Figure 2.7:** Cross section view of the employed rib-waveguide, indicating the main parameters. A nanometric height rib is defined over a silicon nitride core, embedded between two silicon dioxide layers.

Furthermore a rib-waveguide geometry is employed to ensure the lateral light confinement, since single-mode propagation can be achieved with rib widths in the range of few microns, compatible with standard lithographic techniques. Scattering losses due to lateral walls roughness, which usually affect channel waveguides in comparison to slab configurations, are reduced in the case of rib waveguides due to the extremely reduced height of the channel.

Figure 2.7 shows the cross section of the employed waveguide, highlighting the main parameters which must be considered for the design.

### 2.2.2 Single mode requirements

The control of modal behavior is a primary requirement for the implementation of reliable modal interferometers. Since the sensor read-out results from the interaction between two specific modes, the existence of additional modes, with different sensitivities, would introduce additional contributions which would impede a correct evaluation of the sensor response.

Table 2.1 summarizes the parameters employed in the calculation, relative to the materials refractive indices and their thicknesses.

**Table 2.1:** Layers parameters (refractive index and thickness) employed for the evaluation of the single-mode condition.

Layer	Thickness (nm)	Refractive index
Top cladding	1500	1.33 / 1.46
Core	150-350	2.00
Bottom cladding	2000	1.46

**Table 2.2:** Cut-off thickness (nm) for TE<sub>10</sub> and TE<sub>20</sub> modes in the approximation of slab waveguide, with a top cladding of refractive index  $n = 1.33$  /  $n = 1.46$ .

	TE <sub>10</sub>		TE <sub>20</sub>	
	$\lambda_0 = 633$ nm	$\lambda_0 = 660$ nm	$\lambda_0 = 633$ nm	$\lambda_0 = 660$ nm
1.33	262	273	494	515
1.46	232	241	463	483

**Table 2.3:** Cut-off thickness (nm) for TM<sub>10</sub> and TM<sub>20</sub> modes in the approximation of slab waveguide, with a top cladding of refractive index  $n = 1.33$  /  $n = 1.46$ .

	TM <sub>10</sub>		TM <sub>20</sub>	
	$\lambda_0 = 633$ nm	$\lambda_0 = 660$ nm	$\lambda_0 = 633$ nm	$\lambda_0 = 660$ nm
1.33	289	302	521	543
1.46	232	241	463	483

### Vertical modal behavior

In the case of dual-path interferometers, as it is the MZI, normally only the fundamental mode propagates. As a consequence, the cut-off condition for the first order mode TE<sub>10</sub> (TM<sub>10</sub>) represents the maximum core thickness which can be employed. On the other side, for the BiMW architecture the same cut-off thickness establishes the minimum core thickness which ensures the propagation of the first order mode, while the upper limit for the waveguide thickness is given by the cut-off thickness of the second order mode.

The cut-off expression deduced for the slab waveguide can be applied with good approximation to the rib waveguide under exam. Table 2.2 summarizes the values of cut-off thickness for the first and second order TE modes, TE<sub>10</sub> and TE<sub>20</sub>, for different wavelengths and refractive indices, evaluated from Eq.(2.32). The case of TM polarization is shown in Table 2.3.

From the values in Tables 2.2-2.3 we can deduce that the minimum film thickness to ensure the propagation of the TE<sub>10</sub> mode is around 260 nm for a wavelength  $\lambda_0 = 633$  nm and 290 nm for the TM<sub>10</sub> mode, considering a water cladding ( $n = 1.33$ ).

### Lateral single-mode requirement

Once assessed the vertical confinement behavior, the lateral requirement can be analyzed. By employing the effective refractive index method, the cut-off width



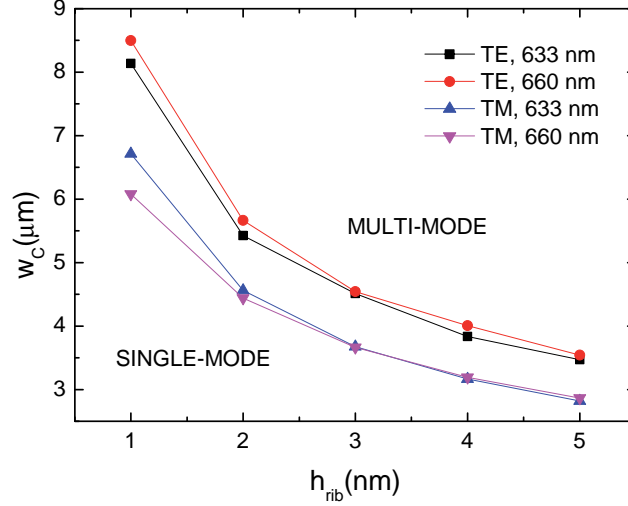


**Figure 2.8:** Single mode condition for core thickness of 340 nm. Cladding refractive index  $n=1.33$ .

for a given rib height can be determined according to Eq.(2.34) for a given core thickness and working wavelength. The single-mode condition will be more restrictive considering a lower cladding refractive index (for example water compared to silicon dioxide) and considering a longer wavelength (i.e. 660 vs 633 nm).

Figure 2.8 shows the cut-off width  $w_c$  for the modes  $\text{TE}_{01}$  and  $\text{TM}_{01}$  as a function of the rib height, evaluated for a core thickness of 340 nm, for working wavelengths of 633 and 660 nm. Both polarizations are taken into account and an external refractive index  $n=1.33$  is considered. The obtained curves represent the single-mode condition for a given pair wavelength/polarization. For example for a rib width of 4  $\mu\text{m}$ , lateral single-mode propagation is ensured for rib heights below **2.5 nm**.

According to these results the single mode section of the BiMW device must show a thickness in the range 100-250 nm, while the bimodal section thickness must be higher than 300 nm. For these core thickness, we chose a rib dimension of 4  $\mu\text{m} \times 1.5 \text{ nm}$  to achieve a lateral single-mode behavior. Taking into account the previous considerations, the mode dispersion curves are finally computed in the environment of Fimmwave (Effective Index solver) by considering this rib structure (4  $\mu\text{m} \times 1.5 \text{ nm}$ ). Figure 2.9 shows the dispersion curves for a working

wavelength  $\lambda_0=660$  nm, for the two situations of bulk refractive index  $n=1.33$  (subfigure 2.9a) and  $n=1.46$  (subfigure 2.9b). These data are in good agreement with the results obtained with the slab waveguide approximation summarized in Tables 2.2-2.3.

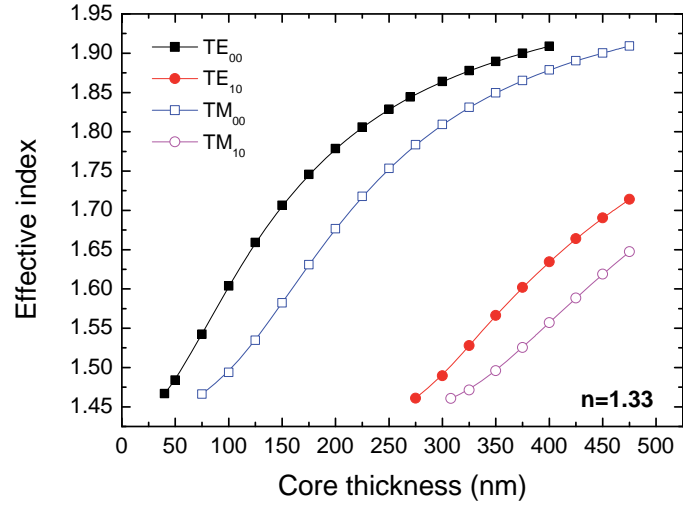
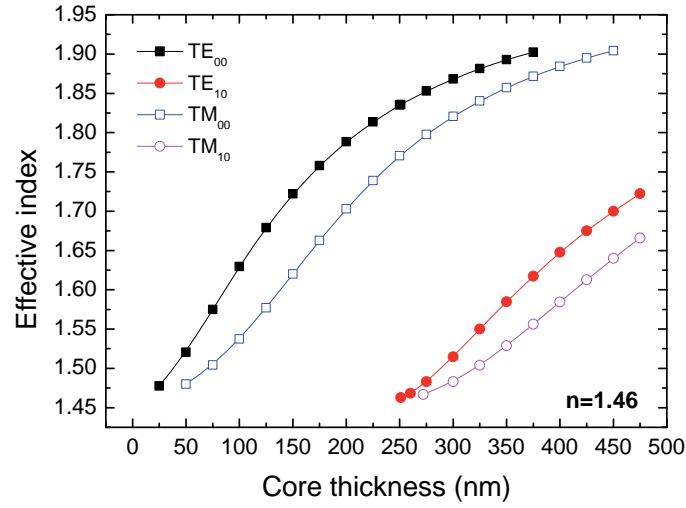
## 2.3 Interferometric biosensor design

As an alternative to the MZI sensor, a novel interferometric configuration avoiding the lateral beam splitting and recombination was recently proposed in our Group [Zinoviev et al., 2011]. In the case of BiMW device, the two beams propagating into separate arms of the MZI are replaced by two modes of different orders propagating along a single straight channel. This results into a device with improved tolerance to fabrication variations and a smaller footprint, opening the possibility to fabricate more devices in the same area, with consequent increased reproducibility and reliability of the sensing evaluations.

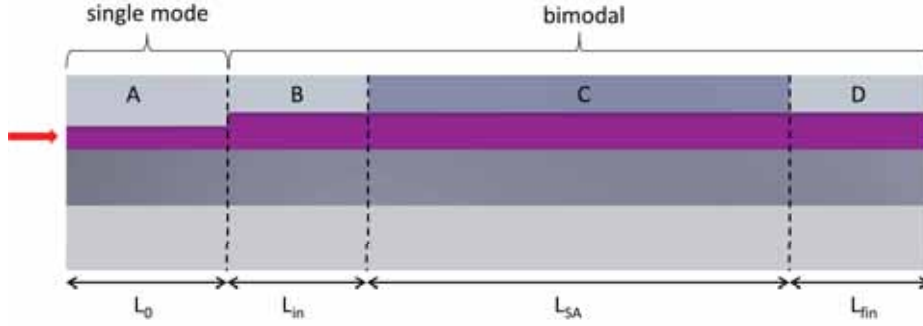
### 2.3.1 BiMW working principle

The BiMW sensor is constituted by the sequence of two different waveguide sections. The first section is a single-mode waveguide, which is coupled to a vertically bimodal waveguide through a step junction, i.e. an abrupt variation in thickness along the propagation direction. A portion of the bimodal section is exposed to the external medium by removing the upper cladding, originating in this way four different sections, represented in Fig. 2.10 as A, B, C, D. In this notation A represents the input single-mode waveguide, B and D are the bimodal regions with silicon dioxide upper cladding layer, and C is the bimodal region responsible for sensing, since the cladding is removed and the core is exposed to the external medium (sensing area).

The working principle is based on the variation of the intensity distribution at the device output due to a change occurring in the sensing area (such as the thickness variation of an adsorbed layer and/or a refractive index variation), which introduces a variation of the phase difference between the two propagating modes. As the fundamental mode is more confined in the core, it can be considered as a virtual reference, while the first order mode is strongly affected by any change occurring in the sensing area. The superposition of these two modes results in an intensity distribution whose variations can be related to the amount of stimulus variation. The evolution of the intensity distribution is recorded by a two-section detector, placed at the output facet. The output signal is defined as:


 (a)  $n=1.33$ 

 (b)  $n=1.46$ 

**Figure 2.9:** Mode dispersion curves for a rib dimension  $4 \mu\text{m} \times 1.5 \text{ nm}$ , wavelength  $\lambda_0=660 \text{ nm}$ , for bulk refractive index  $n=1.33$  (a) and  $n=1.46$  (b).



**Figure 2.10:** Longitudinal view of the BiMW device. Light is injected in the single-mode section (A). After an abrupt step junction two modes can propagate till the end of the device. Regions B and D are covered by silicon dioxide while C is exposed to the external medium (sensing area).

$$S_R = \frac{I_{up} - I_{down}}{I_{up} + I_{down}} \quad (2.37)$$

where  $I_{up}$  and  $I_{down}$  are the intensities collected by the upper and lower sections of the detector, respectively, and is usually expressed as a percentage.

We will assume and later prove that for a constant wavelength excitation, under the proper conditions, the signal  $S_R$  is related to the refractive index change occurring in the sensing area of the device by:

$$S_R \propto V \cos(\Delta\varphi_S(t)) \quad (2.38)$$

where  $\Delta\varphi_S$  is the phase change induced in the sensing area and  $V$  is the fringe amplitude (visibility factor). The phase change,  $\Delta\varphi_S$ , is related to the relative variation of the effective refractive indices of the propagating modes through:

$$\Delta\varphi_S = 2\pi \frac{L_{SA}}{\lambda} (\Delta N_{10} - \Delta N_{00}) \quad (2.39)$$

where  $N_{00}$  and  $N_{10}$  are the effective refractive indices of the fundamental and first order modes, respectively,  $\lambda$  the incident wavelength and  $L_{SA}$  the sensing area length.

Equation (2.38) is the fundamental equation used for the quantification of the experimental data when the device is operated in standard condition, i.e. monochromatic light excitation. The quantity  $\Delta\varphi_S$  is deduced from the analysis of the output intensity interference pattern: a complete oscillation of  $S_R$ , or fringe, corresponds to a  $2\pi$  phase variation.

Preliminary studies [Zinoviev et al., 2011] led to the design and fabrication of a first generation of BiMW devices with core thickness of 150 nm and 340 nm for the single mode and bimodal sections, respectively. This configuration was optimized for a working wavelength of 633 nm, corresponding to the He-Ne laser emission.

A deeper modelization study has been conducted in order to describe the complete device behavior for different configurations (geometry and working wavelength). A wavelength of 660 nm is considered, due to the large availability of laser diodes operating at this wavelength, which will be employed for the implementation of the wavelength-based phase modulation system, as described in the following chapters.

### 2.3.2 Sensitivity

According to the previous modelization results, the sensitivity study is developed for a rib dimension of  $4 \mu\text{m} \times 1.5 \text{ nm}$ . The device response is evaluated in terms of bulk and surface sensitivities, representing the ability of the sensor to transduce a physical change occurring on its surface into a detectable signal.

#### Bulk sensitivity

The intrinsic bulk sensitivity,  $\eta_{bulk}$ , is defined as the variation of the effective index of a guided mode induced by a homogeneous variation of the cladding medium index, through the expression:

$$\eta_{bulk} \equiv \frac{\partial N_{eff}}{\partial n} \quad (2.40)$$

where  $N_{eff}$  is the effective refractive index of the guided mode and  $n$  the absolute refractive index of the cladding.

In the case of interferometric arrangements, the sensitivity depends on the relative variation of a *sensing* mode respect to a *reference* mode, resulting into:

$$\eta_{bulk,int} = \frac{\partial(\Delta N_{eff})}{\partial n} \quad (2.41)$$

being  $\Delta N_{eff} = N_S - N_R$  the difference of the effective refractive indices of the sensing and reference beams,  $N_S$  and  $N_R$ .

We can distinguish two different behaviors according to the geometry. For standard dual-path interferometers, usually the fundamental mode of an input waveguide is split into two single-mode waveguides. Generally the reference arm

is covered by a cladding with fixed refractive index, resulting immune to variations taking place in the sensing area. However in the case of single-path interferometers, where two modes of different order or polarization propagate along the same channel, both modes are affected by a variation of the external medium refractive index, but this variation is different as a consequence of their different confinement factors and sensitivities.

Comparing the specific case of MZI device, representing the dual-path configuration, and the BiMW for the case of single-path arrangement, we can make explicit the expression of Eq.(2.41):

$$\eta_{bulk,int} = \frac{\partial(\Delta N_{eff})}{\partial n} = \begin{cases} \frac{\partial N_S}{\partial n} & \text{MZI} \\ \frac{\partial N_{10}}{\partial n} - \frac{\partial N_{00}}{\partial n} & \text{BiMW} \end{cases} \quad (2.42a)$$

$$(2.42b)$$

where  $N_S$  is the effective refractive index of the sensing arm in the MZI and  $N_{10}$  and  $N_{00}$  are the effective refractive indices of the sensing and 'virtual' reference modes, respectively, for the BiMW sensor. The sensitivity to refractive index changes of the BiMW sensor will therefore depend on the difference of sensitivities of the two propagating modes ( $\partial N_{10}/\partial n > \partial N_{00}/\partial n$ ).

Equation (2.42b) can be computed as a function of the core thickness, as indicated in Fig. 2.11 for the four cases of TE/TM polarizations and for the two central wavelengths 633/660 nm. The function is evaluated for an index value  $n_0 = 1.33$  corresponding to water external medium, as usually employed in biosensing.

All the curves show a similar trend, with an increase starting from small thicknesses close to  $N_{10}$  cut-off, reaching a maximum and then smoothly decreasing. As expected, considering the same polarization, the maximum for the 633 nm case occurs for a thickness lower than in the case of 660 nm.

To summarize the results, Table 2.4 includes the core thickness of the bimodal part corresponding to the maximum intrinsic bulk sensitivity for the different cases TE/TM and the working wavelengths 633/660 nm.

The intrinsic bulk sensitivity takes only into account the variation of the effective refractive index of the propagating modes with the variation of bulk refractive index occurring in the sensing area. Taking into account the interferometric arrangement, the phase sensitivity  $\partial\varphi/\partial n$  is derived from Eq.(2.39) as:

$$\frac{\partial\varphi}{\partial n} = 2\pi \frac{L_{SA}}{\lambda} \frac{\partial\Delta N_{eff}}{\partial n} = 2\pi \frac{L_{SA}}{\lambda} \eta_{bulk,int} \quad (2.43)$$

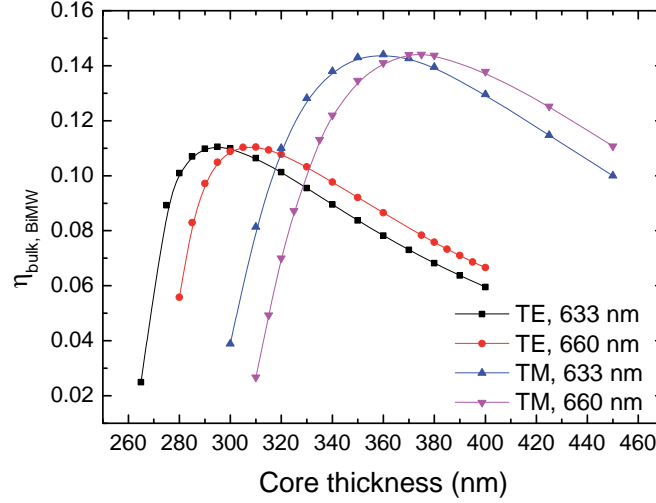


**Figure 2.11:** BiMW intrinsic bulk sensitivity as a function of core thickness for TE and TM polarizations and central wavelengths 633 nm and 660 nm.

**Table 2.4:** Core thickness corresponding to maximum bulk sensitivity for TE and TM polarizations and two working wavelengths.

Wavelength (nm)	Core thickness (nm)	
	TE	TM
633	295	360
660	310	375

and is expressed as rad/RIU. To facilitate the comparison with the experimental results, the phase sensitivity is plotted as a function of the core thickness in Fig. 2.12.

Finally, the global device sensitivity can be derived from the transfer function, given by Eq.(2.38), resulting in:

$$\frac{\partial S_R}{\partial n} = \frac{\partial S_R}{\partial \varphi} \frac{\partial \varphi}{\partial n} = -V \sin(\Delta \varphi_S) 2\pi \frac{L_{SA}}{\lambda} \frac{\partial \Delta N_{eff}}{\partial n} \quad (2.44)$$

and will therefore be lower than the simulated phase sensitivity,  $\partial \varphi / \partial n$ , due to the presence of sine and visibility terms, both smaller than unity. Equation(2.44) is also the responsible for the fading issues described in section 1.4 as limiting

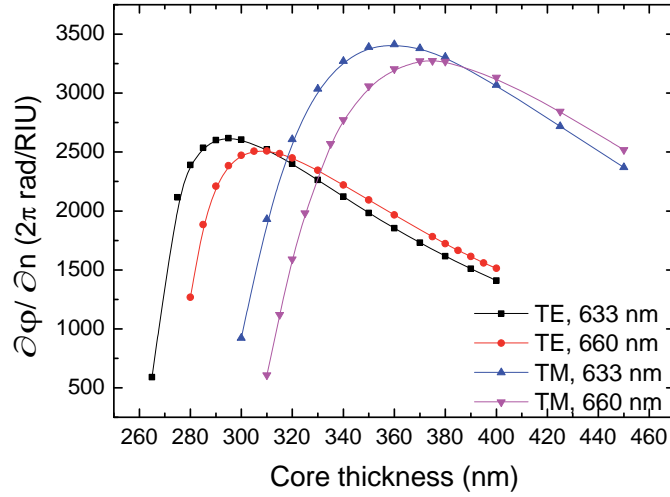


**Figure 2.12:** Phase sensitivity as a function of core thickness for TE and TM polarizations and central wavelengths 633 nm and 660 nm.

factor for the read-out of interferometric sensors.

### Surface sensitivity

When acting as a biosensor, i.e. in an immunoreaction (antibody-antigen) or DNA hybridization, a *thin layer* model can be adopted to calculate the device sensitivity, since only a spatial region much smaller than the penetration depth of the propagating mode is involved in the biomolecular interaction process [Kunz and Cottier, 2006].

For a general waveguide structure, the surface sensitivity is defined as the variation of the effective refractive index of the propagating mode as a function of the thickness of a biological layer,  $t_l$ , assumed with uniform refractive index  $n = 1.45$ , corresponding to a monolayer of proteins.

$$\eta_s \equiv \frac{\partial N_{eff}}{\partial t_l} \quad (2.45)$$

The surface sensitivity is related to the intensity of the guided mode field at the interface between the guiding layer and the outer medium and strongly depends on the waveguide dimensions (thickness) and materials (core and cladding refractive



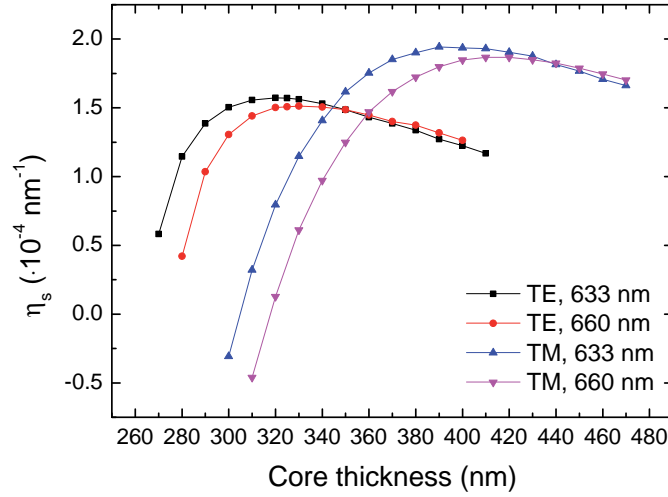


**Figure 2.13:** Surface sensitivity as a function of core thickness for TE and TM polarizations, 633/660 nm.

indices) and on the working wavelength. It has already been demonstrated that in the case of a single mode-based optical waveguide a high surface sensitivity can be achieved with thin core layers and high index contrast [Prieto et al., 2003, Kunz et al., 1996].

In the case of BiMW, since both propagating modes have a non-null dependence on the adsorbed layer thickness, the surface sensitivity will be given by:

$$\eta_{s,int} = \frac{\partial N_{10}}{\partial t_l} - \frac{\partial N_{00}}{\partial t_l} = \frac{\partial(\Delta N_{eff})}{\partial t_l} \quad (2.46)$$

The sensitivity is evaluated from Eq.(2.46) by computing the derivatives of the simulated  $N_{m0}(t_l)$  curves for a layer thickness  $t_{l,0} = 5$  nm.

According to the curves in Fig. 2.13, in the case of TE polarization the surface sensitivity is maximum for core thickness around 320-330 nm and 390-410 nm in the case of TM interrogation. These results justify the choice of 340 nm waveguide thickness for TE interrogation.

A derivation similar to the one proposed in the case of bulk sensing can be done to relate the intrinsic surface sensitivity to the device surface sensitivity.

### 2.3.3 Mode splitter

Once encountered the conditions to achieve a transverse (horizontal) single-mode behavior and the existence of the two vertical modes, the design of the sensor is completed by introducing a mode splitter, consisting of an abrupt variation of the core thickness and referred to as step junction.

In our application the thickness of the bimodal section (B to D in Fig. 2.10) is fixed taking into account the phase sensitivity. The thickness of the input single-mode part (section A in Fig. 2.10) must be chosen to ensure a satisfactory output signal visibility  $V$ , which affects the overall sensitivity through Eq.(2.44). In fact it is the relation between the A and B sections thickness (see Fig. 2.10) which determines how the energy carried by the fundamental mode propagating in A is distributed to the two modes propagating in B. This energy distribution can be quantified through the coupling coefficients, representing the overlapping integrals between the mode profiles in the two faced sections.

The coupling coefficients are defined as:

$$\Gamma = \frac{|\int \int E_1^*(x, y) E_2(x, y) dx dy|^2}{|\int \int E_1(x, y) E_1^*(x, y) dx dy| |\int \int E_2(x, y) E_2^*(x, y) dx dy|} \quad (2.47)$$

where  $E_1(x, y)$  and  $E_2(x, y)$  are the electric field distributions for the two guided modes, which can be directly assessed in the Photon Design environment, as shown in Fig. 2.14, where the field profile of the TE<sub>00</sub> mode of section A is superposed to the TE<sub>00</sub> and TE<sub>10</sub> modes of section B. The overlapping between the curves corresponds to the definition of coupling coefficient.

The signal visibility is defined as:

$$V = \frac{S_{R,max} - S_{R,min}}{2} \quad (2.48)$$

and corresponds to the amplitude of the  $S_R$  oscillations (interference fringes). The visibility factor influences the device performance in terms of LOD evaluation. In the case of BiMW sensor, since the phase signal is deduced from the variations of the  $S_R$  signal, the definition given in (1.1) transforms into:

$$LOD = \frac{\Delta\varphi_{min}}{S} = \frac{\Delta S_{R,min}}{S} \cdot \frac{\pi}{2V} \quad (2.49)$$

as a consequence of the equivalence between  $S_R$  fringes and phase conversion: an  $S_R$  variation of  $2V$  units corresponds to a phase change of  $\pi$  rad. The factor  $\pi/2V$  is necessary for the conversion between the experimentally measured  $S_R$  signal, expressed as a percentage, and the phase (radians).  $S$  is the BiMW sensitivity,

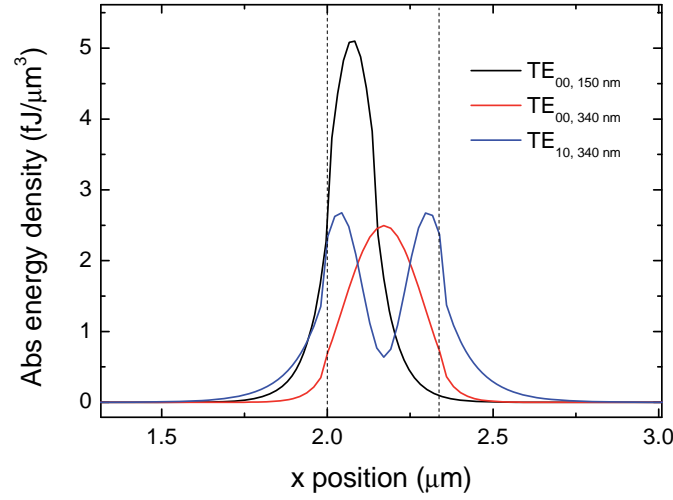


**Figure 2.14:** Superposition of the mode profiles for  $\lambda_0 = 660$  nm, TE polarization. Dashed lines define the core layer (340 nm thickness).

expressed as rad/RIU in the case of bulk sensing or as rad/[analyte] in the case of surface sensing.

The pair single-mode/bimodal thickness must be chosen to ensure a good energy distribution between fundamental and first order modes, keeping moderate losses in the input single-mode part. A previous design of the device set values of 150-340 nm, with simulated coefficients around 67% for  $TE_{00}$  excitation and 22% for  $TE_{10}$ , at 633 nm, resulting in an experimental output visibility around 70%.

Keeping the same layer thicknesses, for a working wavelength of 660 nm the coupling coefficients assume the values of 69% for  $TE_{00}$  and 20% for  $TE_{10}$ , resulting in a slightly reduced experimental output modulation.

#### 2.3.4 Complete device and transfer function

Once encountered the thicknesses of the input single-mode and bimodal core sections, the sensor design is completed by choosing the length of the different sections. A value of 15 mm was adopted for the sensing area to ensure a high sensitivity, while keeping a reasonable total length. The lengths of the different sections, as shown in Fig. 2.10, are  $L_0 = 3$  mm,  $L_{in} = 4.5$  mm and  $L_{fin} = 8.5$  mm.

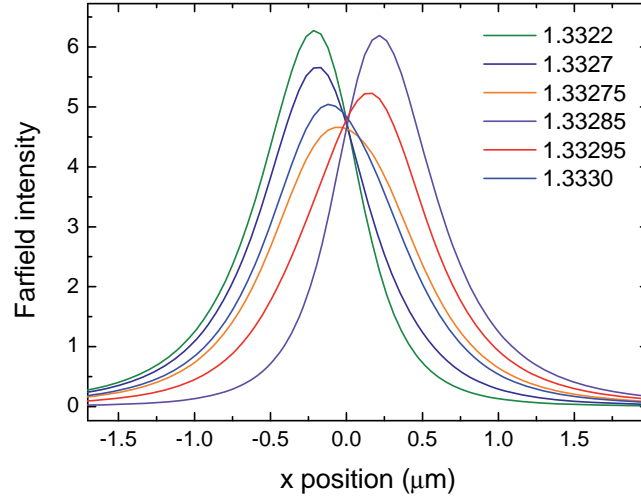


**Figure 2.15:** Far field intensity distribution for different refractive index ( $n = [1.3322 - 1.3330]$ ) in the sensing area. Core dimensions: 150-340 nm.

Figure 2.15 shows the far field intensity corresponding to different refractive indices in the sensing area medium, for a structure of 150-340 nm core thicknesses.

As it can be observed, the position of the intensity maximum and the whole intensity profile vertically shift according to the refractive index value, justifying the proposed detection method. To complete the modelization, these intensity patterns must be evaluated over a finite area, representing the employed detector. For this reason, in the far field option of the Photon Design software, the aperture dimensions have been set to  $3 \times 1.5 \text{ mm}^2$ , placed at distance of 1 mm from the output facet, with a vertical offset of  $\pm 0.75 \text{ mm}$ , to describe the experimental  $I_{up}$  and  $I_{down}$  signals. The device response can be evaluated from its transfer function  $S_R(n)$ , which can be computed for different input parameters.

From the curves in Fig. 2.16, which represent the variations of  $S_R$  as a function of the refractive index for TE polarization and the two working wavelengths of 633 nm and 660 nm, we can deduce relevant information. In the first place, the transfer function  $S_R(n)$  satisfies a sinusoidal dependence with  $n$ , justifying the treatment of the BiMW device as an interferometric sensor and the assumptions presented for the phase signal evaluation. Then, the bulk sensitivity can be assessed from the  $S_R(n)$  curves periodicity, resulting in values of  $2140 \cdot 2\pi \text{ rad/RIU}$  for  $\lambda_0 = 633$

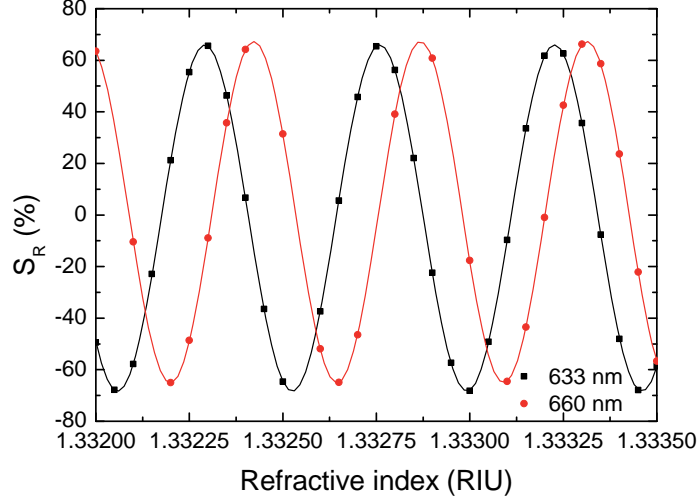


**Figure 2.16:** BiMW transfer function  $S_R(n)$  for TE polarization, evaluated through far field analysis for wavelengths 633 nm (black line) and 660 nm (red line). Sine fit shown.

nm and  $2240 \cdot 2\pi$  rad/RIU for  $\lambda_0 = 660$  nm, in agreement with the results of modal analysis presented in Fig. 2.12.

### 2.3.5 Critical effects

Due to the different relations of dispersion of the involved modes, in spectrally interrogated hetero-modal interferometers a critical point can arise when the condition

$$\frac{\partial}{\partial \lambda} \frac{\Delta N_{eff}(\lambda)}{\lambda} = 0 \quad (2.50)$$

is verified, i.e. when the effective refractive index difference shows a maximum or minimum as a function of the working wavelength [Levy and Ruschin, 2008]. As a consequence, the sensitivity of spectrally interrogated interferometric sensors ( $\partial \Delta \lambda / \partial \Delta n$ ) diverges in proximity of the critical point rendering in potentially ultra-high sensitivity detections, limited only by the system noise [Levy and Ruschin, 2008, Pinheiro-Ortega et al., 2010].

For the sake of clarity, the spectral sensitivity can be made explicit from the definition of the phase difference between two modes, Eq.(2.39), by considering

the phase shift induced by a wavelength variation, resulting in:

$$\frac{\delta\lambda}{\delta(\Delta\varphi)} = \frac{1}{2\pi L \left[ -\frac{1}{\lambda^2} \Delta N_{eff} + \frac{1}{\lambda} \frac{\partial \Delta N_{eff}}{\partial \lambda} \right]}. \quad (2.51)$$

It is now evident that a divergence can occur when the denominator in Eq.(2.51) assumes a null value, corresponding to the condition (2.50), since:

$$\frac{\partial}{\partial \lambda} \frac{\Delta N_{eff}(\lambda)}{\lambda} = -\frac{1}{\lambda^2} \Delta N_{eff}(\lambda) + \frac{1}{\lambda} \frac{\partial \Delta N_{eff}(\lambda)}{\partial \lambda}. \quad (2.52)$$

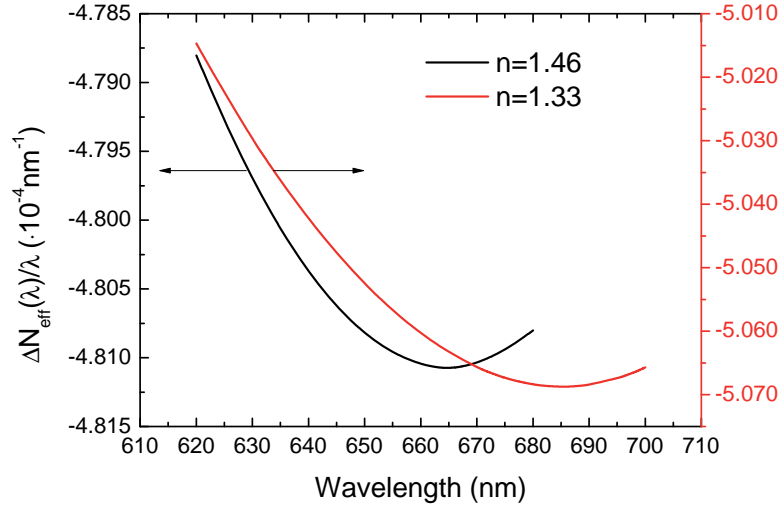
According to the definition provided in (2.50), the critical wavelength for the BiMW device is evaluated as the minimum of the function  $\frac{\Delta N_{eff}(\lambda)}{\lambda}$ , obtained through 2D simulations of the device cross-section reported in Figure 2.7, with a bimodal core thickness of 340 nm. Fig. 2.17 shows the  $\frac{\Delta N_{eff}(\lambda)}{\lambda}$  calculated for the two sections of interest, corresponding to a cladding of water,  $n=1.33$ , and silicon dioxide,  $n=1.46$ . The critical wavelengths corresponding to these configurations have been evaluated as 685 nm and 665 nm for  $n=1.33$  and  $n=1.46$ , respectively [Dante et al., Subm].

Considering the light propagation in the complete device, the critical point in the transmission curve  $S_R$  manifests for an effective critical wavelength of 676 nm, intermediate to the previously presented values of 665 and 685 nm. In Fig. 2.17(b) we can notice how the periodic oscillations of  $S_R(\lambda)$  are interrupted around the critical wavelength and a smoother transition takes place.

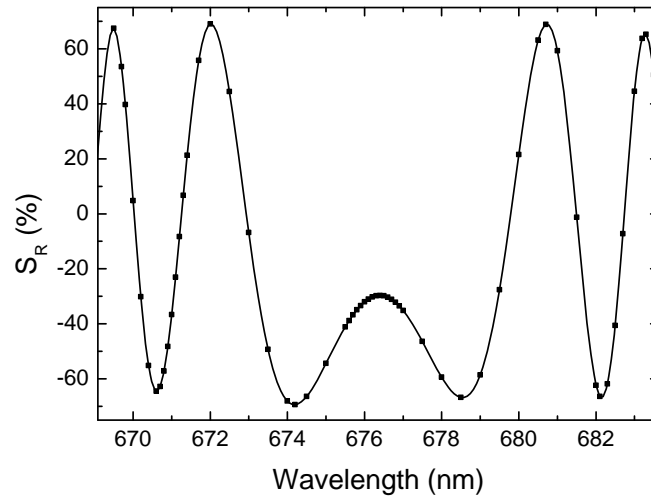
During our studies, we found that a slight variation in the rib dimensions does not lead to substantial variations for the critical effects, being the core thickness the dominant variable. Therefore, in order to achieve a critical-free behavior, we studied the evolution of the critical wavelength for varying refractive index  $n$ , for a rib structure of  $4 \mu\text{m} \times 1.5 \text{ nm}$ . From the curves shown in Fig. 2.18 we can obtain relevant information, since any plotted data point represents the critical wavelength for a given index-thickness pair. Once fixed the core thickness, the critical wavelength shows a parabolic dependence with the refractive index, decreasing for increasing index.

Since in our application the working wavelength is fixed by commercially available laser diodes ( $\lambda_0 = 660 \text{ nm}$ ) it is more convenient to describe the critical behavior in terms of *critical thickness*. The critical thickness and the wavelength are related by a linear relationship.

We numerically studied the response to a variation of the bulk refractive index for sensor chips with core thickness external to the critical region, with core



(a)



(b)

**Figure 2.17:** Critical effects for a 340 nm core thickness, TE polarization. (a) Plots of  $\frac{\Delta N_{\text{eff}}(\lambda)}{\lambda}$  for  $n=1.33$  and  $n=1.46$  obtained with modal analysis and (b) BiMW transfer function for  $n=1.33$  in the sensing area, obtained with far-field analysis. Single-mode core thickness of 150 nm.

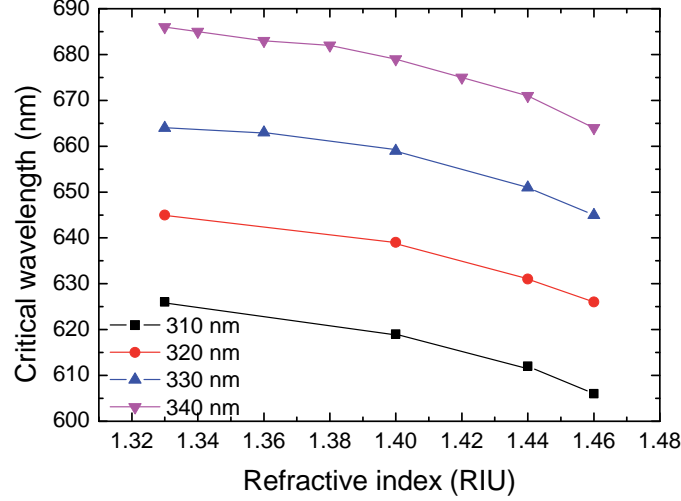


**Figure 2.18:** Critical wavelength as a function of bulk refractive index for different bimodal core thickness, evaluated with modal analysis.

thickness of 320 nm and 340 nm, respectively. The results are shown in Fig. 2.19.

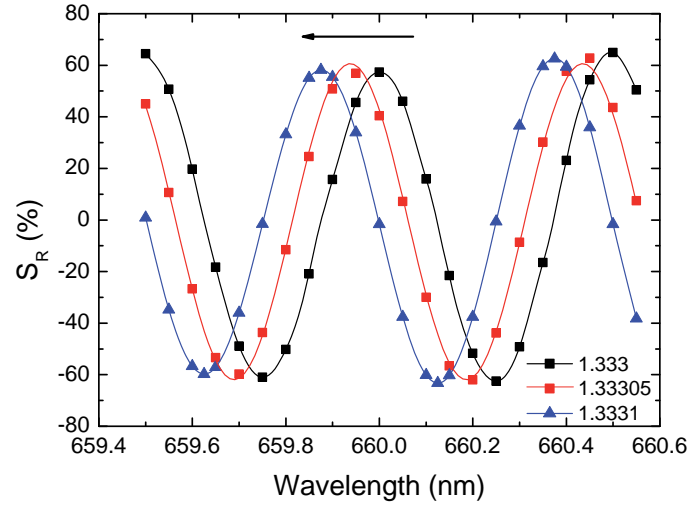
As a consequence of the opposite derivative sign of  $\frac{\Delta N_{eff}(\lambda)}{\lambda}$  before and after the critical point (see Fig. 2.17a) an opposite direction for the spectral shift is observed in response to the same applied stimulus. Similar results were observed for single mode-multimode-single mode fiber sensors, as presented by [Tripathi et al., 2010, Salik et al., 2012].

Because they are a consequence of modal dispersion, critical effects are more evident for single-path interferometers than for standard two-path configurations where dispersion relations of the same order govern both sensing and reference modes and the phase accumulation only takes place in the sensing area.

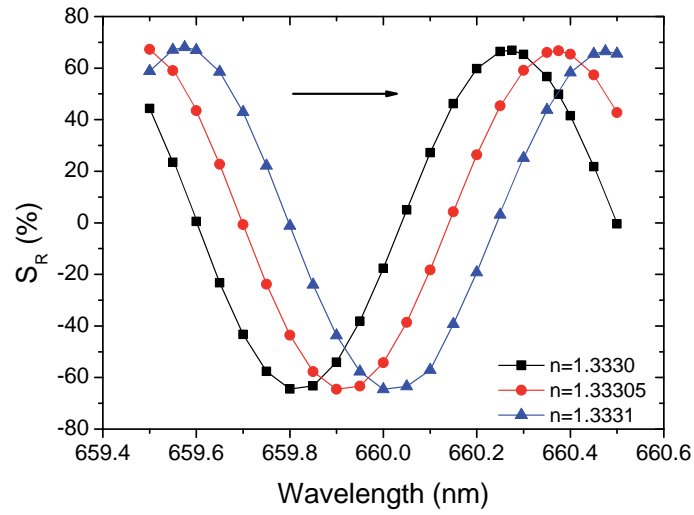
## 2.4 Conclusions

In this chapter the mathematical tools necessary to model an integrated interferometer, based on the resolution of Maxwell's equations, have been reviewed. We have presented numerical methods which can be employed to study the 3D waveguide structures, together with the working principle of the Eigenmode Expansion approach, as it is included in the commercial Photon Design software employed





(a) 320 nm core



(b) 340 nm core

**Figure 2.19:** Transmission curves as a function of wavelength for different refractive indices (1.333, 1.33305, 1.3331). The spectral shift occurs in opposite direction according to the core thickness: (a) 320 nm showing blue-shift and (b) 340 nm core thickness showing red-shift. TE polarization.

for the modelizations.

The design and modelization of a novel sensing device based on two-mode principle have been presented, assessing the requirements of lateral single-mode propagation and high sensitivity to bulk and surface changes. Compared to the traditional MZI configuration, the BiMW sensor offers remarkable advantages as a smaller footprint and the suppression of any lateral mode recombination (i.e. Y-junctions), excluding the possibility to generate higher order modes which can propagate till the device output compromising the detection.

The existence of a critical point in the transmission of the bimodal waveguide sensor, due to the different dispersion relations of the propagating modes, has been theoretically and numerically described.

# Chapter 3

## Fabrication and characterization of IO interferometric biosensors

This first part of this chapter describes the fabrication and the morphological characterization of the BiMW interferometric sensors, followed by the methods used for the chip preparation (polishing and cleaning) prior to the experimental evaluation. Finally the device is evaluated with the standard monochromatic approach and the bulk sensitivity is assessed, highlighting the need for a phase linearization system.

### 3.1 Fabrication

All the devices have been fabricated in the Clean-Room facilities of the Barcelona Microelectronics Institute of the National Microelectronics Centre (IMB-CNM)<sup>1</sup>, belonging to our organization, Spanish National Research Center (CSIC), and located close to our premises.

Taking into account the previous considerations,  $\text{SiO}_2/\text{Si}_3\text{N}_4/\text{SiO}_2$  rib waveguides were fabricated over a silicon substrate. The lateral single-mode behavior can be achieved with rib widths of few microns, obtainable with standard photolithography and etching processes. For the layer thickness, values of 150 nm and 340 nm were selected for the single-mode and bimodal parts, respectively.

Due to their transparency over a broad spectral range ( $\approx 200 - 2000$  nm), silicon dioxide and silicon nitride are excellent material candidates for the fab-

---

<sup>1</sup> <http://www.imb-cnm.csic.es>

rication of sensor devices operating at visible wavelengths. The high refractive index contrast between both materials can render in optimal structures for sensing applications. The layers fabrication must ensure homogeneity, to guarantee a constant refractive index; a low impurity level, to avoid scattering or adsorption; chemical stability to allow a reliable use as biosensor and uniformity to control the guiding properties of the structure [Domínguez et al., 2003]. The adhesion between the different layers must be high to provide a robust structure and the thermal coefficients must be comparable to avoid cracking during the fabrication. Finally yet importantly, the different layers must show similar mechanical hardness in order to facilitate an end-facet polishing as required by the end-fire light in-coupling method.

Lithographic masks and devices were fabricated using standard microelectronics technology. The mask is designed with the open-source software KLayout<sup>2</sup> and the mask fabrication was carried out by Photronics Inc manufacturing<sup>3</sup>.

### Mask layout

For the fabrication of the bimodal devices a set of four lithographic masks (labeled *CNM-327*) is employed. The complete mask layout for the patterning of 12 BiMW chips over a 4-inches wafer is shown in Fig. 3.1. Each chip (1 cm wide  $\times$  3.1 cm long) contains 16 sensors, distributed in 4 groups of 4 devices, with a center-to-center pitch of 250  $\mu\text{m}$  to permit successive integration with standard components.

### Fabrication

The fabrication starts with a 4-inches p-doped silicon wafer, over which a 2  $\mu\text{m}$  thick layer of thermal oxide is grown ( $n = 1.46$  at 660 nm). This layer constitutes the lower cladding of the waveguiding structure and its thickness avoids leakage losses towards the silicon substrate.

Then a 340 nm thick core layer of silicon nitride ( $n = 2.00$ ) is deposited by Low Pressure Chemical Vapor Deposition (LPCVD), due to the good properties of uniformity and mechanical adhesion it offers with respect to other deposition methods. The thickness of the single mode section (device input) is reduced to 150 nm with a wet etching process, done with hot phosphoric acid. A hard mask constituted by a layer of Boron Phosphorous Silicon Glass (BPSG) and defined by photolithography is employed for this step to protect unexposed regions.

In the same process, alignment marks are defined at the chip input and output for each sensor, to facilitate an easier light in-coupling into the waveguides, which

---

<sup>2</sup> <http://www.klayout.de/>    <sup>3</sup> <http://www.photronics.com/plab/mask-services/>

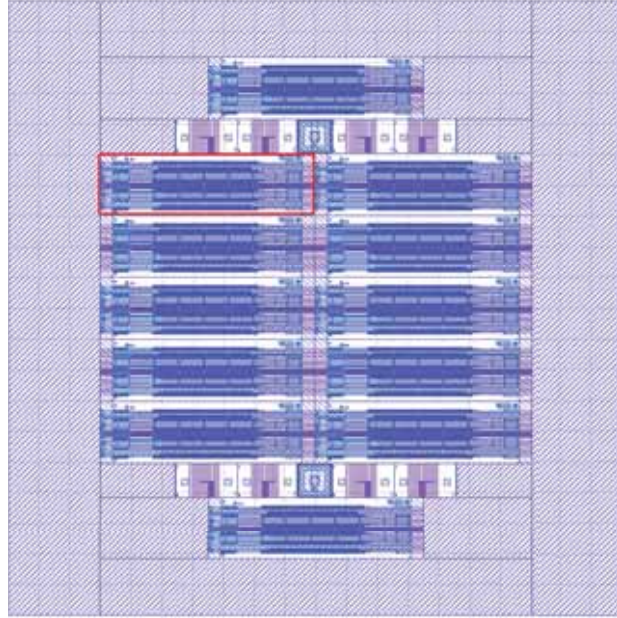


**Figure 3.1:** Mask layout, consisting of four layers, for the definition of 12 BiMW chips through standard lithographic techniques. Each sensor chip ( $1\text{ cm} \times 3.1\text{ cm}$ ) contains 16 BiMW sensors.

are not visible by naked eye.

Once the two different modal sections are defined, the nanometric rib structure of the waveguide (4  $\mu\text{m}$  in width and 1.5 nm in height) is generated by buffered hydrofluoric acid (BHF) etching through a photoresist mask patterned by photolithography. The low etching rate of the etchant BHF for  $\text{Si}_3\text{N}_4$  allows a deeper control of the process and a higher reliability has been demonstrated for a wet approach with respect to a dry (reactive ion etching) solution.

A 100 nm thick layer of poly-crystalline silicon ( $n=3.9$ ) is employed as absorbing material to define lateral bands along the waveguide path. It is deposited over 200 nm of silicon dioxide, introduced to improve the adhesion to the underlying silicon nitride surface.

As a top cladding layer, a silicon dioxide layer 1.5  $\mu\text{m}$  thick is deposited by Plasma Enhanced Chemical Vapor Deposition (PECVD).

The opening of the sensing area constitutes a paramount step in the fabrication: the presence of residual  $\text{SiO}_2$  would reduce or even prevent the sensing capabilities and must be avoided. For the sensing area definition, a sequential combination of dry and wet etching is chosen since it offers a better control of the process than a single step approach. A dry etching (RIE) process can provide vertical sidewalls for the sensing area, which ensure reduced light scattering to the presence of rough  $\text{SiO}_2$  at the sensing area edges. However, its reduced selectivity and the damages to the underlying layer due to ion bombardment, require the use of a wet etch step to finalize the process. Furthermore the wet etching stop can be better controlled thanks to the material selectivity (silicon dioxide over silicon nitride). A schematic view of the complete process flow is shown in Fig. 3.2.

Finally the wafers are spin-coated with a standard photoresist (1.5  $\mu\text{m}$ ) to ensure mechanical protection during the chip dicing operation, which is performed with a saw.

A picture of the complete processed wafer is shown in Fig. 3.3.

Along the fabrication flow the properties of the deposited layers, i.e. refractive index and thickness, are evaluated by ellipsometry and interferometric techniques<sup>4</sup>.

## 3.2 Morphological characterization

### AFM

The quality of the rib definition, fundamental for a correct device behavior, can be verified through Atomic Force Microscopy (AFM) inspection performed at the

---

<sup>4</sup> [www.filmetrics.com](http://www.filmetrics.com)

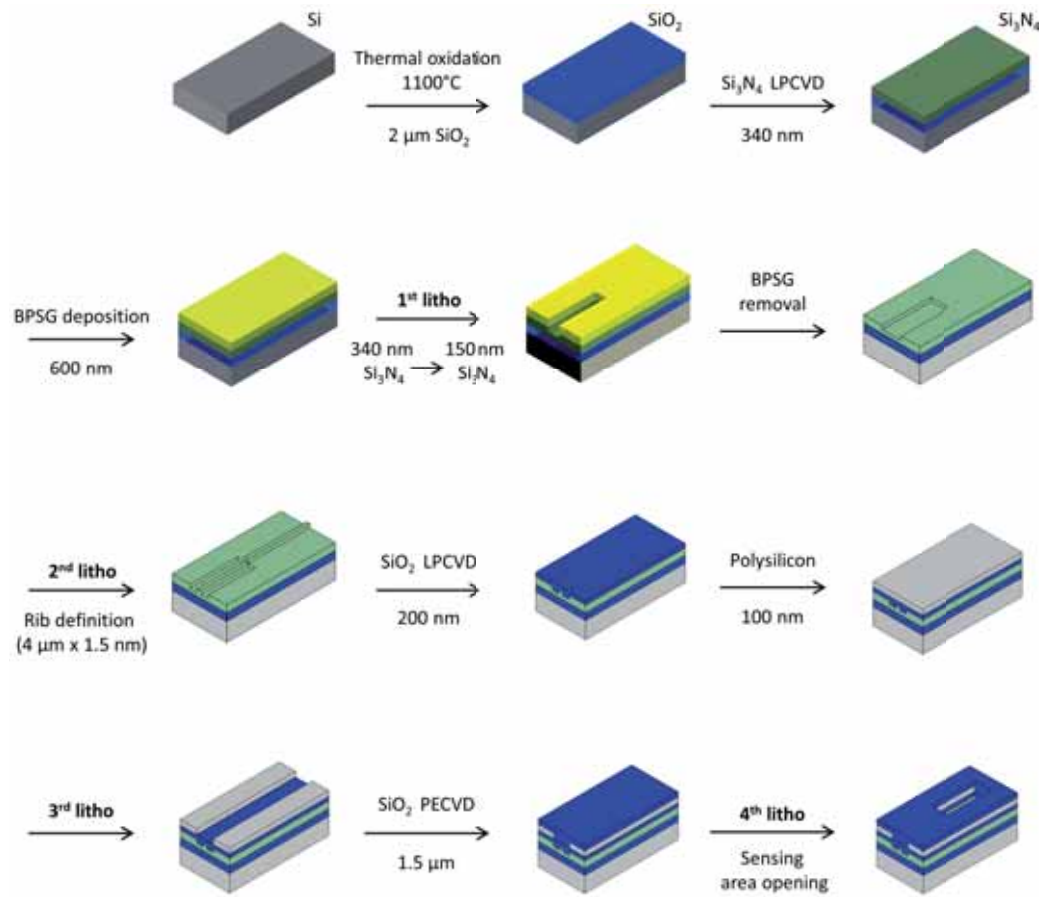


**Figure 3.2:** Scheme of the process flow required for the fabrication of integrated BiMW sensors.

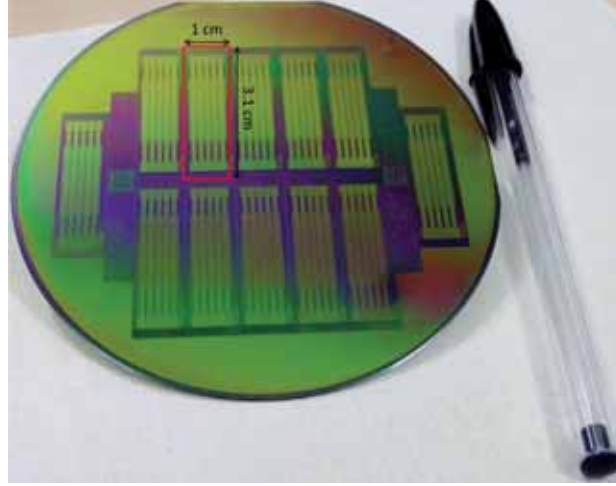


**Figure 3.3:** Photograph of a processed 4-inches wafer with 12 BiMW chips, resulting in a total of 192 sensors.

end of the fabrication process. In the sensing area the silicon dioxide is removed and the rib is exposed to the external environment, available for inspection. Non-contact tapping mode images are recorded with a PicoPlus AFM system (Molecular imaging) by using silver coated silicon probes (PPP-NCHR, NanoandMore). Image processing and rendering is done with the WSxM software [Horcas et al., 2007].

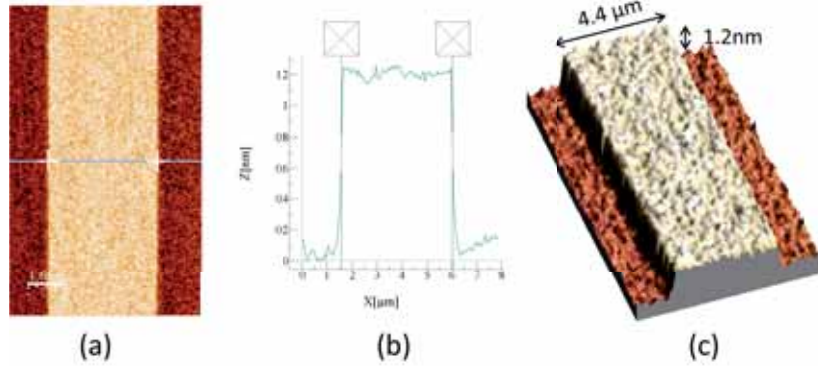
In Fig. 3.4 the amplitude (topography) image, the corresponding average cross section profile and a 3D rendering of one of the inspected ribs are shown, indicating dimensions of  $4.4\mu\text{m} \times 1.2\text{ nm}$ , which ensure a single-mode propagation.

## SEM

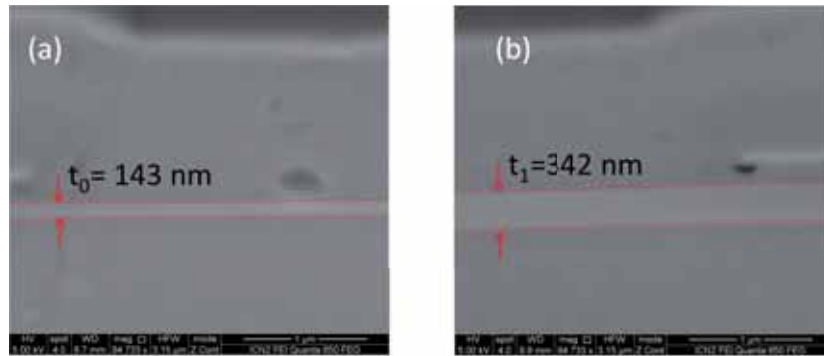
The thickness of the different waveguide films can be inspected by Scanning Electron Microscopy (SEM). In particular we verified the thickness of the silicon nitride core, as this is one of the main parameters for the sensor performance. Back-scattered electron images are acquired on a  $70^\circ$  specimen stub with a Quanta 650 FEG system (FEI) to inspect the input and output facets.

Figure 3.5 shows the input (single-mode) and output (bimodal) cross-section of an inspected BiMW chip, where the silicon nitride core thicknesses have been evaluated as  $t_0 = 143\text{ nm}$  and  $t_1 = 342\text{ nm}$ , respectively, validating the fabrication.





**Figure 3.4:** (a) Amplitude (topography) image, (b) average cross-section profile and (c) 3D rendering of a BiMW rib inspected by tapping-mode AFM.



**Figure 3.5:** SEM images of the BiMW input (a) and output (b) sections.

### 3.3 Materials and methods

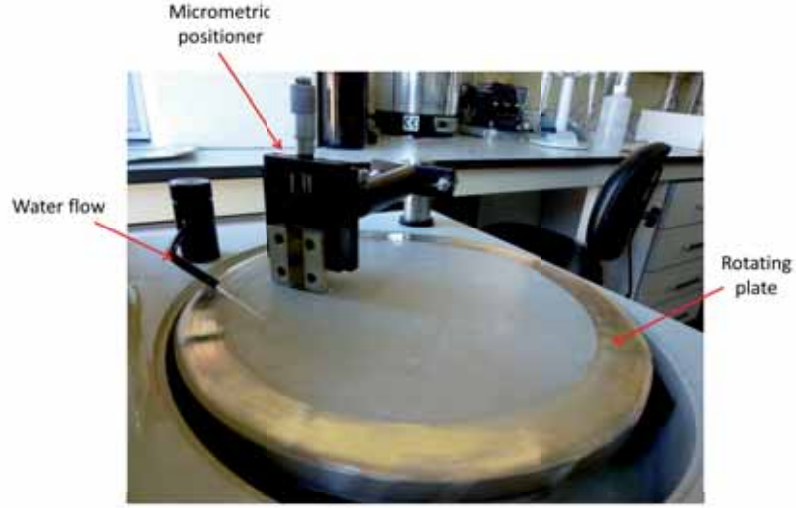
**Reagents.** Absolute ethanol (EtOH, 99%), acetone (Ac, 99.5%) and methanol (MeOH, 99.5%) were purchased from Panreac, Spain. Hydrochloric acid (HCl, 35-38%) was purchased from Poch SA, Poland. Carboxyethyl silanetriol, sodium salt (CTES) was purchased from abcr, Germany. Bovine serum albumin (BSA), monoclonal anti-bovine serum albumin antibody (anti-BSA), N-(3-dimethylaminopropyl)-N'-ethylcarbodiimide (EDC), N-Hydroxysuccinimide (NHS) (98%) and all the components of phosphate buffered saline (PBS; 10 mM phosphate, 2.9 mM KCl, 137 mM NaCl, pH 7.4) were purchased from Sigma-Aldrich, Germany. Purified milli-Q water from Millipore, USA, was always employed.

hTSH and hGH were provided by Dr. Parlow from National Hormone & Peptide Program (NHPP) National Institute of Diabetes and Digestive and Kidney Diseases (NIDDK), Torrance, California (USA). The monoclonal antibodies employed for hTSH and hGH detection were provided by the Department of Immunology and Oncology from National Center of Biotechnology (CNB, CSIC, Madrid, Spain).

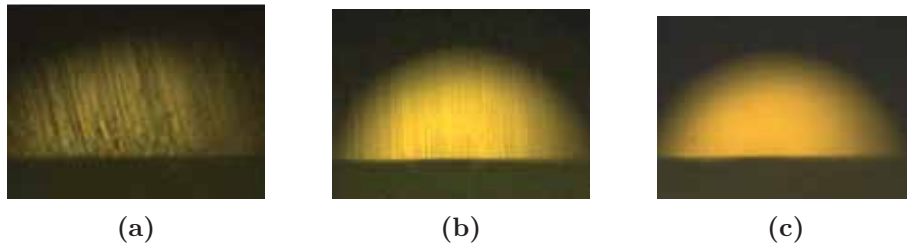
**End-facets polishing.** A polishing step is required prior to the chip optical characterization to achieve an optical quality facet and minimize scattering (insertion) losses during end-fire coupling. The chips are manually polished by employing a lapping machine Logitech CL50. A micrometric positioner is necessary to guarantee a correct positioning of the chip, perfectly vertical, over the rotating platform, as showed in Fig. 3.6. Adhesive abrasive papers with decreasing grain size are used, starting from a roughness of 9  $\mu\text{m}$  till 0.3  $\mu\text{m}$ . A water flow is used to wash out particles and debris which could compromise the surface quality.

Figure 3.7 includes optical images of the chip facet after the three steps of polishing, with paper roughness of 9  $\mu\text{m}$ , 3  $\mu\text{m}$  and 0.3  $\mu\text{m}$ , respectively. After this last step the chip is considered optically flat.

**Chip cleaning.** In order to remove the protective photoresist and eventual residues from the polishing process, the chips undergo an accurate cleaning prior to the optical characterization process. First the chips are sonicated sequentially in acetone, ethanol and water, 2 min each. Then they are sonicated for 10 min in a mixture 1:1 HCl:MeOH in order to remove all organic contaminants, resulting in a highly hydrophilic surface. The chips are rinsed with DI water and blow-dried under a  $\text{N}_2$  stream.



**Figure 3.6:** Chip polishing: a micrometric positioner allows the position of the chip, vertically aligned to the rotating plate.



**Figure 3.7:** Chip input facet after polishing with different roughness paper: (a)  $9\text{ }\mu\text{m}$ , (b)  $3\text{ }\mu\text{m}$  and (c)  $0.3\text{ }\mu\text{m}$ .

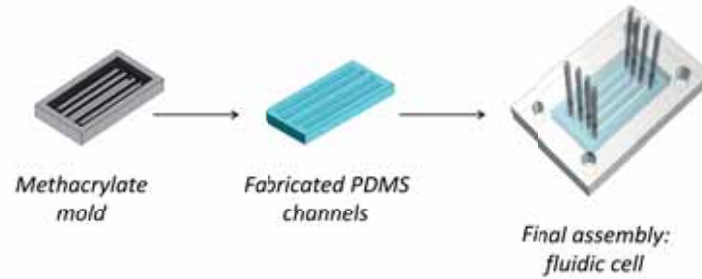


**Figure 3.8:** Scheme of the methacrylate mold, the fabrication of the channels and the final arrangement of the fluidic cell.

**Polymeric channels fabrication.** The Polydimethylsiloxane (PDMS) channels are fabricated by polymer casting using a methacrylate mold, as shown in Fig. 3.8. Elastomer and curing agent are mixed in a ratio 10:1 and air bubbles originating from their mixing are removed by a vacuum degas process. The mixture is then cured for 1 hour at  $75^{\circ}\text{C}$  to ensure cross-linking of the polymer. After this thermal process the channels can be released from the methacrylate mold.

The high hydrophobicity of the resulting PDMS channels is reduced by a Polyethylene glycol coating (PEG200, Sigma-Aldrich), applied after a ozone plasma treatment to expose functional groups on the polymer surface.

Finally, PolyTetraFluoroEthylene (PTFE) tubes are inserted at each channel extremities and fixed with PDMS to avoid leakages or air insertion. The final fluidic cell has four independent channels, with a volume of  $15\ \mu\text{l}$ . Each fluidic channel addresses a group of four BiMW sensors on the fabricated chips.

**Bulk sensitivity evaluation.** The bulk sensitivity can be experimentally determined by measuring the phase shift induced by different variations of the refractive index in the medium in contact with the sensing area. A liquid which does not chemically modify the sensor surface can be employed.

For this reason different solutions of hydrochloric acid (HCl) at low concentration are sequentially supplied to the device under test and the phase change is evaluated with respect to the refractive index of milli-Q water ( $n \approx 1.3327$ ), employed as running buffer. The refractive index of each solution is measured with an Abbe refractometer (Optic Ivymen System, Spain) prior to any injection.

### 3.4 Experimental set-up

The experimental set-up required for the characterization of the integrated BiMW sensors is composed by four main parts: i) input optics, ii) temperature stabilization, iii) fluid delivery and iv) signal acquisition, as schematically shown in Fig. 3.9.

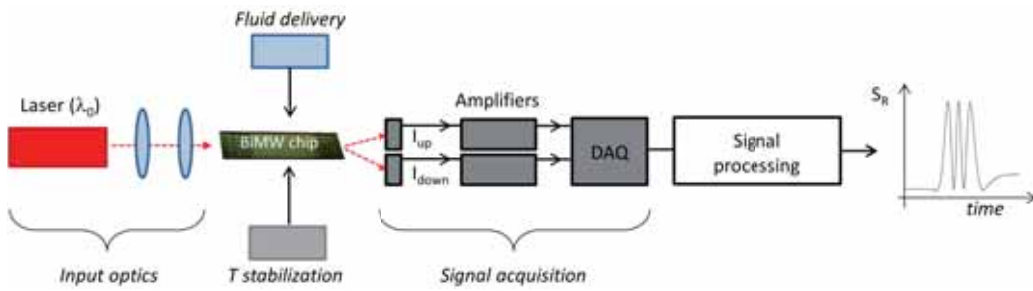


**Figure 3.9:** Scheme of the experimental set-up employed for the evaluation of the BiMW sensors.

#### Optical system

Due to its properties of stable emission, long coherence length and high quality (spectral and spatial) of its emission, a linearly polarized He-Ne laser ( $\lambda = 632.8$  nm,  $P = 5$  mW) is chosen for the standard characterization (i.e. intensity interrogation) of the BiMW sensors.

An optical isolator is introduced along the optical path to solve the double function of laser cavity protection and polarization selection. The existence of back-reflections into the cavity destabilizes the laser emission by introducing additional frequency components in the emitted spectrum, resulting in amplitude and phase noise at the device output. The emitted laser beam is focused at the input of the waveguide using a  $40\times$  objective, as it can be seen in Fig. 3.10. The chip is placed on a custom-made holder, especially designed to fit standard 3-axis translation platform for the proper alignment of the input beam.

A digital camera (AM4113T, Dino-Lite, The Netherlands) is employed for inspection of the chip surface and light in-coupling through the specific alignment marks.

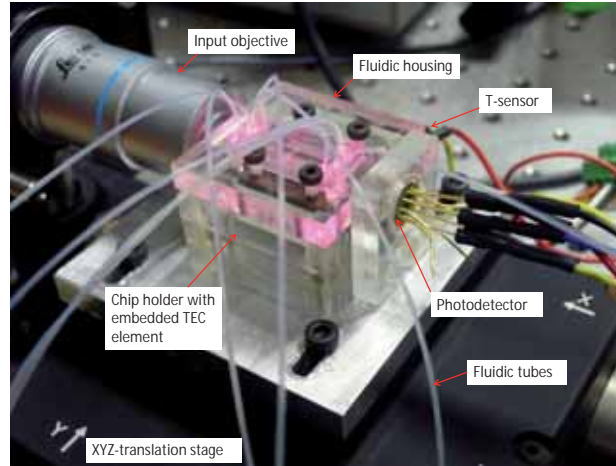


**Figure 3.10:** Detailed view of BiMW chip in the experimental set-up. Polarized light is in-coupled through a 40 $\times$  objective and collected by a two-section detector. Chip temperature is kept constant by a TEC element integrated in the methacrylate support.

### Temperature stabilization

A temperature control is required for the evaluation of the BiMW sensor since the two propagating modes show different sensitivities for temperature variations, which can result in false positive signals [Zinoviev et al., 2011].

A temperature sensor (AD590, Thorlabs) is used to achieve a temperature feedback circuit together with a thermo-electric cooler (TEC3-2.5, Thorlabs), operated through a benchtop temperature controller (TED200C, Thorlabs) allowing a temperature resolution of 0.01 $^{\circ}$ C. The chip holder is fabricated in copper and is embedded in a methacrylate housing which ensures the contact between the different components, i.e. TEC element, temperature sensor and copper support. The contacts among the different components are reinforced by a silver paint with high thermal conductivity.

### Fluid delivery system

Fluid delivery is a fundamental aspect to be dealt with in biosensor applications: tiny amounts of samples must be employed and delivered to the sensing area, where they are probed by the evanescent field of the propagating light. To ensure reproducible results the fluidic system must ensure a constant flow over the device sensing area, with a controllable flow rate according to the application, usually in

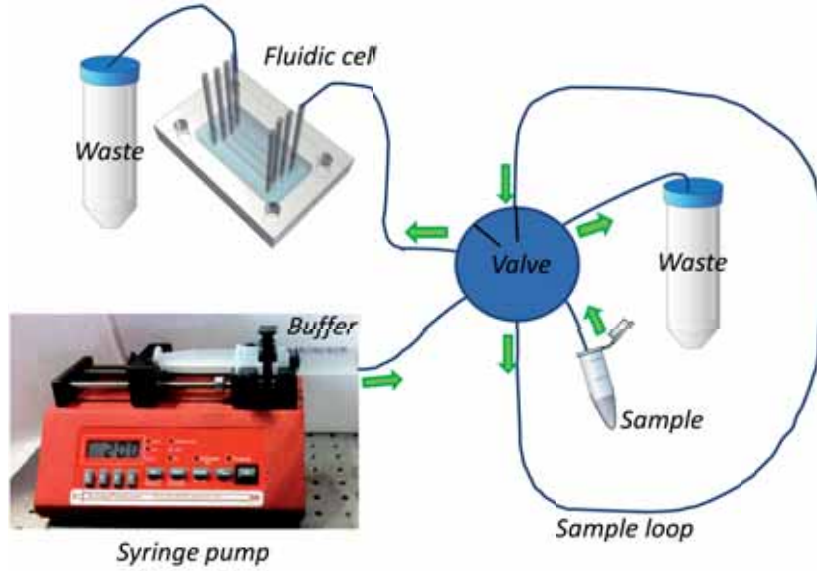


**Figure 3.11:** Scheme of the flow delivery system employed.

the range 10-50  $\mu\text{l}/\text{min}$ .

Figure 3.11 shows the elements required for the flow system, consisting of a syringe pump (NE1000, New Era), a two-position valve (V-451, Idex) which allows to sequentially load the sample loop (volume 250  $\mu\text{l}$ ) with the desired solution and then inject it towards the sensor and a custom-made fluidic cell. This methacrylate fluidic cell hosts a PDMS array of four channels designed to address the four groups of sensors present on each chip. The cell is then fixed to the chip holder by a screw system, ensuring perfect sealing between the PDMS edges and the chip surface. Fluidic tubes are attached through the same methacrylate-PDMS ensemble to provide connections with the external components.

### Data acquisition system

For detecting the variation of the output intensity distribution, a two-section detector is employed (S4349, Hamamatsu), with a spectral sensitivity of 0.45 A/W at the working wavelength. The intensity signals resulting from the two sections of the photo-detector are amplified through standard benchtop instrumentation (PDA200C, Thorlabs), acquired with a USB-acquisition card (6251, National Instruments) and processed in real-time. The acquired samples are time averaged

and the signal:

$$S_R = \frac{I_{up} - I_{down}}{I_{up} + I_{down}} \quad (3.1)$$

is computed and displayed in real-time with a Labview application. Signal analysis is required to convert the  $S_R$  variations, expressed as a %, into phase variations (rad).

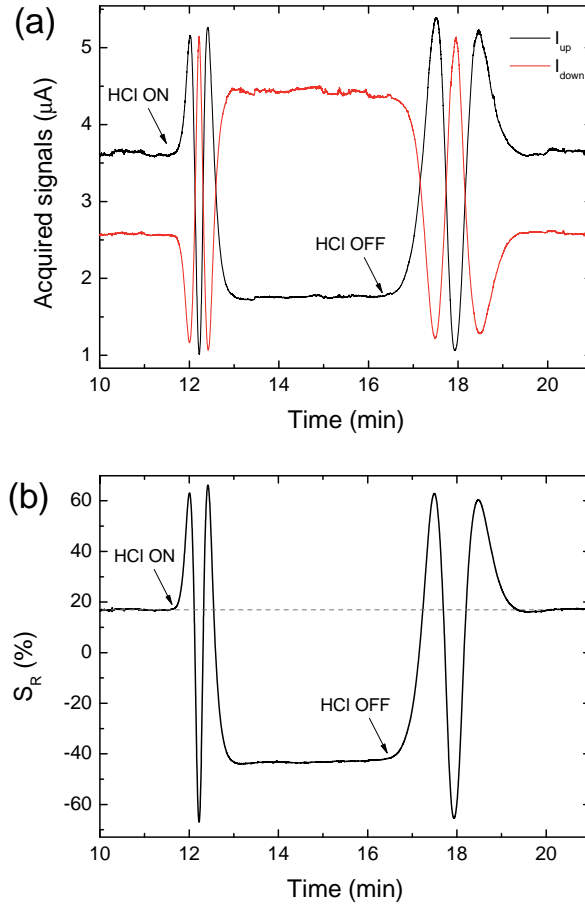


**Figure 3.12:** (a) Acquired  $I_{up}$  and  $I_{down}$  signals and (b) corresponding  $S_R$  during the detection of a refractive index change  $\Delta n = 9 \cdot 10^{-4}$ .

Figure 3.12 shows the time evolution of the  $I_{up}$  and  $I_{down}$  signals during an



index variation  $\Delta n = 9 \cdot 10^{-4}$  (panel (a)) and the corresponding  $S_R$  signal (panel (b)). This last one represents the typical interferometric response for a homogeneous variation in the refractive index of the medium in contact with the sensing area.

$S_R$  signal starts from a constant level (corresponding to water) and varies when HCl reaches the sensing area ('HCl ON' in Fig. 3.12(b)); then stabilizes and returns to the starting level when milli-Q water arrives again to the sensor area ('OFF'). The phase shift induced by the refractive index variation occurring in the sensing area is determined by counting the number of fringes described during the evaluation, according to the equivalence between a complete fringe oscillation and a phase change  $\Delta\varphi = 2\pi$ .

### 3.5 Optical characterization

The modal behavior of the waveguides is verified by collecting the interferometer output with a  $40\times$  objective and using a CCD camera for visual inspection when TE polarized light is coupled at the device input.

For the fabricated waveguides ( $w=4.5 \mu\text{m}$ ,  $h \approx 1.5 \text{ nm}$ ) single-mode behavior in the lateral direction is ensured at the operating wavelength and the output profile is given by the superposition of the fundamental and first order vertical modes,  $\text{TE}_{00}$  and  $\text{TE}_{10}$  respectively. The light distribution at the device output depends on the phase difference between the two propagating modes, which is determined by their effective refractive indices. A variation of the effective refractive indices, i.e. phase change, can be obtained by changing the refractive index of the medium in contact with the sensing area, for example by applying a water droplet on the sensor surface, or by tuning the temperature of the chip holder. Figure 3.13 shows two different situations for the output light distribution. The dependence of the output light distribution with the phase difference between the two propagating modes constitutes the working principle of the BiMW sensor.

The propagation losses in the nanometric rib  $\text{Si}_3\text{N}_4$  waveguides were evaluated during previous studies for single-mode waveguides and vary between  $0.15$  and  $0.25 \text{ dB/cm}^{-1}$  for TE polarization and between  $0.2$  and  $0.35 \text{ dB/cm}^{-1}$  for TM polarization [Prieto et al., 2003, del Río Sáez, 2007].

### 3.6 Homogeneous sensing evaluation

Using the experimental setup previously described, milli-Q water is supplied to the sensor and different solutions of HCl ( $0.05 \text{ M}$ ,  $0.1 \text{ M}$ ,  $0.2 \text{ M}$  and  $0.4 \text{ M}$ )

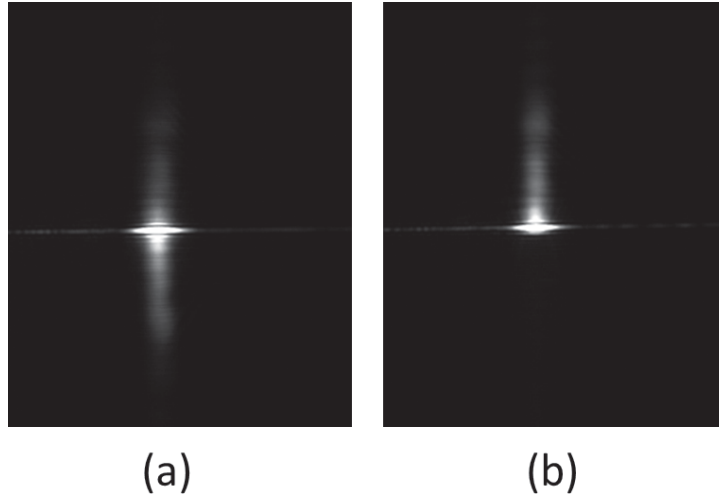


**Figure 3.13:** Light energy distribution at the output of a BiMW sensor for two different states.

**Table 3.1:** Refractive index change induced by a set of HCl solutions and corresponding phase changes evaluated on a BiMW sensor interrogated in the standard monochromatic approach.

HCl concentration (M)	$\Delta n$ (RIU)	$\Delta\varphi$ (rad)
0.05	$3.0 \cdot 10^{-4}$	$0.75 \cdot 2\pi$
0.1	$9.0 \cdot 10^{-4}$	$1.51 \cdot 2\pi$
0.2	$1.7 \cdot 10^{-3}$	$3.1 \cdot 2\pi$
0.4	$3.6 \cdot 10^{-3}$	$6.05 \cdot 2\pi$

are sequentially injected to induce a variation of the bulk refractive index. The refractive index variations  $\Delta n$ , i.e. the difference of refractive index between a certain HCl solution and milli-Q water, corresponding to this set of HCl solutions are summarized in Table 3.1, together with the phase signals ( $\Delta\varphi$ ) experimentally evaluated for one sensor chip under analysis.

The phase difference variation  $\Delta\varphi$  induced by the variation of refractive index  $\Delta n$  is evaluated taking into account that a complete oscillation of the  $S_R$  signal corresponds to a  $2\pi$  phase variation. For example in the case of HCl 0.1 M, showing a  $\Delta n = 9 \cdot 10^{-4}$  RIU with respect to water, a phase difference variation  $1.51 \cdot 2\pi$  rad was evaluated (see Fig. 3.14). The same methodology is applied for the other solutions and by plotting the phase difference variation as a function

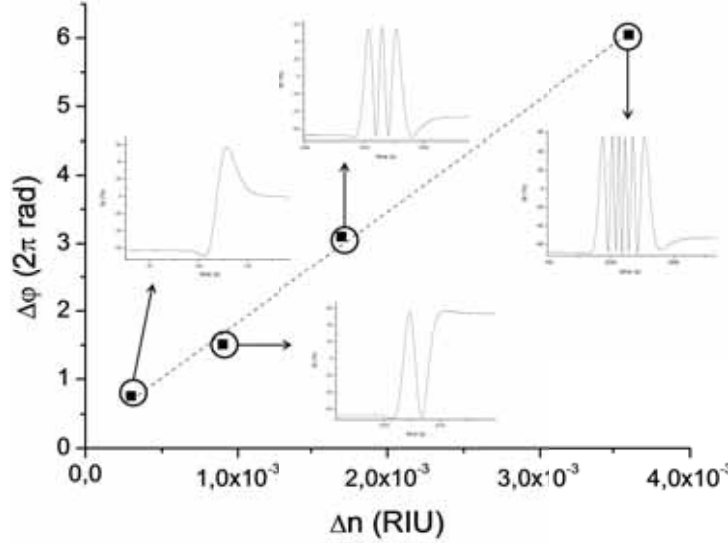


**Figure 3.14:** Calibration curve for a BiMW sensor, TE polarization,  $\lambda = 633$  nm. Insets represent the temporal signals corresponding to the different HCl concentrations.

of the refractive index variation, a calibration curve is obtained, as shown in Fig. 3.14. The insets of Fig. 3.14 show the variation of the BiMW output signal  $S_R$  induced by the change from water to HCl medium, for each HCl solution considered.

For the plot shown in Fig. 3.14 a linear dependence is observed between the refractive index change and the measured phase difference variation. The slope of the calibration curve, expressed in rad/RIU, represents the bulk sensitivity of the sensor. In this particular case, the sensitivity was estimated as  $S_{bulk} = 1630 \cdot 2\pi$  rad/RIU.

The limit of detection  $\Delta n_{min}$  is calculated from Eq.(2.49). The phase resolution  $\Delta \varphi_{min}$  is evaluated from the measured  $S_R$  resolution,  $\Delta S_{R,min}$ , which is estimated as three times the standard deviation on the baseline noise,  $\sigma_{S_R}$ , resulting in the expression:

$$\Delta n_{min} = \frac{\Delta \varphi_{min}}{S_{bulk}} = \frac{\Delta S_{R,min}}{S_{bulk}} \frac{\pi}{2V} = \frac{3 \cdot \sigma_{S_R}}{S_{bulk}} \frac{\pi}{2V} \quad (3.2)$$

For the measurements shown in Fig. 3.14, we have:  $S_{bulk} = 1630 \cdot 2\pi$  rad/RIU,  $V = 62\%$  and  $\sigma = 0.05\%$ , resulting in a limit of detection of  $\Delta n_{min} = 3.7 \cdot 10^{-7}$  RIU.

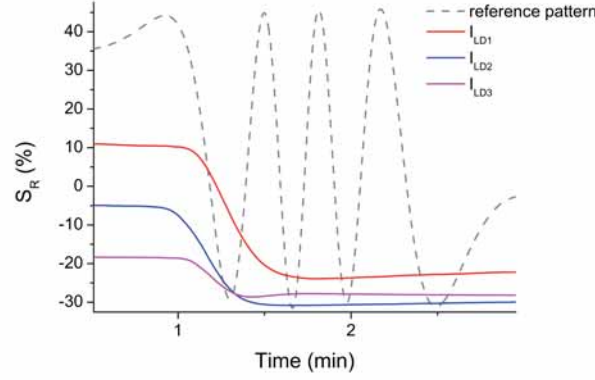


**Figure 3.15:** Demonstration of sensitivity fading for a BiMW sensor. The phase difference variation induced by a refractive index change has been evaluated in three different conditions: in proximity of the quadrature point, in proximity of a minimum of the transfer function and in an intermediate region.

### Sensitivity fading

Despite the high sensitivity and competitive limit of detection demonstrated by the BiMW device, around  $3.7 \cdot 10^{-7}$  RIU, this sensor suffers from the periodicity of the output signal, explained in Section 1.4. The effects of sensitivity fading can be directly assessed by measuring the response for a same index variation starting the detection from different regions of the transmission curve. For example in Fig. 3.15 we show three different starting conditions: one in proximity of the quadrature point, one in proximity of the transmission curve minimum and an intermediate case. The different conditions have been achieved by slightly tuning the working wavelength of a laser diode employed as laser source.

Table 3.2 summarizes the measured  $S_R$  variations and the corresponding phase changes obtained after signal conversion. Clearly the highest response  $\Delta\varphi = 0.22 \cdot 2\pi$  rad is obtained when the detection starts closer to the quadrature point (case 1) and decreases getting closer to a minimum of  $S_R$ , where a value of  $0.07 \cdot 2\pi$  rad is measured.

Even if the sensor operation in proximity of the quadrature point can be easily achieved by a wavelength variation, this is only a partial solution to the interferometric limitations detailed in Section 1.4. The variations in the detected signal consequent from the sensitivity fading are unacceptable in the biosensor practice, specially in the clinical diagnostics, and must be overcome by the introduction of

**Table 3.2:** Sensor response for different initial phase difference.

	$\Delta S_R$	$\Delta\varphi$ (rad)
1	34.3	$0.23 \cdot 2\pi$
2	25.7	$0.17 \cdot 2\pi$
3	10.8	$0.07 \cdot 2\pi$

a phase linearization system.

### 3.7 Conclusions

In this Chapter the fabrication and characterization of highly sensitive integrated interferometers based on Si/SiO<sub>2</sub>/Si<sub>3</sub>N<sub>4</sub> rib waveguides have been presented, together with the techniques employed for the fabrication verification (i.e. AFM and SEM inspections).

We detailed the procedures of end-facets polishing and sensor chip cleaning, which are required prior to the sensor characterization. The experimental setup for the evaluation of the BiMW biosensors has been described, with its optical and fluidics components. We described the data acquisition process and the procedure for the evaluation of bulk detections. The calibration to bulk refractive index changes has been performed with the standard intensity interrogation approach, showing a limit of detection of  $3.7 \cdot 10^{-7}$  RIU.

The sensitivity fading has been demonstrated by comparing the sensor response obtained with different initial phase difference values, indicating a strong dependence on the starting conditions and a lack of reproducibility which is not acceptable in the biosensor practice. A phase linearization system is required to achieve a reliable and competitive sensor.



# Chapter 4

## Phase linearization for IO interferometric biosensors

We have discussed in the previous chapters the limitations of the interferometric read-out due to the periodicity of the output intensity with the phase difference variations. To take full advantage of the high sensitivity offered by the BiMW sensor and to be able to offer a reliable and competitive biosensor device for technological transfer, it is mandatory to incorporate a simple, practical and integrable phase modulation system which converts the periodical signal in a linear and direct read-out.

Phase modulation is a well-known technique in optics and several phase linearization methods have been proposed so far. However all of them show significant drawbacks and then we propose an all-optical phase modulation, based on a wavelength variation, to introduce the required phase change. In this chapter we present the mathematical modelization of this new technique, the experimental realization and the demonstration of the working principle in the case of the well-known MZI sensors.

### 4.1 Phase linearization: overview

#### 4.1.1 Linear readout strategies

Intensity-interrogated interferometric devices strongly suffer from the limitations imposed by the periodicity of their output signal when a variation of the phase change takes place. Due to the wide range of applicability of optical interferom-

etry [Hariharan, 2003], impressive work has been done to solve the complexity of the periodic read-out and to overcome the signal ambiguities. Interferometric detection is widely applied in several metrology areas from distance measurements or surface profiling to microscopy, spectroscopy, sensors or astrophysical applications as for stellar or gravitational wave detectors [Kussrow and Bornhop, 2012, Heinzel et al., 2010].

Different phase linearization methods have been proposed for free-space, fiber optics-based and integrated optics interferometers. We can distinguish between techniques ensuring the phase quadrature, i.e. operation of the sensor in proximity of the quadrature point where the response is almost linear and the sensitivity is maximum, and approaches based on phase modulation techniques, which allow higher flexibility and generality.

- **Static phase quadrature**

The simplest solution is to engineer the sensor design, for example with an optimized sensing area length, to operate around the quadrature point for a given refractive index range (i.e. for a given application). An almost linear response can be achieved without additional fabrication processes or external equipment. However, since the interferometer operation will be restricted to a small fraction of the transmission curve, usually the dynamic range and the sensitivity are strongly compromised with this approach, since a high sensitivity will imply a small working range and vice-versa. Furthermore the tolerance to fabrication variations is very strict, since any variation would drift apart from the working point.

A more general approach involves the use of three output waveguide couplers, where at least one of the three outputs will be in proximity of the quadrature point for any refractive index working range. However in this case a more complex structure must be designed. Alternatively, the interferometer working point can be biased by applying an external phase shift, to ensure the phase quadrature. In this case the sensor can be tuned at the quadrature point for different conditions, but a modulator is required.

- **Dynamic phase quadrature (phase compensation)**

In order to solve the limitations of a static phase quadrature design, an active system can be introduced to keep the interferometer at the quadrature point, by applying a phase variation along the reference arm to oppose the phase change induced in the sensing arm. A feedback system is employed to control the phase of the reference arm, and this signal is employed for the evaluation of the sensor response. The limitations of this approach rely on



the possible confusion introduced by laser power or temperature fluctuations and a limited working range.

- **Phase modulation**

The phase difference between the two arms is constantly varied and an unambiguous phase signal can be extracted through mathematical analysis of the output. With this approach the sensitivity is kept unchanged, the dynamic range is virtually unlimited and the same sensor design can be tailored for different applications (i.e. working on a broader refractive index range).

Due to their advantages with respect to other approaches, from now on we will focus on phase modulation techniques.

Fourier analysis is a powerful technique for deconvolution of the output signal and retrieval of the phase information. For Fourier Transform to be applied, the interference fringes need to be modulated with a spatial carrier. Among the available modulation schemes, a consistent work has been done with Sinusoidal Phase Modulation (SPM) approach, for example in the case of surface profiling interferometers [Sasaki and Okazaki, 1986, Suzuki et al., 1989]. Following this work, different methods based on the analysis of the Bessel's functions  $J_n(x)$  originating from the Fourier spectrum of the modulated signal in the case of sinusoidal input modulation have been studied and implemented [Deferrari et al., 1967, Sudarshanam and Srinivasan, 1989, Sudarshanam and Claus, 1993, Heinzl et al., 2010].

However the above approaches were developed for non-integrated interferometers and require the use of an external phase modulator. Normally a piezo-electric element is employed to induce oscillations of a reference mirror placed along one of the interferometer arms.

#### 4.1.2 Optical effects for phase modulation

In the case of integrated interferometers, different approaches can be chosen to introduce the required phase modulation/compensation. The most common are:

- **Electro-optic**

The principle of operation is based on the linear electro-optic effect (Pockels effect), consisting in the dependence of the refractive index of nonlinear crystals with an applied electric field. LiNbO<sub>3</sub>, LiTaO<sub>3</sub> or GaAs have large Pockels coefficients and are the common choice as electro-optic modulators,

but their incompatibility with standard Si microelectronics fabrication imposes limitations for their application. Despite ZnO is a silicon compatible material, its poor resistance to liquids introduces special requirements for the design of the sensing area and electrode regions. The careful isolation required for the electrodes motivated the investigation of alternative approaches.

- **Thermo-optic**

The thermo-optic effect consists in the variation of the refractive index of a material due to a change of the temperature. Micro-heaters or electrodes are required to achieve a localized temperature increase in order to introduce the required phase shift. Thermo-optic effects are particularly employed for SOI platforms, since silicon possesses a very high thermo-optic coefficient compared to other common semiconductor and optical materials [Chong and Rue, 2004]. Also in this case electrodes and high currents are required, complicating the integration with the fluidic components of the final integrated sensing platform.

- **Magneto-optic**

The magneto-optic effect results from the interaction of electro-magnetic radiation with a material showing net magnetization. For integration with IO sensors strong magnetic materials (ferro or ferrimagnetic) are required to avoid the use of strong external magnetic fields or excessively long propagation distances. However the applicability for sensors operated at visible wavelengths is prevented by the strong absorption that standard ferroelectric materials show in this range [Sepúlveda, 2005].

- **Acousto-optic**

The acousto-optic effect describes the variation of the refractive index due to a mechanical strain induced by the passage of a Surface Acoustic Wave (SAW). SAWs are usually generated by thin-film piezo-electric transducers in proximity of the waveguide to be modulated [Gorecki et al., 1997, Duhring and Sigmund, 2009]. As in the case of electro-optic modulators, piezoelectric materials cannot be directly deposited at wafer level, resulting in a more complex fabrication.

- **All-optical**

Photosensitive materials, whose refractive index can be tuned by an external light source, can be used to introduce an additional phase shift in one arm of the interferometer [Dér et al., 2010].

As an alternative to the above proposed methods, a variation of the phase difference between the two propagating modes can be achieved by tuning the incident wavelength, as proposed in this Thesis. If a periodic phase change between the propagating modes is introduced, Fourier deconvolution allows to achieve a direct and absolute sensor read-out [Dante et al., 2012].

## 4.2 Mathematical model of the phase modulation

For the derivation of the mathematical model we consider a generic interferometer, for which the output intensity  $I_{out}$  is measured. The output signal is related to a variation of the phase difference between the two interfering modes,  $\Delta\varphi_S$ , by the relation:

$$I_{out} \propto \alpha \cos(\Delta\varphi_S) \quad (4.1)$$

where the coefficient  $\alpha$  depends on the particular arrangement (MZI, BiMW or other).

Introducing a phase modulation signifies inserting an additional term as argument of the cosine function in Eq.(4.1). If we consider a sinusoidal phase modulation function  $f(\mu_M) = \mu_M \sin(\omega_M t)$  and we assume that the period of the modulation is much shorter than the response time of the biosensing interactions (which are typically in the order of seconds or minutes), the sinusoidal interferometric output is transformed into:

$$I_{out} \propto \alpha \cos[\mu_M \sin(\omega t) + \Delta\varphi_S] \quad (4.2)$$

Equation (4.2) can be expanded in a Fourier series [Abramowitz and Stegun, 1964], resulting in:

$$I_{out} \propto \alpha \left\{ \cos(\Delta\varphi_S(t)) \left[ J_0(\mu_M) + 2 \sum_{n=1}^{\infty} [J_{2n}(\mu_M) \cos(2n\omega t)] \right] + \sin(\Delta\varphi_S(t)) \left[ 2 \sum_{n=0}^{\infty} [J_{2n+1}(\mu_M) \sin[(2n+1)\omega t]] \right] \right\} \quad (4.3)$$

where  $J_n(\mu_M)$  are the Bessel's functions of order  $n$ . The complete derivation of the Fourier coefficients can be found in Appendix A.

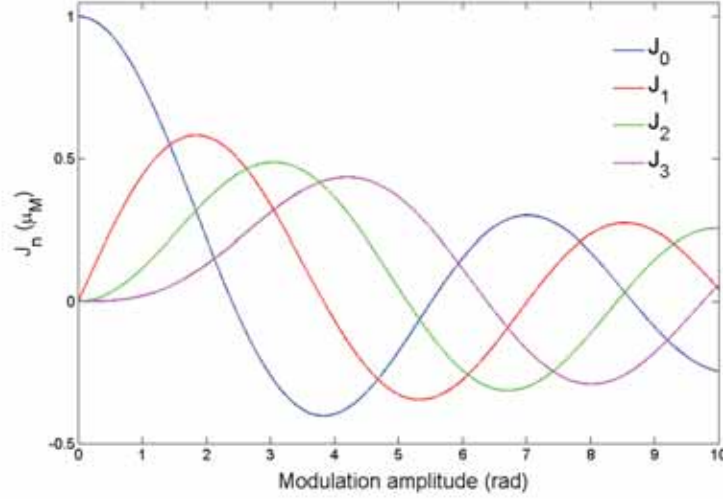


**Figure 4.1:** Bessel's functions of first kind as a function of modulation amplitude.

The DC component and the generic even/odd harmonics are given by:

$$\begin{aligned} I_{DC} &\propto \alpha \cos(\Delta\varphi_S(t)) J_0(\mu_M) \\ I_{2n} &\propto 2\alpha \cos(\Delta\varphi_S(t)) J_{2n}(\mu_M) \\ I_{2n+1} &\propto 2\alpha \sin(\Delta\varphi_S(t)) J_{2n+1}(\mu_M) \end{aligned} \quad (4.4)$$

where the even harmonics depend on the cosine of the phase shift  $\Delta\varphi_S$  while the odd harmonics depend on the sine of the same quantity.

The dependence of the Fourier coefficients with the phase modulation depth is given by the well-known Bessel's functions of the first kind, whose trend is shown in Fig. 4.1 for the first four functions  $J_0 - J_3$ .

If we consider the ratio between two consecutive harmonics:

$$\frac{J_{2n+1}(\mu_M)}{J_{2n}(\mu_M)} = \frac{\sin(\Delta\varphi_S(t)) J_{2n+1}(\mu_M)}{\cos(\Delta\varphi_S(t)) J_{2n}(\mu_M)} \quad (4.5)$$

it is possible to extract a phase signal  $\Delta\varphi$  from the inverse tangent of the harmonics ratio:

$$\Delta\varphi = \arctan\left(\frac{I_{2n+1}}{I_{2n}}\right) = \arctan\left(\frac{\sin(\Delta\varphi_S(t)) J_{2n+1}(\mu_M)}{\cos(\Delta\varphi_S(t)) J_{2n}(\mu_M)}\right) \quad (4.6)$$

which corresponds to the phase change  $\Delta\varphi_S$  if the condition:

$$J_{2n}(\mu_M^*) = J_{2n+1}(\mu_M^*) \quad (4.7)$$

is verified.

According to the theory of Bessel functions, it is possible to find a value of  $\mu_M$  satisfying Eq.(4.7) for each couple of consecutive harmonics, as shown in Fig. 4.1. This value is  $0.84\pi$  in the case  $J_1(\mu_M) = J_2(\mu_M)$ ,  $1.2\pi$  for  $J_2(\mu_M) = J_3(\mu_M)$  and  $1.55\pi$  for  $J_3(\mu_M) = J_4(\mu_M)$ . In our case the harmonics  $I_2$  and  $I_3$  are chosen, since the condition on the phase modulation amplitude can be experimentally satisfied with the proposed all-optical approach.

We can now summarize the main steps of the phase retrieval process. For this, we can consider a variation of refractive index as shown in Fig. 4.2(a), where after a constant part, the refractive index increases, then stabilizes to a new constant level, then decreases and finally returns to the starting value, as in the common bulk detection experiments described in the previous chapter.

As a consequence of Eq.(4.4), a variation in the sensing area refractive index induces variations of both harmonics,  $I_{2\omega}$  and  $I_{3\omega}$ , which show a cosine- and sine-dependence, respectively, with the applied stimulus (see Fig. 4.2(b)). If the proper modulation amplitude  $\mu_M$  is chosen, the two harmonics will show the same fringe amplitude, corresponding to the correct working point (see Eq.(4.7)).

Once verified the correct working point, Eq.(4.6) is used to compute the phase signal from the ratio of the two considered harmonics. The resulting signal will vary in the range  $\pm\pi$  (i.e. phase retrieval modulo- $2\pi$ ), as shown in Fig. 4.2(c). An unwrapping step is required to eliminate the  $2\pi$  abrupt jumps and recover a continuous and monotonic signal, as presented in Fig. 4.2(d).

In this modulation scheme the phase change is not deduced anymore from the variations of the intensity interference pattern but is directly extracted by deconvolution of the periodically modulated output, as shown in Fig. 4.2. An absolute value is obtained, meaning that also small phase changes can be quantified without the need of a reference pattern as required in the standard evaluation (monochromatic approach). Therefore, the proposed phase modulation approach gives a direct and unambiguous read-out, overcoming the four limitations derived from the periodicity of the output signal described in Section 1.4.

This general modulation/deconvolution scheme is valid for any interferometric arrangement and can be practically implemented with several modulation principles, as described in Section 4.1.2.

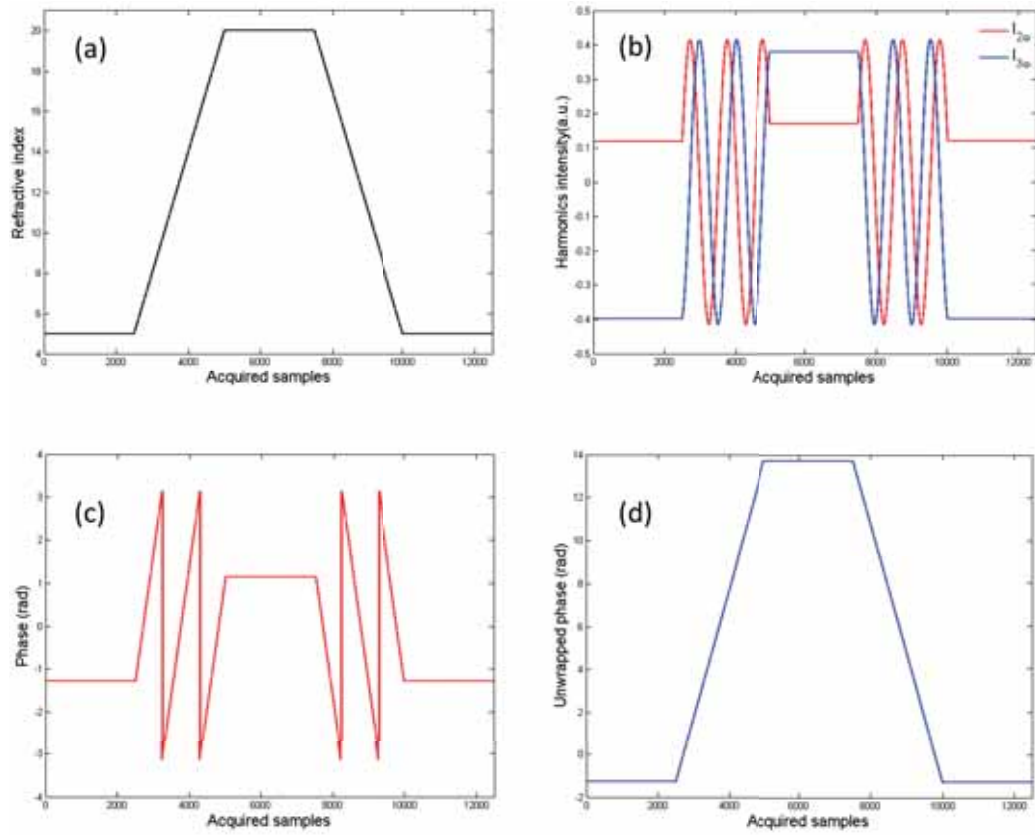


**Figure 4.2:** Phase retrieval modelization. (a) an arbitrary refractive index variation induces (b) a variation of both harmonics  $I_{2\omega}$  and  $I_{3\omega}$ . (c) the phase signal is evaluated modulo- $2\pi$  from the inverse tangent of the harmonics ratio and (d) is unwrapped in real-time to get a monotonic continuous signal.

### 4.3 All-optical phase modulation

The principle of the all-optical wavelength modulation relies on the possibility of introducing a variation of the phase difference between the two modes propagating in the interferometer through a variation of the incident wavelength. In the case of MZI, it is the asymmetry imposed by the sensing area which determines the different properties of  $N_S$  and  $N_R$ , both fundamental modes in their respective arms, while for the BiMW it is the modal dispersion which governs  $N_{00}$  and  $N_{10}$ , fundamental and first order modes respectively, which propagate along the same channel. The condition on the required modulation amplitude  $\mu_M = 1.2\pi$  developed in section 4.2 corresponds in the all-optical approach to a wavelength variation  $\Delta\lambda_M$ .

The use of an all-optical approach, based on the modulation of the laser emission wavelength, facilitates the future integration onto a compact LOC platform, since it does not require any modification of the sensor design, as to include electrodes or modulators, nor external bulky equipment. Furthermore, in order to achieve a low-cost platform, the wavelength variation is introduced by taking advantage of the power-wavelength dependence of the emission of standard commercial Laser Diodes (LDs). For both interferometric sensors, a wavelength variation of **few nms** is required to induce such phase variation and it can be easily obtained by tuning the injection current of commercial Fabry-Perot laser diodes.

The comparison with the standard monochromatic approach is schematically represented in Fig. 4.3. As it will be demonstrated, the proposed phase modulation method is valid for any integrated interferometer.

#### 4.3.1 Laser diodes as modulation source

Fabry-Perot LD are comparatively cheap and small coherent light sources. The emission characteristics, i.e. frequency and maximum gain (amplitude), depend on the injection current and temperature of the cavity. Changes in the laser current produce amplitude modulation by shifting the operating point of the laser diode, and frequency modulation by altering the refractive index of the active region [Goldberg et al., 1981].

While for general applications these dependencies are a drawback with respect to more stable gas lasers, this tunability can also be exploited for other purposes, where a variation is intentionally required [Dandridge and Tveten, 1982, Wiki and Kunz, 2000].

Figure 4.4(a) shows the typical emission of a LD as a function of the injection

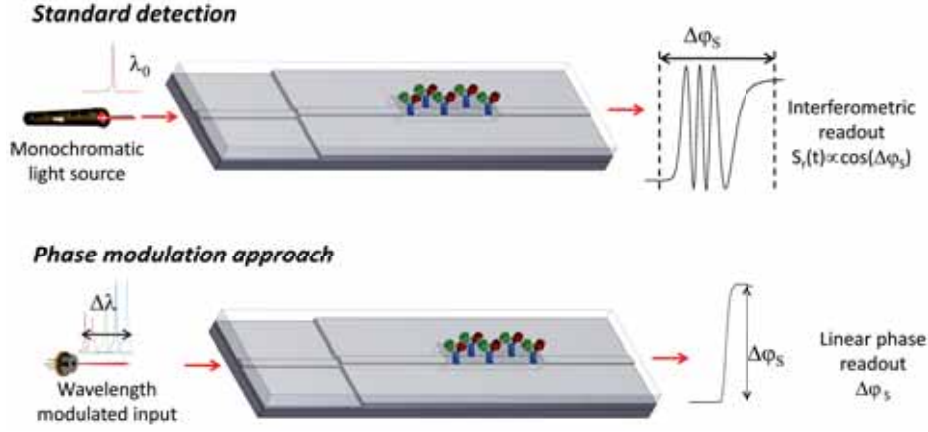


**Figure 4.3:** Schematic comparison of standard monochromatic approach with sinusoidal output and wavelength modulated sensor with linear phase read-out developed in this Thesis.

current. The boundaries for the working range are given by the threshold current  $I_{th}$ , defined as the minimum current required to achieve stimulated emission, and  $I_{max}$  which is the maximum value supported by the diode. By applying a time-varying injection current the emission wavelength can be tuned, as shown in Fig. 4.4(b), in the case of sinusoidal injection current.

#### 4.3.2 Laser diode characterization

As explained above, the phase modulation will be introduced through a periodic variation of the incident wavelength. This wavelength variation is controlled by tuning the LD driving current. In the ideal case, a stable and linear dependence is desired between the driving current and the emission wavelength, since deviations from this situation can complicate the evaluation of the Fourier analysis and introduce additional noise during the measurement.

The first step is therefore the assessment of the emission wavelength as a function of the driving current for a particular laser diode.

During this work two laser diodes have been successfully employed to demonstrate the applicability of the phase modulation for integrated interferometers. The first diode is a AlGaInP semiconductor laser, namely the ML101J27 (Mitsubishi,  $\lambda_0=660$  nm,  $P=120$  mW), which is mounted on a compact temperature-controlled laser diode mount (LDM21, Thorlabs), that allows stable operation at a temperature of 25°C. Two different diodes of this model were employed.



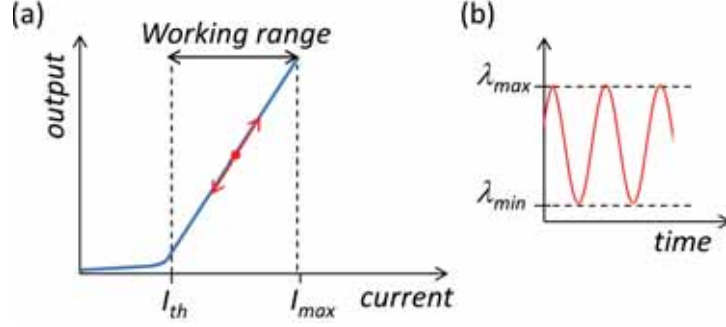


**Figure 4.4:** (a) Laser diode typical emission output power vs current and (b) temporal evolution of the emission wavelength achievable by tuning the injection current with a sinusoidal profile.

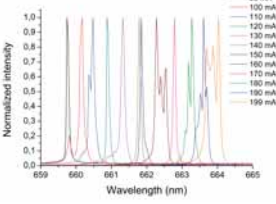
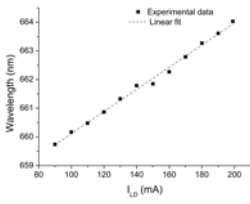
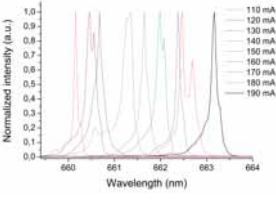
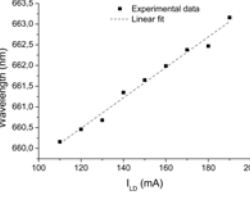
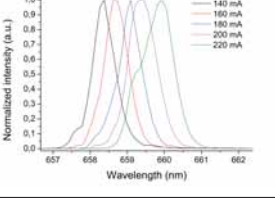
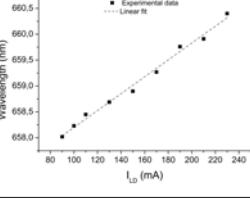
In a second stage a commercial fiber pigtailed source was employed, namely the LP660-SF60 (Thorlabs,  $\lambda_0=660$  nm,  $P=60$  mW), which consists of a diode ML101F27 pigtailed with 1 m single mode fiber and a FC-PC connector. In this case a special mount, optimized for pigtailed sources has been employed (LM9LP, Thorlabs), allowing a better thermal management over the range 10-70°C.

Table 4.1 shows a comparison between the spectra acquired in static conditions for two different devices of the same model ML101J27 and the fiber pigtailed LP660-SF60. During this characterization the laser cavity is kept at a constant temperature of 25°C and the emission spectra are recorded for different values of injection current, after its stabilization. The central wavelength of these emission peaks increases for increasing values of the injection current. For the characterization of the ML101J27 items, a commercial spectrograph (Shamrock SR-303i, Andor) connected to a cooled CCD detector (Newton, Andor) was employed. The spectra reported for the LP660-SF60 were provided by Thorlabs.

Despite the lasers are classified as single-mode, according to the spectra reported in Table 4.1, we can notice some anomalies for specific values of the driving current. These effects are attributed to mode hopping, which can take place in semiconductor laser structures when two longitudinal modes compete for emission.

Once the spectra are acquired, the central wavelength can be plotted as a function of the injection current, resulting in a characteristic slope  $\partial\lambda/\partial I_{LD}$ , which depends on the LD and its working temperature. The two specimens of the ML101J27 show similar performances for the global wavelength-current dependence, with a slope  $\partial\lambda/\partial I_{LD} \approx 0.038$  nm/mA, despite the mode hopping can occur for different values of injection currents. The pigtailed LP660-SF60 shows

**Table 4.1:** Comparison of the emission spectra for different laser diodes and corresponding wavelength-current curves.

Laser diode	Normalized spectra	Emission wavelength vs current	$d\lambda/dI_{LD}$ (nm/mA)
ML101J27, 1 <sup>st</sup>			0.039
ML101J27, 2 <sup>nd</sup>			0.037
LP660-SF60			0.016

a wavelength-current coefficient  $\partial\lambda/\partial I_{LD} \approx 0.016$  nm/mA, which is around the half of the value of the ML101J27, resulting in a lower modulation depth for the same current operation range.

Considering the whole emission range ( $\Delta I_{LD} \approx 110$  mA), a wide wavelength tunability, specifically  $\Delta\lambda > 3$  nm for the ML101J27 and  $\Delta\lambda \approx 2$  nm for the LP660-SF60 is observed as a function of the driving current for a fixed temperature of 25°C.

Since in the experimental set-up the wavelength emission will be periodically tuned, an analysis of the LD emission in dynamic conditions is required. In this case the LD current is driven by a signal generator and data are acquired as an average (accumulate mode with 1000 measurements, acquisition time of 0.0025 s), due to the impossibility of synchronization between signal generation and acquisition. The emission spectra have been acquired with a laser injection

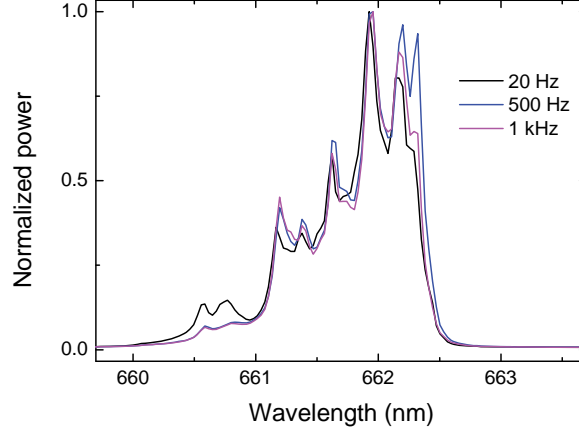


**Figure 4.5:** Normalized cumulative power for the ML101J27 laser diode, for modulation frequencies of 20 Hz, 500 Hz and 1 kHz.

current  $I_{LD} = (150 \pm 46)$  mA, for three frequencies of 20 Hz, 500 Hz and 1 kHz. As demonstrated in Fig. 4.5 for the case of ML101J27, when operated in dynamic conditions, the wavelength excursion range is drastically reduced with respect to the static approach.

As we can observe in Fig. 4.5 the averaged power shows abrupt variations due to mode transitions. The deviations from a linear behavior in the power-wavelength curve will translate into amplitude noise, which can be compensated by the use of a reference signal. A variation in the modulation frequency does not lead to substantial variation of the emission profile.

#### 4.4 Implementation of the all-optical phase modulation

In order to verify the applicability of the all-optical modulation approach, the method has been tested for the well known MZI biosensor, a device previously developed in our Group [del Río Sáez, 2007, Sepúlveda et al., 2006].

#### 4.4.1 Numerical evaluation of the $\lambda$ M-MZI

In the context of the proposed all-optical modulation scheme, the theoretical phase modulation depth  $\mu_M$  must be related to a particular wavelength shift  $\Delta\lambda_M$  which depends on the specific interferometer geometry, the constitutive materials and the working wavelength through the modes dispersion relations [Dante et al., 2012].

According to Eq.(1.4) and to the fact that the effective refractive index depends on the propagating light wavelength, a phase change between the modes propagating in an asymmetric interferometer can be induced by a change in the laser wavelength. The introduction of a small change (few nm) in the wavelength of the guided light will produce a variation of the phase difference given by:

$$\delta(\Delta\varphi_S) = \frac{2\pi L}{\lambda} \left[ -\frac{1}{\lambda}(N_S - N_R) + \frac{\partial(N_S - N_R)}{\partial\lambda} \right] \delta\lambda \quad (4.8)$$

Taking into account the homo-modal nature of the sensor and a small wavelength variation ( $\delta\lambda \ll \lambda_0$ ), in a first approximation the second term on the right side of Eq.(4.8) can be neglected. Under this assumption, the wavelength variation,  $\delta\lambda$ , which must be introduced to achieve a phase difference variation  $\delta(\Delta\varphi_S)$  is given by the expression:

$$\delta\lambda = \frac{-\lambda^2}{2\pi L(N_S - N_R)} \delta(\Delta\varphi_S) \quad (4.9)$$

In our approach a modulation depth  $\delta(\Delta\varphi_S) = \mu_M = 1.2\pi$  must be introduced to achieve the correct working point. The phase modulation depth must be converted to a wavelength modulation depth  $\Delta\lambda_M$  which takes into account the modal dispersion of the interferometer. The wavelength modulation depth can be numerically evaluated from Eq.(4.9). In Fig. 4.6, we plotted the required modulation depth  $\Delta\lambda_M$  as a function of the core thickness of the MZI device. For this purpose, we considered a waveguide structure similar to the one described in Section 2.7. In this structure, a  $\text{Si}_3\text{N}_4$  core is embedded between two  $\text{SiO}_2$  cladding layers (2  $\mu\text{m}$  thickness each), except in the sensing area, where the top cladding is the environment (water). Results are shown for both TE and TM polarizations, for a central wavelength  $\lambda_0 = 660$  nm, assuming  $L = 15$  mm, a rib of  $1 \text{ nm} \times 4 \mu\text{m}$  as in our experimental devices and water as the external medium in the sensing area ( $n = 1.33$ ).

According to the results shown in Fig. 4.6, for a core thickness of 200 nm the  $\Delta\lambda_M$  required to induce a  $1.2\pi$  phase difference variation is **0.7 nm** in the case

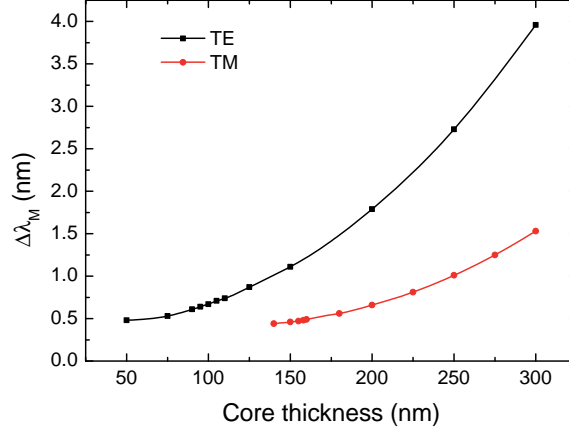


**Figure 4.6:** Wavelength modulation required to introduce a phase change  $\delta(\Delta\varphi_S) = 1.2\pi$ , for a central wavelength  $\lambda_0 = 660$  nm, TE and TM polarization, with water medium in the sensing area ( $n=1.33$ ).

of TM polarization, enabling the use of the previously characterized laser diodes as light sources.

#### 4.4.2 Quasi-static approach

As a verification of the all-optical working principle, we studied the behavior of the MZI output signal,  $I_T$ , for different incident wavelengths, resulting in a transmission curve  $I_T = f(\lambda)$ . The interferometers are interrogated in a quasi-static approach: the laser wavelength is sequentially increased by changing the injection current and the interferometer output is recorded after stabilization of the laser emission. For this study, the refractive index in the sensing area is kept constant (water medium,  $n=1.33$ ).

Sensor chips with different core thickness were characterized, as shown in Fig. 4.7(b), (c) and (d), for the cases of 150 nm, 200 nm and 250 nm, respectively. All the curves show an oscillatory behavior superposed to a linear increase of the average value, this last one due to the power-current dependence of the laser diode as demonstrated in panel (a), where the laser output intensity is plotted as a function of the injection current. The observed periodicity corresponds to the injection current variation (i.e. wavelength variation) that must be applied to obtain a  $2\pi$  variation of the phase difference between the two propagating modes.

**Table 4.2:** Comparison of theoretical and experimental wavelength periodicity for the MZI sensors. TM polarization,  $\lambda_0=660$  nm.

Core thickness (nm)	$\Delta I_{LD}$ (mA)	$\Delta \lambda_{exp}$ (nm)	$\Delta \lambda_{theo}$ (nm)
150	25.7	1.0	0.8
200	30.7	1.2	1.1
250	41	1.6	1.7

For each core thickness a typical periodicity can be evaluated. In the case of 150 nm core thickness a current variation  $\Delta I_{LD} = 25.7$  mA was evaluated.

Taking into account the laser diode characteristic wavelength-current relation, obtained with the static spectra analysis reported in Table 4.1, the periodicity of the intensity variations can be converted into a wavelength variation. For this experiment the ML101J27 laser source was employed, which presented a  $\partial \lambda / \partial I_{LD} = 0.039$  nm/mA. Therefore, for the 150 nm thickness sensor chip we estimated the wavelength periodicity as  $\Delta \lambda = 1.0$  nm.

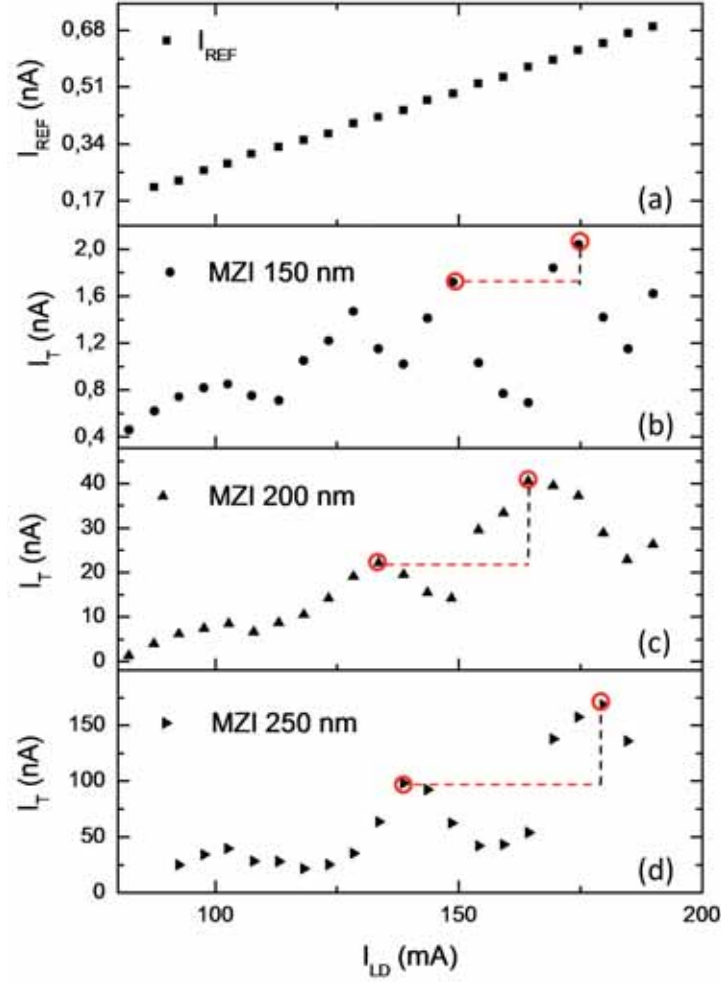
This experimental wavelength shift can be compared with the theoretical expectation, computed from Eq.(4.9), considering a phase variation  $\delta(\Delta \varphi_S) = 2\pi$ .

Table 4.2 summarizes the experimental periodicity in terms of injection current and wavelength shift, which are compared with the theoretical expectations, showing an excellent agreement.

#### 4.4.3 Experimental demonstration

In order to implement the proposed phase modulation approach, the emission wavelength of the laser diode source must be dynamically tuned in order to introduce the required variation of the phase difference between the two propagating modes. This is achieved by applying a sinusoidal injection current of the type  $I_{LD} = I_0 + \delta I_{LD} \sin(\omega t)$ , where  $I_0$  is the DC laser diode offset,  $\delta I_{LD}$  is the variation applied and  $\omega/(2\pi)$  is the modulation frequency. The condition  $I_{th} < I_{LD} < I_{max}$  must be verified in all the measurements.

The main building blocks of the experimental set-up used for the  $\lambda$ M-MZI sensor evaluation are represented in Fig. 4.8(a), while panel (b) shows a photograph of the experimental set-up. The main difference with a standard set-up for intensity interrogated MZI sensors relies on the presence of a reference signal, required to eliminate the amplitude modulation effects. The reference signal is also used to verify the LD emission: in the ideal case a sinusoidal signal is expected in response to the current variation, which can be distorted in presence of mode



**Figure 4.7:** Verification of the wavelength modulation principle by quasi-static approach. (a) power variation of the laser emission (reference signal), MZI output signal in the case of (b) 150 nm core, (c) 200 nm core and (d) 250 nm core. TM polarization,  $\lambda_0=660$  nm.

hopping or other noise sources.

The sensor chip is placed on a custom-made methacrylate holder, fixed to a 1-axis translation stage to allow light in-coupling in the different sensors of the same chip (D). The output beam of the selected laser diode (ML101J27, Thorlabs; element A in Fig. 4.8(b)) is focused at the input of a MZI device by a 40 $\times$  objective placed on a 3-axis precision micro-position stage (Nanomax-TS, Thorlabs; C). Back-reflections to the optical cavity are prevented by the use of an optical isolator (IO-3D-660-VLP, Thorlabs). Both temperature and light reflections are critical parameters to ensure that no mode hopping takes place in the laser cavity which would increase the spectral noise of the system. For the detection of the interferometric output a silicon detector (DET36A, Thorlabs) is employed. The waveguide output is collected by a 40 $\times$  objective and passed through a vertical slit to spatially select the sensor output from environmental noise contributions. Objective, slit and detector are fixed on the same translation stage (E). A second photodetector (G) is employed to collect the reference signal, that is extracted from the main beam with a beam splitter (CM1-BS013, Thorlabs, F). A wavelength excursion of 1 nm corresponds to a percentage variation lower than 0.2 % for the detector responsivity, which can therefore be neglected. Both photodetectors outputs are amplified with standard benchtop photodiode amplifiers with tunable gain (PDA200C, Thorlabs; H) before being processed. Neutral density absorptive filters (NExxA-A, Thorlabs) are introduced along the reference beam to match the amplification range of the two photodiode amplifiers. The sinusoidally varying injection current is fed to the laser controller (current and temperature combined controller ITC510, Thorlabs; B) through an acquisition card (NI USB-6361, National Instruments; I). The same laser controller helps to maintain a constant temperature of the laser cavity.

As described in Section 3.4, a methacrylate fluidic cell is anchored by a screw system over the chip holder to perform dynamic flow measurements. The experimental system is completed by a syringe pump (NE-1000, New era; L) and a 2-position injection valve (V451, IDEX; M) to deliver a controlled volume of the sample at a constant velocity.

### Software application

The main functions of the evaluation software consist in: i) laser control, ii) data acquisition, iii) data processing and iv) data storage in file format for successive analysis. The application was developed in Labview environment<sup>1</sup> and is based on the architecture of *event-driven* program, meaning that the execution of specific

---

<sup>1</sup> <http://www.ni.com/labview/esa/>



#### 4.4. Implementation of the all-optical phase modulation

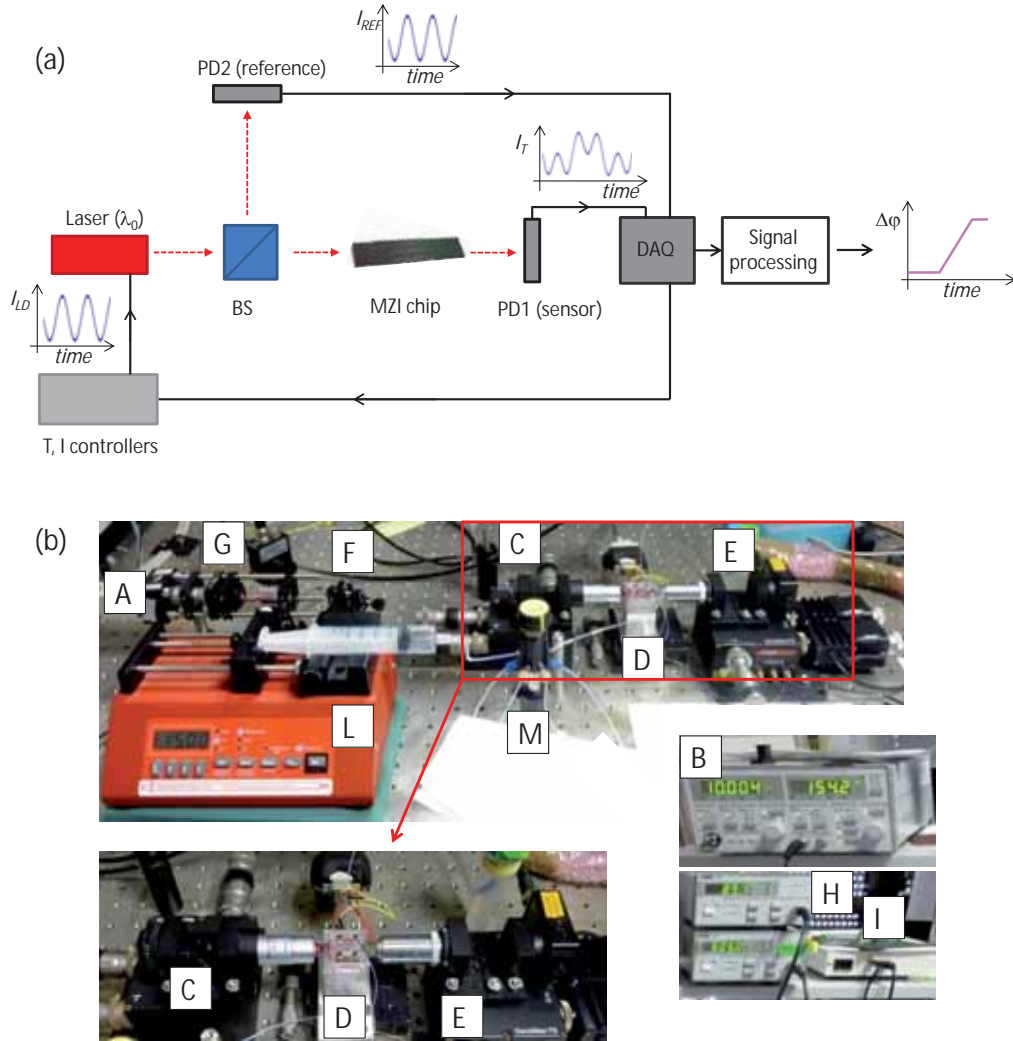


**Figure 4.8:** (a) scheme and (b) photograph of the experimental set-up required for the  $\lambda$ M-MZI biosensor.

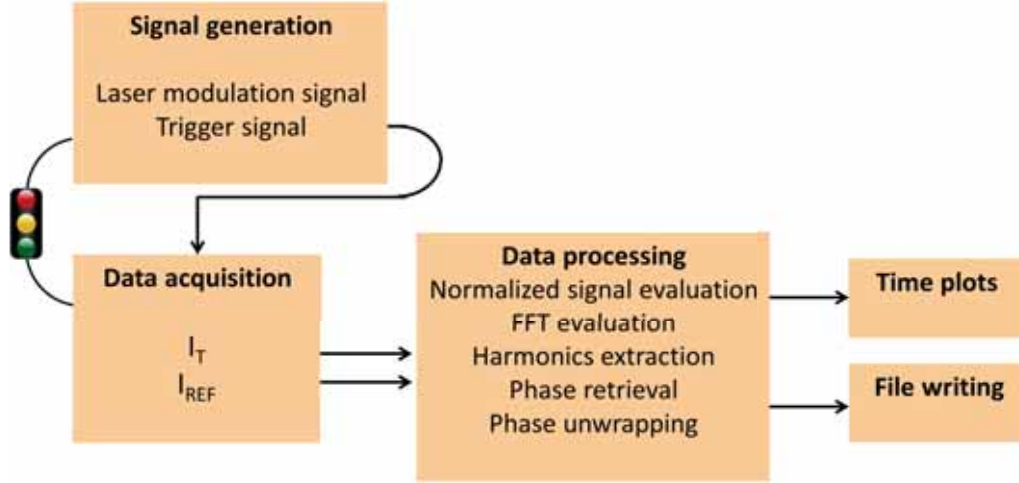


**Figure 4.9:** Scheme of the evaluation software showing the main functionalities and inter-dependencies.

software functions is triggered by a user event instead of being constantly executed, in order to minimize CPU consumptions and to simplify the block diagram. With this approach parallel loops for data generation and acquisition can be easily managed. The data are acquired and processed following the *customer/producer* approach, usually employed when two processes produce/consume data at different rates. In order to speed up the acquisition rate, two separate loops can be employed for data acquisition and data processing, which are independently executed. The acquisition process saves the data in a queue of type FIFO (first in first out) from which are extracted for the processing, performed by another dedicated loop. In this way the acquisition rate is not limited by the processing rate. The access to the acquisition card, required for both generation and acquisition processes, is regulated by a semaphore structure to avoid multiple accesses.

In addition to the laser modulation signal, a trigger signal must be generated to ensure a synchronized data acquisition from the output detectors. Synchronization is fundamental in order to deconvolute the output signal by Fourier transform and to extract the harmonics, from which the phase signal is evaluated. Figure 4.9 shows the main functionalities of this application, together with their inter-dependencies.

The parameters for modulating the input laser beam are DC working point ( $I_0$ ), modulation amplitude ( $\delta I_{LD}$ ) and modulation frequency ( $\omega/(2\pi)$ ), which can be controlled from the user-interface of the Labview application.

### Data processing

Data processing is done according to the modelization presented in Section 4.2 and is graphically schematized in Fig. 4.10. The MZI output  $I_T$  and the reference signal  $I_{REF}$  are synchronously acquired and the normalized signal  $I_N = \frac{I_T}{\alpha I_{REF}}$  is computed from their ratio. A numerical coefficient  $\alpha$  is introduced to compensate for the transmission variability between different sensor chips.

A Fast Fourier Transform (FFT), whose amplitude is shown in Fig. 4.10(b), is then evaluated on the quotient  $I_N(t)$ , by considering a number of signal periods  $N$  satisfying the condition  $N = 2^n$ . The second and third harmonics required for the phase retrieval are extracted from the real and imaginary parts of the spectrum,  $Re\{I_2\}$  and  $Im\{I_3\}$ , respectively.

For the optical characterization a modulation frequency of 214 Hz is employed since it allows to resolve the changes of interest (time scale of minutes) and it is not affected by hardware limitations.

The data processing is illustrated in the following with the example of the detection of an index change  $\Delta n = 5 \cdot 10^{-4}$  RIU, obtained by flowing a solution of HCl 0.05 M in milli-Q water as running buffer on the sensing area.

Panel (c) shows the time evolution of the second and the third harmonics, for the detection of this index change. To set the working point the condition on Bessel's functions stated by Eq.(4.7) must be fulfilled. In practice, to compensate the non-ideal laser diode behavior and the minor variations of the sensor due to fabrication, modulation parameters need to be slightly varied around the theoretical value ( $1.2\pi$ ) till the amplitudes of the two considered harmonics are equal.

As stated by Eq.(4.6), the phase information can be directly extracted from the inverse tangent evaluated on the ratio of two consecutive harmonics, resulting in a signal oscillating in the range  $\pm\pi$  (see panel (d)). Due to the linearity of the inverse tangent and to the abrupt jumps described in correspondence of  $\pm\pi$  values, it can be easily unwrapped in real-time to get a smoother and continuous cumulative response (panel (e)), unaffected by ambiguities.

#### 4.4.4 Bulk characterization

For the assessment of the bulk sensitivity, a set of hydrochloric acid solutions with known refractive index are supplied to the sensor while milli-Q water is employed as running buffer. In this case the phase variation induced by any HCl solution will be directly measured as a variation of the  $\lambda$ M-MZI output signal.

For this experiment a sensor chip with 200 nm core thickness was used and

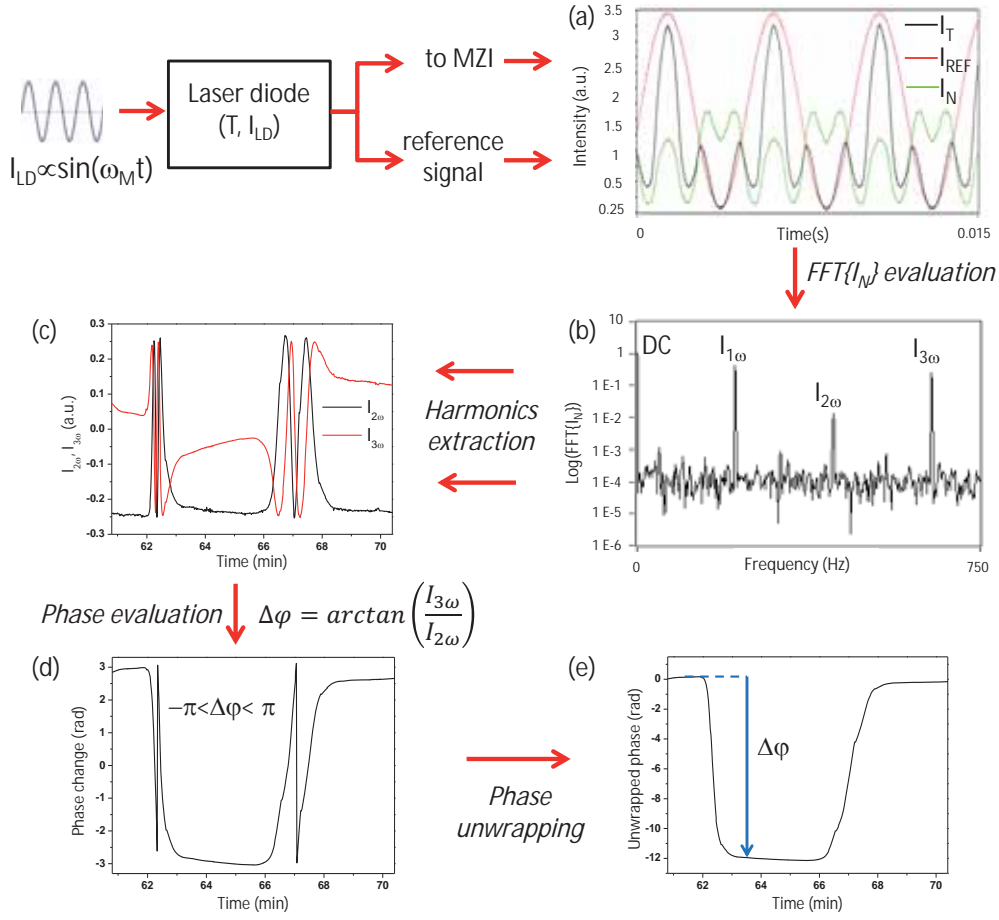


**Figure 4.10:** Scheme of the data acquisition process for the  $\lambda$ M-MZI sensors. (a) acquired signals  $I_T, I_{REF}$  and their ratio  $I_N$ , (b) amplitude of  $\text{FFT}\{I_N\}$ , (c) temporal evolution of  $I_{2\omega}, I_{3\omega}$  harmonics for the detection of a refractive index change  $\Delta n = 5 \cdot 10^{-4}$ , (d) retrieved phase signal modulo- $2\pi$  and (e) unwrapped phase signal, showing continuous and monotonic variation.

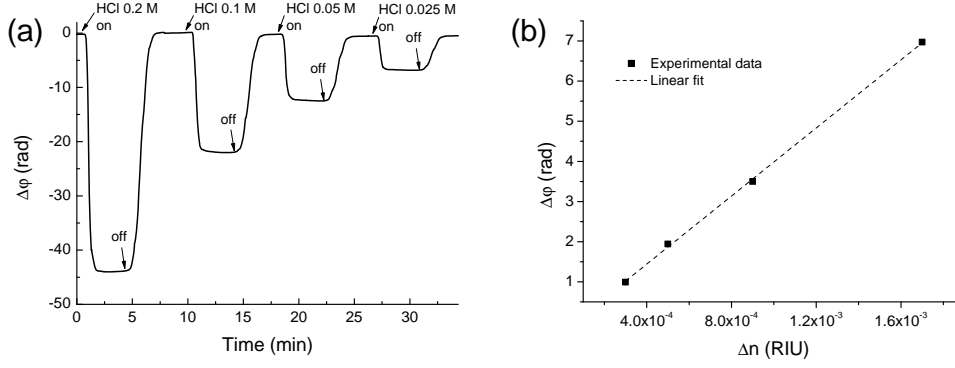


**Figure 4.11:** (a) Real-time evolution of the phase change induced by different HCl injections on a wavelength modulated MZI and (b) corresponding calibration curve  $\Delta\phi(\Delta n)$ .

the modulation set-point was achieved for a laser current  $I_{LD} = (130 \pm 36)$  mA, for TM polarization.

As we can observe in Fig. 4.11(a), the  $\lambda$ M-MZI output signal starts from a constant level corresponding to milli-Q water. When the first HCl solution enters in the sensing area (see "HCl 0.2 M on"), the output signal monotonically decreases until it stabilizes at a new constant level which depends on the specific HCl solution ( $\Delta n$ ). Then water arrives again in the sensing area (see "off" arrow) and the output signal linearly increases till recovering the stable level corresponding to milli-Q water. The signal variation is directly computed as the difference between the constant value corresponding to water and the value corresponding to a given HCl solution. For example, for the injection of a HCl solution 0.2 M, corresponding to a refractive index change  $\Delta n = 1.7 \cdot 10^{-3}$ , a signal variation of 43.7 rad was measured. Then different HCl solutions, specifically 0.1 M, 0.05 M and 0.025 M, are supplied to the sensor and the corresponding signal variations are measured (see Table 4.3).

The phase changes computed for the different solutions can be plotted as a function of the refractive index variation and show a linear dependence, as depicted in Fig. 4.11(b). This plot represents the bulk calibration curve for the  $\lambda$ M-MZI sensor under evaluation, and its slope gives the bulk sensitivity of the device,  $S_{bulk}$ . With a linear fit of the experimental data we evaluated  $S_{bulk} = 4240 \cdot 2\pi$  rad/RIU, with  $R^2 = 0.999$ . Since we achieved a direct phase read-out, the detection limit is computed by considering that the lowest detectable signal variation  $\Delta S_{r,min}$  already corresponds to  $\Delta\phi_{S,min}$ . This last quantity can

**Table 4.3:** Refractive index changes and corresponding phase signals employed for the calibration of a  $\lambda$ M-MZI.

HCl concentration (M)	$\Delta n$	$\Delta\varphi$ (rad)
0.025	$3 \cdot 10^{-4}$	6.19
0.05	$5 \cdot 10^{-4}$	12.1
0.1	$9 \cdot 10^{-4}$	21.9
0.2	$1.7 \cdot 10^{-3}$	43.7

be quantified as three times the standard deviation ( $\sigma$ ) of the system. Since  $\Delta n_{min} = \Delta\varphi_{S,min}/S_{bulk}$  and  $\sigma = 1.7$  mrad, we obtain a detection limit of **1.9**  $\cdot 10^{-7}$  RIU.

This detection limit is comparable with the results achieved with the He-Ne laser operated in standard conditions [Zinoviev et al., 2008]. We demonstrated that the use of a smaller and cheaper laser diode than the He-Ne laser can give an absolute and unambiguous signal.

## 4.5 Conclusions

In this Chapter a simple and innovative phase modulation system for integrated interferometers has been presented. The method is based on Fourier deconvolution of the output signal, after introducing a sinusoidal wavelength modulation. The phase is evaluated from the inverse tangent of the ratio between the second and third signal harmonics, resulting in an absolute, continuous, monotonic and unambiguous signal.

The phase modulation is introduced through an all-optical approach, by tuning the incident wavelength, which produces a variation of the difference between the effective refractive indices of the two propagating modes, resulting in a phase variation at the interferometer output.

Despite the poor quality of the laser diodes emission, it is possible to achieve a controlled wavelength variation which can be used to implement a periodic phase modulation in the interferometric sensor. The use of small and cost-effective laser sources instead of bulky and expensive tunable lasers is an important step towards the integration of interferometric sensors onto a LOC platform.

The method has been developed for the case of MZI sensors, but can be extended to other interferometric configurations by evaluating the corresponding phase-wavelength equivalence, depending on the modal behavior of the device.

# Chapter 5

## $\lambda$ M-BiMW biosensor

In this chapter the wavelength modulation technique developed and demonstrated for the case of integrated MZI sensor is extended for all modal interferometers, rendering in a general method to achieve a direct and linear read-out, overcoming the limitations of traditional interrogation schemes.

As an example of hetero-modal interferometers, the BiMW interferometric sensor is numerically and experimentally characterized. We demonstrate that the critical effects shown by hetero-modal interferometers, i.e. divergence of both the spectral sensitivity and the required modulation depth, can be overcome by a proper choice of operating wavelength and polarization.

### 5.1 General formulation of the wavelength modulation technique

For all modal interferometers, where the propagating modes are governed by different dispersion relations, a variation of their phase difference can be introduced by a variation of the incident wavelength. This wavelength variation will determine a different phase shift for each mode, resulting in a relative phase variation, which can be periodically tuned as required in the proposed modulation scheme. As presented in Section 4.2, if considering the second and third harmonics in Fourier domain, a modulation depth of  $1.2\pi$  must be introduced in order to satisfy the equality of Bessel's functions  $J_2(\mu_M)$  and  $J_3(\mu_M)$ . We must therefore evaluate the corresponding wavelength shift which depends on the device geometry, the constitutive materials and the working wavelength.

In order to compute the required modulation depth in terms of wavelength shift, we start from the phase definition, which relates the variation of the phase difference between the two propagating modes to a variation of their refractive indices:

$$\delta(\Delta\varphi_S) = \frac{2\pi L}{\lambda} \left[ -\frac{1}{\lambda} \Delta N_{eff} + \frac{\partial \Delta N_{eff}}{\partial \lambda} \right] \delta\lambda \quad (5.1)$$

where  $L$  is the propagation length,  $\Delta N_{eff}$  the difference of refractive index of the propagating modes and  $\lambda$  the working wavelength.

As a difference with the MZI sensor where the variation of the phase difference was produced only in the sensing area, i.e. where the two propagating modes show an asymmetry, in the case of modal interferometers all the device length contributes to an accumulation of phase difference induced by a wavelength variation. Considering the BiMW geometry, as illustrated in Fig. 2.10, the bimodal part of the device is constituted by two sections with a silicon dioxide top cladding ( $n=1.46$  and lengths  $L_{in}$  and  $L_{fin}$ , respectively) separated by the sensing area (length  $L_{sens}$ ) with a variable refractive index which depends on the application. Taking into account the complete structure, the variation of the phase difference induced by a wavelength change,  $\delta\lambda$ , is given by the sum over the three regions, resulting in:

$$\begin{aligned} \delta(\Delta\varphi) = \frac{2\pi}{\lambda} \left\{ L_{sens} \left[ -\frac{1}{\lambda} \Delta N_{eff} + \frac{\partial \Delta N_{eff}}{\partial \lambda} \right]_n \right. \\ \left. + (L_{in} + L_{fin}) \left[ -\frac{1}{\lambda} \Delta N_{eff} + \frac{\partial \Delta N_{eff}}{\partial \lambda} \right]_{n=1.46} \right\} \delta\lambda \end{aligned} \quad (5.2)$$

where the contributions from the  $L_{in}$  and  $L_{fin}$  sections have been gathered together.  $n$  is the refractive index of the medium in contact with the sensing area, usually a watery medium with  $n \approx 1.33$ .

The wavelength variation,  $\delta\lambda$ , required to induce a phase variation,  $\delta(\Delta\varphi_S)$ , can be made explicit for each section as:

$$\delta\lambda = \frac{\lambda}{2\pi L \left[ -\frac{1}{\lambda} \Delta N_{eff} + \frac{\partial \Delta N_{eff}}{\partial \lambda} \right]} \delta(\Delta\varphi_S) \quad (5.3)$$

To evaluate the wavelength variation,  $\Delta\lambda_M$ , required to introduce a phase variation  $\delta(\Delta\varphi_S) = 1.2\pi$ , we computed the eigenvalues of the modes  $TE_{00}$  and  $TE_{10}$  as a function of the working wavelength for the two sections of interest, i.e.



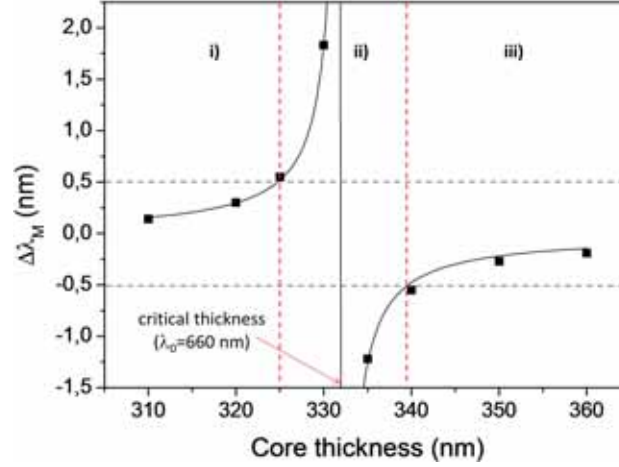


**Figure 5.1:** Required modulation depth as a function of bimodal core thickness.  $\lambda_0 = 660$  nm, TE polarization.

cladding equal to water or dioxide. A small range ( $\pm 2$  nm) around the central wavelength has been considered. The required wavelength shift,  $\Delta\lambda_M$ , can be plotted as a function of the bimodal core thickness, as shown in Fig. 5.1 for the case of TE polarization and a central wavelength  $\lambda_0 = 660$  nm.

As it can be observed in Fig. 5.1, the required modulation amplitude diverges for a critical thickness of  $\approx 330$  nm for  $\lambda_0 = 660$  nm. Taking into account the limited operation range of the laser diode ( $\pm 0.5$  nm), we can set boundaries which determine three different regions: i) sensor chips with waveguide thickness lower than the critical value, ii) sensor chips with waveguide thickness around the critical point and iii) sensor chips with waveguide thickness above the critical point. Sensor chips from family ii) cannot be modulated with the proposed method: the required modulation depth diverges and cannot be introduced with our experimental approach. Sensor chips from families i) and iii) can be modulated and will show opposite directions for the phase variation in response of a same index change, due to the different signs of the required modulation depth. This change in the sensor response direction is in agreement with previous studies with hetero-modal fiber sensors [Tripathi et al., 2010, Salik et al., 2012].

Due to the proximity of the nominal core thickness of the fabricated devices ( $t = 340$  nm) to the critical thickness resulting from Fig. 5.1 ( $t \approx 330$  nm for  $\lambda_0 = 660$  nm), any slight variation due to fabrication tolerances can lead to significant variations on the required modulation depth or even to the impossibility of the phase

linearization. However it is possible to apply the proposed phase linearization method on sensor chips belonging to the external regions shown in Fig. 5.1.

## 5.2 Experimental demonstration

The experimental set-up employed for the  $\lambda$ M-BiMW is a simplified version of the set-up used for the  $\lambda$ M-MZI (see Fig. 5.2(a)). In the case of BiMW the normalized nature of the  $S_R$  signal allows a self-compensation of the amplitude modulation effects resulting from the intensity modulation of the laser diode source, making the external reference signal unnecessary. Furthermore the final translation stage, hosting the collection objective and the detector is eliminated, since the two-sectional detector is directly anchored to the chip holder, resulting in an improved mechanical stability. As already presented in the case of BiMW sensors intensity interrogated (see Section 3.4) a temperature stabilization system must be employed due to the different temperature sensitivities of the two modes, which could result in false positive signals.

Figure 5.2(a) shows a scheme of the set-up employed for the characterization of the  $\lambda$ M-BiMW sensors, while panel (b) shows a picture of the experimental set-up.

In this case a fiber pigtailed laser diode (LP660-SF60,  $\lambda_0 = 660$  nm, Thorlabs) mounted on a pigtailed specific mount (LM9LP, Thorlabs) is used (element A in Fig. 5.2(b)). As included in Table 4.1 the wavelength excursion of this LD is lower than the one achievable with the previously employed ML101J27, but it is sufficient to achieve the modulation working point on the BiMW sensors. A collimation package (F240APC-B, Thorlabs) is directly attached to the fiber end to ensure a collimated beam, which is directed towards an optical isolator and then coupled into the sensor chip through a  $40\times$  microscope objective, placed on a 3-axis position stage (C). As in the case of intensity interrogation, the BiMW sensor chip is placed on a methacrylate housing, mounted on a 1-axis translation stage to evaluate different sensors on the same chip (D). The two-sectional detector is directly anchored at the chip output (F) and the output currents  $I_{up}$  and  $I_{down}$  are amplified with standard amplifiers before being processed (G). The experimental setup is completed with the fluidics components, i.e. the injection valve and the syringe pump (I and L elements).

The laser diode emission is controlled in current and temperature with a bench-top laser controller (ITC510, element B). The modulation signal is controlled with a Labview application and fed to the laser controller through an acquisition card (NI USB-6361, element H).

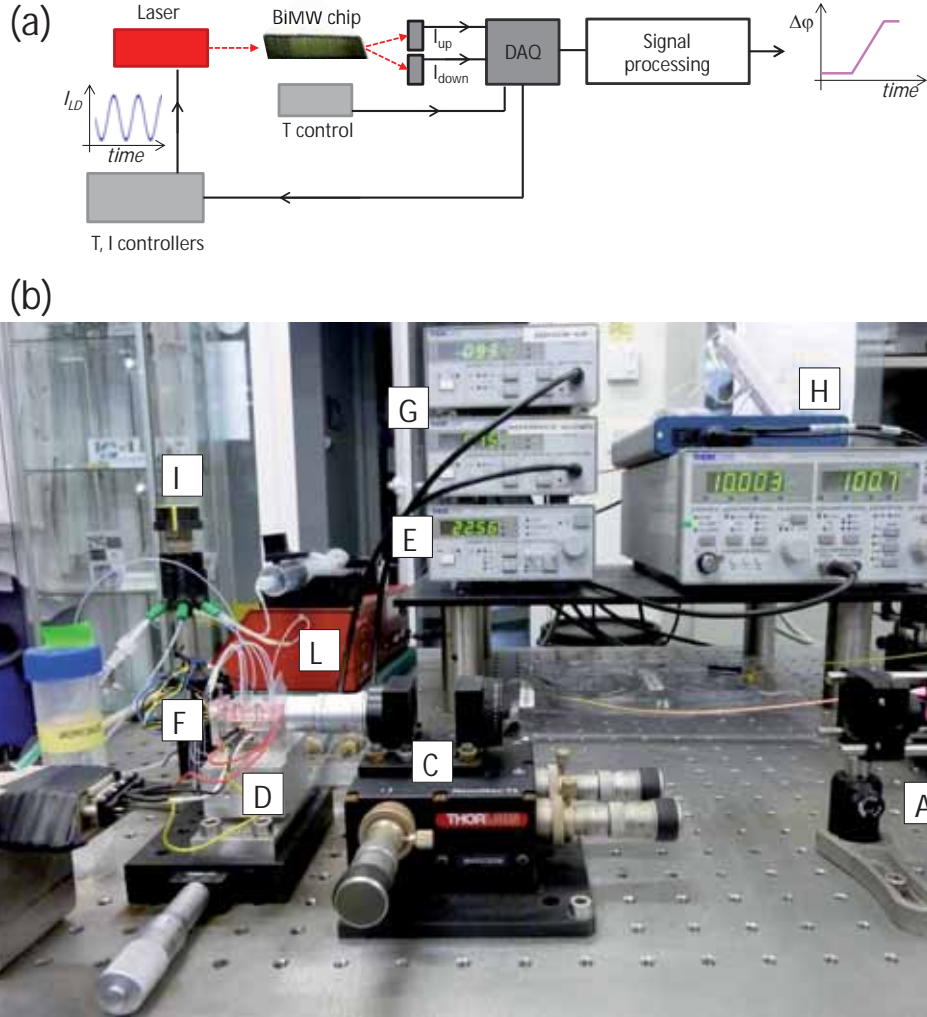


**Figure 5.2:** (a) scheme and (b) photograph of the experimental set-up for the optical characterization of the  $\lambda$ M-BiMW sensors.

Similarly to the case of  $\lambda$ M-MZI, a Labview application was implemented to manage the generation of the modulation signal and the acquisition of the BiMW output, consisting in the two currents  $I_{up}$  and  $I_{down}$  coming from the two sections of the photodetector. Figure 5.3 shows two screen-shots of the Labview user-interface, showing the acquired signals  $I_{up}$  and  $I_{down}$  (see plot (a)), their sum showing a sinusoidal variation due to the laser intensity variations (plot (b)) and the characteristic BiMW signal  $S_R$  showing the phase modulation (plot (c)).

The signal processing is the same as described in Section 4.4.3 after replacing the normalized MZI output  $I_N = \frac{I_T}{\alpha I_{REF}}$  by the BiMW signal  $S_R$ . The FFT is computed on the modulated  $S_R$  (subfigure (d)) and the second and third harmonics are extracted from the real and imaginary parts of the spectrum, respectively. Plot (e) shows the temporal evolution of the two harmonics in response to a variation of the refractive index of the sensing area medium. The corresponding phase variation is evaluated from the inverse tangent of the harmonics ratio, as detailed in Section 4.2 and is displayed in plot (f).

The deviations of the laser emission from an ideal case of perfect linear dependence with the driving current and small fabrication variations are overcome with a pre-set of the working point: the amplitude of the laser current oscillations is varied till the acquired harmonics oscillate in the same range, satisfying Eq.(4.7). For clarity, we show in Fig. 5.4 the three different situations that can be observed as a function of the modulation depth amplitude. For this, we consider a sensor chip from family iii), i.e. with a core thickness higher than the critical value. Panel (a) shows the case of under-modulation, panel (b) represents the correct modulation point and panel (c) represents the case of over-modulation. In the first column the acquired  $S_R$  signals are shown, indicating different periodicities which depend on the applied modulation depth. In the second column of Fig. 5.4 we present the temporal evolution of the second and third harmonics in response to a variation of the refractive index in the sensing area. As it can be noticed only in the case (b) of correct modulation the harmonics  $I_2$  and  $I_3$  oscillate in the same range, while  $I_2 > I_3$  for under-modulation (case (a)) and  $I_2 < I_3$  in the case of over-modulation (case (c)), in agreement with Bessel's function trend (compare with Fig. 4.1).

### Verification of the critical region

In order to verify the theoretical modelization, we experimentally characterized sensor chips belonging to the three regions highlighted in Fig. 5.1.

As presented above, for a sensor chip belonging to family iii) the modulation

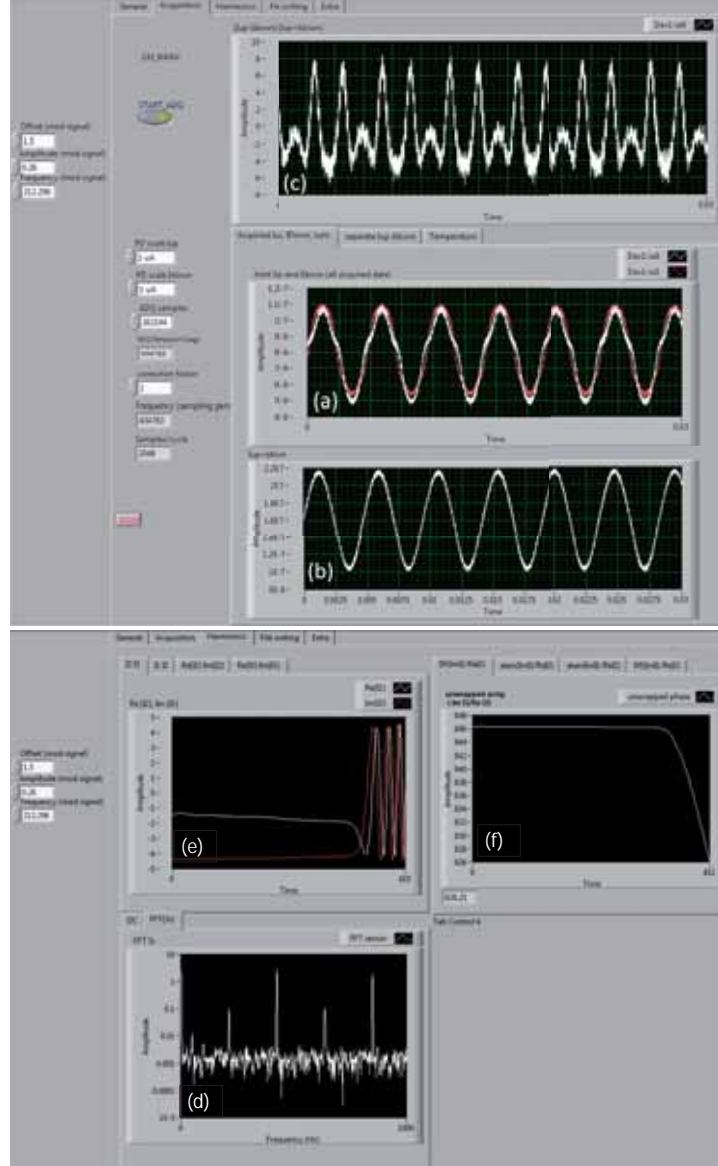


**Figure 5.3:** Screen-shots of the  $\lambda$ M-BiMW acquisition software. (a)  $I_{up}$  and  $I_{down}$ , (b) total intensity  $I_{up} + I_{down}$ , (c) Modulated  $S_R$ , (d)  $\text{FFT}\{S_R\}$  amplitude, (e) harmonics  $I_2$  and  $I_3$  and (f) unwrapped phase signal.

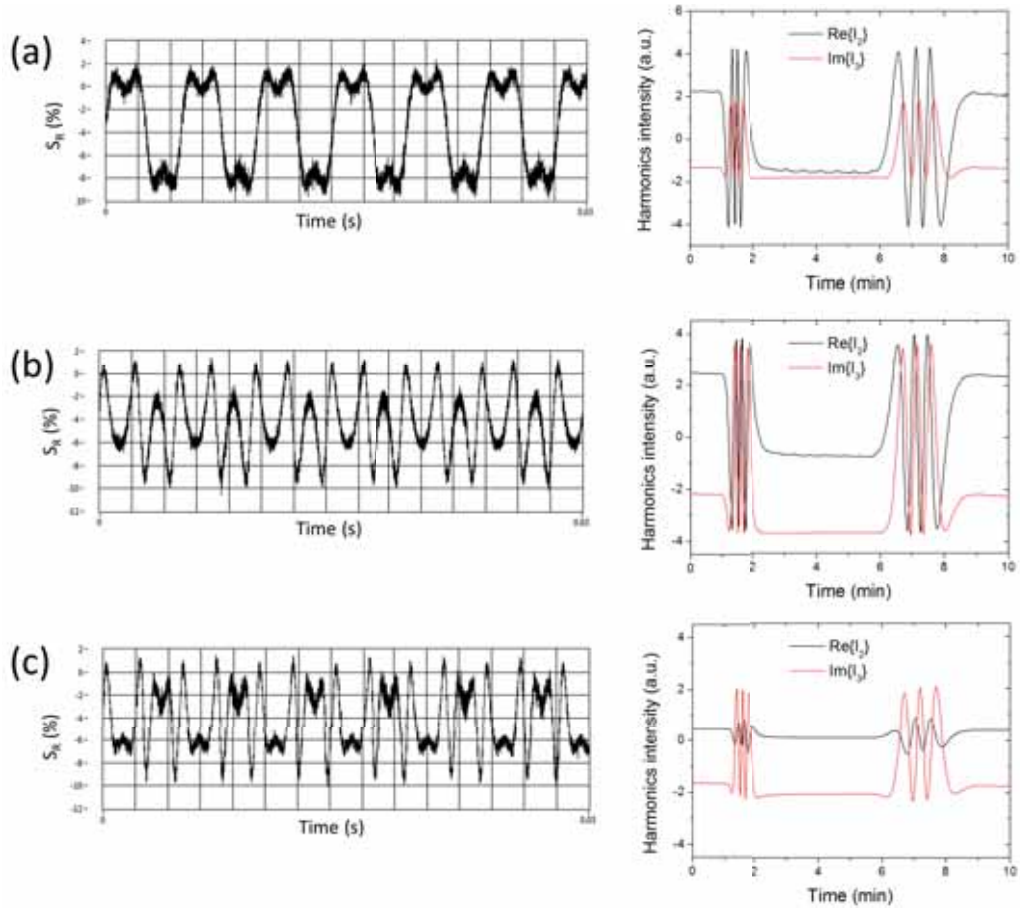


**Figure 5.4:** Acquired  $S_R$  signal and corresponding harmonics for different modulation amplitudes. (a) under-modulation ( $\delta I_{LD} = \pm 15$  mA), (b) correct modulation depth ( $\delta I_{LD} = \pm 26$  mA) and (c) over-modulation ( $\delta I_{LD} = \pm 36$  mA). TE polarization,  $\lambda_0 = 660$  nm.

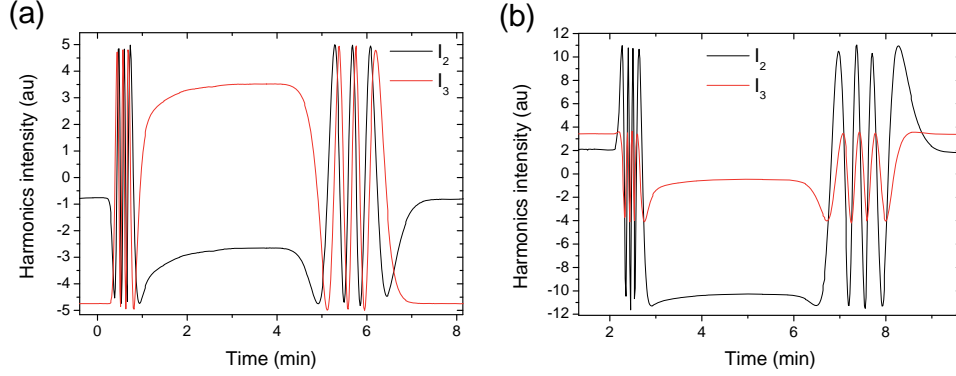


**Figure 5.5:** Comparison of the harmonics behavior in the case of (a) correct modulation setpoint, achieved for a sensor chip from family i) and (b) insufficient modulation depth, observed on a sensor chip from family ii).

working point was achieved with a laser current modulation  $\delta I_{LD} = \pm 26$  mA. Figure 5.5 shows the comparison of the harmonics behavior during a variation of the refractive index in the sensing area for a sensor chip of family i) modulated with a laser current amplitude  $I_{LD} = \pm 28$  mA and a sensor chip from family ii) modulated with a current variation  $I_{LD} = \pm 67$  mA. It can be noted how in the case of the sensor chip i), operated at the correct working point, the second and third harmonic oscillate in the same range, while for the sensor chip ii), despite the use of the maximum current excursion permitted by the experimental set-up, the amplitude of the oscillations of the second harmonic is bigger than the third one. For this last chip the working point cannot be experimentally reached due to the divergence of the required modulation depth (compare Fig. 5.1).

Therefore, in order to achieve a linear read-out with the proposed wavelength modulation scheme, operation close to the critical point must be avoided.

### 5.3 Bulk characterization

Once verified the existence of a critical region for the working wavelength  $\lambda_0 = 660$  nm, we evaluated the performance of BiMW sensor chips belonging to families i) and iii), for which the required modulation amplitude can be experimentally introduced. As a consequence of the opposite signs of the required modulation depth presented in Fig. 5.1,  $\Delta\lambda_M > 0$  for family i) and  $\Delta\lambda_M < 0$  for family ii), we expect an opposite direction for the evolution of the phase response, induced



**Table 5.1:** Refractive index change induced by a set of HCl solutions and corresponding phase changes evaluated with the  $\lambda$ M-BiMW operated at  $\lambda_0 = 660$  nm.

HCl concentration (M)	$\Delta n$	$\Delta\varphi$ (rad)	$\Delta\varphi$ (rad)
		Sensor chip i)	Sensor chip iii)
0.025	$4 \cdot 10^{-4}$	$3.15 \pm 0.02$	$2.77 \pm 0.31$
0.05	$6 \cdot 10^{-4}$	$6.18 \pm 0.02$	$5.33 \pm 0.07$
0.1	$1.1 \cdot 10^{-3}$	$12.61 \pm 0.01$	$11.04 \pm 0.09$
0.2	$2 \cdot 10^{-3}$	$26.51 \pm 0.28$	$22.44 \pm 0.09$

by the same refractive index variation.

Following the procedure detailed in Section 3.6, HCl solutions with different concentrations are sequentially supplied to the sensor chip. First the chip from family i) is characterized. As we can notice in Fig. 5.6(a) a positive refractive index variation induces a positive phase response. HCl solutions with increasing concentrations are sequentially supplied and the corresponding phase changes evaluated. The same set of HCl solutions is then evaluated on the chip from family iii). As shown in Fig. 5.6(b), the sensor response shows a negative evolution for the same positive refractive index variations. Also for this chip different HCl solutions are sequentially supplied. For each chip the calibration procedure is repeated three times and the average sensor responses, together with the refractive index changes of each HCl solution, are summarized in Table 5.1.

The measured phase changes can be plotted as a function of the refractive index variation, resulting in the calibration curves shown in Fig. 5.6(c) and 5.6(d) for the sensor chips i) and iii) respectively. The error bars correspond to the signal deviation obtained after repeating the experiment three times. The experimental sensitivities are evaluated with a linear fit of the data shown in the calibration curves, resulting in values of  $2120 \cdot 2\pi$  rad/RIU for sensor chip i) and  $1790 \cdot 2\pi$  rad/RIU for sensor chip iii). These values confirm the theoretical modelization, for which a higher sensitivity was expected for chips with a core thickness in the range 310-330 nm with respect to chips with core thickness in the range 330-350 nm (compare with Fig. 2.12).

Once the bulk sensitivities have been determined, we can evaluate the limits of detection for each sensor chip. Due to the direct read-out of the measurements, the minimum signal variation  $\Delta\varphi_{min}$  can be considered as three times the standard deviation  $\sigma$  on the baseline noise. For chip i)  $\sigma = 1.42$  mrad and for chip ii)  $\sigma = 2.45$  mrad. Taking into account the previously computed sensitivities, we evaluate limits of detection of  $4 \cdot 10^{-7}$  RIU for sensor chip i) and  $6 \cdot 10^{-7}$  RIU for sensor



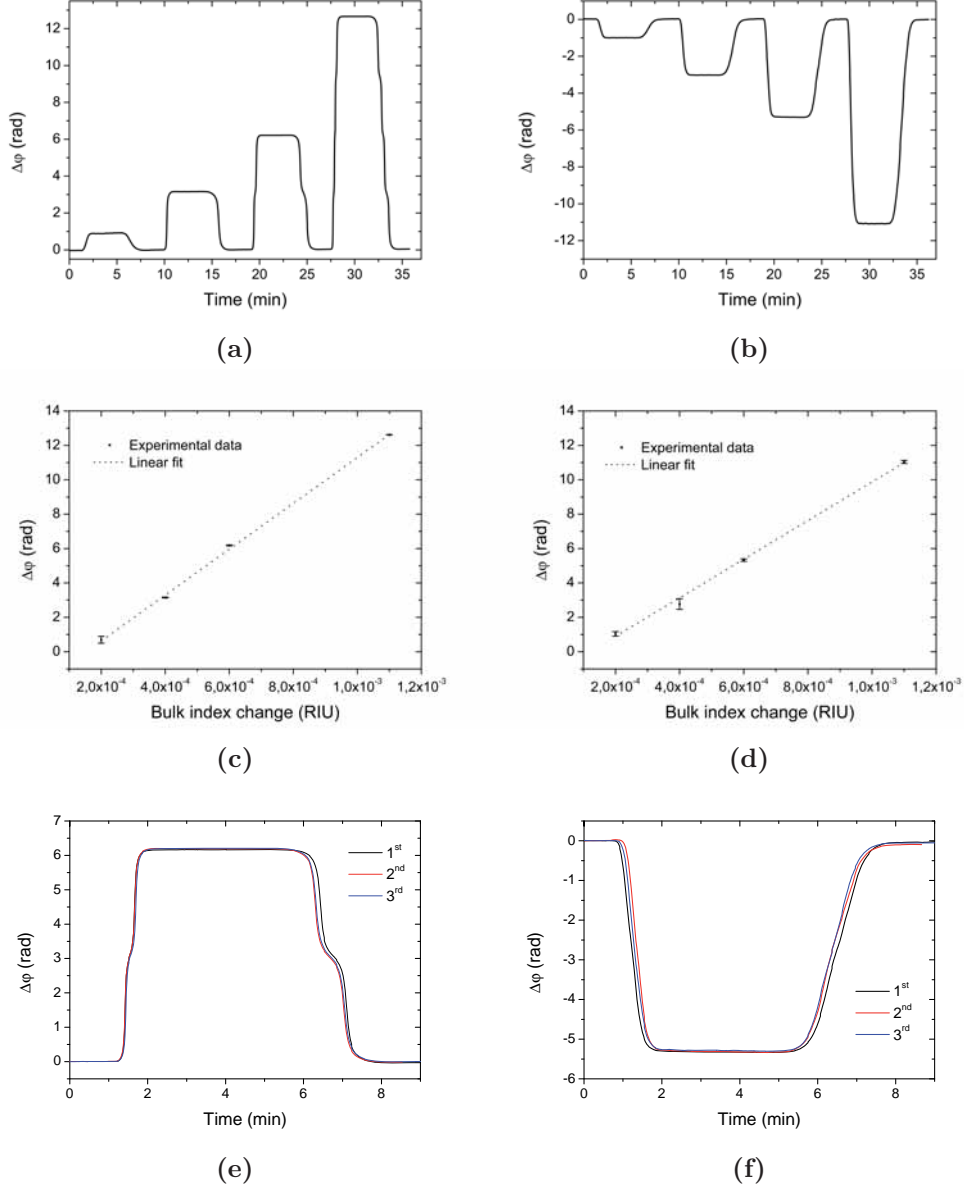


**Figure 5.6:** Time evolution of the sensor response to different HCl solutions for a sensor chip (a) before and (b) after the critical point, resulting in the (c) and (d) calibration curves. Error bars correspond to three replica of the experiment. Triplicate detection of an index change  $\Delta n = 6 \cdot 10^{-4}$  for a sensor chip from family i)(e) and from family iii) (f).

chip iii).

These values are comparable with the results obtained in the standard monochromatic approach with a He-Ne laser [Zinoviev et al., 2011], demonstrating the validity of the all-optical modulation method which can be implemented with a compact and cost-effective laser diode.

Figures 5.6(e) and 5.6(f) show the replica of the detection of the refractive index change  $\Delta n = 6 \cdot 10^{-4}$ , corresponding to HCl 0.05 M, on the sensor chips i) and iii) respectively. For the sensor chip i) we have evaluated phase responses of 6.16 rad, 6.19 rad and 6.20 rad for the three detections, resulting in an average value  $\Delta\varphi = (6.18 \pm 0.02)$  rad. For the sensor chip iii) the same HCl solution induced phase changes of 5.41 rad, 5.27 rad and 5.32 rad, corresponding to an average signal  $\Delta\varphi = (5.33 \pm 0.07)$  rad. For both chips we have observed a low dispersion of results, with relative variations of 0.3% for sensor chip i) and 1.3% for chip iii), demonstrating a high reproducibility of the method.

After assessing the critical behavior of the wavelength modulated BiMW sensor, which results into two spectral regions with opposite sensor response directions, the modelization of the wavelength modulated MZI has been re-examined, as reported in Appendix B.

## 5.4 Overcoming the critical effects

In order to overcome the limitations imposed by the existence of a critical point in the BiMW transmission spectrum in correspondence to the working wavelength  $\lambda_0 = 660$  nm, an alternative central wavelength or a different polarization can be employed.

### Numerical modelization

The theoretical wavelength modulation depth is evaluated from Eq.(5.2) and the results are presented in Fig. 5.7 for the case of TE polarization, comparing the two central wavelengths  $\lambda_0 = 638$  nm and  $\lambda_0 = 660$  nm. As expected, by considering a shorter central wavelength the hyperbole asymptote is displaced towards smaller core dimensions. The critical thickness corresponding to a working wavelength  $\lambda_0 = 638$  nm has been evaluated as 320 nm.

The consequence of this shift of the critical thickness as a function of the working wavelength is the possibility to achieve the modulation working point for some of the devices belonging to family ii) according to the data plotted in Fig. 5.7.

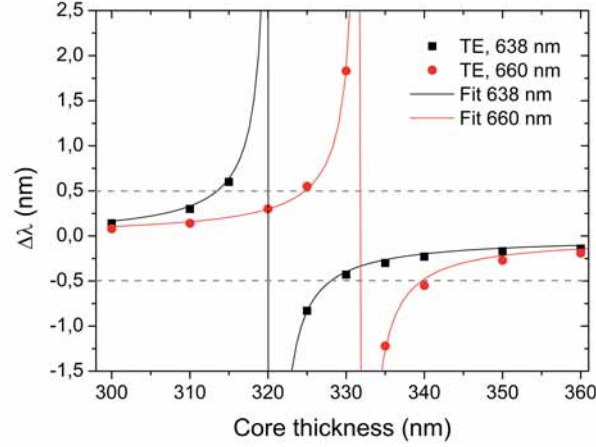


**Figure 5.7:** Comparison of the required wavelength modulation depth for the BiMW sensor for central wavelengths  $\lambda_0 = 638$  and  $\lambda_0 = 660$  nm (TE polarization).

**Table 5.2:** Critical thickness as a function of polarization and working wavelength.

Wavelength (nm)	Critical thickness (nm)	
	TE	TM
638	321	396
660	332	410

Similarly to the shift of the critical thickness observed by a change in the working wavelength also a change in the incident light polarization induces a displacement of the critical region. If considering TM polarization, the core dimension leading to spectral divergence shifts to greater dimensions, in analogy with the trend observed for the bulk sensitivity presented in Section 2.3. For example in the case of  $\lambda_0 = 638$  nm, the asymptote is displaced to 395 nm, while for  $\lambda_0 = 660$  nm it assumes the value of 410 nm, as shown in Fig. 5.8(a) and 5.8(b) respectively. To summarize, Table 5.2 details the critical thickness values evaluated in the four inspected cases (633/660 nm, TE/TM polarization).

It is important to notice that according to the experimental conditions ( $\lambda_0$ , polarization) a same sensor chip will show opposite directions for the phase response, as it can be seen in the plots of Fig. 5.8 where the required modulation depth shows opposite signs for TE and TM in the region comprised between the two asymptotes. This is a consequence of the different slopes of  $\Delta N_{eff}(\lambda)/\lambda$ ,

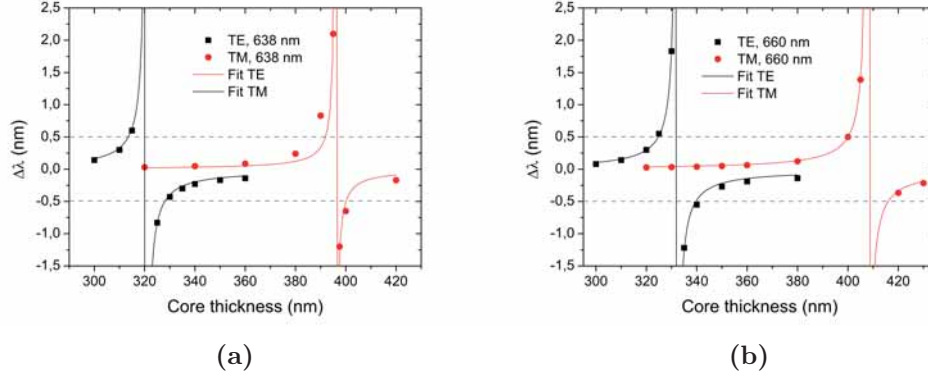


**Figure 5.8:** Comparison of the required wavelength modulation depth for TE and TM polarizations for (a)  $\lambda_0 = 638$  nm and (b)  $\lambda_0 = 660$  nm.

resulting in blue or red shifts for the same applied stimulus.

However, once selected the sensor chip and fixed the working conditions, the direction ambiguity affecting the standard DC measurement is solved since the phase variation will always take place in the same direction.

### Experimental verification

The sensor chip of family ii), i.e. with core thickness close to the critical value for  $\lambda_0 = 660$  nm, has been tested with a central wavelength  $\lambda_0 = 638$  nm. According to the numerical modelization shown in Fig. 5.7, the required modulation depth is lower than 0.5 nm and the sensor will show a negative phase response.

For this experiment a custom-pigtailed laser diode LP638-PA50 was purchased to Thorlabs, by pigtailling the laser diode ML520G55 ( $\lambda_0 = 638$  nm). A TCLDM9 laser diode mount was employed for current and temperature stabilization of the laser cavity, by employing benchtop controllers LDC220C and TED200C for the current and temperature, respectively. The main difference between the LDC220C and the previously employed ITC510 controller, relies on the modulation coefficients for voltage-current conversion, which is around 200 mA/V for the LDC220C and 100 mA/V for the ITC510.

A bulk calibration was performed with the 638 nm-laser source in the case of both polarizations. For this we employed a set of HCl solutions in the range 0.1 M - 0.25 M. The corresponding index change with respect to milli-Q water and the phase variation signals produced on the sensor output are summarized in Table

**Table 5.3:** Refractive index change induced by a set of HCl solutions and corresponding phase changes evaluated with the  $\lambda$ M-BiMW operated at  $\lambda_0 = 638$  nm, TE and TM polarizations.

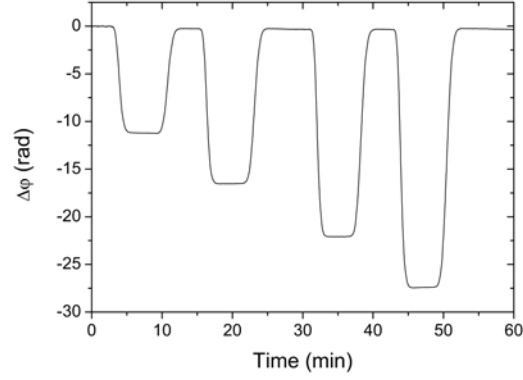
HCl concentration (M)	$\Delta n$	$\Delta\varphi_{TE}$ (rad)	$\Delta\varphi_{TM}$ (rad)
0.1	$1.2 \cdot 10^{-3}$	11.18	15.97
0.15	$1.6 \cdot 10^{-3}$	16.25	23.55
0.2	$2 \cdot 10^{-3}$	21.73	31.68
0.25	$2.5 \cdot 10^{-3}$	27.07	39.37

### 5.3.

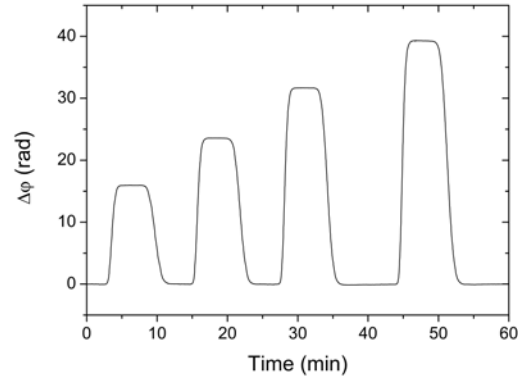
The sensorgrams corresponding to the detection of the four HCl solutions are depicted in Fig. 5.9a and 5.9b for TE and TM, respectively. From the temporal evolution of the sensor response we can observe how the induced phase shift shows opposite directions, in agreement with the theoretical expectations presented in Fig. 5.8a, being negative for TE and positive for TM polarizations.

The phase changes produced by the different HCl concentrations have been evaluated and plotted as a function of the applied refractive index variation, resulting in the calibration curves shown in Fig. 5.9c. The experimental sensitivities have been evaluated as  $1960 \cdot 2\pi$  rad/RIU and  $2890 \cdot 2\pi$  rad/RIU for TE and TM, respectively, in agreement with the theoretical modelization. However the standard deviation of the baseline noise is higher than in the previously evaluated configurations: values of  $\sigma=12$  mrad for TE and  $\sigma=30$  mrad for TM have been evaluated, corresponding to detection limits of  $3 \cdot 10^{-6}$  and  $5 \cdot 10^{-6}$  RIU for TE and TM, respectively. These values are one order of magnitude higher than the previous results, obtained with the 660 nm-laser source. The high noise observed in this configuration is likely related to the presence of longitudinal modes in the laser emission spectrum, as it can be inferred from the screen-shot of the Labview user interface presented in Fig. 5.10, showing the acquired signals  $I_{up}$  and  $I_{down}$  (graph (a)) and the corresponding  $S_R$  signal (graph (b)). As we can notice high-frequency components are superposed to the phase modulated  $S_R$  signal.

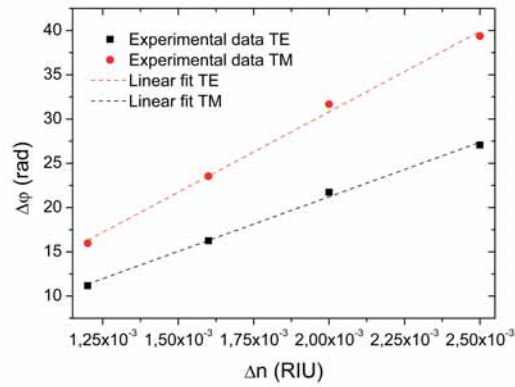
Despite the higher limits of detection achieved, which are related to the employed laser source, we have demonstrated that the use of an alternative laser wavelength ( $\lambda_0 = 638$  nm) can overcome the critical effects shown by the sensor chips previously interrogated at  $\lambda_0 = 660$  nm.



(a) TE polarization.



(b) TM polarization.



(c) Calibration curves.

**Figure 5.9:** Time evolution of the sensor response for different HCl solutions for (a) TE and (b) TM polarization and (c) corresponding calibration curves.  $\lambda_0 = 638$  nm.

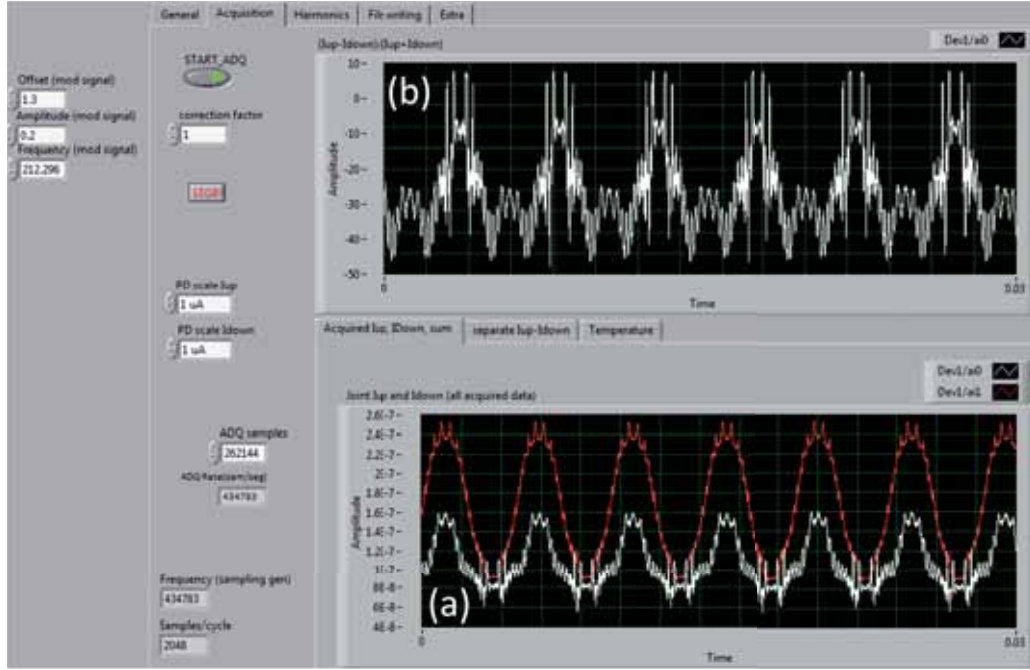


**Figure 5.10:** Screen-shot of the acquired  $I_{up}$  and  $I_{down}$  signals and resulting  $S_R$  for the  $\lambda M$ -BiMW sensor operated at  $\lambda_0 = 638$  nm.

## 5.5 Conclusions

Along this Chapter we have theoretically and experimentally demonstrated the applicability of the all-optical phase modulation approach for the integrated BiMW biosensors. We have obtained a direct and linear phase read-out and, by employing a laser source at 660 nm, and we have demonstrated bulk detection limits in the order of  $4 \cdot 10^{-7}$  RIU. These values are comparable with the results achieved with the He-Ne laser, commonly used in the traditional intensity interrogation approach, indicating that the use of a compact laser diode does not compromise the final biosensor performance.

Due to the non linearity of  $\Delta N_{eff}(\lambda)$  a critical behavior has been observed, which leads to the divergence of the required modulation depth in correspondence of a critical thickness, whose value depends on the working wavelength and polarization (once fixed the sensor dimensions and material composition). We have demonstrated that by choosing the appropriate wavelength and polarization the critical effects can be overcome.

We have presented a general formulation for the required modulation depth, which can be extended to all modal interferometers. As shown along this Chapter the method can be applied for different working wavelengths and polarizations.



# Chapter 6

## Biosensor validation

In this chapter we demonstrate the biosensor capabilities of the phase-modulated sensors which have been previously characterized in terms of non-specific bulk detections. To allow a selective detection, a biological receptor must be incorporated on the transducer surface. We review the main requirements for the bioreceptor immobilization and demonstrate the validity of the phase-linearized biosensors with the evaluation of different immunosensing reactions.

### 6.1 Biosensing: overview

Till this point we have focused on the development of a reliable and sensitive transducer method; however to obtain a biosensor device a biological receptor must be included to ensure selective detections of the target analyte. The bio-functionalization protocol plays a crucial role in the biosensor performance as the immobilization process should guarantee an efficient coverage of the transducer surface and ensure sensitivity, selectivity and stability of the biosensor.

The function of bioreceptor is entrusted to those biomolecules showing a highly remarkable capability of molecular recognition with a strong affinity to the target analyte. Some biological systems are particularly important and exploited in the construction of a sensing layer or in establishing intelligence in the sensors. For example we can cite enzyme/substrate, antibody/antigen and nucleic acids/complementary sequences interactions. In addition to these, sensing layers can also incorporate micro-organisms, animal or plant whole cells and even tissue slices. More recently synthetic receptors as aptamers and molecularly imprinted

polymers (MIP) have been introduced as new recognition elements.

Once chosen the proper receptor, the selected strategy must ensure a stable immobilization, without denaturing its structure; should allow surface regeneration for multiple assays; prevent surface fouling and be non-invasive for the physical-optical properties of the transducer [Bañuls et al., 2013, Hunt and Armani, 2014]. Different immobilization strategies can be employed according to the selected application, i.e. to the nature of the bioreceptor to be immobilized.

Among the available techniques, i.e. physical entrapment, chemical adsorption or chemical bonding, covalent immobilization demonstrated to be a valid strategy, ensuring stable receptor anchoring, versatility for a spread family of biomolecules through their specific functional groups and resistance to regeneration protocols, allowing to decrease the assay costs. In the case of proteins immobilization, amino, carboxylic or thiol groups are the preferred options to couple proteins [Estevez et al., 2012]. Synthetic oligonucleotide chains, as required for DNA or RNA detection, offer a higher flexibility for the assay design since they can be easily tailored with specific reactive groups at the end of the sequence.

When a covalent immobilization strategy is selected, the sensor surface must be provided with chemical functionality. In this context, silanization strategies are well-established for silicon based surfaces, as in the case of MZI and BiMW sensors described in this Thesis. Silane coupling agents are molecules able to form a durable bond between organic and inorganic materials and are normally composed by three parts: the head group, the alkyl chain and the terminal group. The head group is responsible for anchoring onto the substrate, the alkyl chain is a linker proving stability to the monolayer, while the terminal group is responsible to introduce chemical functionality into the system and allow a stable receptor immobilization [Haensch et al., 2010]. According to the substrate and the application (i.e. the bioreceptor to be immobilized) a wide variety of silanes is commercially available. The most common are amino ( $-NH_2$ ) terminated silanes as the (3-Aminopropyl)triethoxysilane (APTES), sulfur ( $-S$ ) terminated as the (3-Mercaptopropyl)trimethoxysilane (MPTMS) or carboxy ( $-COOH$ ) terminated as the carboxyethyl silanetriol, sodium salt (CTES).

## 6.2 Surface biofunctionalization

To covalently attach proteins on the BiMW transducer, we decided to use the CTES silane, which forms a stable and homogeneous silane monolayer on the silicon nitride surface with carboxylic end-groups. Due to its short alkyl chain (6 Å) and the hydrophilicity of the functional carboxylic group, CTES is a water soluble

silane, making this functionalization strategy especially attractive for biosensing. The advantages offered by this approach rely on short incubation and curing times (1 hour each), avoiding the use of dangerous solvents and the possibility of in-flow receptor immobilization, which can be monitored in real-time. The solubility in water of the CTES constitutes an advantage when compared to other traditional silanes which require solvents to be diluted and the mixture is affected by the presence of residual water molecules [González-Guerrero et al., 2013].

Prior to the biofunctionalization step, a chemical activation of the surface is mandatory to create a thin oxide layer, rich in silanol groups (-OH), which will be used for the silane coupling [Diao et al., 2005]. For this reason, after the cleaning procedure detailed in Section 3.3, the silicon nitride surface is initially treated with a weak ozone plasma (1 h) and then oxidized with a solution of nitric acid ( $\text{HNO}_3$ ) at 10% at 75°C for 25 min. The chip is then immersed in a solution of 0.5% of CTES silane in DI-water, ensuring a complete surface coverage. After the silane incubation, the chip is rinsed with DI-water, blown under  $\text{N}_2$  flow and cured at 110° for 1 h, to ensure the formation of the covalent bonding between the silane head-group and the underlying surface. The surface functionalization process is summarized in Fig. 6.1(a).

The carboxy-terminated sensor surface can now be tailored with different bioreceptors. To enable the formation of a stable bond between the carboxylic groups exposed on the sensor surface and the biomolecules in solution, the reactive groups can be activated with the well-known EDC/NHS chemistry [Gao and Rothberg, 2007, Chen et al., 2010]. The functionalized chip is placed in the optical setup and a solution containing EDC/NHS in a molar ratio of (0.2/0.05) in MES buffer is supplied to the sensor surface, at a pump rate of 30  $\mu\text{l}/\text{min}$ . Consequently the solution containing the bioreceptor to be anchored is supplied, at a slower pump rate in the range 10-20  $\mu\text{l}/\text{min}$  to ensure efficient surface coverage. For all the injections sample volumes of 250  $\mu\text{l}$  are employed.

A solution of ethanolamine 1 M (pH 8.5) is used as blocking agent to deactivate unreacted carboxylic groups and prevent non-specific adsorptions. Figure 6.1(b) shows a scheme of the sensor surface after the bioreceptor immobilization.

## 6.3 Biosensing validation

### 6.3.1 $\lambda\text{M}$ -MZI validation: hGH/anti-hGH detection

In order to fully demonstrate the viability of the  $\lambda\text{M}$ -MZI device for biosensing applications, we evaluated the immunoreaction of the pair human Growth Hormone

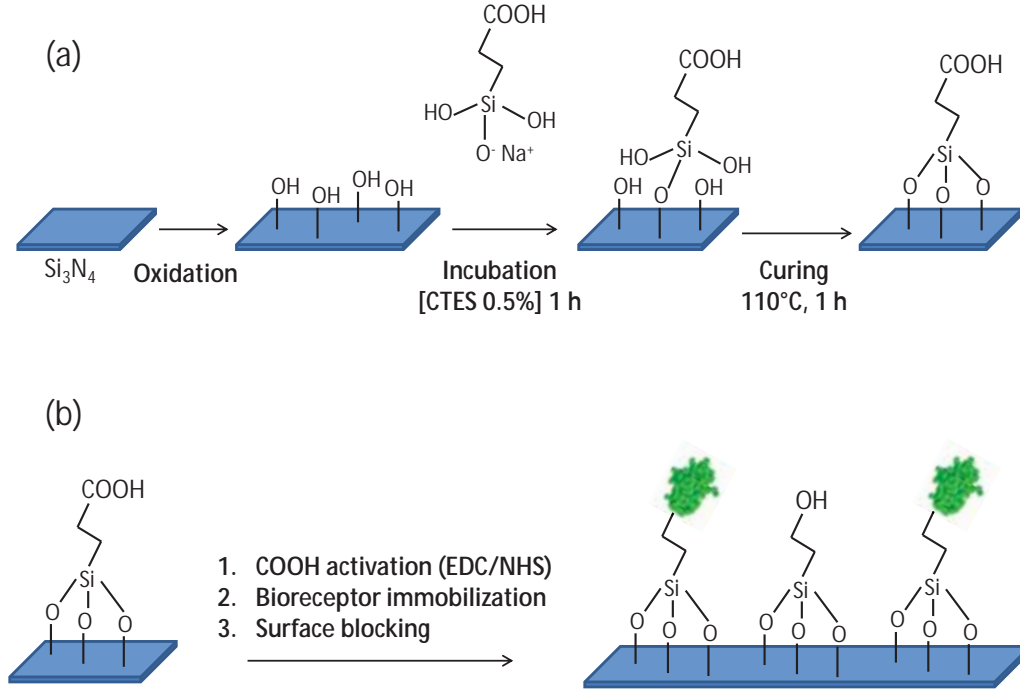


**Figure 6.1:** Scheme of the functionalization process.

(hGH) and its specific antibody (anti-hGH) using the modulated MZI sensor.

hGH is a hormone secreted by the anterior pituitary gland, which is fundamental for the normal growth and development of any person. hGH is clinically interesting since its synthetic counterpart is often employed as performance enhancer in different sportive disciplines and its use has been banned since 1989 by the International Olympic Committee. However due to the complexity of the implementation of a selective assay based on conventional techniques, a specific test has not been included yet in standard anti-doping controls [de Juan-Franco et al., 2013]. For this reason, the integrated interferometric biosensor can offer a highly sensitive platform for hGH detection.

Due to its higher resistance to regeneration processes as compared to the antibody, hGH is employed as bioreceptor in this assay and the immunoreaction is evaluated by supplying different concentrations of antibody on the sensor surface.

After the silanization step described above, the chip is placed in the experi-

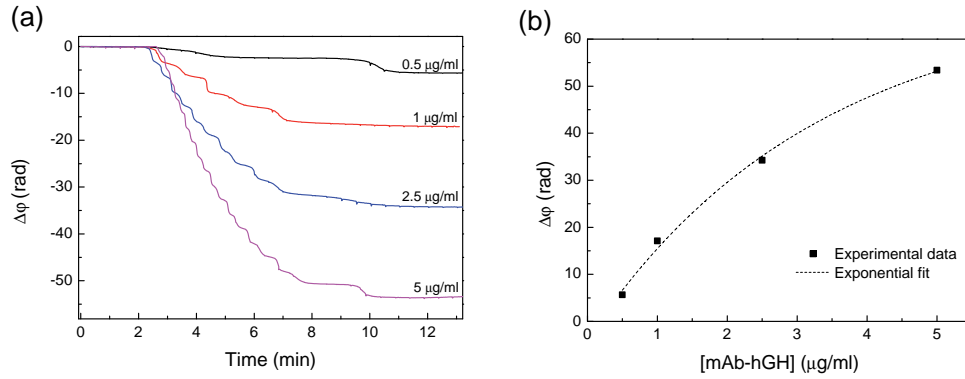


**Figure 6.2:** (a) Real-time detection of different concentrations of mAb-hGH in PBS and (b) corresponding calibration curve.

mental set-up, as detailed in Section 4.4.4. Water is supplied as running buffer and a solution of EDC/NHS is injected to activate the carboxylic groups of the silanized chip surface. Then hGH is immobilized on the sensor surface in a concentration of 50  $\mu\text{g/ml}$ , diluted in acetate buffer. To complete the immobilization process, a solution of ethanolamine is supplied, to reduce non-specific bindings.

The running buffer is then changed from water to phosphate buffered saline (PBS) and, after stabilization, different concentrations of the specific antibody (mAb-hGH) in the range 0.5-5  $\mu\text{g/ml}$  diluted in PBS buffer are later supplied to the sensor area. The corresponding sensorgrams are shown in Fig. 6.2(a). The receptor surface is regenerated by flowing a solution of HCl 10 mM in between the different immunoreactions.

The resulting calibration curve, obtained by plotting the sensor phase variations as a function of the anti-hGH concentration, is presented in Fig. 6.2(b).

The dose response curve well adapts to an exponential growth curve, validating the use of the wavelength modulated MZI as a direct biosensor device. By considering a noise standard deviation of 2.5 mrad, from the interpolation of the exponential fit curve, the LOD of the proposed assay is evaluated as 170 ng/ml.

The importance of these results rely on the achievement of a real-time direct phase read-out for the detection of immunoassay reactions, which extremely simplifies data analysis and overcomes the ambiguity of the standard interrogation scheme, however further optimization of the surface immobilization protocol is required to achieve a lower detection limit.

### 6.3.2 $\lambda$ M-BiMW validation: BSA/anti-BSA detection

The applicability of the wavelength modulated BiMW sensor as biosensor has been verified through the detection of the immunoreaction between the Bovine Serum Albumin (BSA) protein and its specific antibody (mAb-BSA), commercially available. BSA/anti-BSA pair is commonly employed as model system for the proof-of-concept of a new sensor platform [Bañuls et al., 2013].

After the surface activation described above, a solution of BSA 50  $\mu\text{g/ml}$  in PBS buffer was supplied to the sensor area, at a pump rate of 10  $\mu\text{l/min}$ . The phase signal corresponding to this immobilization is shown in Fig. 6.3(a), together with the corresponding standard signal ( $S_R$  fringes) obtained from the DC component extracted from the Fourier spectrum, shown in Fig. 6.3(b). As we can notice, the evaluation of the net immobilization signal is straightforward in the case of phase signal variation, thanks to the real-time linear read-out offered. This extremely simplifies the data analysis process, since following the standard intensity interrogation approach (here represented by the DC component), all the oscillations corresponding to the water-bioreceptor solution change and bioreceptor solution-water variation should be taken into account and subtracted to achieve the net signal of immobilization.

After the blocking step consisting of a solution 1 M of ethanolamine, solutions of specific antibody at different concentration in the range 0.1-1  $\mu\text{g/ml}$  are supplied to the sensor, while PBS is used as running buffer. The phase signal variations induced by each concentration are evaluated, resulting in the dose-response curve shown in Fig. 6.4.

The reproducibility of the biodetection is tested by replicating the detection of the same target concentration. For this reason, a solution 1  $\mu\text{g/ml}$  of BSA is supplied to the sensor three times, separated by a surface regeneration process consisting in flowing a solution of HCl 10 mM. The sensorgrams corresponding to the triplicated detection are shown in Fig. 6.5(a), with signals of 6.51, 6.83 and 7.16 rad, corresponding to an average value of  $(6.8 \pm 0.3)$  rad. The relative error on the assay evaluation is lower than 5%, indicating a good reproducibility of the experiment.

To assess the specificity of the assay a control experiment is done by injecting a non-specific sample containing anti-human Corionic Gonadotropine (mAb-hGH) in a concentration 0.5  $\mu\text{g/ml}$ . In Fig. 6.5(b) the signals corresponding to specific and non-specific detections for the same antibody concentration (0.5  $\mu\text{g/ml}$ ) are compared. In the case of specific mAb-BSA detection a net signal of 5.76 rad is evaluated, while a signal of 0.19 rad is measured for the non-specific detection.

These results clearly validate the use of the  $\lambda$ M-BiMW sensor as highly sensi-

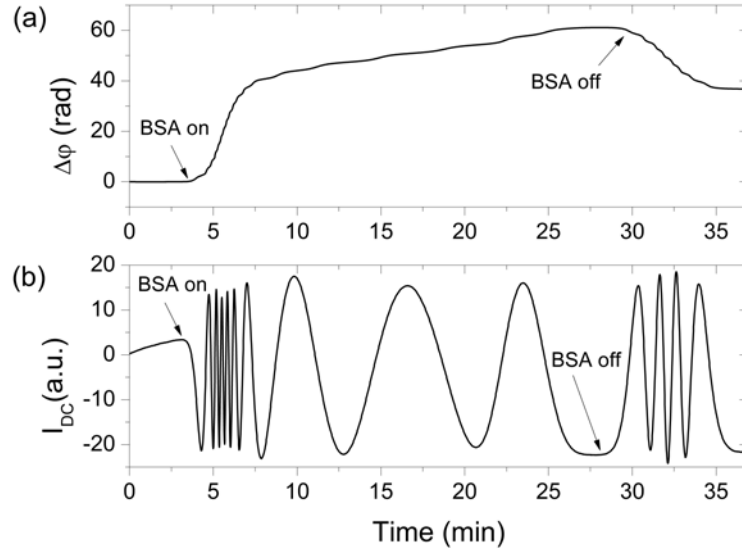


**Figure 6.3:** Real-time monitoring of the covalent attachment of 50  $\mu\text{g}/\text{ml}$  of BSA in PBS buffer on a carboxy-functionalized sensing area. (a) Direct phase read-out and (b) DC component extracted from the deconvoluted output, corresponding to the sensor response with monochromatic excitation.

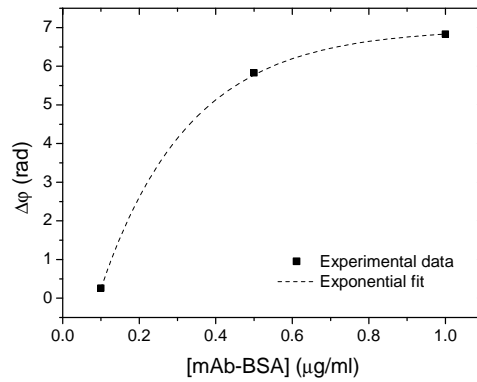


**Figure 6.4:** Dose response curve for the detection of mAb-BSA on a  $\lambda\text{M}$ -BiMW biosensor.

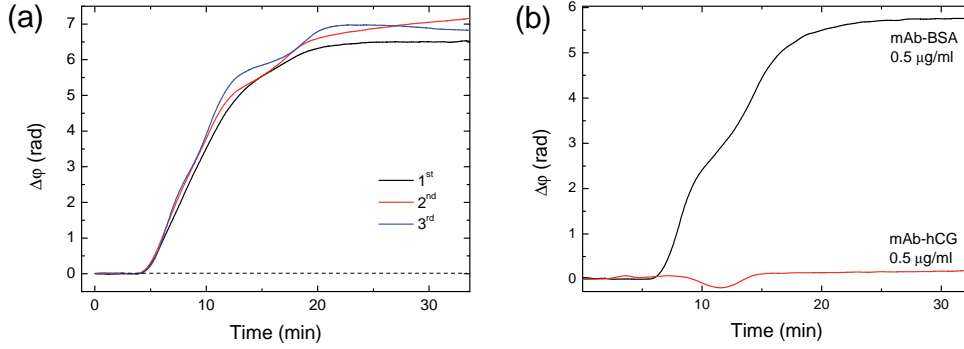


**Figure 6.5:** (a) Replica of mAb-BSA 1  $\mu\text{g/ml}$  detection with  $\lambda\text{M-BiMW}$  and (b) comparison of the specific (black line) and non-specific (red line) detection of 0.5  $\mu\text{g/ml}$  antibody concentration.

tive and reliable biosensor, improving the capabilities of the standard interrogation approach. One of the main advantages is the direct read-out, particularly important for biosensing applications as relevant physiological levels of biomolecules usually produce very small signal variations ( $< \pi$ ) which cannot be directly quantified in the standard approach.

## 6.4 Clinical applications of the $\lambda\text{M-BiMW}$

The  $\lambda\text{M-BiMW}$  has been employed for different applications using the same functionalization process based on the CTES silane. In the following two applications are described, as the detection of the C-reactive protein (CRP) through a direct assay and the detection of human Thyroid Stimulating Hormone (hTSH) by competitive assay. The difference in the two assay methods, summarized in Fig. 6.6, relies on the immobilization of a specific antibody which must recognize the target in the case of direct assay, while in the case of competitive assay the target is first immobilized on the sensor surface. Then a fixed concentration of antibody is incubated with the target to be detected and supplied to the sensor, where only the free antibodies which did not react with the target in solution will bind to the immobilized receptor. In the latter assay format, the sensor signal will be inversely proportional to the target concentration.



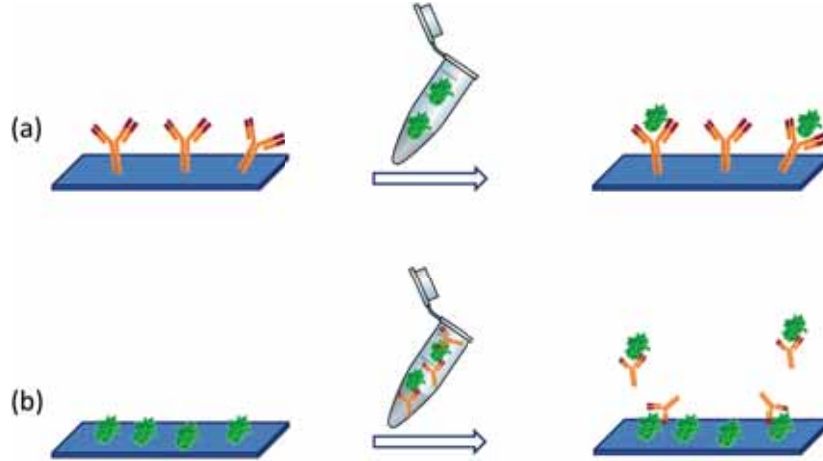


**Figure 6.6:** Comparison of assay formats. (a) direct assay and (b) competitive assay.

#### 6.4.1 CRP protein detection

As a clinical application, we selected the quantification of the immuno-reaction between the CRP protein and its monoclonal antibody (C7 antibody), commercially available (Acris antibodies). CRP is a cyclic pentameric protein produced by the liver which concentration dramatically increases in presence of inflammation or infections. It has been related to hypertension and cardiovascular diseases, and it is one of the biomarkers rapidly evaluated in Emergency Units for any new incomer [Ridker, 2003, Mazer and Rabbani, 2004].

The assay is performed on the BiMW sensor chip from family i), previously characterized for bulk sensing, as described in Section 5.3. After the silanization process, described in Section 6.2, the carboxylic groups are activated by supplying a solution of EDC/NHS. Then the specific antibody is immobilized on the sensor surface by supplying a solution 20  $\mu\text{g}/\text{ml}$ , inducing a net immobilization signal of 23.5 rad (see Fig. 6.7).

After stabilization of the biolayer in PBS buffer, known concentrations of CRP in the range 10-500 ng/ml are supplied to the sensor. The corresponding sensorgrams are shown in Fig. 6.8(a). Regeneration of the bioreceptor layer after CRP immunodetection is achieved with hydrochloric acid 10 mM.

A control experiment is done by injecting a non-specific protein sample containing human corionic gonadotropine (hCG) in a concentration 1  $\mu\text{g}/\text{ml}$ , giving no appreciable signal, as demonstrated in Fig. 6.8(a).

From the data reported in the dose-response curve presented in Fig. 6.8(b)

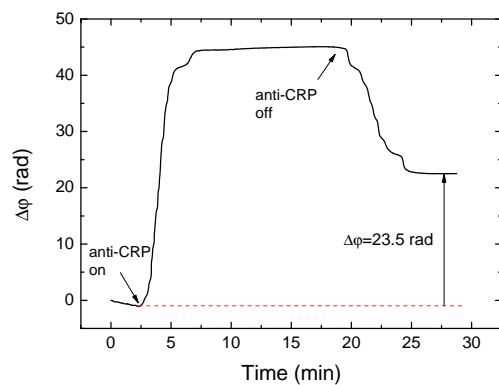


**Figure 6.7:** Real-time immobilization of anti-CRP 20  $\mu\text{g/ml}$  on a  $\lambda\text{M-BiMW}$  biosensor.

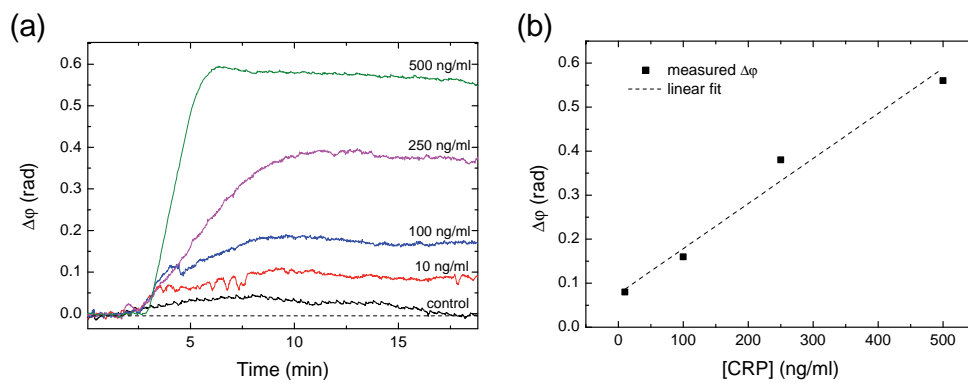


**Figure 6.8:** (a) Sensorgrams of the  $\lambda\text{M-BiMW}$  for the direct detection of CRP protein at different concentrations and (b) corresponding dose-response curve.

the detection limit is estimated as 7 ng/ml [Dante et al., Subm]. This value, obtained with a direct and label-free immunoassay, is comparable with more complicated assay formats implemented for the same pair CRP/anti-CRP in other biosensor devices as Surface Plasmon Resonance sensor [Soler et al., 2014] or electro-chemical sensor [Gupta et al., 2014] and satisfies the requirements of the clinical application.

#### 6.4.2 hTSH hormone detection

As demonstration of another clinical application we selected the detection of the hTSH, secreted by the anterior pituitary gland [Duval et al., 2012]. The determination of low concentrations of hTSH is of clinical importance in the case of hyperthyroid syndromes such as thyroid adenoma, nodular goiter or the autoimmune disorder Graves' disease for which hTSH serum levels are below normal ones (normal concentration is considered to be between 2-20 pM).

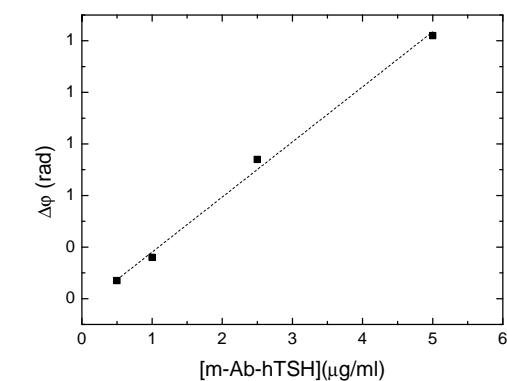
To achieve these detection levels a competitive assay was implemented on the  $\lambda$ M-BiMW. Another advantage offered by this assay format relies on the higher stability of the immobilized hormone with respect to an immobilized antibody, which allows a longer use of the bio-surface through multiple regeneration cycles.

For this experiment, a solution of hTSH 10  $\mu$ g/ml in PBS buffer is supplied to the silanized sensor surface previously activated with EDC/NHS. In order to ensure a complete surface coverage, the hTSH solution is injected twice.

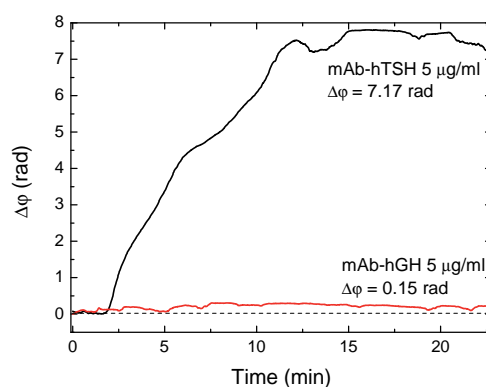
In the first part of the assay, the optimal concentration of antibody to carry on the competitive assay must be selected. For this reason different concentrations of specific antibody solutions in the range 0.5-5  $\mu$ g/ml are injected. Regeneration of the biosensing surface is achieved by an injection of an HCl solution (20 mM). In Fig. 6.9a we show the dose response curve corresponding to the detection of mAb-hTSH. According to these results we select an antibody concentration of 1  $\mu$ g/ml to carry on the competitive assay.

Figure 6.9b shows the detection of the specific mAb-hTSH 5  $\mu$ g/ml compared to the detection of a non-specific antibody (mAb-hGH) employed as a control. The contrast between the specific and non-specific detection of the same concentration (7.17 rad vs 0.15 rad) demonstrates the high-selectivity of the biosensor.

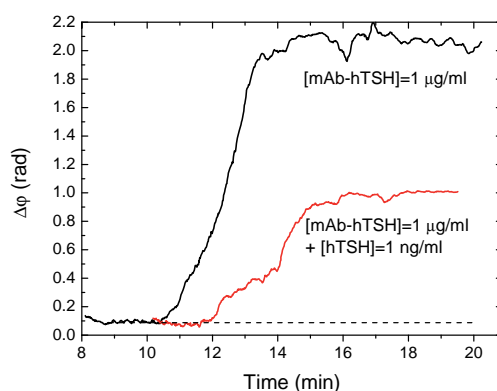
A solution of hTSH 1 ng/ml (20 pM) is incubated with the selected mAb-hTSH concentration and then supplied to the sensor. A net signal variation of 0.88 rad was produced, as shown in Fig. 6.9c, in contrast to the injection of the mAb-hTSH with no additional hormone, which resulted into a phase signal of 1.95 rad. These results validate the use of the  $\lambda$ M-BiMW biosensor for hTSH detection.



(a)



(b)



(c)

**Figure 6.9:** (a) Calibration curve for the detection of specific mAb-hTSH in the range  $0.5 - 5 \mu\text{g/ml}$ ; (b) specific detection of mAb-hTSH  $5 \mu\text{g/ml}$  and control signal (mAb-hGH  $5 \mu\text{g/ml}$ ) and (c) detection of hTSH  $1 \text{ ng/ml}$  through a competitive assay.

## 6.5 Conclusions

In order to demonstrate the biosensor capabilities of the wavelength modulated interferometric biosensors we chose a receptor immobilization strategy based on covalent binding of the bioreceptor via a silane layer. For this, a silanization procedure based on a water soluble silane, the CTES agent, has been described and experimentally applied, resulting in a versatile platform for different applications. The phase-modulated sensors allow a direct, real-time and unambiguous read-out, suitable for the detection of physiologically relevant concentrations, which generally induce very low sensor responses which cannot be directly quantified in the standard intensity interrogation method.

We demonstrated the sensitivity, selectivity and reproducibility of the biosensor devices, and as proof-of-concept for biosensing applications, the  $\lambda$ M-MZI shown a detection limit of 170 ng/ml for the immunoassay detection of anti-hGH. In the case of  $\lambda$ M-BiMW the validation as biosensor has been assessed through the monitoring of the immunoreaction BSA/anti-BSA. As clinical applications we selected the detection of CRP protein by using a direct immunoassay and the detection of hTSH hormone by a competitive immunoassay, resulting in limits of detection of 7 ng/ml and <1 ng/ml, respectively.



# Chapter 7

## Towards a lab-on-chip platform

In this chapter the integration of the interferometric bimodal biosensors into a stand-alone LOC platform for decentralized applications is discussed. The main requirements for the global design are presented and the individual components to be integrated are analyzed. Part of this work is realized with partner researchers, collaborating with our Group to achieve the complete integration of the BiMW sensors. In particular, we are working on the design, fabrication and characterization of an integrated polymeric network based on the polymer SU-8 with the Group of Structural Mechanics and Material Modeling (GEMM<sup>1</sup>, University of Zaragoza). The fabrication of the grating couplers is performed in the Clean Room facilities of the Institute of Photonic Sciences (ICFO<sup>2</sup>, Castelldefels (Barcelona)) by a partner collaborator, and we have a long-time collaboration with a partner group belonging to the Institute for Applied Microelectronics (IUMA)<sup>3</sup> (Las Palmas, Gran Canaria) with whom we are evaluating a possible novel optical read-out strategy for the microchip array.

### 7.1 Specifications and requirements

In a LOC platform all the functionalities required to perform an assay must be integrated in a compact format. This device must be user-friendly, in order to be operated even by non-trained personal, and must allow a fast result, employing a reduced amount of analyte and reagents. To fulfill these requirement, we propose a platform based on the integration of the interferometric BiMW biosen-

<sup>1</sup> [zar.es/datos/grupo/gemm-8](http://zar.es/datos/grupo/gemm-8) <sup>2</sup> <http://www.icfo.eu/> <sup>3</sup> <http://www.iuma.ulpgc.es/content/view/62/123/>

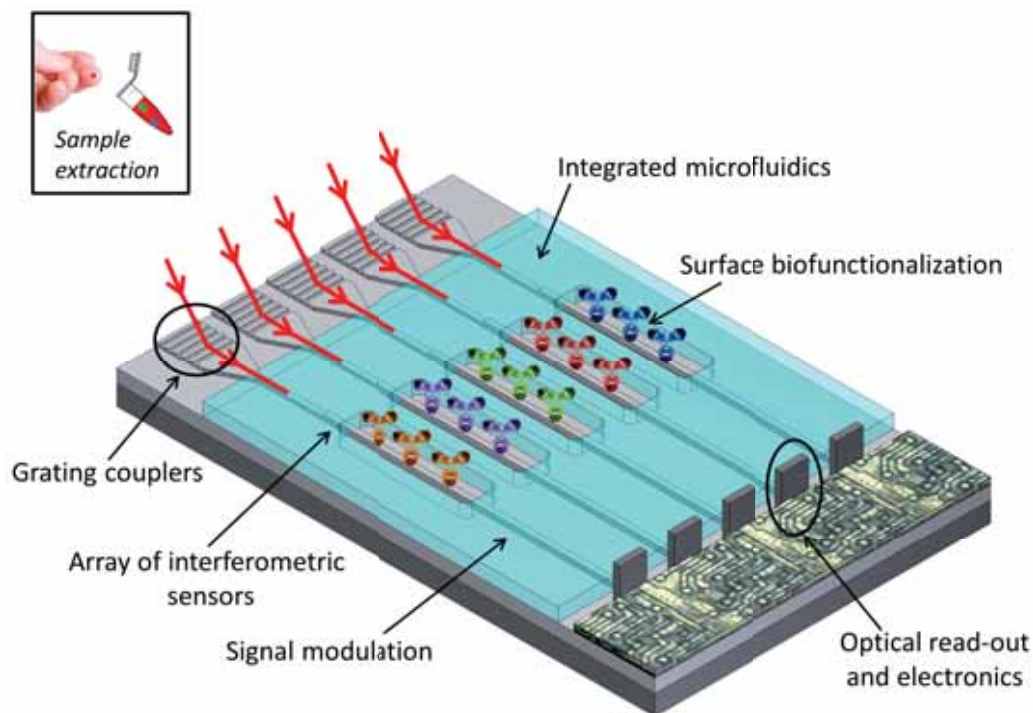


**Figure 7.1:** Envisioned LOC platform based on the integration of interferometric sensors.

sors characterized in this Thesis. The complete platform must include: i) the interferometric sensors in a multiplexed configuration, ii) the flow cells and the flow delivery system (microfluidics), iii) the phase modulation system developed in this Thesis, iv) the surface functionalization, immobilization and regeneration protocols for the receptor, v) the light sources and photodetectors, and vi) the processing electronics and final packaging. Figure 7.1 shows the envisioned LOC platform integrating an array of BiMW biosensors.

The choice of standard silicon processes for the sensor fabrication allows a complete integration with light sources, photodetectors and processing electronics. However for most biosensing applications a hybrid approach based on disposable cartridges, obtained by including points i) to iv), and on reuse of light sources, detectors and electronics will be preferred.



## 7.2 Light in-coupling by diffraction gratings

To obtain a compact, stable and user-friendly LOC platform, the light in-coupling must be efficiently solved, since coupling efficiency and alignment tolerance influence the device performance through the SNR. Standard end-fire method, based on the focusing of the incident light onto the waveguide entrance has shown its validity in laboratory optical benches. However it has important limitations for making portable devices as the requirement of precision alignment equipments and a poor tolerance to alignment deviations. Furthermore labor intensive polishing of the input facet or the use of an advanced cleaving system is mandatory to achieve a good coupling efficiency. In order to overcome these limitations, diffraction gratings couplers have been demonstrated as an excellent alternative in terms of suitability for integration and time stability [Taillaert et al., 2002, Vivien et al., 2006]. The use of surface grating couplers (GCs) overcomes the chip facet polishing and provides a direct access from the surface with an almost perpendicular incidence.

Despite a considerable work has been done for optimized design at telecommunication wavelengths (1310-1550 nm) [Taillaert et al., 2006, Van Laere et al., 2007, Maire et al., 2008, Vermeulen et al., 2010], few contributions have been dealing with gratings employed as couplers to photonic devices in the visible range, due to the stricter requirements on fabrication which cannot be achieved with standard photolithographic processes but require alternative approaches as Electron Beam Lithography (EBL), NanoImprint Lithography (NIL), deep-UV lithography or Focused Ion Beam (FIB) milling. Due to the dimensions of our interferometers and to the operating wavelength ( $\lambda = 633-660$  nm), the diffraction grating length  $L$  cannot exceed  $100\text{ }\mu\text{m}$  with a sub-micronic period. Furthermore, the design of gratings integrated with visible IO biosensors is conditioned by the sensing capabilities of the device, which impede the introduction of complex layer structures, as to provide bottom reflectors which would increase the coupling efficiency [Taillaert et al., 2002, Taillaert et al., 2006].

Taking into account these requirements, the diffraction gratings required to in-couple light to the BiMW biosensors are directly written on the silicon nitride layer by EBL. At the chip entrance the silicon dioxide cladding is removed from a specific region, defining the so-called grating window (2 mm length), enabling the insertion of the grating couplers [Duval et al., 2013].

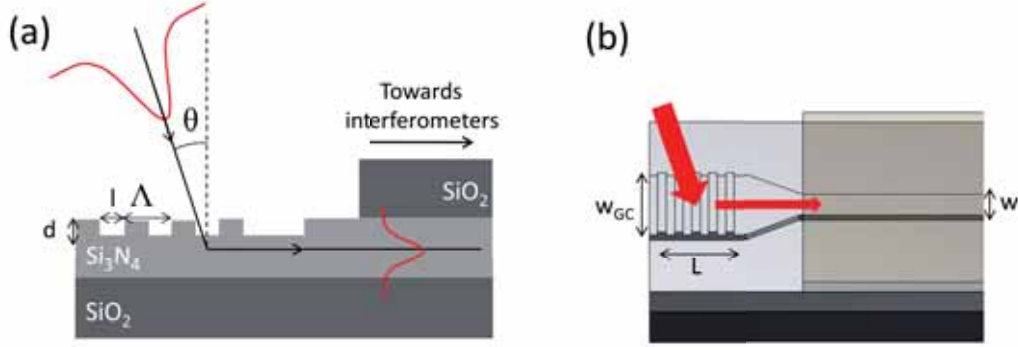


**Figure 7.2:** Scheme of the light in-coupling through diffraction gratings. (a) lateral cross-section and (b) perspective view of the impinging beam.

### 7.2.1 Design and fabrication

The resonant coupling between a waveguide mode and the beam impinging on the periodic structure is achieved when the phase matching condition:

$$\sin \theta = N_{eff} + m \frac{\lambda}{\Lambda} \quad (7.1)$$

is fulfilled, where  $\theta$  is the angle of incidence,  $N_{eff}$  the effective refractive index of the guided mode,  $\lambda$  the vacuum wavelength,  $\Lambda$  is the grating periodicity and  $m$  the diffraction order (here  $m=-1$ ). The grating parameters are indicated in Fig. 7.2.

The gratings were designed taking into account previous studies [Tamir and Peng, 1977, Brazas and Li, 1995, Taillaert et al., 2002] but without modifying the layer structure of the interferometric sensors MZI or BiMW, which had already been optimized for biosensing applications.

According to equation (7.1) the incidence angle can be set in the range  $5^\circ - 15^\circ$ , which should enable an efficient coupling and is compatible with the final LOC requirements. Indeed, for the implementation of a portable platform a minimum space should be occupied by the single components without disturbing each other. Taking into account these considerations, the grating periods were set between 400 and 450 nm with a duty cycle of 0.5. The duty cycle is defined as  $l/\Lambda$ , where  $l$  is the groove width of the grating and  $\Lambda$  its periodicity. Regarding the groove depth,  $d$ , partially etched gratings are preferred as they facilitate a reduction of the diffraction efficiency of the grating and, therefore, an increase of the coupling efficiency into the waveguide. We set a groove depth of 50 nm according to a

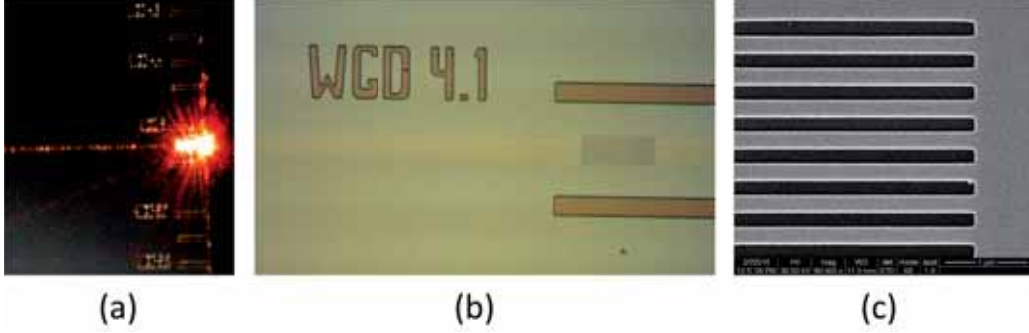


**Figure 7.3:** (a) Photograph of an excited grating and light propagating into the waveguide, (b) optical image of the grating coupler over the tapered waveguide and (c) SEM image of a 400 nm-period grating.

preliminary study performed for depths ranging from 25 to 100 nm.

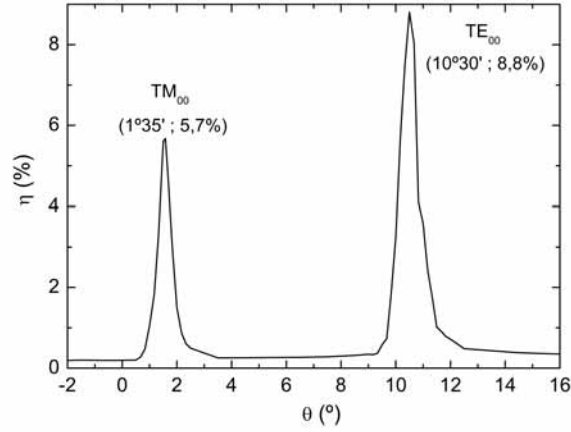
To increase the coupling efficiency, tapered waveguides were previously defined at the entrance of the grating window, with widths in the range 20-50  $\mu\text{m}$  that linearly reduce until reaching the interferometer waveguide widths (4  $\mu\text{m}$ ). The grating couplers are directly written on the  $\text{Si}_3\text{N}_4$  tapered waveguides, with a core thickness of 150 nm as required for the BiMW design. A poly(methyl methacrylate) resist layer is first patterned with electron beam lithography and the gratings are then transferred to  $\text{Si}_3\text{N}_4$  with the desired etch depth by reactive ion etching using  $\text{CHF}_3/\text{O}_2$  gas chemistry.

Figure 7.3 shows (a) an optical picture of the light in-coupling through a GC, (b) an optical image of GC written on the tapered waveguide and (c) a SEM image of the fabricated device with a 400 nm grooves periodicity.

### 7.2.2 Optical characterization

The grating couplers inscribed at the BiMW input were first characterized to determine the excitation angles and the coupling efficiency. Figure 7.4 shows the coupling efficiency experimentally measured, for a central wavelength  $\lambda = 660$  nm and a grating period  $\Lambda = 450$  nm. The maximum efficiencies have been evaluated as 5.7% and 8.8% for TM and TE polarizations, respectively, for resonant angles of  $1^\circ 35'$  and  $10^\circ 30'$  respectively.

The angle tolerance ranges from  $0^\circ 25'$  to  $0^\circ 45'$  at -3dB, resulting in an improved alignment tolerance with respect to the end-fire method commonly adopted [Duval et al., 2013].



**Figure 7.4:** Coupling efficiency at 660 nm as a function of the incident angle for a BiMW device excited through a grating coupler with period  $\Lambda = 450$  nm.

**Table 7.1:** Refractive index changes induced by a set of HCl solutions and corresponding phase changes evaluated on a BiMW excited via a grating coupler.

HCl concentration (M)	$\Delta n$	$\Delta\varphi$ (rad)
0.05	$6 \cdot 10^{-4}$	$0.91 \cdot 2\pi$
0.1	$1 \cdot 10^{-3}$	$1.89 \cdot 2\pi$
0.2	$2 \cdot 10^{-3}$	$3.89 \cdot 2\pi$
0.3	$2.9 \cdot 10^{-3}$	$5.66 \cdot 2\pi$

In order to verify the validity of the grating couplers as alternative to the standard end-fire method, a bulk calibration was performed to assess the device sensitivity and limit of detection. A set of HCl solutions in the range 0.05 M to 0.3 M are sequentially supplied to the sensor surface and the corresponding sensor responses are evaluated. Table 7.1 shows the refractive index changes for each HCl solution and the corresponding phase variations evaluated from the  $S_R$  output evolution. The resulting calibration curve can be seen in Fig. 7.5, together with the sensor response for the different HCl solutions employed.

According to the experimental results of Fig. 7.5, a bulk sensitivity of  $2050 \cdot 2\pi$  rad/RIU was evaluated. With a standard deviation of the baseline signal  $\sigma = 0.042$  %, the corresponding phase resolution is  $\Delta\varphi_{min} = 3.9$  mrad, corresponding to a limit of detection of  $\Delta n_{min} = 3.3 \cdot 10^{-7}$  RIU. This detection limit is comparable

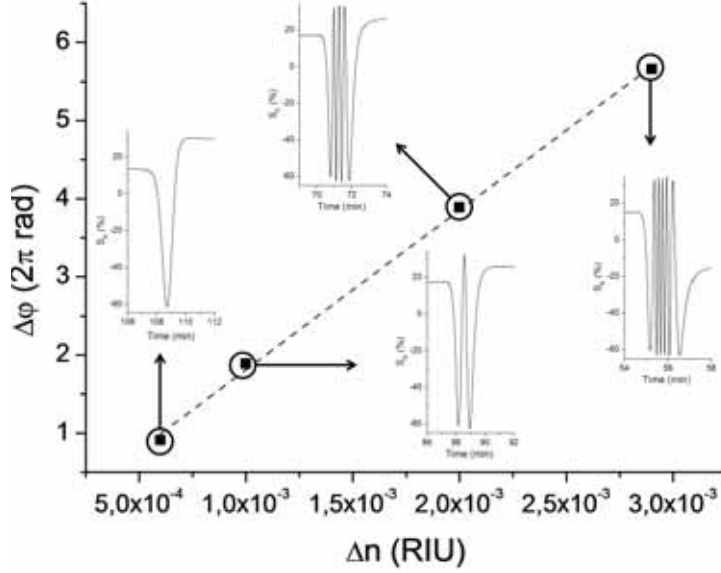


**Figure 7.5:** Calibration curve obtained with a BiMW excited via a grating coupler (TE polarization,  $\Lambda = 450$  nm).

with the results achieved with the He-Ne laser source in the end-fire coupling arrangement (see section 3.6), but has been achieved with a pigtailed laser diode source, demonstrating the validity of the grating in-coupling method.

### 7.2.3 Wavelength dependence

In order to verify the compatibility of the proposed wavelength modulation approach and the light in-coupling through grating couplers, the chromatic dispersion introduced by the grating has been experimentally analyzed. As a consequence of Eq.(7.1), a decrease of the resonant angle is expected for increasing wavelengths in the working range ( $\lambda_0 = 656\text{--}660$  nm) for the considered waveguide geometry. This variation of the resonance condition can result in an additional amplitude modulation superposed to the desired phase modulation.

To assess only the amplitude modulation effects introduced by the grating, a single-mode waveguide has been analyzed (i.e. no phase modulation effects). The first step consists in evaluating the effects of a variation of the incident wavelength on the angular transmission curves of the grating coupled waveguide. For this, we considered a 400 nm-period grating inscribed over a 200 nm-core waveguide, with an initial taper width of 20  $\mu\text{m}$ . We use the pigtailed laser source LP660-

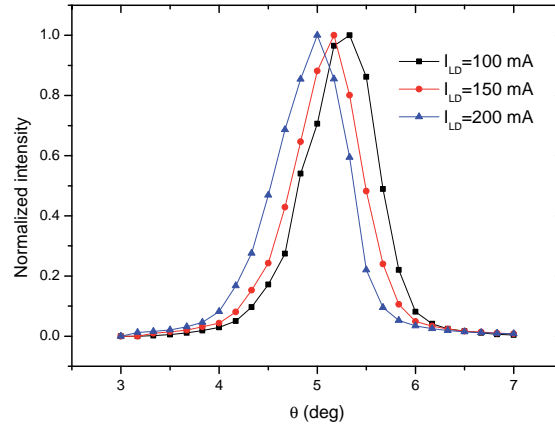


**Figure 7.6:** Grating transmission for different laser injection currents (wavelengths).  $\Lambda = 400$  nm, TE polarization.

SF60 and its incidence angle over the chip surface is controlled by a goniometer (GNL10/M, Thorlabs,  $10^{-2}$ -resolution). The grating response has been evaluated over the range 657.5-659.5 nm, where the BiMW sensors are usually interrogated, by considering injections currents in the range 100-200 mA (compare with spectra included in Table 4.1). The corresponding transmission curves are shown in Fig. 7.6. As expected, the maximum in the transmission curves is slightly increased for increasing wavelengths. We obtained maximum coupling efficiency at angles of  $5^\circ$ ,  $5^\circ 10'$  and  $5^\circ 20'$  for the currents of 100, 150 and 200 mA, respectively. Therefore an angular variation of only  $20'$  is observed for a variation of the incident wavelength of 2 nm.

Then, we performed the quasi-static modulation approach, consisting in the evaluation of the waveguide output power as a function of the incident wavelength, for a fixed incidence angle. Different incidence angles around the value corresponding to the maximum coupling efficiency ( $5^\circ$ ) have been tested, and the corresponding curves are shown in Fig. 7.7(a). All the curves show a similar trend with an almost linear increase till the resonant wavelength is achieved and then a decrease in the output intensity.

By taking into account the intrinsic power-wavelength variation of the laser diode source, the curves shown in Fig. 7.7(a) can be normalized, resulting in the curves included in Fig. 7.7(b).

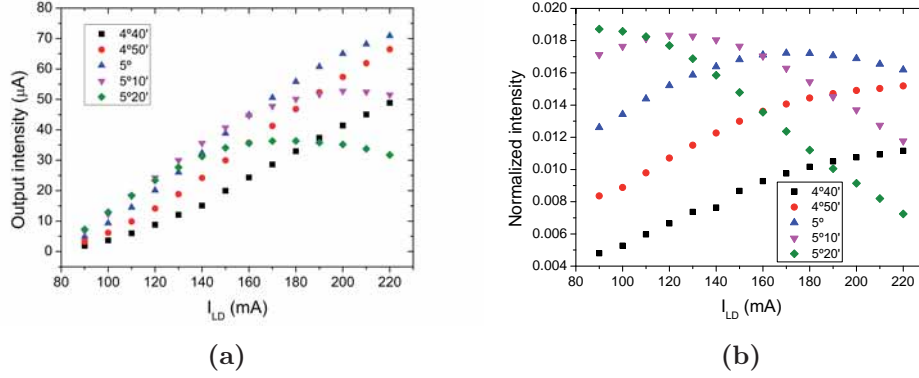


**Figure 7.7:** (a) Quasi-static approach for a 200 nm waveguide for different incidence angles and (b) normalized waveguide output after grating assisted light in-coupling. TE polarization.

The effect of the grating coupler for a small wavelength variation is traduced into an additional amplitude modulation which sums up or can even compensate the intrinsic laser source power variations, according to the selected excitation angle.

Once verified the quasi-static effects of a wavelength variation on the grating efficiency, we investigated the dynamic wavelength modulation approach. For this, we monitored the waveguide output when a sinusoidally varying injection current was supplied to the laser diode source. The waveguide with 200 nm core, excited through a 400 nm-period GC at  $\theta = 5^\circ 30'$  was interrogated with a laser current variation  $\delta I_{LD} = \pm 41$  mA, for TE polarization. As shown in Fig. 7.8 a sinusoidal response is achieved in response to the sinusoidal input modulation. An increase in the laser current modulation depth leads to an increase of the output oscillation range, implying that no distortion takes place as a consequence of the grating assisted light in-coupling.

Finally we have tested the dynamic wavelength modulation approach on the grating coupled BiMW sensors. For this we have considered a grating with periodicity  $\Lambda = 450$  nm, a working wavelength  $\lambda_0 = 660$  nm and TE polarization. Preliminary results show that the signal harmonics can be correctly retrieved, as shown in Fig. 7.9, where we plot the time-evolution of the output signal harmonics corresponding to the detection of an index change  $\Delta n = 6 \cdot 10^{-4}$ , for a laser current variation  $\delta I_{LD} = \pm 61$  mA. Despite the use of the maximum current modulation allowed by the experimental set-up, the modulation set-point cannot

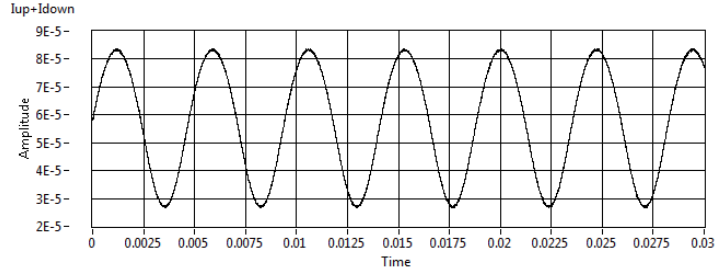


**Figure 7.8:** Intensity modulated waveguide output for an input modulation depth  $\delta I_{LD} = \pm 41$  mA.

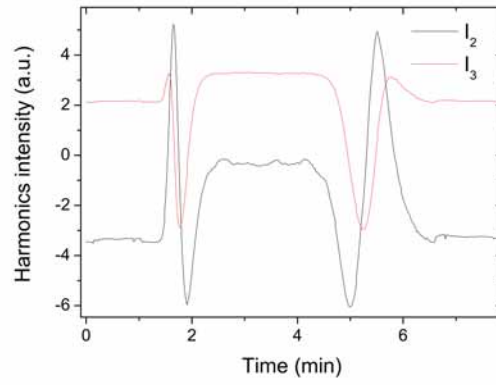


**Figure 7.9:** Harmonics time-evolution for the detection of an index change  $\Delta n = 6 \cdot 10^{-4}$  on a  $\lambda$ M-BiMW sensor excited through diffraction grating.

be reached due to the thickness of the bimodal waveguide (330-340 nm) and the operating wavelength ( $\lambda = 660$  nm).

Work is in progress to complete the characterization of grating-coupled sensor chips belonging to families i) and iii), where the modulation working point can be experimentally achieved.

### 7.3 Multiplexed sensor schemes

One of the requirements for a complete LOC platform is the capability to simultaneously detect several analytes from a same sample, in order to reduce analysis time and reagents volume. For this reason a multiplexed platform has to be de-



veloped, where different bioreceptors are immobilized on the same chip to address different target molecules.

For that, different approaches can be adopted for the light distribution to the sensor array. Two main design configurations can be defined as: i) a single input waveguide for each element of the sensor array or ii) a single input waveguide to address multiple sensors through power division. Care must be taken in the power splitting design to ensure a satisfactory SNR for the sensors. For strategy ii) power divisors (i.e. Y-branching, directional couplers or MMIs) can be designed to distribute the optical power to the different sensors. For example we designed a cascade of two Y-junctions to achieve the light coupling into two parallel MZI biosensors, as shown in Fig. 7.10(a). The aperture angles of the three Y-junctions are equal in order to split uniformly the power into the four arms and an S-shape divisor was chosen to minimize the bend losses along the structure. These structures have been fabricated at our Clean Room facilities and experimentally characterized. Work is in progress to design alternative methods for power splitting to achieve a higher number of output waveguides without compromising the final chip length.

The two general multiplexed configurations can then be implemented with grating assisted in-coupling or direct coupling through the polished end-facet. Figure 7.10 shows the two strategies in the case of grating assisted in-coupling: in Fig. 7.10(b) an array of gratings is fabricated at the chip entrance, to allow in-coupling of the source beam into each sensor waveguide, while in Fig. 7.10(c) a single light beam is shined over a single grating and later distributed to multiple sensors, five in this example.

Once fixed the multiplexed platform design, the light in-coupling can be achieved in different ways. For example if choosing strategy i) and the use of grating couplers, the excitation of light propagation can be achieved by using an array of laser sources, each one addressing a single grating, or with a single source beam impinging on multiple gratings, or with a single laser source which is sequentially scanned over the grating array. Similarly, if choosing the in-coupling through the polished end-facet different methods can be adopted as a sequential scan of a single laser source, or the use of an array of laser sources, or a fiber array unit (FAU).

In the context of strategy i), where each sensor is fed from a single waveguide, and choosing a butt-coupling approach, we have achieved the light in-coupling to four adjacent sensors by employing a FAU, constituted by 8 single-mode polarization maintaining optical fibers placed at a distance of  $250\text{ }\mu\text{m}$  over a V-groove support, which matches the lateral separation ( $250\text{ }\mu\text{m}$ ) between two adjacent

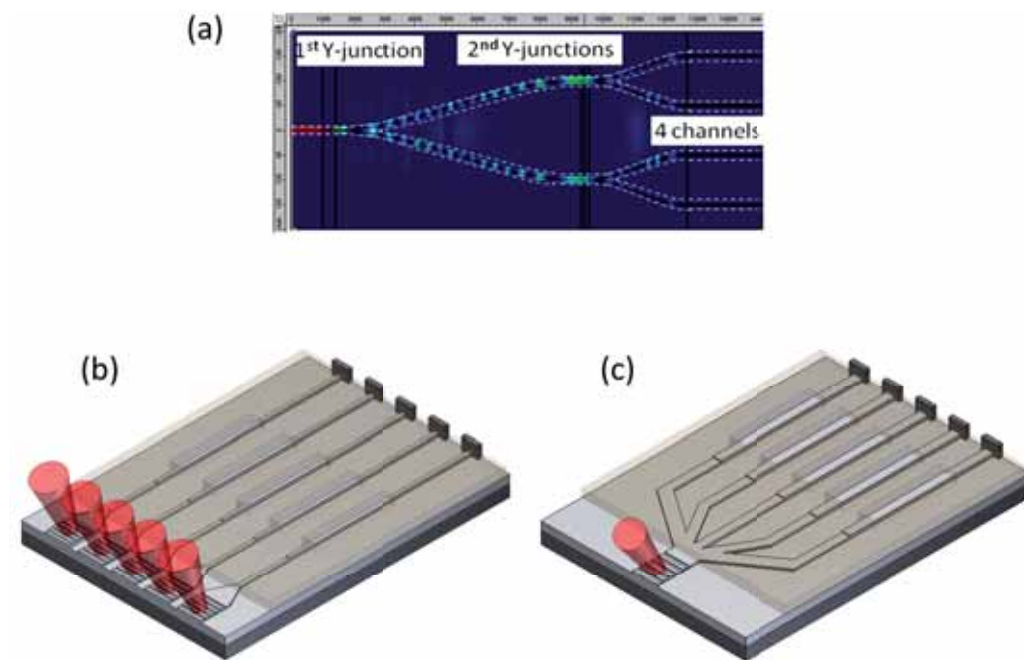


**Figure 7.10:** (a) Multiplexed MZI sensor, consisting in the cascade of 2 Y-junctions to achieve power splitting and schemes for the BiMW multiplexed platform based on grating coupler excitation: (b) each sensor of the array has a single input waveguide and (c) a single input waveguide addresses multiple sensors in the array.

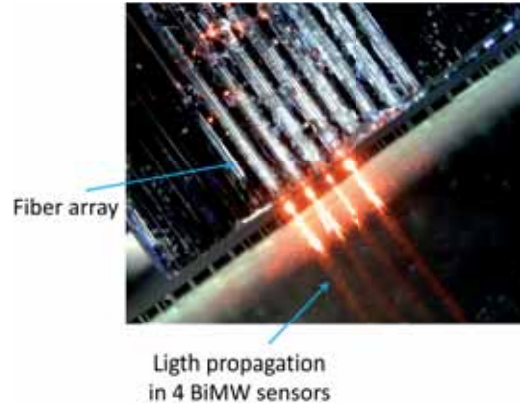


**Figure 7.11:** Light in-coupling into four BiMW sensors through a fiber array unit ( $\lambda_0=635$  nm).

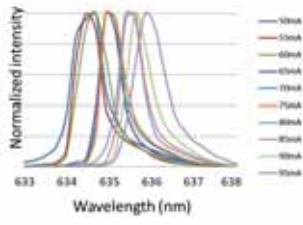
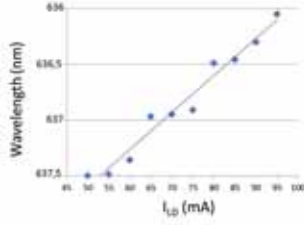
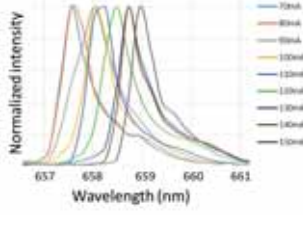
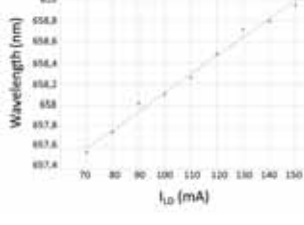
interferometric sensors. The four required fibers are connected to a commercial 4-output laser source (MCLS635, Thorlabs,  $\lambda_0=635$  nm). Figure 7.11 shows a picture of the light in-coupling and propagation in a group of four BiMW sensors as a proof-of-concept of this method.

To fulfill the integration with the wavelength modulation system, we have considered different commercial fiber sources, but at the moment none of them satisfied the requirements of single-mode behavior and sufficient wavelength excursion. Table 7.2 reports the emission spectra of two different laser sources, namely the MCLS1-635 and MCLS1-660 (Thorlabs), operating at  $\lambda_0=635$  nm and 660 nm, respectively. As it can be observed from the spectra and the wavelength-current curves shown in Table 7.2, the first laser diode, the MCLS1-635 laser, is strongly affected by mode-hopping, resulting in abrupt jumps in the wavelength-current curve, while the second diode, the MCLS1-660 laser, shows a more linear wavelength-current response, however its working range is very limited ( $\approx 1.2$  nm in static conditions). Further commercial solutions are currently under evaluation.

## 7.4 Surface biofunctionalization

Multiplexed detection allows to simultaneously study different analytes on a same sensor chip. To achieve this goal, different bioreceptors must be efficiently immobilized on the different sensors constituting the array. Due to the reduced dimensions of the interferometric sensing areas ( $50\text{ }\mu\text{m}$  width) and the distance between adjacent sensors (pitch =  $250\text{ }\mu\text{m}$ ), nanodeposition equipment can be used in order

**Table 7.2:** Comparison of the emission spectra for different fiber coupled laser sources and corresponding wavelength-current curves.

Laser diode	Normalized spectra	Emission wavelength vs current	$d\lambda/dI_{LD}$ (nm/mA)
MCLS1-635			0.033
MCLS1-660			0.017

to achieve the immobilization of different receptors on neighboring sensors.

For example the NanoeNabler<sup>TM</sup> system (BioForce Nanosciences, USA)<sup>4</sup> allows the deposition of attoliter to picoliter volumes of liquid with a high degree of spatial accuracy (20 nm). The working principle of the platform is based on a microcantilever, similar to those employed in standard Scanning Probe Microscopy techniques, which is integrated with a passive microfluidic system [Korostynska et al., 2008]. Receptors to be deposited are previously loaded into the cantilever reservoir with a pipette and later released when the cantilever tip contacts the sensor surface. The volume of the deposited drops depends on the contact time and applied force between the cantilever tip and the surface.

The biofunctionalization protocol involves an ex-situ silanization, and eventually activation, of the sensor chip surface, followed by the receptor immobilization which is performed with the BioForce tool. After the deposition, the bioreceptor solution is left for incubation for 1 hour, in a chamber with controlled humidity to avoid the evaporation of the small volume drops. For the same reason, glycerol is normally added to the bioreceptor solution to be patterned.

Figure 7.12 shows the top side of the microcantilever when spotting the two

<sup>4</sup> <http://nanob2a.cin2.es/biodeposition-unit>

sensing areas of a double-MZI sensor. The center-to-center distance of two sensing areas is  $200\ \mu\text{m}$ .

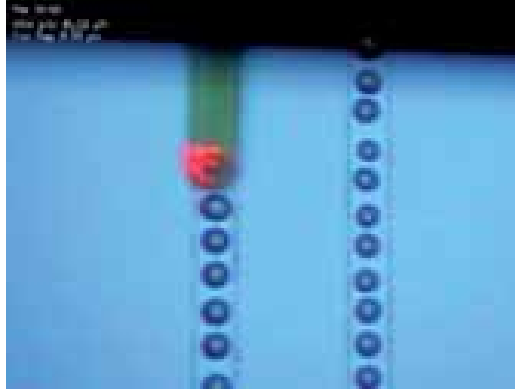


**Figure 7.12:** Bioreceptor deposition over the two sensing areas of a double-MZI sensor by employing the BioForce deposition platform.

## 7.5 Microfluidics

For some applications the use of an external platform and the time-consuming protocols required to achieve a localized receptor immobilization constitute a limitation. For this reason alternative immobilization techniques must be implemented to increase the analysis throughput and avoid the use of external equipments. A possible solution comes from the use of individual fluidics channels to address each sensor of the chip array.

For this reason we decided to implement a SU-8 microfluidic network to address the 16 BiMW sensors fabricated on each chip. The fluidic network is fabricated at wafer level, resulting in the reduction of the manufacturing times and final costs. Sample volume and flow rate are critical parameters especially for clinical testing, which must be addressed with careful design of the channels size, dimensions and arrangement over the sensor array. According to previous studies [Blanco et al., 2006], the channels were designed with dimensions of  $100\ \mu\text{m}$  width,  $50\ \mu\text{m}$  height and a length of 15 mm, to completely cover the BiMW sensing area [Duval et al., 2012]. The schematic process flow for the fabrication of the integrated micro-fluidic network is depicted in Fig. 7.13.

The SU-8 biocompatible polymer is spin-coated on top of the sensor wafer in two sequential steps consisting on polymer spinning and soft-bake, to achieve a

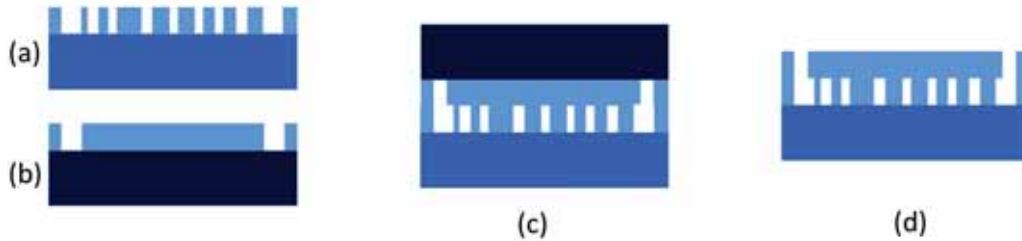


**Figure 7.13:** Fabrication flow for the definition of micro-fluidics channels on top of the BiMW sensors array.

final thickness of 50  $\mu\text{m}$ . This layer is then patterned by UV photolithography ( $\lambda_0=365\text{ nm}$ ) to form individual channels on top of each sensing area, with a width of 100  $\mu\text{m}$  (Fig. 7.13(a)). Since any debris left on the sensor surface will dramatically affect the resolution of the optical sensor, an oxygen plasma step is performed to ensure complete cleaning of the area. AFM inspection of the patterned chips showed that 1 hour plasma treatment is required to completely remove the SU-8 residues.

In parallel, another SU-8 UV photo-lithographic process is performed on top of a Pyrex-Kapton substrate in order to close the previously defined channels and to define the microfluidic inlet/outlet (subfigure (b)). Then the patterned wafers are aligned and bonded together to form the 3D embedded microchannel structure, using a pressure of 3 bars at 90°C for a 30 min time interval, ensuring that a stable bonding is achieved, without deforming the channels topography (7.13(b)). Finally the Pyrex substrate is manually released, leaving the patterned channels over the silicon sensor chip (subfigure (d)).

Due to the high density of microchannels on the chip, the device and the packaging were designed to use one dedicated inlet for each microchannel, but a common outlet for every group of four sensors, as shown in Fig. 7.14. Figure 7.14(a) shows the complete SU-8 microfluidic network including 16 independent channels; 7.14(b) represents the separate inlets, while 7.14(c) shows the common outlet. With this approach only 20 fluidic connections, instead of 32, are required between the chip and the external packaging. The external microfluidic connection is done by standard fluidic connectors and O-rings, ensuring a perfect sealing. The complete platform is shown in 7.14(d).

Experimental results have shown that the plasma treatment applied for cleaning of the sensing areas (1 hour duration for optimal results) was affecting the bonding strength. However it was possible to achieve the same results by applying

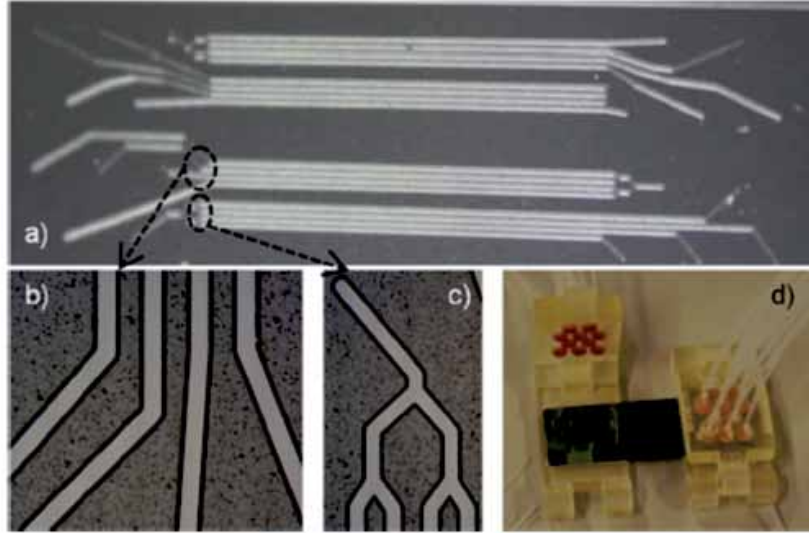


**Figure 7.14:** Optical images of the 3D SU-8 microfluidic network: (a) BiMW chip with 16 channels, (b) individual inlets for a group of four sensors, (c) common outlet for a group of four sensors and (d) final encapsulation.

two separate plasma treatments, one when the channels are still open (compare with Fig. 7.13(a)) and another one at the end of the process, corresponding to Fig. 7.13(d). As it can be seen in Fig. 7.15 if polymer residues are present the sensor surface shows certain topography surface undulations, as shown in panel (a). After a double plasma treatment of 30+30 min the silicon dioxide is completely clean and the topography oscillations measured in the first case are eliminated (see panel (b)). After this treatment the surface roughness is comparable to the one of a freshly prepared PECVD  $\text{SiO}_2$  surface, included for comparison as panel (c).

Work is in progress to complete the integration of the fluidic network onto the fabricated BiMW sensors. Next steps will involve the optimization of the surface bio-functionalization protocols for in-flow immobilization of different bioreceptors in each channel.

## 7.6 Optical read-out and electronics

For the interrogation of a single BiMW sensor, commercial two-sectional photodetectors are required in order to monitor the spatial variations of the output power



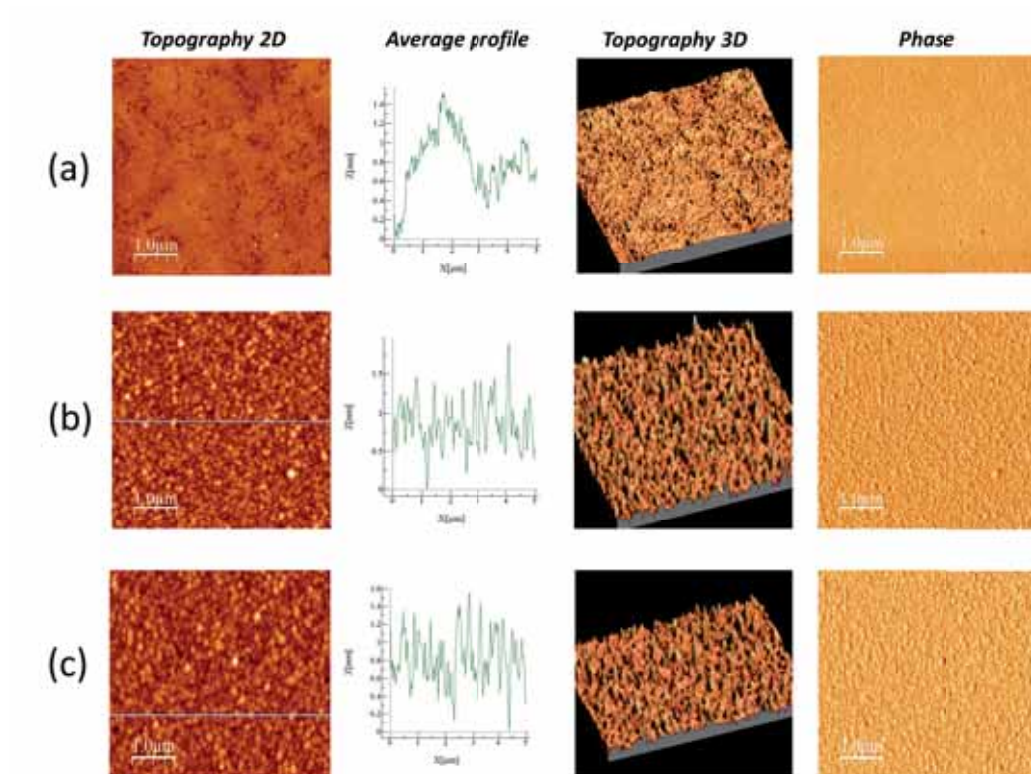


**Figure 7.15:** AFM analysis of the chip surface during channel fabrication. (a) 30 min plasma treatment, (b) 1 h total plasma treatment (2 steps) and (c) reference dioxide surface.



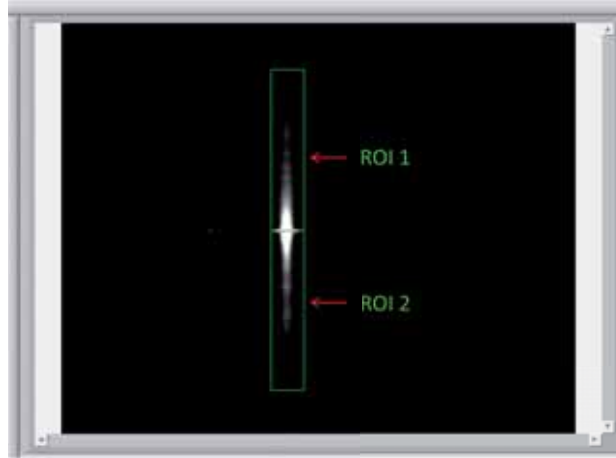


**Figure 7.16:** Definition of the two regions of interest necessary for the detection of the BiMW output by CCD camera.

distribution, which depends on the phase difference between the two propagating modes. To achieve a multiplexed detection, the same principle of two-sectional detector must be extended to an array concept. In the sensor chips, 16 interferometers are available, with a center-to-center distance of  $250\ \mu\text{m}$ .

After a commercial survey, no commercial solution based on photodetectors arrays with the required characteristics of array pitch and sensing area dimensions was encountered. For this reason, alternative detection approaches have been considered.

**CCD cameras** offer a viable solution for the intensity-interrogated sensor array, since the image area can be divided into customized Region Of Interests (ROIs) in correspondence of each BiMW sensor output, mimicking the two sections of the standard photodetector, as shown in Fig. 7.16. For multiplexed detection, an array of dual ROIs can be easily implemented and the simultaneous data acquisition from the different sensors can be achieved in the Labview environment.

Previous studies performed with the MZI biosensor shown that, after optimization of the ROI dimension and exposure time, a resolution comparable with the standard photodetector can be achieved using the CCD method. Figure 7.17 shows a comparison between the signal variations induced by a HCl solution 0.2 M flown on the sensing area of a MZI sensor, detected with the standard Si-photodetector (7.17(a)) and with the CCD camera (7.17(b)). The SNR have been

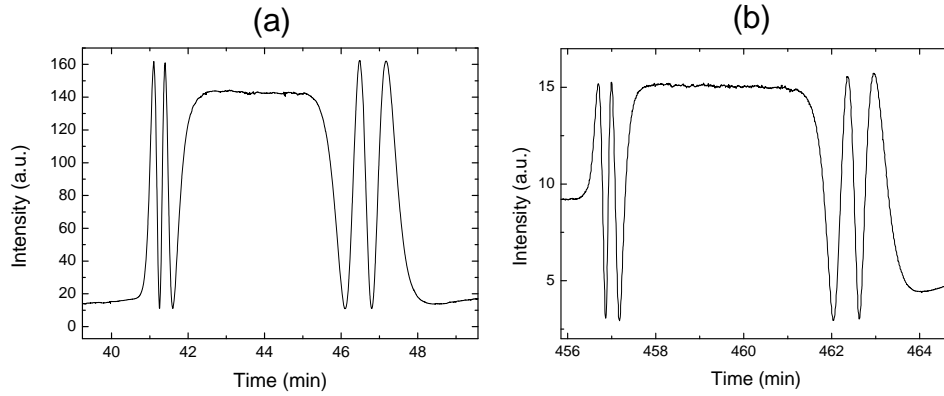


**Figure 7.17:** Comparative detection of a bulk index change on a MZI sensor by (a) standard Si-photodetector and (b) CCD camera.

computed as  $8.72 \cdot 10^{-4}$  and  $10.2 \cdot 10^{-4}$  in the case of Si-photodetector and CCD approach, respectively, validating the use of commercial CCD cameras as alternative detection method.

However the moderate acquisition rate of commercial CCD devices (max 60 frames per second for the DCU223M currently employed) will impede the integration with the phase modulation approach.

Based on commercially available Si photodiode array, as the S4111.35Q provided by Hamamatsu photonics<sup>5</sup>, a **customized photodetector array** can be purchased with the required array elements and pitch size. Due to the waveguide distribution on the currently available BiMW sensor chips, uniform arrays of  $28 \times 2$  elements must be designed. Final dimensions of the packaging (PCK) will vary between  $23 \times 10 \text{ mm}^2$  and  $50.8 \times 15.1 \text{ mm}^2$ . Our customized photodiode array will be similar to the commercial Si photodiode array configuration presented in Fig. 7.18(a), consisting of  $16 \times 2$  elements, and will be hybrid integrated at the output of the sensor chip, as schematically shown in Fig. 7.18(b).

To overcome the limitations of commercial solutions and to avoid the high costs of a customized design through external factories, an alternative solution comes from the use of *Configurable Quadrant Photodetectors (CQDs)*. This innovative solution is based on a matrix of  $20 \times 20$  photodetectors, similarly to standard photodiodes arrays. Through a digital configuration the device electronically gathers

<sup>5</sup> <http://www.hamamatsu.com>

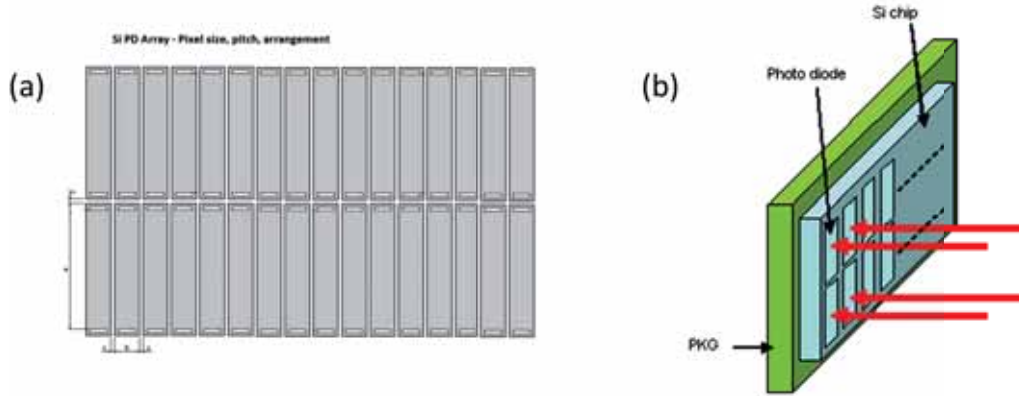


**Figure 7.18:** Customized photodiode array based on (a) commercial  $16 \times 2$  configuration and (b) schematic view of the detector array to be hybrid integrated at the sensor chip output.

a set of neighbor photodetectors, creating a virtual photodetector of the desired size. This control of the photodetector element numbers and size allows to define a *virtual* array of two-sectional detectors aligned to the output spot of the BiMW sensor array.

A preliminary design of the CQD was fabricated through standard  $0.35 \mu\text{m}$  AMS C35OPTO process, where each sensor has an area of  $75.8 \times 75.8 \mu\text{m}^2$ . Images of the CQD architecture, fabricated chip and testing instrumentation are shown in Fig. 7.19.

The CQD chip will be hybrid integrated at the output of the BiMW chip. Work is in progress for the second generation of CQD, especially designed for the BiMW sensors. Smaller pixel area, higher number of elements and denser communication buses are required for this case.

At this moment no ideal solution was underlined for the multiplexed detection of the BiMW sensor array. The selected detection approach will depend on the final application (costs, required resolution, etc).

## 7.7 Multiplexed biosensing

Adopting the CCD detection approach, where a customized number of ROIs can be easily defined and the final costs are reduced, we demonstrated a proof-of concept of the multiplexed biosensor platforms.

In particular, by employing the multiplexed MZI structure previously de-

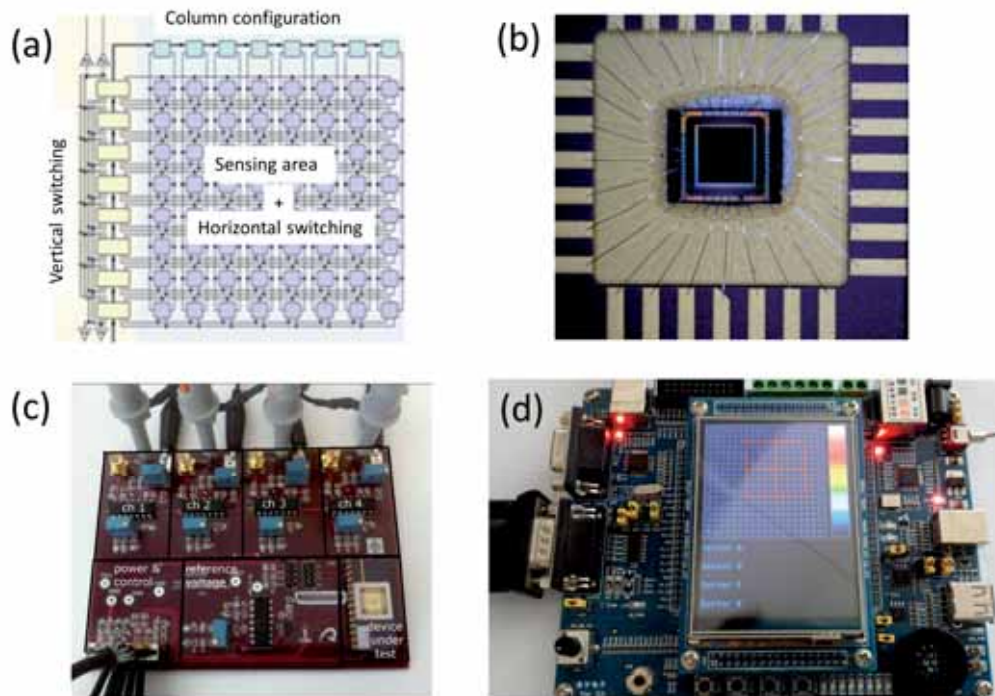


**Figure 7.19:** Configurable Quadrant Sensor (a) architecture, (b) picture of fabricated die and connections, (c) test platform and (d) virtual quadrant detector configuration.

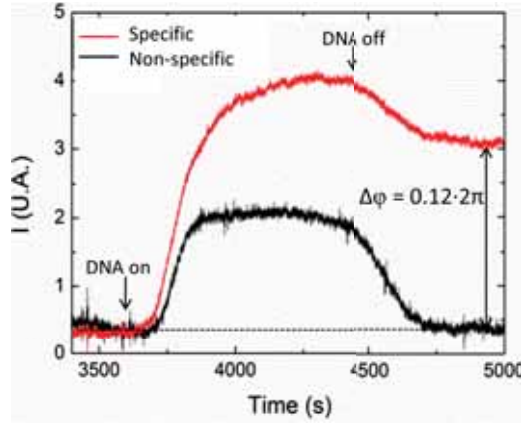


**Figure 7.20:** Detection of a concentration 50 nM of DNA target on one MZI sensor in a double-MZI arrangement.

scribed, we have demonstrated preliminary multiplexed detections of DNA hybridization. The light in-coupling is achieved with standard end-fire method, employing a He-Ne laser as source. The Labview application allows to simultaneously acquire the output from the two interferometers and their evolution is monitored in real-time.

The chips are silanized ex-situ with (3-Mercaptopropyl)trimethoxysilane (MP-TMS), following the protocol detailed in [Zinoviev et al., 2008] and two different DNA receptors are immobilized on the two sensing areas with the BioForce deposition tool. The fluid delivery is done with a single fluidic channel addressing the two sensing areas. When a sample solution containing only the target for one receptor specie is supplied to the sensors, only one of the two interferometers will show a variation of the output signal, while the other is unaffected.

In Fig. 7.20 we show the multiplexed MZI response when a sample containing only one target is supplied. The specific sensor response to a target concentration of 50 nM corresponds to a net signal variation of  $0.12 \cdot 2\pi$  rad. As we can notice no appreciable signal variation is observed on the second MZI, where a non-specific receptor was immobilized.

In the case of BiMW sensor array, we have demonstrated the feasibility of simultaneous detection of four integrated sensors, when they are excited with a single laser beam impinging on an array of four grating couplers. A fiber pigtailed laser source ( $\lambda = 660$  nm) is employed and the output light is collected with a

20 $\times$  objective before being imaged on the CCD screen. Through the Labview application 4 $\times$ 2 ROIs must be defined, as shown in Fig. 7.21(a).

Figure 7.21 shows the time evolution of the sensors output signal in response to a bulk refractive index variation. Work is progress with a new generation of chips to improve these preliminary results.

## 7.8 Conclusions

The first steps towards the implementation of a compact LOC platform based on the highly sensitive interferometric biosensors have been demonstrated. The integration of all the elements is non-trivial, since they must coexist in a minimum of space without interfering.

We have demonstrated efficient light in-coupling through diffraction gratings directly written at the waveguide input, resulting in a higher alignment tolerance with respect to traditional end-fire method. The compatibility of the grating assisted light in-coupling and the phase modulation approach has been preliminary validated, however further experiments with a new generation of chips immune to the critical behavior are required for a complete characterization.

We have presented different solutions for multiplexed biosensing and a method for a multi-receptor immobilization, performed with an auxiliary nanodeposition platform. To have independent access to any sensor in the chip array and to take full advantage of the multiplexing capabilities of the platform, we are working on the integration of a SU-8 microfluidic network on the sensor array.

Since no commercial solution is available, different alternatives have been considered to achieve a multiplexed read-out, involving the use of cost-effective CCD camera, customized Si photodiode array and a novel architecture based on configurable quadrant detectors.

Adopting a detection strategy based on CCD cameras, we have presented preliminary experimental results of multiplexed detection for both MZI and BiMW biosensors.

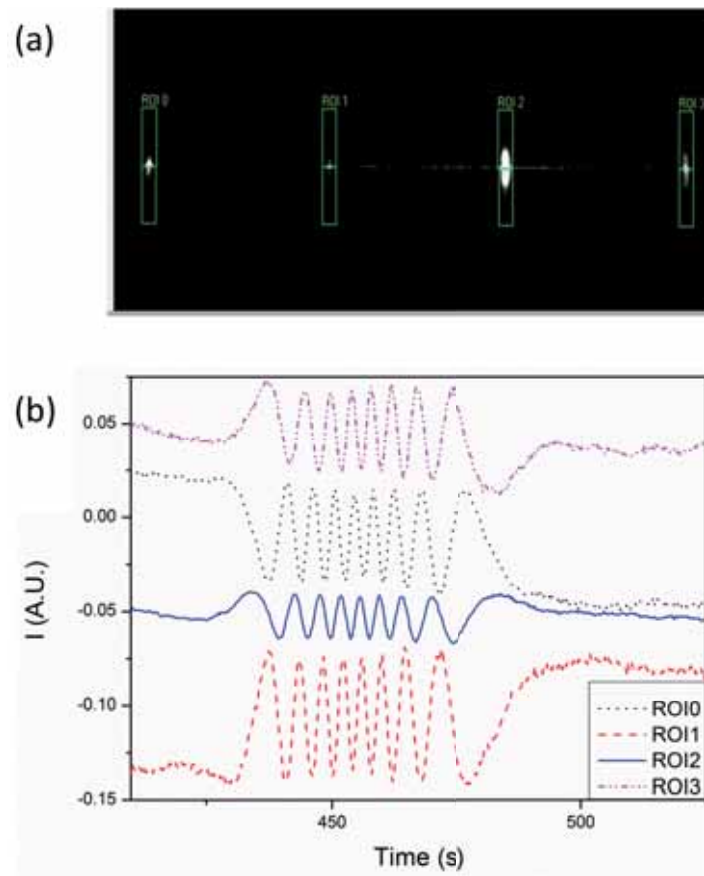


**Figure 7.21:** (a) CCD image showing the output of four BiMW sensors, with the corresponding dual-ROIs and (b) time-variation of the BiMW output signal in response to a variation of the sensing area refractive index.





## General conclusions and future perspectives

Optical biosensors based on interferometric arrangements have demonstrated superior capabilities in terms of sensitivity and limits of detection with respect to other transducers. However the complexity of their read-out still prevents their successful commercialization and their application in the clinical practice. The traditional intensity-interrogation approach is limited by the periodicity of the output signal with the phase variations, which impede a direct and non-ambiguous read-out.

In order to solve these limitations a simple, reliable and cost-effective phase modulation system has been demonstrated in this Thesis to achieve a direct, real-time and unambiguous read-out. This technique is based on the introduction of a periodic phase modulation by varying the wavelength of the incident laser beam and can be implemented by using compact and cost-effective laser diodes, replacing the He-Ne laser source. The drawbacks relative to the periodic nature of the interferometric output are therefore solved without the need of any additional fabrication processes or external equipment. The proposed wavelength modulation method can be extended to all integrated interferometric arrangements once assessed the modal dispersion relations of the specific interfering modes.

The method has been tested for two different interferometric configurations: the Mach-Zehnder and the Bimodal Waveguide interferometers. The MZI is well-known from the telecommunication area and was previously developed in our Group, demonstrating highly sensitive detections. As an alternative, the BiMW biosensor was introduced since its simplified geometry allows improved fabrication tolerances and eliminates the lateral beam recombination which affects the MZI

performance. In the case of the BiMW sensor two modes of different order are allowed to propagate along the same straight waveguide. The indirect excitation of the two modes is achieved by a variation in the core thickness, after the fundamental mode is injected at the device input. Moreover the normalized nature of the BiMW output signal  $S_R$  allows to compensate for input light power fluctuations, avoiding false positive signals which are unacceptable in the clinical practice. The devices are fabricated at wafer level in our Clean Room facilities using silicon-based technology and employing standard processes of optical lithography and etching, resulting in 200 sensors on each processed 4-inches wafer.

Characterization of the BiMW sensors has been done in a standard optical bench, consisting of a visible light source, photodetectors and temperature controller. The delivery of liquid samples over the sensor area was possible using a multi-channel PDMS cell previously fabricated, which allows the sequential measurements of four different sensors across the same chip. For bulk refractive index detection, the BiMW showed limits of detection in the range of  $10^{-7}$  RIU, competitive with state-of-the-art label-free biosensors.

Silanization methods have been applied to the wavelength modulated interferometric sensors and the biosensor capabilities have been demonstrated by the detection of the specific immunoreaction of different analytes as BSA, CRP protein and hTSH hormone at picomolar level, validating the versatility of the platform and of the silanization strategy. Further experiments will be focused on the detection of target molecules in real samples and extending the applications towards DNA, RNA and bacteria detection.

In order to achieve a compact platform for decentralized clinical applications, the so-called LOC platform, grating couplers have been integrated at the input of the interferometer waveguides, resulting in improved setup compactness and tolerance to mechanical displacements. The diffraction gratings are directly written at chip level through EBL and reactive ion etching. The compatibility of the grating couplers and the phase modulation has been demonstrated with preliminary experiments, showing that the dispersion introduced by the gratings is negligible over the small spectral range required for the optical phase modulation.

For the implementation of a truly multiplexed platform work is in progress to integrate a microfluidic network based on SU-8 polymer in order to provide an independent access to each interferometer and to detect the sensors outputs by a detector array. For the light in-coupling in the sensor array different solutions

have been preliminary examined, as the in-coupling through multiple diffractive gratings, the use of fiber units arrays or power-splitters. We have demonstrated preliminary results of multiplexed biosensing detections by employing a CCD detection approach.

The simplicity of the proposed phase modulation, which can be implemented with common laser diodes, provides a direct and linear read-out while keeping the ultra high sensitivity of the interferometric arrangement, rendering in a promising platform for biological assays detection. The BiMW sensor has demonstrated superior performances in comparison with conventional diagnostic tests due to the real-time, direct and label-free assay format it offers, reducing the time and the cost of conventional analysis, and a high sensitivity for different bioapplications, which traduces in low limits of detection. Although much margin is left for improvement, the results achieved in this Thesis can be considered as a solid basis towards future developments of an integrated LOC platform based on the BiMW integrated interferometers.

In order to improve the fabrication reproducibility, the hard mask employed for the definition of the step junction (modal splitter) has been recognized as a critical element, since its removal affects the thickness of the underlying silicon nitride film. This mask, which initially consisted of 600 nm of BPSG can be substituted by a 200 nm of PECVD silicon dioxide. A test process has been conducted in order to validate this alternative, showing that the thinner silicon dioxide layer can still satisfactory withstand the attack with hot phosphoric acid. Two main advantages would result from this change since i) a thinner mask layer would require shorter times for etching to be removed and less over-etching of the underlying structures and ii) the silicon dioxide does not require an annealing process as it is necessary for the BPSG, resulting in better mechanical stability (no cracks).

Alternative fabrication methods as deep-UV or Nano Imprint Lithography (NIL) are currently under evaluation to increase the fabrication throughput and reduce the final costs. For example for the grating couplers, once optimized their parameters, the fabrication should be transferred from electron beam lithography to a more cost-effective technique, as it is NIL. The advantages offered by EBL rely in fact on the facility of parameter change, ideal for prototyping, but cannot be used for mass production.

Part of the results achieved in this Thesis helped to start a technological transfer process with a private Spanish company in 2014, with whom we are working on the realization of a LOC prototype to be commercialized in the near-future.

# Appendix A

## Fourier expansion

Considering a sinusoidal phase modulation  $f(\mu_M) = \mu_M \sin(\omega_M t)$  the standard MZI output given by (1.5) is transformed into:

$$I_T = I_S + I_R + 2\sqrt{I_S I_R} \cos[\mu_M \sin(\omega_M t) + \Delta\varphi_S(t)] \quad (\text{A.1})$$

The global expression for the phase modulation can be decomposed into two terms:

$$\begin{aligned} \cos[\mu_M \sin(\omega_M t) + \Delta\varphi_S(t)] &= \cos[\Delta\varphi_S(t)] \cos[\mu_M \sin(\omega_M t)] + \\ &\quad - \sin[\Delta\varphi_S(t)] \sin[\mu_M \sin(\omega_M t)] \end{aligned} \quad (\text{A.2})$$

each of which can be expanded as a Fourier series, according to [Abramowitz and Stegun, 1964]. The general expressions are given by:

$$\cos[z \cdot \sin(\theta)] = J_0(z) + 2 \sum_{k=1}^{\infty} J_{2k}(z) \cos(2k\theta) \quad (\text{A.3})$$

$$\sin[z \cdot \sin(\theta)] = 2 \sum_{k=0}^{\infty} J_{2k+1}(z) \sin((2k+1)\theta) \quad (\text{A.4})$$

where  $z$  is the amplitude and  $J_n(z)$  is the Bessel's function of order  $n$ .

After a change of variables  $z = \mu_M$  and  $\theta = \omega t$  and substituting Eq.(A.4) into (A.2), we obtain the complete expression for the phase modulated signal.

$$I_T = I_S + I_R + 2\sqrt{I_S I_R} \left\{ \cos(\Delta\varphi_S(t)) \left[ J_0(\mu_M) + 2 \sum_{m=1}^{\infty} J_{2m}(\mu_M) \cos(2m\omega t) \right] \right. \\ \left. + \sin(\Delta\varphi_S(t)) \left[ 2 \sum_{m=0}^{\infty} J_{2m+1}(\mu_M) \sin[(2m+1)\omega t] \right] \right\} \quad (\text{A.5})$$

The complete harmonics expressions for the case of MZI are given by:

$$\begin{cases} I_{DC} = I_S + I_R + 2\sqrt{I_S I_R} \cos(\Delta\varphi_S(t)) J_0(\mu_M) \\ I_{1\omega} = 4\sqrt{I_S I_R} \sin(\Delta\varphi_S(t)) J_1(\mu_M) \\ I_{2\omega} = 4\sqrt{I_S I_R} \cos(\Delta\varphi_S(t)) J_2(\mu_M) \\ I_{3\omega} = 4\sqrt{I_S I_R} \sin(\Delta\varphi_S(t)) J_3(\mu_M) \end{cases} \quad (\text{A.6})$$

## Appendix B

### $\lambda$ M-MZI complete modelization

Similarly to the results achieved with different BiMW sensors, experimental results have shown that the phase shift measured on  $\lambda$ M-MZI sensors, induced by a same positive index change, can take place in different directions, i.e. up or down, according to the MZI core thickness. For example Fig. B.1 shows the detection of the same index change  $\Delta n = 7 \cdot 10^{-4}$  RIU for a sensor chip of 150 nm core thickness (see Fig. B.1a), showing a positive slope response, and for a chip of 250 nm core thickness (Fig. B.1b), showing a negative response, both characterized in TM polarization. The working point has been achieved with laser current variations of  $\pm 53$  mA for the 150 nm chip and  $\pm 41$  for the 250 nm one.

Considering the numerical modelization presented in Fig. 4.6 there is no explanation for the variation of the phase direction characterizing the 150 nm-sensor chip with respect to the 200 and 250 nm ones.

In order to understand this unexpected behavior the expression relating the wavelength shift to the induced phase shift, Eq.(4.8), was re-evaluated. In Fig. B.2 we compare the required modulation depth evaluated with the simplified and the complete forms of Eq.(4.8). By considering the complete expression, the required modulation depth shows opposite signs before and after a divergence of the function. Around 160 nm, a divergence is observed for the required modulation depth and the sensors belonging to this region cannot be modulated with the proposed approach since the required wavelength shift cannot be experimentally introduced.

Therefore, despite the homo-modal nature of the Mach-Zehnder configuration, it also shows critical effects due to the different dispersion relations resulting from the different cladding (water medium in the sensing area and silicon dioxide in

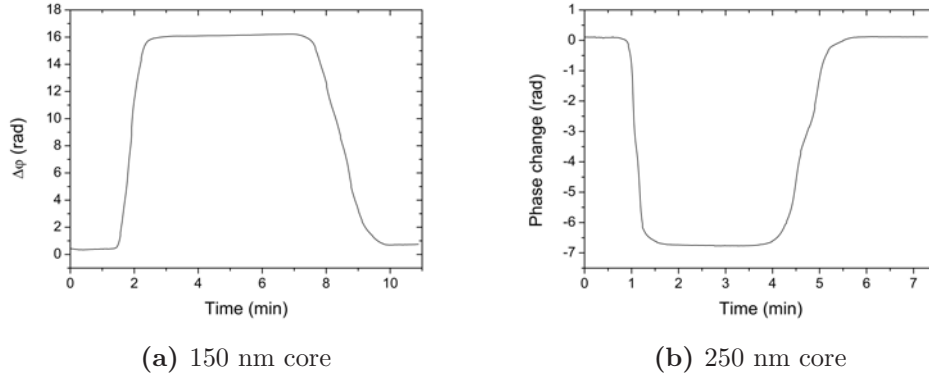


**Figure B.1:** Detection of an index change  $\Delta n = 7 \cdot 10^{-4}$  for a (a) chip with 150 nm core and (b) 250 nm core.

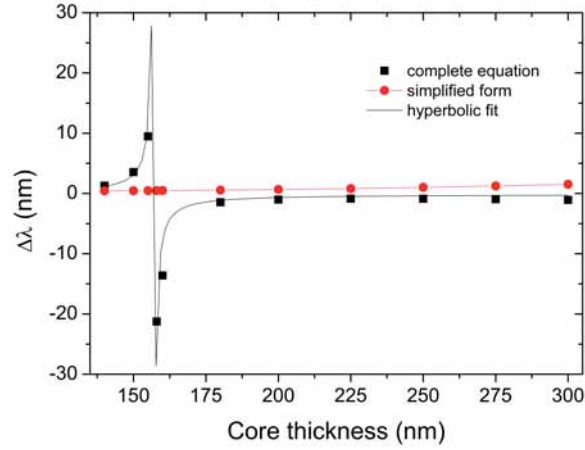


**Figure B.2:** Comparison of approximate versus simplified expressions of the required modulation depth, for TM polarization and central wavelength  $\lambda_0 = 660$  nm.



---

the reference arm).

A similar behavior, i.e. a variation of the sensor response direction, was numerically described by Kitsara *et al.* for a spectrally interrogated MZI biosensor operated over a broad-spectral range [Kitsara et al., 2010].

Critical effects, typical of hetero-modal interferometric arrangements, have been observed for the MZI interferometric biosensor as a consequence of the different claddings of the sensing and reference arms. As a consequence, the required modulation depth diverges in correspondence of a core thickness value which depends on the working wavelength and polarization, and the sensor response shows opposite directions according to the core thickness.



# Publications related to this doctoral thesis

## Articles in peer-reviewed international journals

1. S. Dante, D. Duval, B. Sepúlveda, A. B. González-Guerrero, J. R. Sendra and L. M. Lechuga, *All-optical phase modulation for integrated interferometric biosensors*, Optics Express, vol. 20(7), pp. 7195-7205, **2012**
2. D. Duval, A. B. González-Guerrero, S. Dante, J. Osmond, R. Monge, L. J. Fernández, K. E. Zinoviev, C. Domínguez and L. M. Lechuga *Nanophotonic lab-on-a-chip platforms including novel bimodal interferometers, microfluidics and grating couplers*, Lab chip, vol. 12(11), pp. 1987-94, **2012**
3. D. Duval, J. Osmond, S. Dante, C. Domínguez and L. M. Lechuga, *Grating couplers integrated on Mach-Zehnder interferometric biosensors operating in the visible range*, IEEE Photonics Journal, vol. 5(2), pp. 3700108, **2013**
4. S. Dante, D. Duval, D. Fariña, A. B. González-Guerrero and L. M. Lechuga, *Linear read-out of integrated interferometric biosensors using a periodic wavelength modulation*, Submitted.
5. A. B. González-Guerrero, J. Maldonado, S. Dante, D. Duval and L. M. Lechuga, *Label-free detection of protein biomarker in urine at relevant physiological level by a bimodal waveguide interferometer*, to be submitted.

### Articles in peer-reviewed national journals

6. S. Dante, D. Duval, A.B. González-Guerrero, J. Osmond, K. Zinoviev, B. Sepúlveda, C. Domínguez and L. M. Lechuga, *Towards a complete Lab-on-a-Chip system using integrated Mach-Zehnder interferometers*, Óptica Pura y Aplicada, vol. 45(2), **2012**

### Proceedings

7. A. B. González-Guerrero, S. Dante, D. Duval, J. Osmond and L. M. Lechuga, *Advanced photonic biosensors for point-of-care diagnostics*, Proc. Eurosenors in Procedia Engineering, vol. 25, pp71-75, **2011**
8. A. B. González-Guerrero, S. Dante, D. Duval, K. Zinoviev, C. Domínguez and L. M. Lechuga, *Silicon photonic biosensors for high innovative point-of-care diagnostic platforms*, IEEE Proceedings, ICO International Conference on Information Photonics (IP), PS-18-1-1, pp.1-2, **2011**
9. D. Duval, A. B. González-Guerrero, S. Dante, C. Domínguez and L.M. Lechuga, *Interferometric waveguide biosensors based on Si-technology for point-of-care diagnostic*, Proceedings of SPIE, vol. 8431, pp. 843101/11, **2012**
10. D. Duval, S. Dante A. B. González-Guerrero, L. J. Fernandez and L. M. Lechuga, *Silicon Photonics-based Nanobiosensors for Lab-on-a-chip Integration*, OSA Proceedings, Latin America Optics and Photonics Conference (LAOP), pp LT3B.1, **2012**

### Conference participation

11. S. Dante, D. Duval, A. B. González Guerrero, J. Osmond, K. Zinoviev, B. Sepúlveda, C. Domínguez and L. M. Lechuga, *Through a complete lab-on-chip system using integrated Mach-Zehnder interferometers*, OPTOEL 2011, Santander, Spain, June 29 - July 1 **2011** (poster)
12. S. Dante, D. Duval, B. Sepúlveda, A. B. González-Guerrero, A. Garcia-Castaño and L. M. Lechuga, *Phase modulated interferometric biosensors for real-time and ultra-sensitive evaluations*, Europtrode XI, Barcelona, Spain, April 1-4 **2012** (poster)

- 
13. S. Dante, D. Duval, C. Domínguez and L. M. Lechuga, *Solving the interferometric readout in sensor devices by an all-optical phase modulation technique*, 16<sup>th</sup> European Conference on Integrated Optics (ECIO) 2012, Sitges, Spain, April 18 – 20 **2012** (poster)
  14. S. Dante, D. Duval, J. Osmond, and L. M. Lechuga, *Ultra-sensitive silicon interferometric biosensors with linear read-out*, EUROMAT 2013, Sevilla, Spain, September 8-13 **2013** (poster)
  15. S. Dante, D. Duval, C. S. Huertas, and L. M. Lechuga, *Analysis of miRNA biomarkers related to thyroid cancer using a bimodal waveguide interferometric biosensor*, Europtrode XII, Athens, Greece, April 13-16 **2014** (poster)
  16. S. Dante, D. Duval, D. Fariña, A. B. González-Guerrero, C. Domínguez and L. M. Lechuga, *Wavelength Modulated Bimodal Interferometer for Highly Sensitive Biosensing Applications*, Advanced Photonics 2014 (Optical Sensors meeting), Barcelona, Spain, July 27-31 **2014** (oral)



# List of Figures

1.1	Ideal LOC platform. . . . .	2
1.2	Evanescient field working principle. . . . .	4
1.3	Comparison of the grating-based biosensor interrogation schemes. . . . .	8
1.4	Ring resonator biosensors. . . . .	10
1.5	Comparison of Mach-Zehnder and Young interferometric biosensors. . . . .	10
1.6	Scheme of the dual polarization interferometer (from [Swann et al., 2004]). . . . .	12
1.7	Scheme of the Bimodal Waveguide interferometric biosensor. . . . .	14
1.8	Comparison of different LOC architectures. . . . .	16
1.9	Interferometric output ambiguities. . . . .	19
1.10	Comparison of MZI architectures proposed for overcoming traditional output ambiguities. . . . .	20
2.1	Asymmetric slab waveguide configuration. . . . .	25
2.2	(a) TE and (b) TM modes propagation in an asymmetric planar waveguide. . . . .	26
2.3	TE modes profile for an asymmetric slab waveguide, $n_3 < n_2 < n_1$ . . . . .	29
2.4	Main 3D-waveguide geometries. . . . .	32
2.5	Guided modes labeling. . . . .	32
2.6	Effective index method . . . . .	33
2.7	Cross section view of the employed rib-waveguide. . . . .	37
2.8	Single mode condition for core thickness of 340 nm. . . . .	39
2.9	Mode dispersion curves for a rib dimension $4 \mu\text{m} \times 1.5 \text{ nm}$ , $\lambda_0=660 \text{ nm}$ . . . . .	41
2.10	Longitudinal view of the BiMW device. . . . .	42

## LIST OF FIGURES

---

2.11	BiMW intrinsic bulk sensitivity as a function of core thickness for TE and TM polarizations. . . . .	45
2.12	Phase sensitivity as a function of core thickness for TE and TM polarizations. . . . .	46
2.13	Surface sensitivity as a function of core thickness for TE and TM polarizations . . . . .	47
2.14	Superposition of the mode profiles for $\lambda_0 = 660$ nm, TE polarization. . . . .	49
2.15	Far field intensity distribution for different refractive index . . . . .	50
2.16	BiMW transfer function $S_R(n)$ for TE polarization . . . . .	51
2.17	Critical effects for 340 nm core thickness, TE polarization. . . . .	53
2.18	Critical wavelength as a function of bulk refractive index. . . . .	54
2.19	Transmission curves as a function of wavelength for different refractive indices. . . . .	55
3.1	Mask layout for the definition of 12 BiMW chips through standard lithographic techniques. . . . .	59
3.2	BiMW sensor chip fabrication process flow. . . . .	61
3.3	Photograph of a processed 4-inches wafer with 12 BiMW chips, resulting in a total of 192 sensors. . . . .	62
3.4	AFM characterization of the nanometric rib. . . . .	63
3.5	SEM characterization of the BiMW sensor chips. . . . .	63
3.6	Polishing machine. . . . .	65
3.7	Optical images of the polished chip facets. . . . .	65
3.8	Scheme of the fluidic cell fabrication. . . . .	66
3.9	Scheme of the experimental set-up employed for the evaluation of the BiMW sensors. . . . .	67
3.10	Detailed view of the BiMW experimental set-up. . . . .	68
3.11	Scheme of the flow delivery system employed. . . . .	69
3.12	(a) Acquired $I_{up}$ and $I_{down}$ signals and (b) corresponding $S_R$ during the detection of a refractive index change $\Delta n = 9 \cdot 10^{-4}$ . . . . .	70
3.13	Light energy distribution at the output of a BiMW sensor for two different states. . . . .	72
3.14	Bulk calibration of the BiMW sensor. TE polarization, $\lambda = 633$ nm. . . . .	73
3.15	Demonstration of sensitivity fading for a BiMW sensor. . . . .	74
4.1	Bessel's functions of first kind as a function of modulation amplitude. . . . .	82
4.2	Phase retrieval modelization. . . . .	84



4.3	Schematic comparison of standard monochromatic approach and wavelength modulated sensor. . . . .	86
4.4	Laser diode typical emission. . . . .	87
4.5	Normalized cumulative power for the ML101J27 laser diode. . . . .	89
4.6	Required modulation depth for the MZI sensor. . . . .	91
4.7	Quasi-static approach modulation for the MZI biosensor. . . . .	93
4.8	(a) scheme and (b) photograph of the experimental set-up required for the $\lambda$ M-MZI biosensor. . . . .	95
4.9	Scheme of the evaluation software showing the main functionalities and inter-dependencies. . . . .	96
4.10	Data acquisition process for the $\lambda$ M-MZI. . . . .	98
4.11	Bulk calibration of the $\lambda$ M-MZI sensor. . . . .	99
5.1	Required modulation depth for the BiMW sensor. . . . .	103
5.2	(a) scheme and (b) photograph of the experimental set-up for the optical characterization of the $\lambda$ M-BiMW sensors. . . . .	105
5.3	Screen-shots of the $\lambda$ M-BiMW acquisition software. . . . .	107
5.4	Effects of modulation depth. . . . .	108
5.5	Comparison of the harmonics behavior in presence of critical effects. . . . .	109
5.6	Bulk calibration of the $\lambda$ M-BiMW sensor. TE polarization, $\lambda_0 = 660$ nm. . . . .	111
5.7	Comparison of the required wavelength modulation depth for the BiMW sensor for central wavelengths $\lambda_0 = 638$ and $\lambda_0 = 660$ nm (TE polarization). . . . .	113
5.8	Comparison of the required wavelength modulation depth for TE and TM polarizations for (a) $\lambda_0 = 638$ nm and (b) $\lambda_0 = 660$ nm. . . . .	114
5.9	Bulk calibration of the $\lambda$ M-BiMW sensors operated at $\lambda_0 = 638$ nm. . . . .	116
5.10	Screen-shot of the acquired $I_{up}$ and $I_{down}$ signals and resulting $S_R$ for the $\lambda$ M-BiMW sensor operated at $\lambda_0 = 638$ nm. . . . .	117
6.1	Scheme of the functionalization process. . . . .	122
6.2	anti-hGH detection through direct assay on a $\lambda$ M-MZI biosensor. . . . .	123
6.3	Real-time monitoring of the covalent attachment of 50 $\mu$ g/ml of BSA in PBS buffer on a carboxy-functionalized sensing area. . . . .	125
6.4	Dose response curve for the detection of mAb-BSA on a $\lambda$ M-BiMW biosensor. . . . .	125
6.5	mAb-BSA specific detection and control experiment on a $\lambda$ M-BiMW biosensor. . . . .	126

## LIST OF FIGURES

---

6.6	Comparison of assay formats. (a) direct assay and (b) competitive assay. . . . .	127
6.7	Real-time immobilization of anti-CRP 20 $\mu\text{g}/\text{ml}$ on a $\lambda\text{M}$ -BiMW biosensor. . . . .	128
6.8	CRP immunoassay detection on a $\lambda\text{M}$ -BiMW biosensor. . . . .	128
6.9	hTSH detection through competitive assay on a $\lambda\text{M}$ -BiMW biosensor. . . . .	130
7.1	Envisioned LOC platform based on the integration of interferometric sensors. . . . .	134
7.2	Scheme of the light in-coupling through diffraction gratings. . . . .	136
7.3	Optical images of the fabricated grating couplers. . . . .	137
7.4	Coupling efficiency at 660 nm as a function of the incident angle for a BiMW device excited through a grating coupler with period $\Lambda = 450$ nm. . . . .	138
7.5	Bulk calibration of the BiMW sensor excited via grating coupler. . . . .	139
7.6	Grating transmission for different laser injection currents (wavelengths). $\Lambda = 400$ nm, TE polarization. . . . .	140
7.7	Normalized waveguide output after grating assisted light in-coupling. . . . .	141
7.8	Intensity modulated waveguide output for an input modulation depth $\delta I_{LD} = \pm 41$ mA. . . . .	142
7.9	Harmonics time-evolution for the detection of an index change $\Delta n = 6 \cdot 10^{-4}$ on a $\lambda\text{M}$ -BiMW sensor excited through diffraction grating. . . . .	142
7.10	Scheme of multiplexed interferometric biosensors. . . . .	144
7.11	Light in-coupling into four BiMW sensors through a fiber array unit ( $\lambda_0 = 635$ nm). . . . .	145
7.12	Bioreceptor deposition over the two sensing areas of a double-MZI sensor by employing the BioForce deposition platform. . . . .	147
7.13	Fabrication flow for the definition of micro-fluidics channels on top of the BiMW sensors array. . . . .	148
7.14	Optical images of the 3D SU-8 microfluidic network: (a) BiMW chip with 16 channels, (b) individual inlets for a group of four sensors, (c) common outlet for a group of four sensors and (d) final encapsulation. . . . .	149
7.15	AFM analysis of the chip surface during channel fabrication. . . . .	150
7.16	Definition of the two regions of interest necessary for the detection of the BiMW output by CCD camera. . . . .	151
7.17	Comparitive detection of a bulk index change on a MZI sensor by (a) standard Si-photodetector and (b) CCD camera. . . . .	152

---

7.18	Customized photodiode array based on (a) commercial $16 \times 2$ configuration and (b) schematic view of the detector array to be hybrid integrated at the sensor chip output. . . . .	153
7.19	Configurable Quadrant Sensor architecture. . . . .	154
7.20	Detection of a concentration 50 nM of DNA target on one MZI sensor in a double-MZI arrangement. . . . .	155
7.21	(a) CCD image showing the output of four BiMW sensors, with the corresponding dual-ROIs and (b) time-variation of the BiMW output signal in response to a variation of the sensing area refractive index. . . . .	157
B.1	Phase evolution of $\lambda$ M-MZI sensors with different core thickness. .	166
B.2	Comparison of approximate versus simplified expressions of the required modulation depth for the $\lambda$ M-MZI sensor. . . . .	166



# List of Tables

1.1	Integrated optical biosensors compared in terms of architecture and detection limits. . . . .	14
2.1	Layers parameters (refractive index and thickness) employed for the evaluation of the single-mode condition. . . . .	37
2.2	Cut-off thickness (nm) for TE <sub>10</sub> and TE <sub>20</sub> modes in the approximation of slab waveguide, with a top cladding of refractive index n= 1.33 / n=1.46. . . . .	38
2.3	Cut-off thickness (nm) for TM <sub>10</sub> and TM <sub>20</sub> modes in the approximation of slab waveguide, with a top cladding of refractive index n= 1.33 / n=1.46. . . . .	38
2.4	Core thickness corresponding to maximum bulk sensitivity for TE and TM polarizations and two working wavelengths. . . . .	45
3.1	Refractive index change induced by a set of HCl solutions and corresponding phase changes evaluated on a BiMW sensor interrogated in the standard monochromatic approach. . . . .	72
3.2	Sensor response for different initial phase difference. . . . .	75
4.1	Comparison of the emission spectra for different laser diodes and corresponding wavelength-current curves. . . . .	88
4.2	Comparison of theoretical and experimental wavelength periodicity for the MZI sensors. TM polarization, $\lambda_0=660$ nm. . . . .	92
4.3	Refractive index changes and corresponding phase signals employed for the calibration of a $\lambda$ M-MZI. . . . .	100

## LIST OF TABLES

---

5.1	Refractive index change induced by a set of HCl solutions and corresponding phase changes evaluated with the $\lambda$ M-BiMW operated at $\lambda_0 = 660$ nm. . . . .	110
5.2	Critical thickness as a function of polarization and working wavelength. . . . .	113
5.3	Refractive index change induced by a set of HCl solutions and corresponding phase changes evaluated with the $\lambda$ M-BiMW operated at $\lambda_0 = 638$ nm, TE and TM polarizations. . . . .	115
7.1	Refractive index changes induced by a set of HCl solutions and corresponding phase changes evaluated on a BiMW excited via a grating coupler. . . . .	138
7.2	Comparison of the emission spectra for different fiber coupled laser sources and corresponding wavelength-current curves. . . . .	146

# List of acronyms

**AFM** Atomic Force Microscopy

**BHF** buffered hydrofluoric acid

**BiMW** Bimodal Waveguide

**BPM** Beam Propagation Method

**BPSG** Boron Phosphorous Silicon Glass

**BSA** Bovine Serum Albumin

**CCD** Charge-Coupled Device

**CMOS** complementary metal oxide semiconductor

**CQD** Configurable Quadrant Photodetector

**CRP** C-reactive protein

**CTES** carboxyethyl silanetriol, sodium salt

**DPI** Dual Polarization Interferometry

**EBL** Electron Beam Lithography

**EDC** N-(3-dimethylaminopropyl)-N'-ethylcarbodiimide

**EI** Effective Index

<b>EME</b>	Eigenmode Expansion
<b>FAU</b>	fiber array unit
<b>FDTD</b>	Finite Difference Time Domain
<b>FEM</b>	Finite Element Method
<b>FFT</b>	Fast Fourier Transform
<b>GC</b>	grating coupler
<b>hGH</b>	human Growth Hormone
<b>hTSH</b>	human Thyroid Stimulating Hormone
<b>IO</b>	Integrated Optics
<b>LD</b>	Laser Diode
<b>LOC</b>	Lab-On-Chip
<b>LOD</b>	Limit of Detection
<b>MZI</b>	Mach-Zehnder Interferometer
<b>NHS</b>	N-Hydroxysuccinimide
<b>OWLS</b>	Optical Waveguide Light Spectroscopy
<b>PBS</b>	phosphate buffered saline
<b>PDMS</b>	Polydimethylsiloxane
<b>PECVD</b>	Plasma Enhanced Chemical Vapor Deposition
<b>POC</b>	Point-of-Care
<b>PTFE</b>	PolyTetraFluoroEthylene
<b>RIU</b>	Refractive Index Unit



<b>ROI</b>	Region Of Interest
<b>SAW</b>	Surface Acoustic Wave
<b>SEM</b>	Scanning Electron Microscopy
<b>SNR</b>	Signal-to-noise-ratio
<b>SOI</b>	Silicon on Insulator
<b>SPM</b>	Sinusoidal Phase Modulation
<b>SPR</b>	Surface Plasmon Resonance
<b>SPRi</b>	Surface Plasmon Resonance imaging
<b>TE</b>	transverse electric
<b>TIR</b>	Total Internal Reflection
<b>TM</b>	transverse magnetic
<b>WGM</b>	Whispering Gallery Mode
<b>WIOS</b>	Wavelength Interrogated Optical Sensor
<b>YI</b>	Young Interferometer



# Bibliography

- [Abramowitz and Stegun, 1964] Abramowitz, M. and Stegun, I. (1964). *Handbook of Mathematical Functions with Formulas, Graphs, and Mathematical Tables*. Dover, New York, ninth dover printing, tenth gpo printing edition.
- [Azzazy and Elbehery, 2014] Azzazy, H. M. and Elbehery, A. H. (2014). Clinical laboratory data: Acquire, analyze, communicate, liberate. *Clinica Chimica Acta*.
- [Bañuls et al., 2013] Bañuls, M., Puchades, R., and Maquieira, A. (2013). Chemical surface modifications for the development of silicon-based label-free integrated optical (IO) biosensors: A review. *Analytica Chimica Acta*, 777(0):1–16.
- [Barrios, 2009] Barrios, C. A. (2009). Optical slot-waveguide based biochemical sensors. *Sensors*, 9(6):4751–4765.
- [Batrak and Plisyuk, 2006] Batrak, D. and Plisyuk, S. (2006). Applicability of the effective index method for simulating ridge optical waveguides. *Quantum Electronics*, 36(4):349.
- [Bernard and Bosshard, 1995] Bernard, A. and Bosshard, H. (1995). Real-time monitoring of antigen-antibody recognition on a metal oxide surface by an optical grating coupler sensor. *European Journal of Biochemistry*, 230(2).
- [Blanco et al., 2006] Blanco, F., Agirregabiria, M., Berganzo, J., Mayora, K., Elizalde, J., Calle, A., Domínguez, C., and Lechuga, L. (2006). Microfluidic-optical integrated CMOS compatible devices for label-free biochemical sensing. *Journal of Micromechanics and Microengineering*, 16:1006–1016.
- [Bogaerts et al., 2012] Bogaerts, W., Heyn, P. D., Vaerenbergh, T. V., Vos, K. D., Selvaraja, S. K., Claes, T., Dumon, P., Bienstman, P., Thourhout, D. V., and Baets, R. (2012). Silicon microring resonators. *Laser & Photonics Reviews*, 6(1):47–73.
- [Brandenburg, 1996] Brandenburg, A. (1996). Integrated optical interferometers for refractometry and chemical sensing. In *Lasers, Optics, and Vision for Productivity in Manufacturing I*, pages 266–276. International Society for Optics and Photonics.

- [Brandenburg and Henninger, 1994] Brandenburg, A. and Henninger, R. (1994). Integrated optical Young interferometer. *Applied optics*, 33(25):5941–5947.
- [Brazas and Li, 1995] Brazas, J. and Li, L. (1995). Analysis of input-grating couplers having finite lengths. *Applied optics*, 34(19):3786–3792.
- [Brockman et al., 2000] Brockman, J., Nelson, B., and Corn, R. (2000). Surface plasmon resonance imaging measurements of ultrathin organic films. *Annual review of physical chemistry*, 51(1):41–63.
- [Bruck et al., 2011] Bruck, R., Melnik, E., Muellner, P., Hainberger, R., and Lämmerhofer, M. (2011). Integrated polymer-based Mach-Zehnder interferometer label-free streptavidin biosensor compatible with injection molding. *Biosensors and Bioelectronics*, 26(9):3832–3837.
- [Carlborg et al., 2010] Carlborg, C. F., Gylfason, K. B., Kaźmierczak, A., Dortu, F., Polo, M. B., Catala, A. M., Kresbach, G., Sohlström, H., Moh, T., Vivien, L., et al. (2010). A packaged optical slot-waveguide ring resonator sensor array for multiplex label-free assays in labs-on-chips. *Lab on a Chip*, 10(3):281–290.
- [Chen et al., 2010] Chen, Y., Xu, P., Liu, M., and Li, X. (2010). Bio/chemical detection in liquid with self-sensing Pr-Oxi-Lever (piezo-resistive SiO<sub>2</sub> cantilever) sensors. *Microelectronic Engineering*, 87(12):2468–2474.
- [Chiang, 1986] Chiang, K. (1986). Dual effective-index method for the analysis of rectangular dielectric waveguides. *Applied optics*, 25(13):2169–2174.
- [Chin et al., 2012] Chin, C., Linder, V., and Sia, S. (2012). Commercialization of microfluidic point-of-care diagnostic devices. *Lab on a Chip*, 12(12):2118–2134.
- [Chong and Rue, 2004] Chong, H. and Rue, R. D. L. (2004). Tuning of photonic crystal waveguide microcavity by thermo-optic effect. *Photonics Technology Letters, IEEE*, 16(6):1528–1530.
- [Chow et al., 2004] Chow, E., Grot, A., Mirkarimi, W., Sigalas, M., and Girolami, G. (2004). Ultracompact biochemical sensor built with two-dimensional photonic crystal microcavity. *Optics letters*, 29(10):1093–1095.
- [Cottier et al., 2003] Cottier, K., Wiki, M., Voirin, G., Gao, H., and Kunz, R. (2003). Label-free highly sensitive detection of (small) molecules by wavelength interrogation of integrated optical chips. *Sensors and Actuators B*, 91(1–3):241 – 251.
- [Crespi et al., 2010] Crespi, A., Gu, Y., Ngamsom, B., Hoekstra, H. J., Dongre, C., Pollnau, M., Ramponi, R., van den Vlekkert, H. H., Watts, P., Cerullo, G., et al. (2010). Three-dimensional Mach-Zehnder interferometer in a microfluidic chip for spatially-resolved label-free detection. *Lab on a Chip*, 10(9):1167–1173.
- [Cross et al., 2003] Cross, G., Reeves, A., Brand, S., Popplewell, J., Peel, L., Swann, M., and Freeman, N. (2003). A new quantitative optical biosensor for protein characterisation. *Biosensors and Bioelectronics*, 19(4):383–390.

- [Dandridge and Tveten, 1982] Dandridge, A. and Tveten, A. (1982). Phase compensation in interferometric fiber-optic sensors. *Optics letters*, 7(6):279–281.
- [Dante et al., Subm] Dante, S., Duval, D., Fariña, D., González-Guerrero, A., and Lechuga, L. (Subm). Linear read-out of integrated interferometric biosensors using a periodic wavelength modulation. *Submitted*.
- [Dante et al., 2012] Dante, S., Duval, D., Sepúlveda, B., González-Guerrero, A., Sendra, J., and Lechuga, L. (2012). All-optical phase modulation for integrated interferometric biosensors. *Optics Express*, 20(7):7195–7205.
- [de Juan-Franco et al., 2013] de Juan-Franco, E., Rodríguez-Frade, J., Mellado, M., and Lechuga, L. (2013). Implementation of a SPR immunosensor for the simultaneous detection of the 22k and 20k hGH isoforms in human serum samples. *Talanta*, 114:268–275.
- [De Vos et al., 2007] De Vos, K., Bartolozzi, I., Schacht, E., Bienstman, P., and Baets, R. (2007). Silicon-on-Insulator microring resonator for sensitive and label-free biosensing. *Optics Express*, 15(12):7610–7615.
- [Deferrari et al., 1967] Deferrari, H., Darby, R., and Andrews, F. (1967). Vibrational displacement and mode-shape measurement by a laser interferometer. *Journal of the Acoustical Society of America*, 42(5):982–990.
- [del Río Sáez, 2007] del Río Sáez, J. S. (2007). *Desarrollo de un biosensor fotónico de alta sensibilidad basado en interferómetros Mach-Zehnder integrados en tecnología microelectrónica de silicio*. PhD thesis, Universidad Autónoma de Madrid.
- [Densmore et al., 2009] Densmore, A., Vachon, M., Xu, D.-X., Janz, S., Ma, R., Li, Y.-H., Lopinski, G., Delâge, A., Lapointe, J., and Luebbert, C. (2009). Silicon photonic wire biosensor array for multiplexed real-time and label-free molecular detection. *Optics letters*, 34(23):3598–3600.
- [Dér et al., 2010] Dér, A., Valkai, S., Mathesz, A., Andó, I., Wolff, E., and Ormos, P. (2010). Protein-based all-optical sensor device. *Sensors and Actuators B: Chemical*, 151(1):26 – 29.
- [Diao et al., 2005] Diao, J., Ren, D., Engstrom, J., and Lee, K. (2005). A surface modification strategy on silicon nitride for developing biosensors. *Analytical biochemistry*, 343(2):322–328.
- [Domínguez et al., 2003] Domínguez, C., Rodríguez, J., and Lechuga, L. (2003). Chapter 13. Integrated optical transducers for (bio)chemical sensing. In Alegret, S., editor, *Integrated Analytical Systems*, volume 39 of *Comprehensive Analytical Chemistry*, pages 541–586. Elsevier.
- [Drapp et al., 1997] Drapp, B., Piehler, J., Brecht, A., Gauglitz, G., Luff, B., Wilkinson, J., and Ingenhoff, J. (1997). Integrated optical Mach-Zehnder interferometers as simazine immunoprobes. *Sensors and Actuators B: Chemical*, 39(1):277–282.

- [Duhring and Sigmund, 2009] Duhring, M. and Sigmund, O. (2009). Improving the acousto-optical interaction in a Mach-Zehnder interferometer. *Journal of Applied Physics*, 105(8):083529.
- [Duval et al., 2012] Duval, D., González-Guerrero, A., Dante, S., Osmond, J., Monge, R., Fernandez, L., Zinoviev, K., Domínguez, C., and Lechuga, L. (2012). Nanophotonic lab-on-a-chip platforms including novel bimodal interferometers, microfluidics and grating couplers. *Lab on a Chip*, 12(11):1987–1994.
- [Duval and Lechuga, 2014] Duval, D. and Lechuga, L. (2014). Optical waveguide biosensors. In Andrews, D., editor, *Biomedical Photonics, Spectroscopy and Microscopy*. Wiley-Blackwell.
- [Duval et al., 2013] Duval, D., Osmond, J., Dante, S., Domínguez, C., and Lechuga, L. (2013). Grating couplers integrated on Mach-Zehnder interferometric biosensors operating in the visible range. *IEEE Photonics Journal*, 5(2):3700108.
- [Estevez et al., 2012] Estevez, M., Álvarez, M., and Lechuga, L. (2012). Integrated optical devices for lab-on-a-chip biosensing applications. *Laser & Photonics Reviews*, 6(4):463–487.
- [Fan et al., 2008] Fan, X., White, I., Shopova, S., Zhu, H., Suter, J., and Sun, Y. (2008). Sensitive optical biosensors for unlabeled targets: A review. *Analytica Chimica Acta*, 620(1):8–26.
- [Gallagher and Felici, 2003] Gallagher, D. and Felici, T. (2003). Eigenmode expansion methods for simulation of optical propagation in photonics - pros and cons. In *Photonics West, San Jose*.
- [Gallegos et al., 2013] Gallegos, D., Long, K., Yu, H., Clark, P., Lin, Y., George, S., Nath, P., and Cunningham, B. (2013). Label-free biodetection using a smartphone. *Lab Chip*, 13:2124–2132.
- [Gao and Rothberg, 2007] Gao, T. and Rothberg, L. (2007). Label-free sensing of binding to microarrays using Brewster angle straddle interferometry. *Analytical Chemistry*, 79(20):7589–7595.
- [Gervais et al., 2011] Gervais, L., Rooij, N. D., and Delamarche, E. (2011). Microfluidic chips for point-of-care immunodiagnostics. *Advanced Materials*, 23(24):H151–H176.
- [Goldberg et al., 1981] Goldberg, L., Taylor, H., and Weller, J. (1981). Time-dependent thermal effects in current-modulated semiconductor lasers. *Electronics Letters*, 17(14):497–499.
- [González-Guerrero, 2012] González-Guerrero, A. (2012). *Bimodal waveguide interferometer device based on silicon photonics technology for label-free and high sensitive biosensing*. PhD thesis, Universitat Autònoma de Barcelona.

- [González-Guerrero et al., 2013] González-Guerrero, A., Álvarez, M., Castaño, A. G., Domínguez, C., and Lechuga, L. (2013). A comparative study of in-flow and micro-patterning biofunctionalization protocols for nanophotonic silicon-based biosensors. *Journal of Colloid and Interface Science*, 393(0):402 – 410.
- [Gorecki et al., 1997] Gorecki, C., Chollet, F., Bonnotte, E., and Kawakatsu, H. (1997). Silicon-based integrated interferometer with phase modulation driven by surface acoustic waves. *Optics letters*, 22(23):1784–1786.
- [Gupta et al., 2014] Gupta, R., Periyakaruppan, A., Meyyappan, M., and Koehne, J. (2014). Label-free detection of C-reactive protein using a carbon nanofiber based biosensor. *Biosensors and Bioelectronics*, 59(0):112–119.
- [Haensch et al., 2010] Haensch, C., Hoeppeener, S., and Schubert, U. S. (2010). Chemical modification of self-assembled silane based monolayers by surface reactions. *Chemical Society Reviews*, 39(6):2323–2334.
- [Halir et al., 2013] Halir, R., Vivien, L., Roux, X. L., Xu, D.-X., and Cheben, P. (2013). Direct and sensitive phase readout for integrated waveguide sensors. *IEEE Photonics Journal*, 5(4):6800906–6800906.
- [Hariharan, 2003] Hariharan, P. (2003). *Optical interferometry*. Academic Press.
- [Heideman et al., 1993] Heideman, R., Kooyman, R., and Greve, J. (1993). Performance of a highly sensitive optical waveguide Mach-Zehnder interferometer immunosensor. *Sensors and Actuators B*, 10(3):209–217.
- [Heideman and Lambeck, 1999] Heideman, R. and Lambeck, P. (1999). Remote opto-chemical sensing with extreme sensitivity: design, fabrication and performance of a pigtailed integrated optical phase-modulated Mach-Zehnder interferometer system. *Sensors and Actuators B*, 61(1-3):100–127.
- [Heinzel et al., 2010] Heinzel, G., Cervantes, F. G., Marin, A. G., Kullmann, J., Feng, W., and Danzmann, K. (2010). Deep phase modulation interferometry. *Optics Express*, 18(18):19076–19086.
- [Homola, 2003] Homola, J. (2003). Present and future of surface plasmon resonance biosensors. *Analytical and Bioanalytical Chemistry*, 377(3):528–539.
- [Horcas et al., 2007] Horcas, I., Fernandez, R., Gomez-Rodriguez, J., Colchero, J., Gómez-Herrero, J., and Baro, A. (2007). WSXM: a software for scanning probe microscopy and a tool for nanotechnology. *Review of Scientific Instruments*, 78(1):013705.
- [Hua et al., 2002] Hua, P., Jonathan Luff, B., Quigley, G. R., Wilkinson, J. S., and Kawaguchi, K. (2002). Integrated optical dual Mach-Zehnder interferometer sensor. *Sensors and Actuators B: Chemical*, 87(2):250–257.
- [Hunt and Armani, 2014] Hunt, H. and Armani, A. (2014). Bioconjugation strategies for label-free optical microcavity sensors. *Selected Topics in Quantum Electronics, IEEE Journal of*, 20(2):121–133.

- [Hutter et al., 2013] Hutter, T., Elliott, S. R., and Ruschin, S. (2013). Dynamic range enhancement and phase-ambiguity elimination in wavelength-interrogated interferometric sensor. *Sensors and Actuators B*, 178(0):593 – 597.
- [Iqbal et al., 2010] Iqbal, M., Gleeson, M., Spaugh, B., Tybor, F., Gunn, W., Hochberg, M., Baehr-Jones, T., Bailey, R., and Gunn, L. (2010). Label-free biosensor arrays based on silicon ring resonators and high-speed optical scanning instrumentation. *Selected Topics in Quantum Electronics, IEEE Journal of*, 16(3):654–661.
- [Jane et al., 2009] Jane, A., Dronov, R., Hodges, A., and Voelcker, N. H. (2009). Porous silicon biosensors on the advance. *Trends in biotechnology*, 27(4):230–239.
- [Janz et al., 2013] Janz, S., Xu, D.-X., Vachon, M., Sabourin, N., Cheben, P., McIntosh, H., Ding, H., Wang, S., Schmid, J., Del  ge, A., et al. (2013). Photonic wire biosensor microarray chip and instrumentation with application to serotyping of *Escherichia coli* isolates. *Optics express*, 21(4):4623–4637.
- [Jokerst et al., 2009] Jokerst, N., Luan, L., Palit, S., Royal, M., Dhar, S., Brooke, M., and Tyler, T. (2009). Progress in chip-scale photonic sensing. *IEEE Transactions on Biomedical Circuits and Systems*, 3(4):202–211.
- [Kitsara et al., 2010] Kitsara, M., Misiakos, K., Raptis, I., and Makarona, E. (2010). Integrated optical frequency-resolved Mach-Zehnder interferometers for label-free affinity sensing. *Optics Express*, 18(8):8193–8206.
- [Kogelnik, 1975] Kogelnik, H. (1975). Theory of dielectric waveguides. In *Integrated Optics*, volume 7 of *Topics in Applied Physics*, pages 13–81. Springer Berlin Heidelberg.
- [Korostynska et al., 2008] Korostynska, O., Arshak, K., Gill, E., and Arshak, A. (2008). Microsensors arrays manufacture using the NanoeNabler<sup>TM</sup>. In *Nanotechnology, 2008. NANO’08. 8th IEEE Conference on*, pages 440–443. IEEE.
- [Koster and Lambeck, 2002] Koster, T. and Lambeck, P. (2002). Fully integrated optical polarimeter. *Sensors and Actuators B*, 82(2):213–226.
- [Kozma et al., 2014] Kozma, P., Kehl, F., Ehrentreich-F  rster, E., Stamm, C., and Bier, F. F. (2014). Integrated planar optical waveguide interferometer biosensors: a comparative review. *Biosensors and Bioelectronics*, 58(0):287 – 307.
- [Krioukov et al., 2002] Krioukov, E., Klunder, D., Driessen, A., Greve, J., and Otto, C. (2002). Sensor based on an integrated optical microcavity. *Optics letters*, 27(7):512–514.
- [Ksendzov and Lin, 2005] Ksendzov, A. and Lin, Y. (2005). Integrated optics ring-resonator sensors for protein detection. *Optics letters*, 30(24):3344–3346.
- [Kumar et al., 1983] Kumar, A., Thyagarajan, K., and Ghatak, A. (1983). Analysis of rectangular-core dielectric waveguides: an accurate perturbation approach. *Optics letters*, 8(1):63–65.



- [Kunz and Cottier, 2006] Kunz, R. and Cottier, K. (2006). Optimizing integrated optical chips for label-free (bio-)chemical sensing. *Analytical and Bioanalytical Chemistry*, 384(1):180–190.
- [Kunz et al., 1996] Kunz, R., Dübendorfer, J., and Morf, R. (1996). Finite grating depth effects for integrated optical sensors with high sensitivity. *Biosensors and Bioelectronics*, 11(6):653–667.
- [Kussrow and Bornhop, 2012] Kussrow, A. and Bornhop, C. E. D. (2012). Interferometric methods for label-free molecular interaction studies. *Analytical Chemistry*, 84(2):779–792.
- [Lechuga, 2005] Lechuga, L. (2005). Optical biosensors. In Gorton, L., editor, *Biosensors and Modern Biospecific Analytical Techniques*. Elsevier B.V.
- [Levy and Ruschin, 2008] Levy, R. and Ruschin, S. (2008). Critical sensitivity in hetero-modal interferometric sensor using spectral interrogation. *Optics Express*, 16(25):20516–20521.
- [Lifante, 2003] Lifante, G. (2003). *Integrated photonics: fundamentals*. Wiley.
- [Ligler, 2009] Ligler, F. (2009). Perspective on optical biosensors and integrated sensor systems. *Analytical Chemistry*, 81(2):519–526.
- [Lillie et al., 2006] Lillie, J. J., Thomas, M. A., Jokerst, N.-M., Ralph, S. E., Dennis, K. A., and Henderson, C. L. (2006). Multimode interferometric sensors on silicon optimized for fully integrated complementary-metal-oxide-semiconductor chemical-biological sensor systems. *JOSA B*, 23(4):642–651.
- [Luan et al., 2012] Luan, L., Royal, M. W., Evans, R., Fair, R. B., and Jokerst, N. M. (2012). Chip scale optical microresonator sensors integrated with embedded thin film photodetectors on electrowetting digital microfluidics platforms. *Sensors Journal, IEEE*, 12(6):1794–1800.
- [Luchansky and Bailey, 2012] Luchansky, M. and Bailey, R. (2012). High-Q optical sensors for chemical and biological analysis. *Analytical Chemistry*, 84(2):793–821.
- [Luff et al., 1998] Luff, B., Wilkinson, J. S., Piehler, J., Hollenbach, U., Ingenhoff, J., and Fabricius, N. (1998). Integrated optical Mach-Zehnder biosensor. *Journal of lightwave technology*, 16(4):583.
- [Lukosz et al., 1997] Lukosz, W., Stamm, C., Moser, H., Ryf, R., and Dübendorfer, J. (1997). Difference interferometer with new phase-measurement method as integrated-optical refractometer, humidity sensor and biosensor. *Sensors and Actuators B*, 39(1):316–323.
- [Maire et al., 2008] Maire, G., Vivien, L., Sattler, G., Kazmierczak, A., Sanchez, B., Gylfason, K. B., Griol, A., Marris-Morini, D., Cassan, E., Giannone, D., et al. (2008). High efficiency silicon nitride surface grating couplers. *Optics Express*, 16(1):328–333.

- [Makarona et al., 2011] Makarona, E., Petrou, P. S., Bourkoula, A., Botsialas, A., Kitsara, M., Kakabakos, S., Stoffer, R., Jobst, G., Nounesis, G., Raptis, I., et al. (2011). Monolithically integrated Mach-Zehnder biosensors for real-time label-free monitoring of biomolecular reactions. In *Engineering in Medicine and Biology Society, EMBC, 2011 Annual International Conference of the IEEE*, pages 7654–7657. IEEE.
- [Marcatili, 1969] Marcatili, E. (1969). Dielectric rectangular waveguide and directional coupler for integrated optics. *Bell System Technical Journal*, 48(7):2071–2102.
- [Mazer and Rabbani, 2004] Mazer, S. and Rabbani, L. (2004). Evidence for C-reactive protein’s role in (CRP) vascular disease: Atherothrombosis, immuno-regulation and CRP. *Journal of Thrombosis and Thrombolysis*, 17(2):95–105.
- [McClellan et al., 2012] McClellan, M., Domier, L., and Bailey, R. (2012). Label-free virus detection using silicon photonic microring resonators. *Biosensors and Bioelectronics*, 31(1):388–392.
- [Misiakos et al., 2014] Misiakos, K., Raptis, I., Salapatias, A., Makarona, E., Botsialas, A., Hoekman, M., Stoffer, R., and Jobst, G. (2014). Broad-band Mach-Zehnder interferometers as high performance refractive index sensors: Theory and monolithic implementation. *Optics Express*, 22(8):8856–8870.
- [Mulder et al., 2012] Mulder, H., Ymeti, A., Subramaniam, V., and Kanger, J. (2012). Size-selective detection in integrated optical interferometric biosensors. *Optics Express*, 20(19):20934–20950.
- [Nellen et al., 1988] Nellen, P., Tiefenthaler, K., and Lukosz, W. (1988). Integrated optical input grating couplers as biochemical sensors. *Sensors and Actuators*, 15(3):285 – 295.
- [Nishihara et al., 1989] Nishihara, H., Haruna, M., and Suhara, T. (1989). *Optical integrated circuits*. Citeseer.
- [Ozcan, 2014] Ozcan, A. (2014). Mobile phones democratize and cultivate next-generation imaging, diagnostics and measurement tools. *Lab on a Chip*.
- [Park et al., 2013] Park, M., Kee, J., Quah, J., Netto, V., Song, J., Fang, Q., Fosse, E. L., and Lo, G.-Q. (2013). Label-free aptamer sensor based on silicon microring resonators. *Sensors and Actuators B: Chemical*, 176:552–559.
- [Passaro et al., 2005] Passaro, V., Magno, F., and Tsarev, A. (2005). Investigation of thermo-optic effect and multi-reflector tunable filter/multiplexer in SOI waveguides. *Optics Express*, 13(9):3429–3437.
- [Pinheiro-Ortega et al., 2010] Pinheiro-Ortega, T., Silvestre, E., Andres, P., Maes, B., and Bienstman, P. (2010). Design of bimodal PCFs for interferometric gas sensors with high sensitivity. *Sensors Journal, IEEE*, 10(7):1180–1184.

- [Preechaburana et al., 2012] Preechaburana, P., Gonzalez, M. C., Suska, A., and Filipini, D. (2012). Surface plasmon resonance chemical sensing on cell phones. *Angewandte Chemie*, 124(46):11753–11756.
- [Preston et al., 2009] Preston, K., Manipatruni, S., Gondarenko, A., Poitras, C., and Lipson, M. (2009). Deposited silicon high-speed integrated electro-optic modulator. *Optics Express*, 17:5118.
- [Prieto et al., 2003] Prieto, F., Sepúlveda, B., Calle, A., Llobera, A., Domínguez, C., Abad, A., Montoya, A., and Lechuga, L. (2003). An integrated optical interferometric nanodevice based on silicon technology for biosensor applications. *Nanotechnology*, 14(8):907.
- [Ramaswamy, 1974] Ramaswamy, V. (1974). Strip-loaded film waveguide. *Bell System Technical Journal*, 53(4):697–704.
- [Ridker, 2003] Ridker, P. (2003). Clinical application of C-reactive protein for cardiovascular disease detection and prevention. *Circulation*, 107(3):363–369.
- [Rio et al., 2007] Rio, J. S. D., Carrascosa, L., Blanco, F., Moreno, M., Berganzo, J., Calle, A., Domínguez, C., and Lechuga, L. (2007). Lab-on-a-chip platforms based on highly sensitive nanophotonic Si biosensors for single nucleotide DNA testing. In *Integrated Optoelectronic Devices 2007*, pages 64771B–64771B. International Society for Optics and Photonics.
- [Rothenhäusler and Knoll, 1988] Rothenhäusler, B. and Knoll, W. (1988). Surface plasmon microscopy.
- [Salik et al., 2012] Salik, E., Medrano, M., Cohoon, G., Miller, J., Boyter, C., and Koh, J. (2012). SMS fiber sensor utilizing a few-mode fiber exhibits critical wavelength behavior. *IEEE Photonics Technology Letters*, 24(7):593–595.
- [Sasaki and Okazaki, 1986] Sasaki, O. and Okazaki, H. (1986). Sinusoidal phase modulating interferometry for surface profile measurement. *Applied optics*, 25(18):3137–3140.
- [Schipper et al., 1997] Schipper, E., Brugman, A., Domínguez, C., Lechuga, L., Kooyman, R., and Greve, J. (1997). The realization of an integrated Mach-Zehnder waveguide immunosensor in silicon technology. *Sensors and Actuators B*, 40(2):147–153.
- [Schmitt et al., 2007] Schmitt, K., Schirmer, B., Hoffmann, C., Brandenburg, A., and Meyrueis, P. (2007). Interferometric biosensor based on planar optical waveguide sensor chips for label-free detection of surface bound bioreactions. *Biosensors and Bioelectronics*, 22(11):2591–2597.
- [Sepúlveda, 2005] Sepúlveda, B. (2005). *Efectos magneto-ópticos en dispositivos biosensores de campo evanescente*. PhD thesis, Universidad Autónoma de Madrid.
- [Sepúlveda et al., 2007] Sepúlveda, B., Armelles, G., and Lechuga, L. (2007). Magneto-optical phase modulation in integrated Mach-Zehnder interferometric sensors. *Sensors and Actuators A*, 134(2):339 – 347.

- [Sepúlveda et al., 2006] Sepúlveda, B., del Río, J. S., Moreno, M., Blanco, F. J., Mayora, K., Domínguez, C., and Lechuga, L. M. (2006). Optical biosensor microsystems based on the integration of highly sensitive Mach-Zehnder interferometer devices. *Journal of Optics A: Pure and Applied Optics*, 8(7):S561–S566.
- [Snyder and Love, 1983] Snyder, A. and Love, J. (1983). *Optical waveguide theory*, volume 190. Springer.
- [Soler et al., 2014] Soler, M., Estevez, M.-C., Álvarez, M., Otte, M., Sepúlveda, B., and Lechuga, L. (2014). Direct detection of protein biomarkers in human fluids using site-specific antibody immobilization strategies. *Sensors*, 14(2):2239–2258.
- [Sudarshanam and Claus, 1993] Sudarshanam, V. and Claus, R. (1993). Generic  $J_1 \cdots J_4$  method of optical phase detection: accuracy and range enhancement. *Journal of Modern Optics*, 40(3):483–492.
- [Sudarshanam and Srinivasan, 1989] Sudarshanam, V. and Srinivasan, K. (1989). Linear readout of dynamic phase change in a fiber-optic homodyne interferometer. *Optics letters*, 14(2):140–142.
- [Suzuki et al., 1989] Suzuki, T., Sasaki, O., and Maruyama, T. (1989). Phase locked laser diode interferometry for surface profile measurement. *Applied optics*, 28(20):4407–4410.
- [Swann et al., 2004] Swann, M., Peel, L., Carrington, S., and Freeman, N. (2004). Dual-polarization interferometry: an analytical technique to measure changes in protein structure in real time, to determine the stoichiometry of binding events, and to differentiate between specific and nonspecific interactions. *Analytical biochemistry*, 329(2):190–198.
- [Taillaert et al., 2002] Taillaert, D., Bogaerts, W., Bienstman, P., Krauss, T. F., Van Daele, P., Moerman, I., Verstuyft, S., De Mesel, K., and Baets, R. (2002). An out-of-plane grating coupler for efficient butt-coupling between compact planar waveguides and single-mode fibers. *Quantum Electronics, IEEE Journal of*, 38(7):949–955.
- [Taillaert et al., 2006] Taillaert, D., Laere, F. V., Ayre, M., Bogaerts, W., Thourhout, D. V., Bienstman, P., and Baets, R. (2006). Grating couplers for coupling between optical fibers and nanophotonic waveguides. *Japanese Journal of Applied Physics*, 45(8R):6071.
- [Tamir, 1988] Tamir, T. (1988). *Guided-Wave Optoelectronics*, volume 26 of Springer Series in Electronics and Photonics. Springer-Verlag, Berlin.
- [Tamir and Peng, 1977] Tamir, T. and Peng, S.-T. (1977). Analysis and design of grating couplers. *Applied physics*, 14(3):235–254.
- [Tripathi et al., 2010] Tripathi, S., Kumar, A., Marin, E., and Meunier, J.-P. (2010). Critical wavelength in the transmission spectrum of SMS fiber structure employing GeO-doped multimode fiber. *IEEE Photonics Technology Letters*, 22(11):799–801.

- [Van Laere et al., 2007] Van Laere, F., Roelkens, G., Ayre, M., Schrauwen, J., Taillaert, D., Van Thourhout, D., Krauss, T. F., and Baets, R. (2007). Compact and highly efficient grating couplers between optical fiber and nanophotonic waveguides. *Journal of Lightwave Technology*, 25(1):151–156.
- [Vermeulen et al., 2010] Vermeulen, D., Selvaraja, S., Verheyen, P., Lepage, G., Bogaerts, W., Absil, P., Van Thourhout, D., and Roelkens, G. (2010). High-efficiency fiber-to-chip grating couplers realized using an advanced CMOS-compatible silicon-on-insulator platform. *Optics Express*, 18(17):18278–18283.
- [Vivien et al., 2006] Vivien, L., Pascal, D., Lardenois, S., Marris-Morini, D., Cassan, E., Grillot, F., Laval, S., Fédéli, J.-M., and El Melhaoui, L. (2006). Light injection in SOI microwaveguides using high-efficiency grating couplers. *Journal of Lightwave technology*, 24(10):3810–3815.
- [Vollmer and Yang, 2012] Vollmer, F. and Yang, L. (2012). Label-free detection with high-Q microcavities: a review of biosensing mechanisms for integrated devices. *Nanophotonics*, 1(3-4):181–291.
- [Wang et al., 2012] Wang, M., Hiltunen, J., Liedert, C., Hakalahti, L., and Myllylä, R. (2012). An integrated Young interferometer based on UV-imprinted polymer waveguides for label-free biosensing applications. *Journal of the European Optical Society-Rapid publications*, 7.
- [Washburn and Bailey, 2011] Washburn, A. and Bailey, R. (2011). Photonics-on-a-chip: recent advances in integrated waveguides as enabling detection elements for real-world, lab-on-a-chip biosensing applications. *Analyst*, 136:227–236.
- [Washburn et al., 2009a] Washburn, A., Gunn, L., and Bailey, R. (2009a). Label-free quantitation of a cancer biomarker in complex media using silicon photonic microring resonators. *Analytical chemistry*, 81(22):9499–9506.
- [Washburn et al., 2009b] Washburn, A., Luchansky, M., Bowman, A., and Bailey, R. (2009b). Quantitative, label-free detection of five protein biomarkers using multiplexed arrays of silicon photonic microring resonators. *Analytical chemistry*, 82(1):69–72.
- [White and Fan, 2008] White, I. M. and Fan, X. (2008). On the performance quantification of resonant refractive index sensors. *Optics Express*, 16(2):1020–1028.
- [Wiki and Kunz, 2000] Wiki, M. and Kunz, R. (2000). Wavelength-interrogated optical sensor for biochemical applications. *Optics letters*, 25(7):463–465.
- [Wong and Olivo, 2014] Wong, C. and Olivo, M. (2014). Surface plasmon resonance imaging sensors: A review. *Plasmonics*, pages 1–16.
- [Xu et al., 2008] Xu, D., Densmore, A., Delâge, A., Waldron, P., McKinnon, R., Janz, S., Lapointe, J., Lopinski, G., Mischki, T., Post, E., et al. (2008). Folded cavity SOI microring sensors for high sensitivity and real time measurement of biomolecular binding. *Optics Express*, 16(19):15137–15148.

- [Xu et al., 2010] Xu, D.-X., Vachon, M., Densmore, A., Ma, R., Del  ge, A., Janz, S., Lapointe, J., Li, Y., Lopinski, G., Zhang, D., et al. (2010). Label-free biosensor array based on silicon-on-insulator ring resonators addressed using a wdm approach. *Optics letters*, 35(16):2771–2773.
- [Yang et al., 2014] Yang, T., Wang, T., Zheng, C., Wang, X., and Zhang, D. (2014). Linear response and enhanced sensitivity of Mach–Zehnder interferometer with optimized sensing length. *Microwave and Optical Technology Letters*, 56(7):1697–1701.
- [Ymeti et al., 2002] Ymeti, A., Kanger, J. S., Wijn, R., Lambeck, P., and Greve, J. (2002). Development of a multichannel integrated interferometer immunosensor. *Sensors and Actuators B*, 83(1-2):1–7.
- [Zhu et al., 2011] Zhu, H., Yaglidere, O., Su, T.-W., Tseng, D., and Ozcan, A. (2011). Cost-effective and compact wide-field fluorescent imaging on a cell-phone. *Lab on a Chip*, 11(2):315–322.
- [Zinoviev et al., 2008] Zinoviev, K., Carrascosa, L., del R  o, J. S., Sep  lveda, B., Dom  nguez, C., and Lechuga, L. (2008). Silicon photonic biosensors for lab-on-a-chip applications. *Advances in Optical Technologies*, 2008.
- [Zinoviev et al., 2011] Zinoviev, K., Gonzalez-Guerrero, A., Dom  nguez, C., and Lechuga, L. (2011). Integrated Bimodal Waveguide interferometric biosensor for label-free analysis. *Journal of Lightwave Technology*, 29(13):1926–1930.